

Sandy Suet To · Hao Wang  
Wing Bun Lee

# Materials Characterisation and Mechanism of Micro- Cutting in Ultra-Precision Diamond Turning

 Springer

Materials Characterisation and Mechanism  
of Micro-Cutting in Ultra-Precision  
Diamond Turning

Sandy Suet To · Hao Wang  
Wing Bun Lee

# Materials Characterisation and Mechanism of Micro-Cutting in Ultra-Precision Diamond Turning

 Springer

Sandy Suet To  
The Hong Kong Polytechnic University  
Hong Kong  
China

Wing Bun Lee  
The Hong Kong Polytechnic University  
Hong Kong  
China

Hao Wang  
National University of Singapore  
Singapore  
Singapore

ISBN 978-3-662-54821-9

ISBN 978-3-662-54823-3 (eBook)

DOI 10.1007/978-3-662-54823-3

Library of Congress Control Number: 2017939305

© Springer-Verlag GmbH Germany 2018

This work is subject to copyright. All rights are reserved by the Publisher, whether the whole or part of the material is concerned, specifically the rights of translation, reprinting, reuse of illustrations, recitation, broadcasting, reproduction on microfilms or in any other physical way, and transmission or information storage and retrieval, electronic adaptation, computer software, or by similar or dissimilar methodology now known or hereafter developed.

The use of general descriptive names, registered names, trademarks, service marks, etc. in this publication does not imply, even in the absence of a specific statement, that such names are exempt from the relevant protective laws and regulations and therefore free for general use.

The publisher, the authors and the editors are safe to assume that the advice and information in this book are believed to be true and accurate at the date of publication. Neither the publisher nor the authors or the editors give a warranty, express or implied, with respect to the material contained herein or for any errors or omissions that may have been made. The publisher remains neutral with regard to jurisdictional claims in published maps and institutional affiliations.

Printed on acid-free paper

This Springer imprint is published by Springer Nature

The registered company is Springer-Verlag GmbH Germany

The registered company address is: Heidelberger Platz 3, 14197 Berlin, Germany

# Preface

Ultra-precision single point diamond turning is a key technology in the manufacture of mechanical, optical and optoelectronics components with a surface roughness of a few nanometres and form accuracy in the sub-micrometric range. As a type of subtractive manufacturing, ultra-precision diamond turning technology was established on the pillars of materials science, machine tools, modelling and simulation technologies, etc., bestowing the intrinsic inter-disciplinary characteristics upon the study of such machining process. However, in contrast to the substantial advances that have been achieved in machine design, laser metrology and control systems, relatively little research has been conducted on material behaviour and its effect on surface finish, such as the material anisotropy of crystalline materials. The feature of the significantly reduced depth of cut of the order of a few micrometres or less, which is much smaller than the average grain size of work-piece materials, unavoidably renders the existing metal cutting theories to have only partial success in the investigation of the mechanism of the micro-cutting process in ultra-precision diamond turning. With such a background, this book is dedicated to an in-depth study and elucidation on the mechanism of the micro-cutting process, with a particular emphasis and a novel viewpoint on materials characterisation and its influences in ultraprecision machining.

This book probes into the two critical problems in ultra-precision diamond turning, i.e. materials characterisation and the mechanism of micro-cutting, and contributes to the development of metal cutting theory for ultraprecision diamond turning. As for the organisation of the book: In Chap. 1, an overview of ultra-precision machining technology and ultraprecision diamond turning is elaborated with the existing metal cutting theory tailor-made for conventional and precision machining and its unsolved problems. A detailed literature review on a variety of hot research topics in ultraprecision machining is presented in Chap. 2, which takes account of material characteristics and machinability, the mechanism of metal cutting, the dynamics of machine tools, surface generation and characterisation, modelling techniques, etc. This book began to unfold from the investigation on the machinability of single crystals in diamond turning in Chap. 3. The effect of crystallography on surface roughness and the variation in cutting force is studied by

the degree of roughness anisotropy (DRA) factor. The study of machined surface integrity and the deformation behaviour of diamond-turned surface layer is presented in Chap. 4, followed by the orientation changes of substrate materials that are characterised by X-ray texture study in Chap. 5. A novel technology involving electropulsing treatment (EPT) is explored to enhance the machinability of work materials in Chap. 6. A microplasticity analysis of shear angle and micro-cutting force variation is provided in Chap. 7. In Chap. 8, the mechanism of elastic strain induced shear bands and regularly space shear bands are presented and a generalised model for shear angle prediction is developed. In the final part of this book (Chap. 9), the high frequency tool-tip vibration and its effect on surface generation as well as the representative surface measurement method are presented. The integrated dynamic modelling of shear band formation and tool-tip vibration is elaborated in Chap. 10.

This book serves as a practical tool for investigating materials characterisation in ultra-precision machining with carefully documented experimental techniques and analytical methodology accumulated over the years through the authors' research endeavours. This book contributes to enhancing the understanding of the metal cutting theory of ultraprecision diamond turning from the perspective of materials science and machining dynamics. The multidisciplinary work in this book also covers the modelling approaches based on the theory of microplasticity.

The authors would like to thank the Research Committee and the Department of Industrial and Systems Engineering of The Hong Kong Polytechnic University and the Department of Mechanical Engineering, Faculty of Engineering, National University of Singapore for providing the financial support for this book. Many thanks are extended to the Guangdong Innovative Research Team Program and the National Natural Science Foundation of China for providing the partial financial support under the Project Nos. 201001G0104781202 and 51275434 respectively.

Hong Kong, China  
Singapore

Sandy Suet To  
Hao Wang

# Contents

## Part I Fundamentals

<b>1</b>	<b>Single Point Diamond Turning Technology</b> . . . . .	3
	References. . . . .	6
<b>2</b>	<b>Factors Influencing Machined Surface Quality</b> . . . . .	7
	2.1 Machine Tools . . . . .	7
	2.2 Vibration in Machining. . . . .	8
	2.3 Cutting Conditions . . . . .	9
	2.4 Single Point Diamond Tools. . . . .	11
	2.5 Environmental Conditions. . . . .	12
	2.6 Workpiece Materials. . . . .	13
	2.7 Deformation Behaviour of Materials in Machining. . . . .	15
	References. . . . .	17
<b>3</b>	<b>Modelling and Simulation for Ultra-Precision Machining</b> . . . . .	21
	3.1 Analytical and Numerical Methods for Machining Process Modelling. . . . .	21
	3.1.1 Slip-Line Field Modelling of Machining. . . . .	21
	3.1.2 Molecular Dynamics Simulation of Machining. . . . .	22
	3.1.3 Quasicontinuum (QC) Method . . . . .	23
	3.1.4 Meshfree Method . . . . .	24
	3.1.5 Discrete Element Method . . . . .	26
	3.1.6 Finite Element Method . . . . .	27
	3.2 Models of Chip Formation and Shear Bands Theory . . . . .	29
	3.2.1 The Chip Formation Process and Models in Metal Cutting . . . . .	29
	3.2.2 Shear Band Formation and Chip Morphology. . . . .	32
	3.2.3 The Shear Angle Relationship. . . . .	34
	References. . . . .	35

## **Part II Materials Characterisation in Ultra-Precision Diamond Turning**

<b>4</b>	<b>Machinability of Single Crystals in Diamond Turning</b> . . . . .	43
4.1	Key Aspects in Diamond Turning of Single Crystals . . . . .	43
4.1.1	The Ultra-Precision Machine. . . . .	43
4.1.2	Diamond Tools . . . . .	43
4.1.3	Measurement of Surface Roughness . . . . .	46
4.1.4	Measurement of Cutting Force . . . . .	50
4.1.5	Work Materials and Cutting Conditions . . . . .	50
4.2	Effect of Crystallography on Surface Roughness . . . . .	52
4.2.1	Surface Features with Crystallographic Orientation. . . . .	52
4.2.2	Surface Roughness Profiles Along Radial Sections. . . . .	56
4.2.3	Degree of Roughness Anisotropy (DRA) . . . . .	57
4.3	Variation of Cutting Force . . . . .	59
4.3.1	Effect of Feed Rate on the Cutting Force . . . . .	59
4.3.2	Effect of Depth of Cut on the Cutting Force. . . . .	60
4.4	Observation on Chip Formation . . . . .	61
	References. . . . .	68
<b>5</b>	<b>Materials Deformation Behaviour and Characterisation</b> . . . . .	71
5.1	Techniques for Materials Characterisation . . . . .	71
5.1.1	X-ray Diffraction. . . . .	71
5.1.2	Nano-indentation Measurements . . . . .	73
5.1.3	Nanoscratch Testing . . . . .	76
5.1.4	Transmission Electron Microscopy (TEM) . . . . .	77
5.2	Characterisation of the Diamond-Turned Surface Layer . . . . .	79
5.2.1	X-ray Diffraction Line Profile Analysis. . . . .	79
5.2.2	Microhardness and Elastic Modulus of Machined Surface . . . . .	79
5.2.3	Friction Coefficient . . . . .	81
5.2.4	Dislocation Density and Structure of Diamond-Turned Surface Layers . . . . .	82
5.3	Influences of Material Swelling upon Surface Roughness. . . . .	89
5.3.1	Materials Swelling Effect . . . . .	89
5.3.2	Characterisation Techniques . . . . .	95
5.3.3	Formation of Surface Roughness in Machining. . . . .	101
	References. . . . .	103
<b>6</b>	<b>Material Electropulsing Treatment and Characterisation of Machinability</b> . . . . .	105
6.1	Basics of Electropulsing Treatment. . . . .	106
6.1.1	Development of Electropulsing Treatment. . . . .	106
6.1.2	Theory of Electropulsing Treatment . . . . .	106



6.2	Effect of Electropulsing Treatment on Microstructural Changes . . . . .	112
6.2.1	Technical Aspects of Electropulsing Treatment. . . . .	112
6.2.2	Phase Transformation and Microstructural Changes . . . . .	116
6.2.3	Dislocation Identity . . . . .	127
6.2.4	Driving Forces for Phase Transformations . . . . .	129
6.2.5	Electropulsing Kinetics . . . . .	130
6.3	Machinability Enhancement by Electropulsing Treatment. . . . .	131
	References. . . . .	144
<b>7</b>	<b>Microplasticity Analysis for Materials Characterisation. . . . .</b>	<b>147</b>
7.1	Shear Angle and Micro-Cutting Force Prediction . . . . .	147
7.1.1	Microplasticity Model for Shear Angle Prediction . . . . .	147
7.1.2	Texture Softening Factor. . . . .	151
7.1.3	Criterion for Shear Angle Prediction. . . . .	154
7.1.4	Prediction of Micro-Cutting Forces Variation . . . . .	156
7.2	Variation in Shear Angle and Cutting Force. . . . .	159
7.2.1	Shear Angle Predictions and Experimental Methods . . . . .	160
7.2.2	Power Spectrum Analysis of Cutting Force. . . . .	168
7.3	Microstructural Characterisation of Deformation Banding . . . . .	175
7.3.1	Typical Cutting-Induced Shear Band. . . . .	175
7.3.2	Orthogonal Cutting-Induced Kink Band . . . . .	177
7.3.3	Cutting Induced Kinking Within the Sliding Region. . . . .	179
	References. . . . .	184
 <b>Part III Theory and Mechanism of Ultra-Precision Diamond Turning</b>		
<b>8</b>	<b>Shear Bands in Ultra-Precision Diamond Turning . . . . .</b>	<b>189</b>
8.1	Shear Band Theory for Deformation Processes in Machining. . . . .	189
8.2	Regularly Spaced Shear Bands and Morphology of Serrated Chips . . . . .	191
8.3	Finite Element Method Modelling for Elastic Strain-Induced Shear Bands . . . . .	197
8.3.1	Characterisation of Elastic Strain-Induced Shear Bands . . . . .	197
8.3.2	Finite Element Method Modelling. . . . .	198
8.4	Analytical Model of Shear Band Formation and Influences . . . . .	207
8.4.1	Onset of the Formation of Shear Bands . . . . .	208
8.4.2	Formation of Shear Bands. . . . .	210
8.4.3	An Analytical Model of Cyclic Fluctuation of Cutting Force . . . . .	211
8.4.4	The Cyclic Fluctuation of the Displacement of the Tool Tip . . . . .	213
8.5	Generalised Shear Angle Model . . . . .	215
	References. . . . .	217

<b>9</b>	<b>Tool-Tip Vibration at High Frequencies</b> . . . . .	219
9.1	Identification of Tool-Tip Vibration by Power Spectrum Analysis . . . . .	219
9.2	Characteristic Twin Peaks and Material Properties . . . . .	221
9.3	Modelling of Tool-Tip Vibration . . . . .	226
9.3.1	An Impact Model Without Damping . . . . .	226
9.3.2	Non-harmonic Periodic Excitation with Process Damping Effect . . . . .	229
9.4	Representative Measurement Method . . . . .	234
9.4.1	Influence of Tool-Tip Vibration on the Machined Surface . . . . .	234
9.4.2	Effect of Sample Locations on Surface Roughness . . . . .	240
9.4.3	Effect of Sample Area Ratios and Representative Measurement . . . . .	242
9.5	Modelling and Characterisation of Surface Roughness Generation . . . . .	246
9.5.1	Surface Generation Model with Tool-Tip Vibration . . . . .	246
9.5.2	Formation of Spiral Marks on the Machined Surface . . . . .	248
9.5.3	Spatial Error on the Profile in the Feed Direction . . . . .	250
	References . . . . .	250
<b>10</b>	<b>Dynamic Modelling of Shear Band Formation and Tool-Tip Vibration in Ultra-Precision Diamond Turning</b> . . . . .	253
10.1	A Transient Analysis for Shear Band Formation . . . . .	256
10.2	Dynamic Model for Shear Band Formation . . . . .	257
10.2.1	Dynamic Model . . . . .	257
10.2.2	The Effect of Equivalent Cutting Velocity . . . . .	259
10.2.3	Validation and Application . . . . .	260
	References . . . . .	265

**Part I**  
**Fundamentals**

# Chapter 1

## Single Point Diamond Turning Technology

**Abstract** Manufacturing with high precision is a development which has been gathering momentum over the last 200 years and accelerating over the last 30 years in terms of research, development and applications in product innovation. It has been driven by demands for much higher performance of products, higher reliability, longer life and miniaturisation. This development is widely known as precision engineering and today is generally understood as manufacturing to tolerances smaller than one part in  $10^4$  or perhaps one part in  $10^5$ . This chapter profiles the categorisation of machining processes with a highlight on the ultra-precision single point diamond turning technology.

Trent and Wright (2000) definition defines the term machining as chip-forming operations in the engineering industry, ranging from large-scale production to extremely delicate components (Fig. 1.1). In terms of achievable tolerance and part dimensions, machining processes can be categorised into normal machining, precision machining and ultra-precision machining, corresponding to specific industrial and/or scientific applications.

“Ultra-precision machining” means the achievement of dimensional tolerance of the order of  $0.01\ \mu\text{m}$  and surface roughness of  $0.001\ \mu\text{m}$  (1 nm). The dimensions of parts or elements of parts produced may be as small as  $1\ \mu\text{m}$  and the resolution and repeatability of the machines used must be in the order of  $0.01\ \mu\text{m}$  (10 nm) (Taniguchi 1983). These accuracy targets for today’s ultra-precision machining cannot be achieved by a simple extension of conventional machining process and techniques. Satisfying such high accuracy is one of the most important challenges facing the manufacturing engineering today. In fact, we have seen the development and introduction into practice of a whole new range of materials processing technologies for the manufacture of parts to this order of accuracy. A comprehensive review of the elements of machine tools, e.g. guideway bearings, displacement transducers/measuring equipment and servo-positioning techniques has been given by Taniguchi (1983) (Fig. 1.2).

The history of single point diamond turning (SPDT) technology started in the 1960s. In the early stages, SPDT was usually used to produce components with simple cylindrical or flat shapes to meet the demands of computers, electronics and

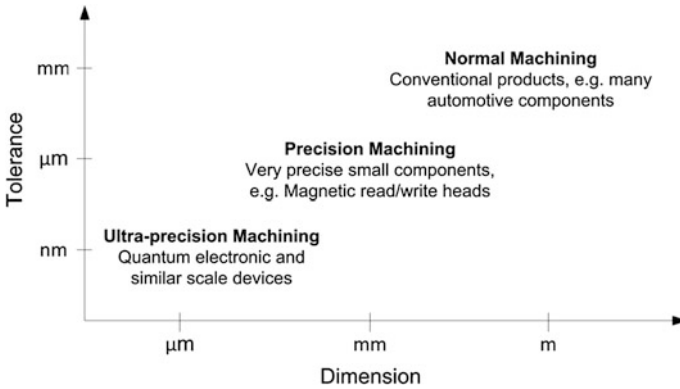


Fig. 1.1 Relationship between part dimension and dimensional tolerance for three groups of machining processes (Trent and Wright 2000)

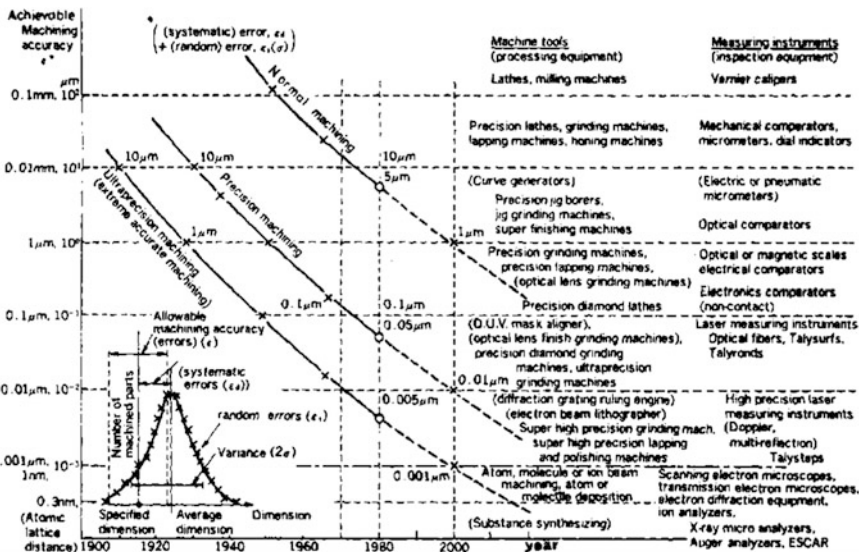


Fig. 1.2 The development of achievable accuracy (after Taniguchi 1983)

defence applications. Typical products were disks for computer memory systems. The pioneering work led by Bryan et al. (1967) was carried out in its application to optical components of complex forms at the Lawrence Livermore National Laboratory USA (Taniguchi 1983; Ikawa et al. 1991). The rapid development of diamond turning technology emerged in the USA and the UK in the 1970s. A high-quality mirror with a surface roughness  $0.01 \mu\text{m } R_{\text{max}}$  and with a profile accuracy of about  $0.1 \mu\text{m}$  was achieved. In the 1970s, the technique was applied to the production of a variety of optical components for its high precision, versatility and

low overall manufacturing cost. In the 1980s, the technique was extended to industrial use for the manufacturing of aluminium scanner mirrors, aluminium substrate drums in photocopying machines and aluminium substrates for computer memory disks, all of which require very fine surface finish of a few tens of nanometres roughness and micrometre to submicrometre form accuracy (To and Lee 1995; To et al. 2006a, b, c, 2007, 2008, 2013, 2015a, 2015b; To and Wang 2011). These extensive efforts have resulted in the development of highly advanced machine tools with sophisticated metrology and the control of diamond tools of reliable quality. Summaries of the machine tools developed for ultra-precision metal cutting research and manufacturers of the early complex components, together with the builders of ultraprecision machine tools are given by Taniguchi (1983) and McKeown (1997). Ultra-precision diamond cutting critically depends on a number of highly developed “subsystem” techniques, e.g. the machine tool, metrology and control, cutting tool, environmental control and machining strategies and software. A collection of representative SPDT machines at different development stages is shown in Fig. 1.3. The critical factors associated with ultra-precision diamond turning which directly affect the nanosurface generation are discussed in the forthcoming chapter.



**Fig. 1.3** From *top left* anticlockwise: ca 1975 Moore M18 DTM, Cranfield LDTM (1979), Cranfield NION DTM (1989) and Moore 500FG (1999). Courtesy of Moore, CUPE, CPE Ltd and Moore Nanotechnology Systems (reprinted from the work by Shore and Morantz 2012)

## References

- Bryan, J. B., Clauser, R. W., & Holland, E. (1967). Spindle accuracy. *American Machinist*, 4, 149.
- Ikawa, N., Donaldson, R. R., Komanduri, R., König, W., Aachen, T. H., McKeown, P. A., et al. (1991). Ultraprecision metal cutting—the past, the present and the future. *Annals of the CIRP*, 40, 587–594.
- McKeown, P. A. (1997). *From precision to micro and nano-technologies*. Nanotechnology, UNIDO Emerging Technology Series (p. 1).
- Shore, P., & Morantz, P. (2012). Ultra-precision: enabling our future. *Philosophical Transactions of the Royal Society A*, 370, 3993–4014.
- Taniguchi, N. (1983). Current status in, and future trends of, ultraprecision machining and ultrafine materials processing. *Annals of the CIRP*, 32(2), 573.
- To, S., & Lee, W. B. (1995). *A study of the surface microtopography of aluminium alloys in single point diamond turning*. America Society of Precision Engineering (ASPE) (pp. 124) (October 15–20).
- To, S., & Wang, H. (2011). Finite element modelling of squeezing effect in ultra precision diamond turning. *Materials Research Innovations*, 15(suppl. 1), S175–S178.
- To, S., Wang, E. Q., Lee, W. B., & Cheung, C. F. (2006a). A study of a digital manufacturing procedure for freeform optics. *Materials Science Forum*, 532–533, 693–696.
- To, S., Wang, E. Q., Lee, W. B., & Cheung, C. F. (2006b). Investigation into virtual manufacturing procedure for freeform optics. *Journal of Applied Optics*, 27(6), 485–490. (in Chinese).
- To, S., Wang, E. Q., Lee, W. B., & Cheung, C. F. (2007). Investigation on error factor of injection molding plastic for freeform optics. *Journal of Applied Optics*, 28(6), 684–688. (in Chinese).
- To, S., Wang, H., Li, B., & Cheung, C. F. (2008). An empirical approach for identification of sources of machining errors in ultra-precision raster milling. *Key Engineering Materials*, 364–366, 986–991.
- To, S., Wang, H., Li, B., Cheung, C. F., & Wang, S. J. (2006c). Study on the tool path generation of an automotive headlamp reflector in ultra-precision raster milling. *Materials Science Forum*, 532–533, 673–676.
- To, S., Wang, H., & Jelenković, E. V. (2013). Enhancement of the machinability of silicon by hydrogen ion implantation for ultra-precision micro-cutting. *International Journal of Machine Tools and Manufacture*, 74, 50–55.
- To, S., Zhu, Z. W. & Wang, P. (2015a). Evolutionary diamond turning of optics for error correction covering a wide spatial spectrum. *Optical Engineering*, 54, No. 1, paper no. 015103.
- To, S., Zhu, Z. W. & Zeng, W. H. (2015b). Novel end-fly-cutting-servo system for deterministic generation of hierarchical micro–nanostructures. *CIRP Annals - Manufacturing Technology*, 64, Issue 1, pp. 133–136.
- Trent, E. M. & Wright, P. K. (2000). *Metal cutting*, 4th edn (pp. 98–102).

# Chapter 2

## Factors Influencing Machined Surface Quality

**Abstract** Ultra-precision diamond turning aims at producing advanced components with not only a high-dimensional accuracy but also a good surface roughness and form accuracy. Since the achievable machining accuracy is governed by the accuracy of the relative motion between the cutting edge and the workpiece, the performance of machine tools is of prime importance. Optimum conditions of factors such as machine tools, cutting tools, workpiece materials, cutting variables, cutting fluid, working environment, etc., need to be chosen to achieve a good result in diamond turning. This chapter elaborates all these key factors influencing the machined surface finish.

### 2.1 Machine Tools

In diamond turning, as in any metal cutting operation, the geometry of the cutting tool and the characteristics of the machine tool determine the achievable form accuracy and surface finish. Improvements in surface finish and form accuracy in diamond turning have depended mainly upon advances in the design of the machine tool. In the early stages of development of ultra-precision cutting, hydrostatic bearings (either gas or fluid) for machine tool spindles played a dominating role through their ability to operate at submicron rotational accuracy. The development of air bearing spindles in the 1960s most significantly affected progress in ultra-precision machining (Krauskopf 1984; Ikawa et al. 1991). The introduction of machine tools with high stiffness, laser position feedback, hydrostatic slideways, materials with high thermal stability and techniques to characterise machine tool errors have also improved the diamond turning process. Along with the refinement of conventional mechanical elements in machine tools, new designs have arisen; traction or friction drives for linear motion and positioning with nanometric resolution (Bryan 1979; Donaldson and Patterson 1983; Shimokohbe et al. 1989), piezoelectric microfeed devices for nanometric tool positioning (Patterson and Magrab 1985) and the error compensation of hydrostatic bearings (Kanai 1983; Shimokohbe et al. 1989).



## 2.2 Vibration in Machining

For decades, vibration has been recognised in the force measurement of real cutting processes such as conventional machining, high-speed machining (HSM) and ultra-precision machining. Based on these vibration signals, a branch of research work focused on the sources of nonlinearities and chatter generation, in which the single-degree-of-freedom (SDOF) and the multi-degree-of-freedom (MDOF) dynamic models of cutting system are employed. Such models are capable of determining the stability of the cutting system, i.e. the transition between stable cutting and chatter vibration with regard to the change of cutting parameters, such as depth of cut and spindle speed (Wiercigroch and Budak 2001). The starting points of such dynamic models are the nonlinearities in metal cutting systems.

Early work in such area was done by Wu (1986) to model the shear angle oscillation in dynamic orthogonal cutting based on the work-hardening slip line field theory. Wiercigroch and Budak (2001) proposed a closed-loop model of dynamic and thermodynamic interaction in the metal cutting system. They investigated the four mechanisms of machining chatter: variable friction, regenerative cutting, mode coupling, and the thermomechanics of chip formation on the variation of shear angles in the course of machining. Moon and Kalmar-Nagy (2001) reviewed the prediction of complex, unsteady and chaotic dynamics associated with the material cutting process through nonlinear dynamical models. The developed dynamic models of cutting systems have been widely applied in the prediction and monitoring of system stability (Liu et al. 2004b; Schmitz et al. 2001; Khraisheh et al. 1995; Chae et al. 2006; Berger et al. 1998). Complex mathematical tools have been employed to establish the nonlinear models, such as Receptance Coupling Substructure Analysis (RCSA) (Schmitz et al. 2001), and wavelet decomposition (Berger et al. 1998). Khraisheh et al. (1995) used wavelet transform with the traditional Gaussian wavelet, phase plane, power spectrum, Poincaré map and fractal dimensions to analyse the experimental data to ascertain system stability and cutting status. Vela-Martinez et al. (2008) used a multiple degree of freedom model for chatter prediction in turning. Abouelatta and Madl (2001) used a regression method to find a correlation between surface roughness and cutting vibrations in turning, while Baker and Rough (2002) used the finite element method (FEM) to include both cutting tool and workpiece flexibility in the analysis.

The correlation between vibration and surface roughness has become another focus of research. Abouelatta and Madl (2001) employed a mathematical tool to analyse the vibration and surface roughness data obtained in a series of cutting experiments. The proposed correlation model did not take account of the material removal mechanism in metal cutting process; therefore, no physical model was sought to explain the vibration effect on surface roughness of the machined surface. Cheung and Lee (2000a, b) proposed a surface roughness simulation model which considered the effect of process parameters, tool geometry and relative vibration between the tool and the workpiece. The authors assumed that the relative vibration between the tool and the workpiece was a steady simple harmonic motion with

small amplitude and a low frequency. The same low frequency range has also been investigated by Sze et al. (2006), Lee et al. (2002), among others. Moreover, only the relative vibration in the infeed cutting direction was considered which was adopted from the assumptions made by Takasu et al. (1985) and Bispink (1992), while the influences of self-excited chatter and tool wear were neglected. Their investigated vibration frequency range belonged to a very low part of the entire spectrum. Those frequencies above 10 kHz were neglected in both the experimental work (Liu et al. 2004b) and the simulation models (Takasu et al. 1985). In addition to the common understanding that the relative vibration in the infeed (thrust force) cutting direction (Cheung and Lee 2000b) was regarded as a predominant factor in the generation of good surface finish, the effect of relative vibration in the cutting direction also significantly contributes to surface generation which was featured by high-frequency tool-tip vibration (HFTTV) (Wang et al. 2010b).

In light of the fact that materials behave differently in material removal due to their mechanical and thermal properties, work material also plays a critical role in the study of machining processes. Material swelling and recovery have attracted a lot of attention due to its influence on surface roughness in the micro-cutting process. To et al. (2001) clarified the concept of material swelling, and elaborated on the influence of material swelling based on the measured surface profile in diamond turning of single crystal materials. The plastically deformed material underwent an elastic recovery behind the cutting edge (on the clearance face of the cutting tools) to form the freshly cut surface. Liu et al. (2004a) reviewed such elastoplastic deformation in the micromachining process, and proposed two mechanisms—chip removal and ploughing/rubbing. The ploughing effect, which is induced by the cutting edge radius and tool wear, is of great importance in the analysis of cutting mechanism and chip formation. Guo and Chou (2004) studied the ploughing force based on the data of cutting forces acquired in the metal cutting experiments with a large uncut chip thickness ranging from 0.03 to 0.2 mm, and at very slow (0.073 m/s) and medium (1 m/s) cutting speeds. The induced elasticity and the swelling/recovery effects in work materials were pronounced, so that the ploughing force could be clearly observed in their experiments. In the research by Shawky and Elbestawi (1997), the ploughing force was regarded as the source of process damping embedded in their dynamic model of tool vibration in the conventional turning process. In single point diamond turning (SPDT), a large strain rate and a small depth of cut are guaranteed by the accuracy of ultra-precision machine tools, which in turn results in the ploughing effect being less pronounced in SPDT than that in conventional machining.

### 2.3 Cutting Conditions

It is well known that the machined surface finish and form accuracy are produced as a result of the transfer of the tool profile onto a workpiece; hence, the level of the roughness is governed by the controllability of the relative motion between the

cutting tool and workpiece. The state and dynamic behaviour of an ultra-precision machine is a dominant parameter for attaining a high surface quality (Weck and Hartel 1986; Weck and Modemann 1987, 1988; Takasu et al. 1985). The machined surface roughness of non-ferrous metals using diamond tools was found to be larger than the theoretical geometrical surface roughness derived from the tool geometry and the feed rate (Kobayshi 1978). A reason for this phenomenon was that the steady, small amplitude vibration between the cutting tool and the workpiece surface caused the deterioration of the machined surface (Takasu et al. 1985). In many practical setups for ultra-precision machining, a few tens of nm peak-to-valley ( $P-V$ ) roughness might be a practically achievable limit due to the combined effects of a variety of error sources.

Proper selection of cutting variables not only increases the manufacturing efficiency but also influences the surface roughness of the workpiece. Optimum conditions such as cutting speed, feed rate and depth of cut are essential in order to achieve a good surface finish. In general, the surface roughness of a workpiece is of small value when the cutting speed is either very high or low. If the cutting speed is within a range that produces a built-up edge (BUE), the machined surface roughness is always comparatively large. Machined surface roughness is closely related to an even rotational speed of every machine tool at each designated speed. It is suggested that the best way for precision cutting is to select the optimum cutting speed in an assumed range by testing the roughness obtained for every rotational speed of the spindle. As a general rule, the smaller the feed rate, the smaller the machined surface roughness. However, in precision and ultra-precision cutting, whether a diamond tool or carbide tool is used, the machined surface roughness will again increase if the feed rate is smaller than a certain critical value. This is because at a too slow feed rate the feeding mechanism of the machine tool is apt to produce stick-slip motion. Therefore, there is an optimum value for feed, and this can be determined individually by experimental methods (Zhang 1986). With the increase of depth of cut, the contact length of the cutting edge with the workpiece being cut increases, thus increasing the cutting force. The temperature in the cutting zone shows little change, because the dissipation of heat from the cutting edge is improved with an increase in depth of cut. As the depth of cut decreases to a certain value, the machined surface roughness starts to increase. This is because the metal layer being cut becomes too thin to be cut off; the squeezing action on the workpiece by the rounded portion of the cutting edge (tool edge radius) is intensified, thus increasing the friction, deformation volume, and the machined surface roughness accordingly. The fine depths of cut (submicrometre), finite edge radius of the tool, low ratio of depth of cut to the edge radius, quality of cutting edge, and even minute amounts of wear on the clearance face of the tool add to the complexity of the ultra-precision machining process.

Arcona (1996) summarised the studies on the tool force, chip formation, and surface finish in diamond turning. The measured tool force contains useful information on cutting parameters and tool condition which influences the finish of the machined surface. An empirical tool force model was developed by Arcona and

Dow (1998) for tool force feedback. The important material-related data such as the coefficient of friction and shear angle have to be determined experimentally and a truly predictive theory was not yet attempted in these early works.

## 2.4 Single Point Diamond Tools

Cutting tools directly affect machining quality and manufacturing efficiency. The sharpness of a cutting edge is a primary factor which determines the minimum depth of cut. The sharper the cutting edge, the smaller the minimum depth of cut and hence lower surface roughness (Ikawa et al. 1987; Zhang 1986). High-quality cutting tools that can produce very fine chips are essential for machining components to a high-dimensional accuracy and surface quality. Natural single point diamond tools are exclusively used in micro-cutting for their nanometric edge sharpness, form reproducibility and wear resistance. They are recognised to be ideal ultra-precision cutting tools. The design, manufacturing and proper use of diamond tools are among the key elements of the single point diamond turning (SPDT) technique.

The cutting tool in ultra-precision machining systems must have the capability of stable cutting in the submicron/nanometre region, e.g. in diamond cutting aluminium substrates for X-ray telescope optics. The surface finish and form accuracy are influenced by the tool sharpness and its stability. Small increases in the temperature of the tool shank due to tool wear and the associated increase in the specific cutting energy affect the machining accuracy (Moriwaki et al. 1990). Tool sharpness has a further effect on diamond-turned surfaces through the minimum chip thickness, or the depth of cut at which no chip forms due to the finite edge radius of the tool. The rounded cutting edge radius of diamond tools may be as small as 0.01  $\mu\text{m}$ , but cutting tools made of other materials cannot be sharpened to such an extent due to their structural restriction, and their cutting edge roughness is also limited for the same reason. Therefore, the performance of other tool materials on the machined surface finish cannot be as good as a diamond tool. There may be a physical limitation in the radius of the cutting edge or the cutting edge sharpness. Based on the energy balance between the surface and elastic strain energies at the cutting edge, the critical edge radius of diamond tools was calculated to be about 2 nm. From these observations, it is considered that the cutting edge of diamond tools can be polished to a radius less than a few nanometres, and the possible minimum depth of cut can be of the same order.

The profile of a machined surface is basically composed of the repetition of the tool profile transferred in the plane normal to the cutting direction; therefore, the geometrical accuracy of the cutting edge and its stability have a great influence on the machined surface roughness. The process of profile transfer will be disturbed due to the complicated and unidentified interfacial phenomena between the cutting edges and workpiece materials, such as interfacial affinity. As diamond has little

affinity for a variety of materials, a diamond cutting edge is considered to have high transfer fidelity, which is the ability to transfer the profile of a cutting edge to a work surface.

Even when machining soft materials such as non-ferrous metal, the wear on the cutting edge grows substantially as the cutting length increases (Ko and Cho 1992; Taminau and Dautzenberg 1991; Keen 1971; Hara 1988). It is generally recognised that the tool wear has a great influence on the cutting force and the quality of the machined surface. A less sharp tool will lead to higher cutting forces, and hence more power dissipation in the cutting process and more heat development (Lucca et al. 1990; Komanduri and Shaw 1975; 1976; Evans 1991). Cutting with a blunt tool therefore decreases the machining accuracy.

Ultra-precision diamond tools, which are used to produce high-precision optical components, should be not only sharp but also highly accurate in regard to cutting edge geometry. Accurate measurement of the cutting edge radius is needed in the manufacture and assessment of diamond tools. Edge structure is said to be preferably evaluated by an SEM (Scanning Electron Microscope) in terms both of topography and in establishing the cutting edge radius down to a few tens of nm (Asai et al. 1990). The profile accuracy of the cutting edge also has a great influence on the machine surface quality. With natural and synthetic single crystal diamonds, diamond tools are manufactured with various geometries for different applications like diffractive tools, milling tools, half-radius tools, etc. (Fig. 2.1)

## 2.5 Environmental Conditions

The achievable surface finish and form accuracy are dependent upon the stability of the machining environment. Any minute changes in the machining environment may cause a considerable variation in the machining accuracy. Variations in the temperature and delivery of the coolant can lead to form errors. The surface can be degraded through any motion that affects the relative position of the tool and workpiece. The sources of such disturbances can be acoustic vibrations, electrical noise, spindle runout, slideway vibration or inhomogeneity of the workpiece

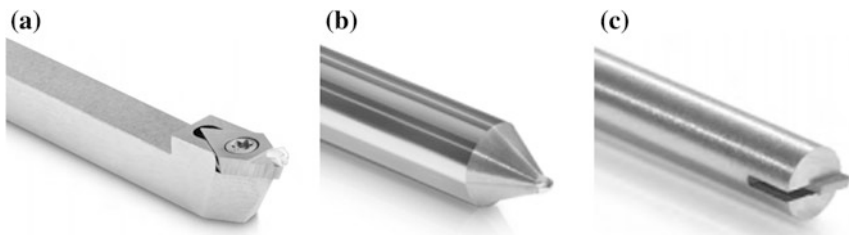


**Fig. 2.1** Typical diamond tools for (a) diamond turning (lens tool), (b) ball end milling, and (c) toric milling tool. *Courtesy Contour Fine Tooling Company*

material that produces high-frequency variations in the cutting forces and tool vibration. The stiffness of the machine tool also influences the characteristics of the machine surface. The currently available ultra-precision diamond turning machines are usually installed in large air-conditioned and vibration-isolated rooms to control the vibration, temperature, moisture and also cleanliness. A completely stable diamond turning environment is often difficult and costly to maintain. In an extended period of time required for a specific manufacturing operation, thermal deformation of the whole ultraprecision cutting system will have an adverse effect on the achievable machining accuracy (Moriwaki 1990).

In the study of the changing environment in the cutting process, power spectrum analysis is becoming a powerful tool to identify degenerating manufacturing conditions either due to process faults (such as tool wear) or machine tool problems (such as vibration, slideway error, etc.) (Whitehouse 1994). From the spectral information below the feed frequency, a tremendous amount of information about the process and machine tool is available, such as bearing chatter, slideway error and vibration external to the machine. Some of the longer wavelengths occurring in the subharmonic region of the power spectrum are illustrated in Fig. 2.2.

## 2.6 Workpiece Materials

The material removal process is not governed solely by the cutting tool but also critically by the material of the workpiece. The proper selection of work materials gives acceptable machinability which results in the desired nanometric surface finish. At present, typical materials that can be successfully machined are copper alloys, aluminium alloys, nickel alloys, silver, gold, electroless nickel, PMMA plastics and some of the infrared materials such as silicon and germanium. Ferrous materials such as steels cannot be diamond turned due to the rapid tool wear caused by the chemical affinity between the diamond tool and workpiece. Silicon and germanium are brittle materials and machining has to be done in the ductile regime, i.e. below a critical depth of cut to avoid crack propagation.

The crystallography of the workpiece substrate has also drawn much interest in order to optimise the surface finish (Koenig and Spermath 1991; Lee and Zhou 1993). In general, a material with fine grain size is preferred to eliminate the grain boundary effect. An amorphous material is most desirable as it is considered to possess a high degree of homogeneity and can give a superfinish with diamond turning. Single crystals and polycrystals, which exhibit strong crystallographic textures (i.e. highly directional properties), are to be avoided in coaxial machining processes such as turning operations. But for non-coaxial machining processes such as fly cutting, the best crystallographic cutting direction should be selected (e.g. the cutting of KDP single crystals used in laser optics). Despite the importance of the effect of material crystallography and anisotropy on the diamond turning process, there is still no scientific model or quantitative theory to predict the optimum crystallography cutting direction and our knowledge in this area is still largely empirical.

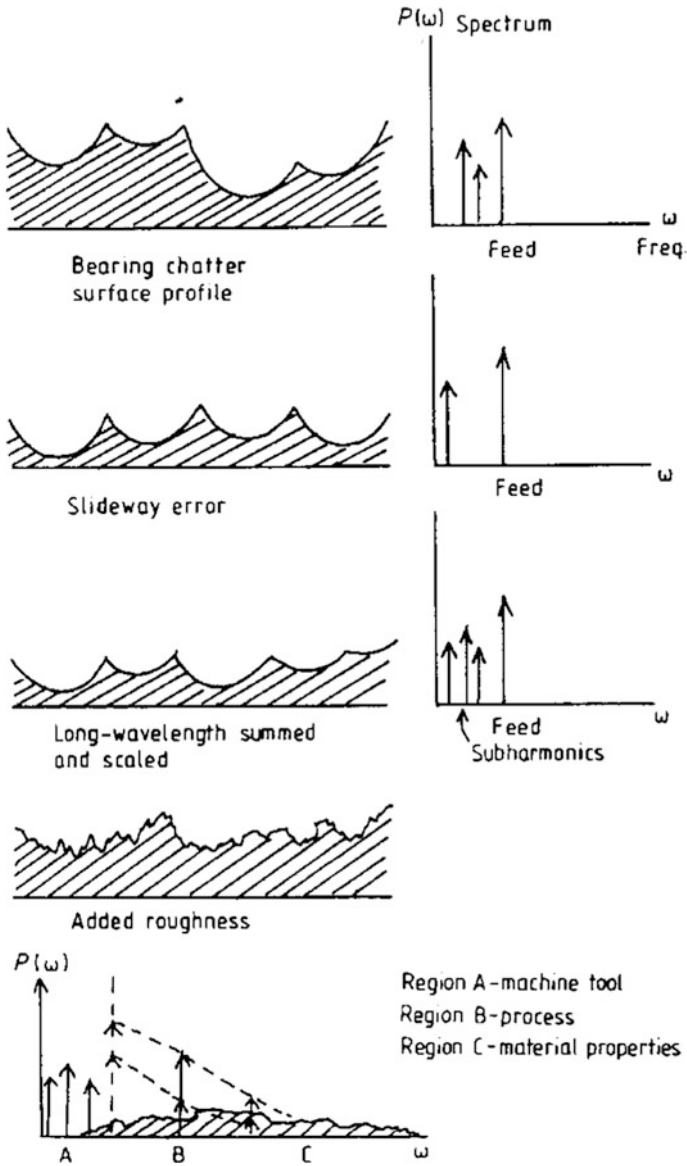


Fig. 2.2 Long-wavelength effect and total signature. A, subharmonic machine tool; B, harmonic tool wear; C, high-frequency material process parameters. From Whitehouse (1994)

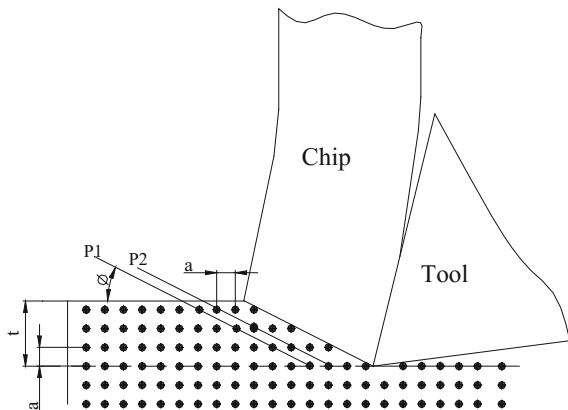
## 2.7 Deformation Behaviour of Materials in Machining

The chip removal process in diamond turning can be classified into two types. One is due to plastic deformation on the dislocation slip planes and the other is due to cleavage fracture on the cleavage plane. Ductile region machining is possible in brittle materials at a critical depth of cut where the energy in propagating cracks equals the energy of plastic deformation. A better understanding of the basic plastic behaviour at the micrometre and submicrometre undeformed chip thickness is vital for understanding the formation of the chip model at this level of cut. The plastic behaviour and properties that were thought important in influencing the metal cutting process have been summarised by Shaw (1984). A mechanism for large strain plastic flow was proposed by Shaw et al. (1953) which was considered as an add-on to dislocation theory (Taylor 1938). Crystal imperfections were reckoned to be reasons for the inhomogeneous strain. In metal cutting, the shear planes were thought to be very closely spaced corresponding to the closeness of spacing of the “weak spots” in the metal. Figure 2.3 shows a specimen with a uniform distribution of weak points with a spacing of  $a$ . The amount of slip on a given shear plane is determined by the shear strain ( $\gamma$ ):

$$[X = \frac{a^2 \sin \phi}{t} \gamma] \quad (2.1)$$

The relationship in Eq. (2.1) was then used by Shaw to estimate the shear stress on shear plane with  $[(\gamma \sin \theta)/2t]$ . The model, although grossly oversimplified, served to explain the change in specific cutting energy with undeformed chip thickness ( $t$ ) and the backs of thin chips showing inhomogeneous strain. The shear front-lamellar structure in metal cutting chips has been studied by Black (1971, 1972) in detail using transmission electron microscopy. The shear plane was thought to be a dislocated glide plane (i.e.  $\{111\} \langle 110 \rangle$  in FCC metals). When the primary slip system does not coincide with the direction of maximum strain,

**Fig. 2.3** Specimen with uniform distribution of points of stress concentration (weak points). After Shaw (1950)





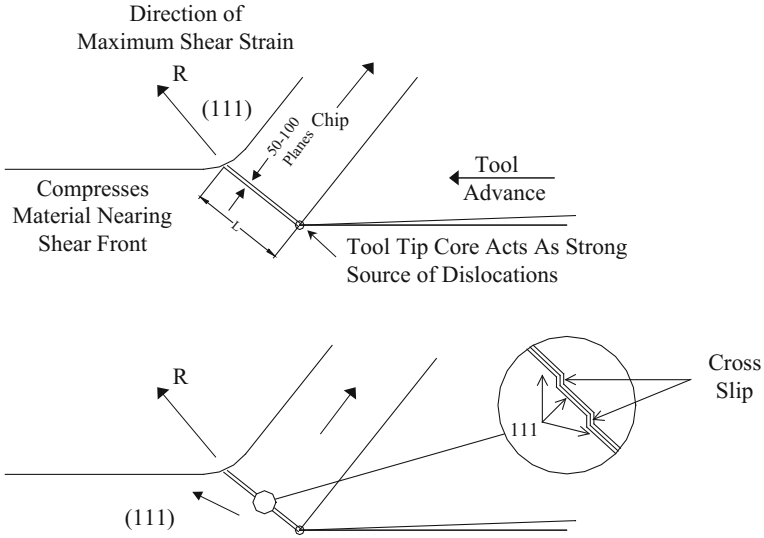


**Fig. 2.4** The effect of cross slipping of the dislocations from one parallel (111) plane to another when the direction of maximum strain does not coincide well with the {111} plane. From Black (1971)

cross-slipping of the dislocation from one parallel (111) plane to another will then occur (Fig. 2.4). Most researchers since the 70s have thought that (111) planes played a dominant role in the formation of the shear plane in metal cutting, although it was also recognised by Williams and Gare (1977) that other planes with a less favourable orientation also serve as shear planes. The possibility of a simple model to predict the shear angle was ruled out by Shaw (1984).

Although the crystallographic aspect of the deformation process was well recognised, it was not until the widespread use of ultra-precision diamond turning technology that the importance of the material imperfection and crystal plasticity emerged once again. The role of imperfections in diamond turning was discussed by Hashimoto (1989). Figure 2.5 shows the imperfections in materials that influence micromachining.

As the cutting proceeds, the material will be plastically deformed, triggered by microscopic defects such as precipitates, the generation of dislocations, voids, etc. It can be seen from Fig. 2.5 that the cutting process leads to a multiplication of defects, a considerable number of which will remain in the subsurface layer and will thus influence the integrity of the surface (Iwata and Ueda 1974, 1976; Brown and Luong 1976; LeMaitre and Bizeul 1974). These defects include not only dislocations but also fine cracks, cavities, delamination and cracked particles which may have lost their binding power to the base material.

The crystallographic orientation of the substrate material being cut exerts a great influence on the micromachining process (Koenig and Spenrath 1991; Sato et al. 1978, 1983; Stadler et al. 1987; Ohmori and Takada 1982). As the depth of cut in

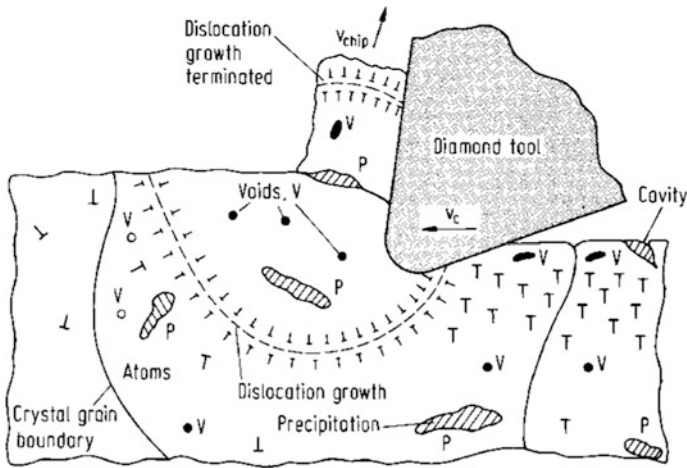


Fig. 2.5 Imperfections in materials that influence micromachining. From Hashimoto (1989)

ultra-precision cutting is usually less than the average grain size of a polycrystalline aggregate, cutting is generally performed within a grain. The polycrystalline workpiece material, which may be considered to be an isotropic and homogeneous continuum in conventional analysis, must be treated as a series of single crystals which usually have quite random orientations and anisotropic properties. Therefore, the machined surface quality and the mechanism of chip formation depend very much on the crystallographic orientation of the material being cut (Whitehouse 1994). The effect of crystallographic orientation on the surface quality cannot be avoided in the cutting of polycrystalline materials.

## References

- Abouelatta, O. B., & Mádl, J. (2001). Surface roughness prediction based on cutting parameters and tool vibrations in turning operations. *Journal of Materials Processing Technology*, 118, 269–277.
- Arcona, C. (1996). *Tool force, chip formation and surface finish in diamond turning*. PhD thesis, North Carolina State University, p. 1.
- Arcona, C., & Dow, T. A. (1998). An empirical tool force model for precision machining. *Journal of Manufacturing Science and Engineering*, 120, 700.
- Asai, S., Taguchi, Y., Horio, K., & Kasai, T. (1990). Measuring the very small cutting edge radius for a diamond tool using a new kind of SEM having two detectors. *Annals of the CIRP*, 39(1), 85.
- Baker, J. R., & Rough, K. E. (2002). Use of finite element structural models in analyzing machine tool chatter. *Finite Elements in Analysis and Design*, 38, 1029–1046.
- Berger, B. S., Minis, L., Harley, J., Rokni, M., & Papadopoulos, M. (1998). Wavelet based cutting state identification. *Journal of Sound and Vibration*, 213, 813–827.

- Bispink, T. (1992). Performance analysis of feed-drive systems in diamond-turning by machining specified test samples. *Annals of the CIRP*, 41, 601–604.
- Black, J. T. (1971). On the fundamental mechanism of large strain plastic deformation. *Journal of Engineering for Industry*, 93, 507.
- Black, J. T. (1972). Shear front-lamella structures in large strain plastic deformation processes. *Journal of Engineering for Industry*, 94(2), 307.
- Brown, R. H., & Luong, H. S. (1976). The influence of microstructure discontinuities on chip formation. *Annals of CIRP*, 25, 49.
- Bryan, J. B. (1979). Design and construction of an ultraprecision 84 in diamond turning machine. *Precision Engineering*, 1, 13.
- Chae, J., Park, S. S., & Freiheit, T. (2006). Investigation of micro-cutting operations. *International Journal of Machine Tools and Manufacture*, 46, 313–332.
- Cheung, C. F., & Lee, W. B. (2000a). A multi-spectrum analysis of surface roughness formation in ultra-precision machining. *Precision Engineering*, 24, 77–87.
- Cheung, C. F., & Lee, W. B. (2000b). A theoretical and experimental investigation of surface roughness formation in ultra-precision diamond turning. *International Journal of Machine Tools and Manufacture*, 40, 979–1002.
- Donaldson, R. R., Patterson, S. R. (1983). Design and construction of a large vertical axis diamond turning machine. Proc. SPIE, p. 433
- Evans, C. (1991). Cryogenic diamond turning of stainless steel. *Annals of CIRP*, 40, 571.
- Guo, Y. B., & Chou, Y. K. (2004). The determination of ploughing force and its influence on material properties in metal cutting. *Journal of Materials Processing Technology*, 148, 368–375.
- Hara, N. (1988). Study on estimating characteristics of natural diamond tools. In *Proceedings of the Spring Conference on JSPE*, p. 391 (in Japanese).
- Hashimoto, (1989). *Proceedings of 4th International Precision Engineering Seminar*, Monteey, USA.
- Ikawa, N., Shimada, S., & Morooka, H. (1987). Technology of diamond tool for ultraprecision metal cutting. *Bulletin of the Japan Society of Precision Engineering*, 21, 233.
- Ikawa, N., Shimada, S., Tanaka, H., & Ohmori, G. (1991). An atomistic analysis of nanometric chip removal process as affected by tool—Work interaction in diamond turning. *Annals of the CIRP*, 44(1), 551.
- Iwata, K., Ueda, K. (1974). Dynamic behaviour of manganese sulphide inclusions in machining under scanning electron microscope observation. In *Proceedings of the 1st International Conference On Production Engineering*, Tokyo, Japan, p. 516.
- Iwata, K., & Ueda, K. (1976). The significance of dynamic crack behaviour in chip formation. *Annals of CIRP*, 25, 65.
- Kanai, A. (1983). Nanometer positioning characteristics of closed looped differential hydro or Aerostatic actuator. *Annals of the CIRP*, 32(1), 287.
- Keen, D. (1971). Some observation on the wear of diamond tools used in piston machining. *Wear*, 17, 195.
- Khraisheh, M. K., Pezeshki, C., & Bayoumi, A. E. (1995). Time series based analysis for primary chatter in metal cutting. *Journal of Sound and Vibration*, 180, 67–87.
- Ko, T. J., & Cho, D. W. (1992). Fuzzy pattern recognition for tool wear monitoring in diamond turning. *Annals of CIRP*, 41, 125.
- Kobayashi, A. (1978). High precision cutting with a new ultraprecision spindle. *Annals of the CIRP*, 27, 283.
- Komanduri, R., & Shaw, M. C. (1975). Wear of synthetic diamond when grinding ferrous materials. *Nature*, 255, 211.
- Komanduri, R., & Shaw, M. C. (1976). On the diffusion wear of diamond in grinding pure iron. *Philosophical Magazine*, 34, 195.
- König, W., & Spenrath, N. (1991). The influence of the crystallographic structure of the substrate material on surface quality and cutting forces in micromachining. In *Proceedings of the 6th International Precision Engineering Seminar*, Braunschweig, Germany, p. 141.

- Krauskopf, B. (1984). Diamond turning: Reflection demand for precision. *Manufacturing Engineering*, 92, 90.
- Lee, W. B., Cheung, C. F., & To, S. (2002). A microplasticity analysis of micro-cutting force variation in ultra-precision diamond turning. *Journal of Manufacturing Science and Engineering*, 124, 170–177.
- Lee, W. B., & Zhou, M. (1993). A theoretical analysis of the effect of crystallographic orientation on chip formation in micro-machining. *International Journal of Machine Tools and Manufacture*, 33(3), 439.
- LeMaitre, F., & Bizeul, D. (1974). Contribution to the study of periodic phenomena in dynamic deformations. *Annals of the CIRP*, 23, p. 5.
- Liu, X., DeVor, R. E., & Kappor, S. G. (2004a). The mechanics of machining at the microscale: Assessment of the current state of the science. *Transaction of ASME, Journal of Manufacturing Science and Engineering*, 126, 666–678.
- Liu, X., Jun, M. B. G., DeVor, R. E., & Kapoor, S. G. (2004b). Cutting mechanisms and their influence on dynamic forces, vibrations and stability in micro-endmilling. In *Proceedings of the ASME Manufacturing Engineering Division (MED-15), ASME International Mechanical Engineering Congress and Exposition, Anaheim CA*, Paper no. IMECE2004–62416.
- Lucca, D. A., Rhorer, R. L., & Komanduri, R. (1990). Energy dissipation in the ultra-precision machining of copper. *Annals of the CIRP*, 40(1), 69.
- Moon, F. C., & Kalmár-Nagy, T. (2001). Nonlinear models for complex dynamics in cutting materials. *Philosophical Transactions of the Royal Society of London A*, 359, 695–711.
- Moriwaki, T., Horiuchi, A., & Okuda, K. (1990). Effect of cutting heat on machining accuracy in ultraprecision diamond turning. *Annals of the CIRP*, 39(1), 81.
- Patterson, S.R., Magrab, E.B. (1985). *Design and testing of a fast tool servo for diamond turning*, Abstracts, 3rd IPES, Inter Laken, p. 29.
- Ohmori, G., & Takada, S. (1982). Primary factors affecting accuracy in ultraprecision machining by diamond turning. *Bull. Japan Society of precision Engineering*, 16, p.3.
- Sato, M., Kato, K., & Tuchiya, K. (1978). Effect of material and anisotropy upon the cutting mechanism. *Transactions of JIM*, 9, 530.
- Schmitz, T. L., Davies, M. A., & Kennedym, M. D. (2001). Tool point frequency response prediction for high-speed machining by RCSA. *Transactions of ASME, Journal of Manufacturing Science and Engineering*, 123, 700–707.
- Shaw, M. C. (1984). Shear strain in cutting. In J. R. Crookall & M. C. Shaw (Eds.), *Metal cutting principles*. Oxford: Clarendon Press.
- Shaw, M. C., Cook, N. H., & Finnie, I. (1953). The shear-angle relationship in metal cutting. *Transactions of the ASME*, 75, 273.
- Shawky, A. M., & Elbestawi, M. A. (1997). An enhanced dynamic model in turning including the effect of ploughing forces. *Transactions of ASME, Journal of Manufacturing Science and Engineering*, 119, 10–20.
- Shimokohbe, A., Horikawa, O., & Sato, K. (1989). An active air journal bearing with ultraprecision, infinite static stiffness, high damping capability and new functions. *Annals of the CIRP*, 38, 529.
- Stadler, H., freisleben, B., & Heubeck, C. (1987). Response of metallic material to micromachining, 4th IPES, Cranfield, U.K.
- Sze, Y. K., Lee, W. B., Cheung, C. F., & To, S. (2006). A power spectrum analysis of effect of rolling texture on cutting forces in single-point diamond turning. *Journal of Materials Processing Technology*, 180, 305–309.
- Takasu, S., Masuda, M., & Nishiguchi, T. (1985). Influence of steady vibration with small amplitude upon surface roughness in diamond machining. *Annals of the CIRP*, 34(1), 463.
- Taminiau, D. A., & Dautzenberg, J. H. (1991). Bluntness of tool and process forces in high—Precision cutting. *Annals of the CIRP*, 40, 65.
- Taylor, G. I. (1938). Plastic strain in metals. *Journal of Institute of Metals*, 62, p. 307.
- To, S., Cheung, C. F., & Lee, W. B. (2001). Influence of material swelling on surface roughness in diamond turning of single crystals. *Materials Science and Technology*, 17, 102–108.

- Vela-Martinez, L., Jauregui-Correa, J. C., Rubio-Cerda, E., Herrera-Ruiz, G., & Lozano-Guzman, A. (2008). Analysis of compliance between the cutting tool and the workpiece on the stability of a turning process. *International Journal of Machine Tools and Manufacture*, 48, 1054–1062.
- Wang, H., To, S., Chan, C. Y., Cheung, C. F., & Lee, W. B. (2010). A theoretical and experimental investigation of the tool-tip vibration and its influence upon surface generation in single-point diamond turning. *International Journal of Machine Tools and Manufacture*, 50, 241–252.
- Weck, M., & Hartel, R. (1986). *Test and measuring methods to analyze indulation effect on micro-machined optical surfaces generated by vibration on precision machinery*. Orlando: Proc. SPIE.
- Weck, M., & Modemann, K. (1987). *Checking surface modulation on metal-optics by analysing ultraprecision machines*. Den Haag: Proc. SPIE.
- Weck, M. & Modemann, K. (1988). Surface quality as function of the static and dynamic machine tool behaviour. In *Proceedings of the 4th International Conference On Metrology and Properties of Engineering Surface*, Washington D.C., USA.
- Whitehouse, D. J. (1994). *Handbook of surface metrology*. Bristol, Philadelphia: Institute of Physics Publishing.
- Wiercigroch, M., & Budak, E. (2001). Sources of nonlinearities, chatter generation and suppression in metal cutting. *Philosophical Transactions of the Royal Society of London A*, 359, 663–693.
- Williams, J. A., & Gare, N. (1977). Some observations on the flow stress of metals during metal cutting. *Wear*, 42, 341.
- Wu, D. W. (1986). Governing equations of the shear angle oscillation in dynamic orthogonal cutting. *Transaction of ASME, Journal of Engineering for Industry*, 108, 280–287.
- Zhang, J. H. (1986). *Theory and technique of precision cutting*. Oxford: Pergamon Press.

# Chapter 3

## Modelling and Simulation for Ultra-Precision Machining

**Abstract** This chapter thoroughly reviews the modelling and simulation of ultra-precision machining. The analytical and numerical methods and their applications are summarised, including the Slip-line Field Modelling, Molecular Dynamics Simulation, Quasicontinuum Method, Meshfree Method, Discrete Element Method, Finite Element Method, etc. The dedicated models for chip morphology and shear band theory are further explained in details.

### 3.1 Analytical and Numerical Methods for Machining Process Modelling

#### 3.1.1 *Slip-Line Field Modelling of Machining*

Slip-line field modelling is a technique developed to study the stresses and forces involved in the deformation of metals based on the maximum shear stress. Slip-line field models have been widely adopted in the investigation of plastic deformation in metal cutting processes. A common assumption on rigid-plasticity is adopted in various slip-line field models of the machining process, where the elastic behaviour is not taken into consideration, since the slip-line field model solely concerns the pure and unrecoverable deformation of work materials. Further assumptions are explicitly stated as plane strain, perfectly plastic and constant friction shear stress, etc. (Fang 2003a, b; Fang and Dewhurst 2005; Toropov and Ko 2003). As explained by Fang (2003a), the well-received Merchant's model (Merchant 1945) based on cutting forces, can be derived from Fang's model as one of the eight special cases, as shown in Fig. 3.1.

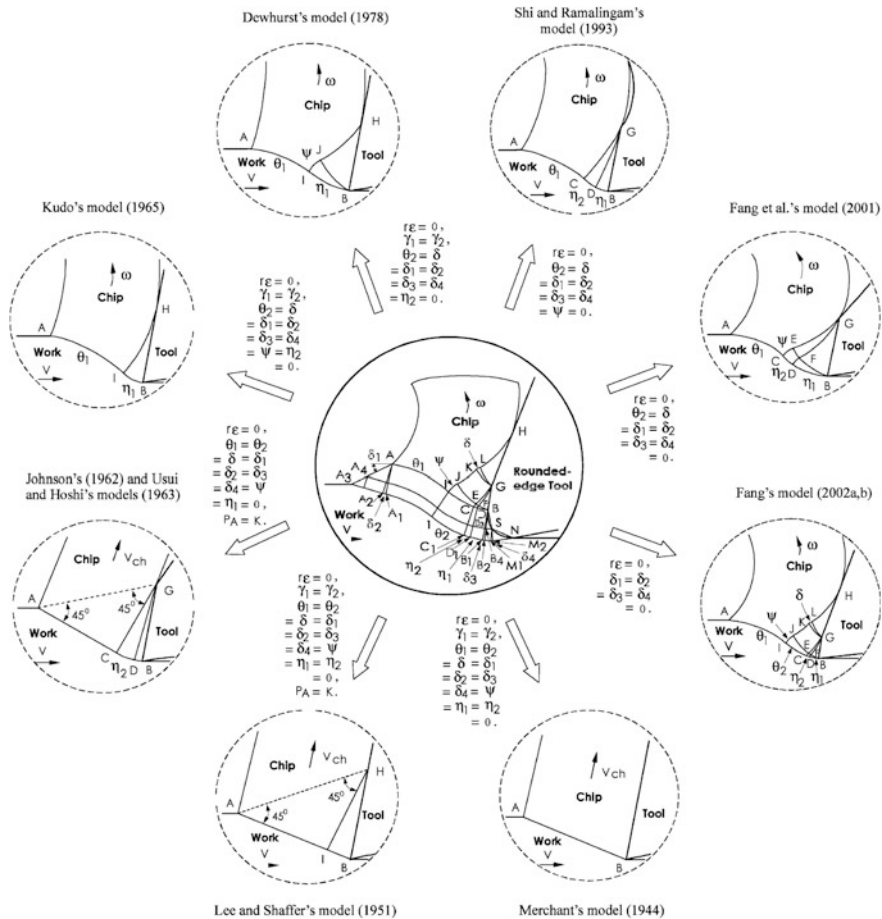


Fig. 3.1 Eight special cases of Fang’s slip-line model (Fang 2003a)

### 3.1.2 Molecular Dynamics Simulation of Machining

Based on statistical mechanics, MDS is a form of computer simulation in which atoms and molecules are allowed to interact for a period of time by approximations of known physics, to visually show the motion of the particles. MDS is frequently used in the study of proteins and biomolecules, as well as in materials science. Recently, MDS has been employed in the modelling and simulation of nano-indentation tests, scratching tests and nanoscale cutting, etc. (Tresoff 1986; Lin and Huang 2004; Fang et al. 2005, 2007; Shimada et al. 1993; Inamura et al. 1997). Further research on tool wear has also been simulated by MDS (Komanduri et al. 1998, 2000). A typical MDS model for the simulation of nano-cutting is shown in Fig. 3.2.

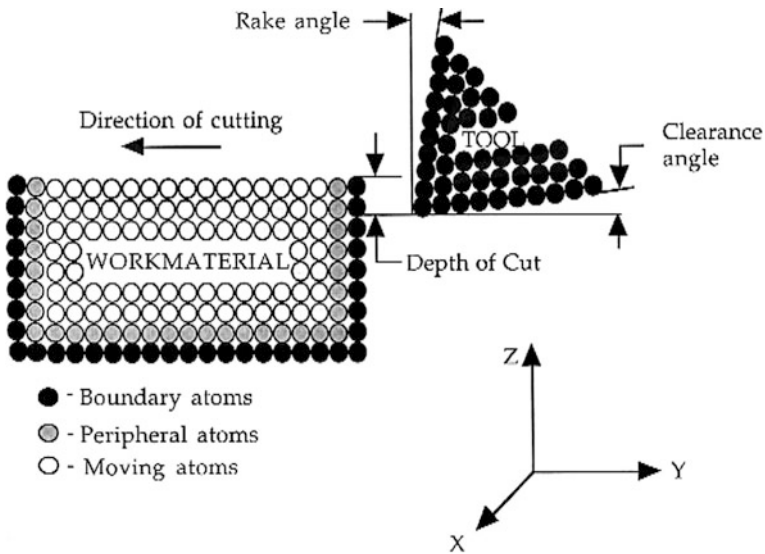


Fig. 3.2 MD simulation of nanometric cutting (Komanduri et al. 2000)

The most significant advantage of MDS in the simulation of the nano-cutting process is that the anisotropy of a single crystal material is an intrinsic property in the setup of an MDS model. At the nanometric scale, MDS is the most suitable method to implement the simulation, compared with the finite element method for the micro-, meso- and macro-scales. However, due to the high-computational intensity, MDS has been successfully applied in the deformation layer of less than tens of nanometres and for a very short period of time, such as femtoseconds. A typical example can be found in the work of Fang et al. (2007), where the uncut chip thickness was not larger than 3 nm and the time step was merely 39 fs. This result of MD simulation is difficult to verify in the micro-cutting process of ultra-precision diamond turning, since the depth of cut of the micro-cutting process is usually 100–1000 times higher than the simulated uncut chip thickness by MD simulation. To facilitate large-scale MD simulation, parallel MD codes based on the graphic processing units (GPU) have recently been developed to study the undeformed chip thickness in ductile-to-brittle transition at an augmented scale of tens of nanometres (Xiao et al. 2015).

### 3.1.3 Quasicontinuum (QC) Method

The Quasicontinuum (QC) method is a mixed continuum and atomistic approach adopted in the simulation of the mechanical response of single crystalline and polycrystalline materials at zero temperature. Differing from molecular dynamics



simulation, the QC method reproduces the results of standard Lattice Statics techniques at a fraction of the computational cost. The key idea is that of selective representation of atomic degrees of freedom. Instead of treating all atoms making up the system, a small relevant subset of atoms is selected to represent, by appropriate weighting, the energetics of the system as a whole. The QC method was proposed in the early research works by Tadmor et al. (1996) and Tadmor and Phillips (1996). The method was applied to single crystal FCC metals and employed to study nano-indentation in thin films (Tadmor et al. 1999). The QC method was also extended by Miller et al. (1998a, b) to study the effect of grain orientation on fracture and the interaction of cracks with grain boundaries.

Compared with molecular dynamics simulation, the QC method possesses advantages that make it applicable for extending atomistic simulation to the sub-micron and micrometric scale, especially in terms of computational intensity. To this end, researchers have made efforts to implement the QC method in the simulation of the ultra-precision machining process. Based on the QC method, an integrated MD-FE multiscale simulation approach was proposed by Sun et al. (2006) to simulate the ultra-precision nano/micro machining process with diamond tools, and to investigate surface integrity generation and surface functionality control. Another recent project follows the same path to simulate the cutting process of single crystal copper and to determine the effect of cutting speed on the deformation mechanism and cutting forces in the nanometric range (Pen et al. 2009), as shown in Fig. 3.3. However, their model could only deal with the nanometric cutting of single crystal materials. Although the size of the work material could be as large as several hundreds of nanometres to several micrometres, the actual cutting range was still confined within the nanometric range, which was speculated to yield similar results to those obtained in molecular dynamics simulation. Furthermore, the QC method possesses no ability, in the current stage, to simulate at higher temperature than absolute zero. Therefore, their methods disregarded the heat generation and related temperature effect, such as work softening in metal cutting. However, heat generation and its induced work softening was identified to be of paramount importance in explaining the physics of regularly spaced shear bands in serrated chip morphology which is the most commonly observable type of chip in the micro-cutting process (Wang et al. 2010b). Despite the tremendous computational intensity of the QC method and molecular dynamics simulation, certain assumptions and oversimplified constitutive equations adopted in these methods hinder their applications in the modelling and simulation of the micro-cutting process.

### ***3.1.4 Meshfree Method***

Meshfree or meshless methods are types of numerical simulation algorithms for physical phenomena which utilise the geometry of the simulated object directly for computation, without introducing a mesh. Meshfree methods include many

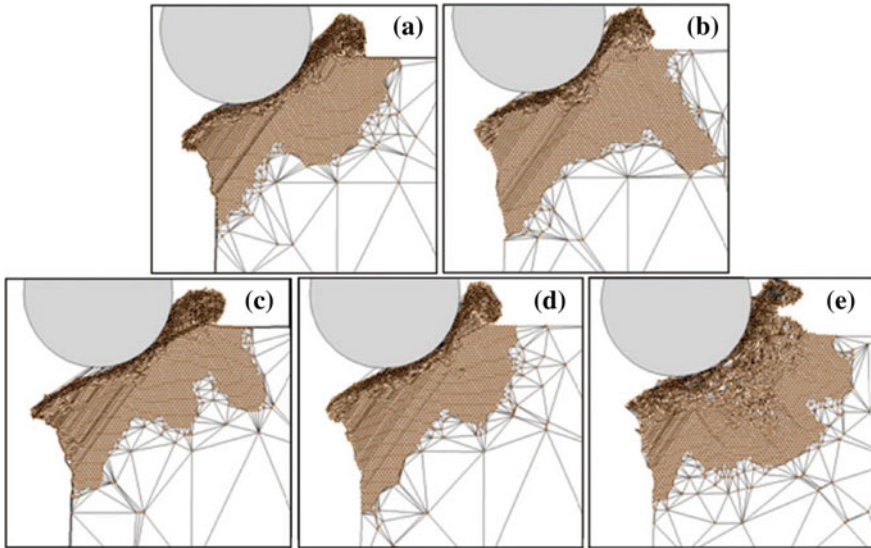


**Fig. 3.3** Chip formation process for five different cutting speeds with QC method: **a** 20 m/s; **b** 200 m/s; **c** 300 m/s; **d** 400 m/s; **e** 800 m/s (Pen and Bai 2009)

branches of simulation techniques, such as the element-free Galerkin method (EFGM), reproducing Kernel particle method (RKPM), natural element method (NEM), meshless local Petrov Galerkin (MLPG), etc., among which Smoothed Particle Hydrodynamics (SPH) has the longest history (Gingold and Monaghan 1977) and has already been implemented in commercialised software packages, such as LS-DYNA (Livermore Software Technology Company). SPH has been widely applied in the research fields of astrophysics, ballistics, volcanology, fluid dynamics, etc.

The SPH method was introduced to model high-speed cutting by Limido et al. (2007) to bypass the requirement for a numerical grid to calculate the spatial derivatives. The modelling of the cutting process has the nature of finite deformation and rotation as well as geometrical and material nonlinearity. The related problems in Lagrangian analyses lead to large distortion of the meshes, which was not properly addressed in most of the early finite element software packages. Therefore, the SPH method was employed to avoid mesh problems by way of allocating the material properties and state variables at a discrete set of disordered points, i.e. SPH particles. The SPH method was recently employed to study the tool wear effect and chip formation (Calamaz et al. 2009) as shown in Fig. 3.4. Based on an assumption of plane strain, 2D orthogonal cutting was studied with a set of calibrated parameters by the Johnson–Cook model (Johnson and Cook 1983) which is also widely applied as the constitutive equation for finite element simulation.

With the same constitutive equations (Johnson–Cook) as adopted in most research work done with the finite element method, similar simulation results are

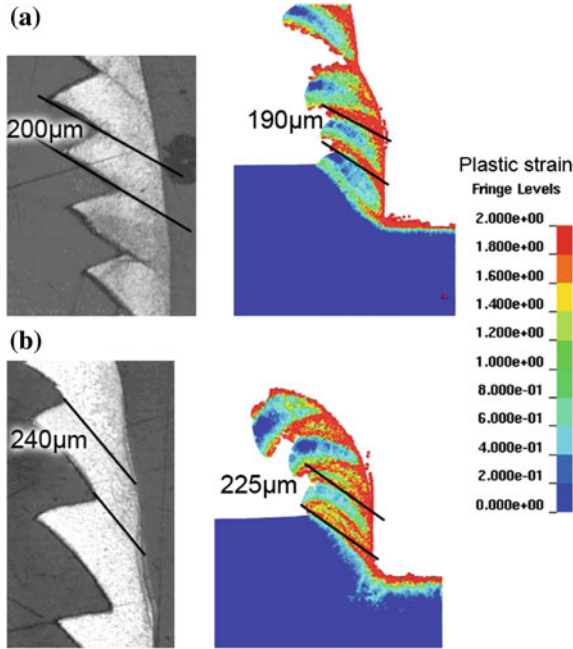


**Fig. 3.4** Experimental/numerical chip formation using **a** new tool and **b** worn tool geometry (Calamaz et al. 2009)

expected to be achieved with different modelling techniques. The simulated localised shear bands and chip formation were observed in (Calamaz et al. 2008). However, with the integration of the global remeshing ability in the commercial FEM software, such as MSC.Marc, the severe problem of mesh distortion can be properly solved. Therefore, the advantage of the meshfree methods becomes less significant. With the same constitutive equations, the SPH method can merely be regarded as a different numerical simulation technique and enhances understanding on the physics of cutting process, based on the outcome of the current research works. On the other hand, more challenges can be identified for the meshfree method that takes account of the anisotropy and meso-scale constitutive equations, such as crystal plasticity and its related strain-gradient effects, etc. However, the evidence is still lacking for verifying its applicability and complexity in the modelling of ultra-precision machining.

### 3.1.5 Discrete Element Method

The discrete element method (DEM) or distinct element method has been under development since 1971 (Cundall 1971), and was applied to cope with physical

process that involves the disaggregation and movement of materials in industries like mining, mineral processing, civil engineering, oil and gas, chemistry, etc.

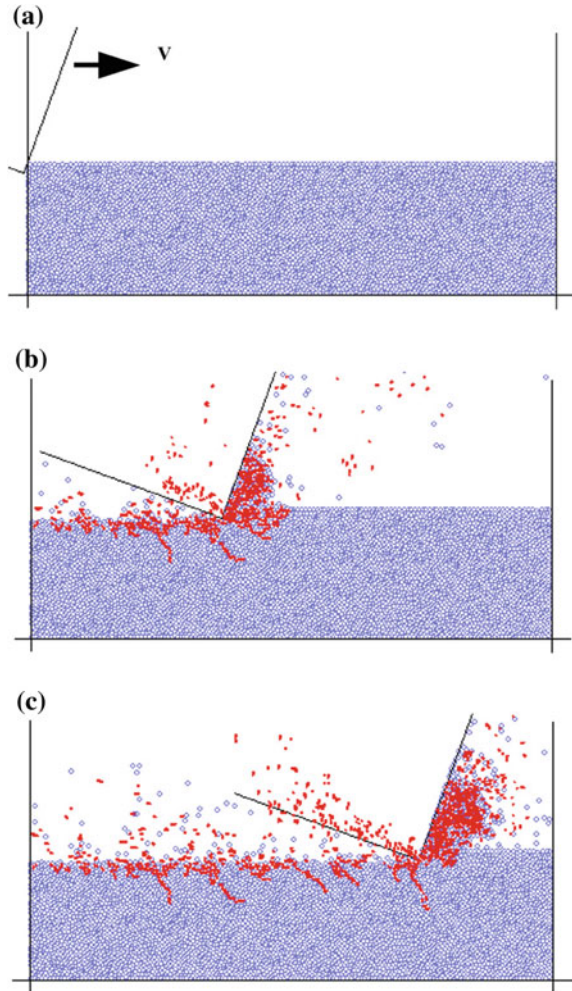
DEM was introduced into the modelling of machining processes (Lei and Yang 2005; Tan et al. 2008, 2009) to study the initiation of machining cracks in brittle materials. Since the resultant defects on the machined surface had direct influence on the quality of ceramic products, the authors (Tan et al. 2009) extended the DEM simulation of the scratching process (Zhang et al. 1988) to the cutting process. The commercialised DEM software PFC2D and PFC3D were employed in their research following the bonded-particle model (Potyondy and Cundall 2004), in which the particles were allowed to be bonded together at the contacts and to be separated under external forces. Without the requirement on mesh generation, DEM can be readily applied to study the dynamic process of initiation and propagation of the micro-cracks under various machining conditions, explicitly at the micro-scale, as shown in Fig. 3.5. As a similar technique to DEM, MDS has been applied to simulate the machining process at the nanoscale, to overcome the considerable computational intensity.

### ***3.1.6 Finite Element Method***

The earliest finite element model was proposed by Zienkiewicz (1971) and Kakino (1971) to study chip formation and simulate the loading of a tool against a pre-formed chip without modelling large-volume flows of the work material. The pioneering model ignored the friction between the chip and tool, the effect of strain rate and temperature, etc. Shirakashi and Usui (1976) further proposed a model to take account of more factors in simulation. They developed an iterative approach of changing the shape of the pre-form until the generated plastic flow was consistent with the assumed shape. The model also included realistic tool-chip friction conditions, a temperature calculation and material flow stress variations with strain, etc. Iwata et al. (1984) proposed a steady state rigid-plastic model within an Eulerian framework to adjust an initially assumed flow field to bring it into agreement with the computed field. Updated Lagrangian elastic-plastic analysis was introduced in the mid-1980s. A shift from Eulerian to Lagrangian modelling also appeared in Ueda and Manabe (1993) and Ueda et al. (1996). For chip formation simulation, both the rigid-plastic (Sekhon and Chenot 1993; Ceretti et al. 1996) and elastic-plastic (Marusich and Ortiz 1995) adaptive remeshing software has been developed. At the same time, the Arbitrary Lagrangian–Eulerian (ALE) methods in which the mesh is neither fixed in space nor in the workpiece, are implemented in the commercial FEM software, such as ABAQUS, DEFORM, etc. The ALE methods have been adopted by many researchers, such as Rakotomolala et al. (1993).

Due to the large deformation in chip formation, chip-separation criteria were developed to solve the problem of severe mesh distortion, as proposed by Strenkowski and Carrol (1985). In order to overcome the shortcomings of the pre-defined chip-separation rules, the pure deformation technique was introduced

**Fig. 3.5** Micro-cracks in the simulation of the cutting process with DEM (Tan et al. 2009)



by Liu et al. (2004, b). The remeshing technique has been developed and integrated into the FEM software ABAQUS. Actually, the adaptive remeshing technique has been provided as a modelling function in the FEM package MSC.Marc. Users can simulate the pure deformation process without further development.

The constitutive equations determine the simulation results and the related factors that can be considered in the models. A coupled thermal-stress analysis is required when the stress analysis is dependent on the temperature distribution, and the temperature distribution depends on the stress solution. A number of finite element studies (Liu and Melkote 2004; Kim et al. 1999; Guo 2004; Shi and Liu 2004) have used the empirical flow stress equations, combining power law strain hardening, power law or logarithmic strain-rate effects and linear or power law thermal softening—the most popular formulation is that of Johnson and Cook

(1985). On the other hand, based on the notion of geometrically necessary dislocations in dislocation mechanics, strain-gradient plasticity theories have been proposed where strain gradient dependence of the flow stress is introduced into the material constitutive model (Fleck et al. 1994; Fleck and Hutchinson 1993; Gao et al. 1999; Acharya and Bassani 2000).

Since the depth of cut is comparable to the grain size in the micro-cutting process, Zhou et al. (2001) and Liang et al. (1994) investigated the effect of tool-work anisotropy, and the first finite element models were proposed by Chuzhoy et al. (2001) who developed an FE model for the orthogonal cutting of ductile iron considering the various phases of the iron. A crystal plasticity FE model was proposed by Chen et al. (2008) in the simulation of the micro-cutting process in single point diamond turning.

The geometry of the cutting tool is another important aspect to be considered in the finite element simulation of the micro-cutting process due to the comparable size to the uncut chip thickness causing the effective rake angle to be negative. Such models have been developed by Kim et al. (1999) and Yen et al. (2004).

Heat generation and temperature distribution have been considered in the majority of works (Carroll and Strenkowschi 1988; Kim et al. 1999a, b; Shi and Yang 1993; Sekon and Chenot 1993; Chandrashekhara and Thuvander 1998; Ng et al. 1999) using Jaeger's moving heat source model (Jaeger 1942). Interaction between the chip and workpiece has been alternatively modelled as a simple Coulomb friction type interaction consisting of stick and slip regimes (Marusich and Ortiz 1995; Ng et al. 1999; Komvopoulos and Erpenbeck 1991) or as a continuous relationship between frictional and normal components (Obikawa et al. 1997). Other friction models are currently available in commercial FEM software, such as MSC.Marc to overcome the limitation of the Coulomb friction model.

## 3.2 Models of Chip Formation and Shear Bands Theory

### 3.2.1 *The Chip Formation Process and Models in Metal Cutting*

The process of chip formation plays an important role in cutting mechanics. There is a need for a better understanding of the chip formation of the material removal process at the tip of a cutting tool. With this knowledge, a greater accuracy in diamond turning can be achieved. Figure 3.6a shows an orthogonal cutting operation and a cross-section of the tool/workpiece interface. In orthogonal machining, the normal to a plane containing the cutting edge of the tool is parallel to the direction of the tool motion. The width of the tool is usually large compared to the width of cut. The process, therefore, can be regarded as causing plain strain. Figure 3.6b shows that the interaction between the tool and the workpiece displaces material in the form of a chip. This chip is formed through shear in a thin region

(the primary shear zone) that extends from the tool tip to the free surface of the workpiece. The angle at which this shearing occurs with respect to the cutting direction is designated the shear angle ( $\phi$ ).

Fundamental to the understanding and modelling of metal cutting is the knowledge of how chips form. In 1870, Thime first proposed that chip formation involves deformation in zones extending from the tool tip to the free surface of the work (Finnie 1956; Shaw 1968; Ernst and Merchant 1941; Boothroyd and Knight 1989; Bailey and Boothroyd 1968). In 1873, however, Tresca proposed that chip formation is due to compression of the material ahead of the tool and shear along planes parallel to the surface of the workpiece (Finnie 1956). Thime refuted the work of Tresca, and wrote again in 1877 that the material ahead of the tool is sheared. This argument was given further support by Mallock (1881).

The chip removal process in diamond machining can be classified into two types. One is due to plastic deformation on the slip planes and the other is due to fracture on the cleavage plane. In machining a homogeneous material, the shear plane and the cleavage plane coincide with the planes of maximum shear or tensile stress. The criteria of chip removal, however, are more complex for a crystalline material.

The shear angle is a very important parameter which can represent macroscopically the state of chip formation in machining. In metal cutting, deformation of the chip usually does not occur uniformly. Rather, intermittent failure of the material in the primary deformation zone causes the chip to have a sectioned or lamellar appearance (Black 1971). This representation of chip formation has been termed the “card model” (Fig. 3.7), as each chip segment is thought of as a playing card sliding over the remaining deck of the workpiece (Shaw 1984).

In metal cutting, the chip formation from the metal layer being cut can be divided approximately into four stages which are: compressing stage, sliding stage, segmenting stage and terminating stage (Zhang 1986). There are three regions of interest in the cutting process, which are the primary deformation zone or sliding zone, the second deformation zone or frictional deformation zone, and the tertiary

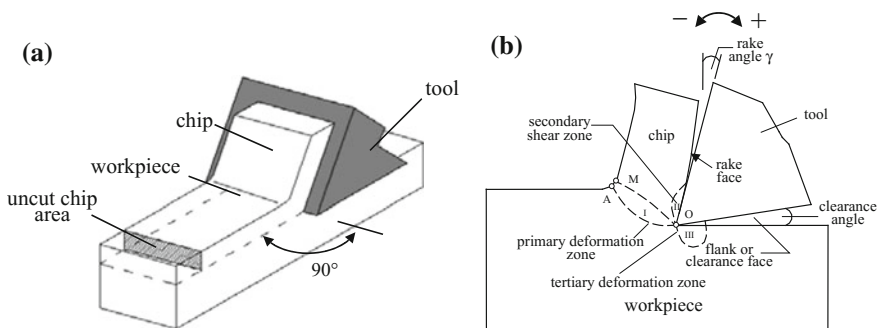
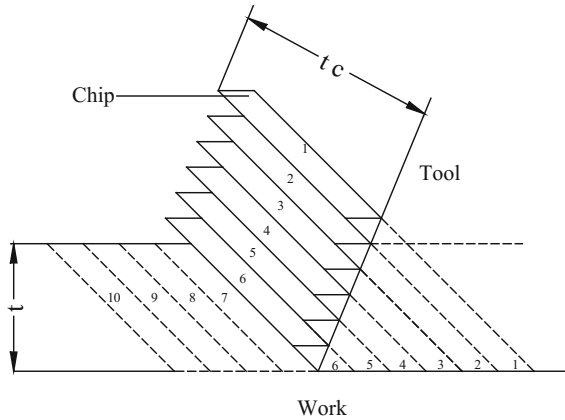


**Fig. 3.6** Schematic of **a** orthogonal cutting operation and **b** the deformation zone (after Arcona 1996)

**Fig. 3.7** Piispanen's idealised model of the cutting process (from Piispanen 1948)



deformation or deformation region of the machined surface. These are illustrated in Fig. 3.6b.

In the first stage, when the cutting tool is in contact with the workpiece, the workpiece experiences pressure at the contact point under the action of the applied cutting force. This leads to a localised part of the workpiece deforming elastically. As the tool penetrates the workpiece metal, the stresses increase linearly in the layer being cut. When the stresses reach the yield point of the metal, the displacement of certain layers of metal, with reference to other layers, occurs. Such displacements occur with definite direction; this is referred to as sliding and is a plastic deformation. As shown in Fig. 3.6b, the line OA in which the sliding begins is called the original line and the line OM in which the sliding ceases is called the final sliding line. The area between the two lines is called the sliding region or primary deformation zone. As the tool penetrates the metal further, the stresses and strains will increase at a constant rate. When the stress reaches a value exceeding the strength of the metal, the first segment will crack along a certain plane. This is called segmenting. Once the metal passes through the final slip line its deformation due to shearing will cease. However, the underside layer of the chip touching the tool rake face continuously undergoes additional deformation due to friction and compression as the chip slides along the tool face. Therefore, the crystal grains of the underside layer of the chip will be elongated in a direction parallel to the tool face by the action of compression and friction generated at the tool-chip interface. This stage is referred to the terminating stage; the tool-chip interface constitutes the secondary deformation zone and is named the frictional deformation zone. The tertiary deformation zone includes the finished or machined surface and the material adjacent to that surface.

Understanding of what happens in each of the three regions of the cutting process involves a knowledge of several fields of engineering and science including solid state physics, engineering mechanics, materials behaviour, engineering plasticity, fundamentals of lubrication, friction and wear, principles of physical metallurgy, thermodynamics and heat transfer.



### 3.2.2 *Shear Band Formation and Chip Morphology*

Shear bands are common phenomena reported in various metal working processes, such as forming, forging, hot rolling, cold rolling, high-speed cutting, etc. In the micro-cutting process, there is strong experimental evidence that the fluctuation in cutting force is related to the variation of chip thickness and is related to the shear plane angle of the metals being cut. The earliest attempts to establish this relationship were described by Black (1971) and Sato et al. (1978). The formation of shear bands and the shear direction are among the key factors affecting the surface finish in ultra-precision machining technology. Lee and co-authors (Lee 2005; Lee et al. 2003) proposed a mesoplasticity model to study the relationship between cutting force and shear direction in the orthogonal metal cutting process in single point diamond turning.

Two major areas have been extensively examined by researchers: (1) the modelling of the cutting process and the formation of shear bands and (2) the development of material constitutive equations to improve the simulation results of chip morphology.

Fang (2003a, b) developed a new slip-line model for machining with a round-edge tool. He proposed a hodograph on which he derived a set of analytical equations to predict the thickness of and the shear strain rate in the primary shear zone. However, his new slip-line model was designed for orthogonal cutting with continuous chip formation only and was based on the assumption that the rigid-plastic material was under plane-strain compression. Thus, the material used in his model could not bounce back when the imposed strain was removed. Moreover, the effect of elastic strain stored in the material in the course of cutting was neglected.

Burns and Davies (2002) postulated a localised plastic deformation zone right on top of the tool tip in the primary shear zone, and proposed that the shear band in high-speed machining was induced by the localised compressive stress which caused a gradient in the shear stress, i.e. the shear band was initiated in the region around the tool tip and was then propagated outward to the free edge of the chip.

To take account of the effect of the formation of shear bands, a number of material constitutive models have been proposed to establish the necessary criteria for shear band propagation and to model the phenomenon of stress collapse inside shear bands. In the earlier work, Recht (1964) studied the dynamic plastic behaviour of materials which was then named catastrophic thermoplastic shear. Recht proposed a model to further explain the adiabatic shear theory of saw-tooth chip formation (Recht 1985). In the model, an assumption was made that for some reason thermoplastic instability occurred which extended from the tool tip upward towards the free surface. However, this model could not predict why shear bands could be initiated at the free edge. Recently, Medyanik et al. (2007) proposed a new ductile failure criterion which assumed that dynamic recrystallisation took place during shear band propagation. Rhim and Oh attempted to prove that the recrystallisation conditions could be satisfied using FEM simulation (Rhim and Oh 2006).

However, these models did not cope with the more fundamental problem of what preceded and later induced shear band propagation.

In a more general case, the phenomenon of adiabatic shear banding was studied in a direct compressive Hopkinson pressure (DCHP) bar system followed by FEM simulation (Teng et al. 2007). In the FEM simulations, the Johnson–Cook model was selected for the constitutive equations, with different mesh sizes, and it was concluded in their simulation results that sufficiently small meshes must be used in the FEM models so that the resolution of the FEM simulation could be high enough to capture the same phenomena as in the experiments. However, a complicated constitutive model is not a necessary condition, since the mechanism of adiabatic shear banding was believed to be driven by mechanics rather than materials (Teng et al. 2007).

High strain rate, such as encountered in high-speed machining and impact and torsion experiments, favours the formation of shear bands (Guduru et al. 2001). Most of the solid material in the vicinity of shear bands experiences relatively little plastic deformation whereas the bands themselves experience very large plastic strains ( $10\text{--}10^2$ ) and propagate at very high rates of  $10^5\text{--}10^7\text{ s}^{-1}$ . At such high strain rates, the rate of local heat generation is much larger than the rate of heat conduction to the surrounding material. To form an adiabatic shear band, the initiation process demands a high strain rate to cause strain inhomogeneity which is later aggravated by adiabatic softening. Since shear bands can be observed in cold-rolled copper and brass under a much lower imposed strain rate, it is always an intriguing question to ask why the low imposed strain rate can trigger a higher strain rate inside the shear bands.

Research attributes the formation of shear bands to the effect of work softening. Most of the constitutive models, though widely diversified in their formulations and assumptions, unanimously predict that localised shearing within the shear bands will induce softening. However, the effect of elastic strain building up in work materials in the course of machining on shear band formation has been neglected. According to the experimental observations, conventional and precision machining of metals can produce three basic types of chip: continuous, discontinuous, and continuous chips with built-up edge (Merchant 1945a). However, experimental results reveal that in ultra-precision machining of non-ferrous materials, serrated chips with regularly spaced shear bands (RSSB) are the most common chip type in single point diamond turning. The shear bands are initiated at the free edge of the chip and propagate through the tool tip almost along a planar path (Wang et al. 2010). Different types of deformation bands and their formation were studied by Lee et al. (1999) on single crystal materials. However, their shear bands were not very thick or well defined. Recently, Duan and Wang have observed thick shear bands of up to  $3\text{ }\mu\text{m}$  wide in high-speed orthogonal cutting of high strength low alloy (HSLA) steel (Duan and Wang 2005). However, they did not mention the necessary conditions favouring the production of such thick RSSB. Inspired by their work, heavily cold-rolled brass with high yield strength is considered in this study. Ferrous materials are avoided because they cannot be machined by diamond tools without inducing excessive tool wear.

Merchant's model holds well for continuous (uniform) chip formation, as applied in the machining of amorphous material (Jiang and Dai 2009) which can be regarded as homogeneous with isotropic properties, but discrepancies have been identified between the theory and experimental data, since most engineering materials are crystalline in nature. Much effort has been therefore exerted to modify the Merchant's model to comply with the different experimental results, such as the results produced by Lee and Shaffer (1951), Stabler (1951), Molinari and Moufki (2008), etc. However, their modification did not consider the presence and effect of material anisotropy and the occurrence of regularly spaced shear bands. In addition, their corrections hold better for cutting tools with a zero rake angle, but fail for those with a negative rake angle. Therefore, they cannot be applied in ultra-precision machining since a large error exists in the prediction of shear angle by their modified models. This book addresses this importance problem through the investigation on RSSB, and presents a physical explanation for cutting force and shear angle prediction.

### 3.2.3 The Shear Angle Relationship

In the machining of ductile metal, the magnitude of the shear plane angle  $\phi$  is an important parameter which represents the machinability of the work materials and the efficiency of the process. The shear angle has to be determined experimentally by measuring the chip thickness and is given by:

$$\sin \phi = \frac{\cos \alpha}{t_0/t_c - \sin \alpha} \quad (3.1)$$

where  $\alpha$  is the tool rake angle,  $t_0$  is the depth of cut and  $t_c$  is the deformed chip thickness as shows in Fig. 3.8.

When the depth of cut is small, the thickness of the chip can be derived from the length, width and the weight of chip collected. The shear angle has been found to

**Fig. 3.8** Geometrical relationship among chip thickness, depth of cut, shear angle and rake angle

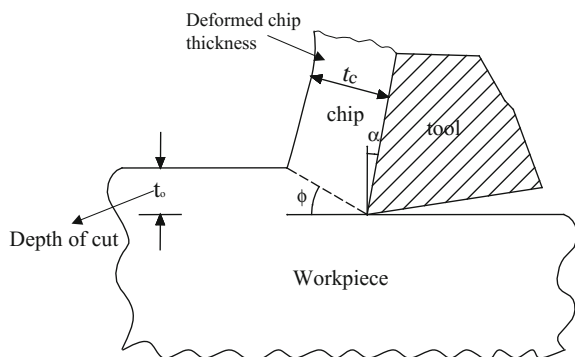


**Table 3.1** Early equations for shear angle (from Shaw 1984)

Source	Theory	Equations
Ernst and merchant (1941)	Force equilibrium and minimum energy principle	$\phi = \frac{\pi}{4} - \frac{1}{2}(\beta - \alpha)$
Merchant (1945a)	Force equilibrium and minimum energy principle	$\phi = \frac{\cot^{-1} K}{2} - \frac{\beta}{2} + \frac{\alpha}{2}$
Stabler (1951)	Force equilibrium and minimum energy principle	$\phi = 45 - \beta + \frac{\alpha}{2}$
Lee and Shaffer (1951)	Slip line theory	$\phi = 45 - \beta + \alpha$
Lee and Shaffer (1951)	Slip line theory	$\phi = 45 + \delta - \beta + \alpha^a$
Hücks (1951)		$\phi = 45 - \frac{\tan^{-1} 2\mu}{2} + \alpha$
Hücks (1951)		$\phi = \frac{\cot^{-1} K}{2} - \frac{\tan^{-1} 2\mu}{2} + \alpha$

<sup>a</sup>With built-up edge of magnitude  $\delta$

$\beta$  friction angle,  $\alpha$  rake angle,  $\mu$  coefficient of friction on the rake angle,  $K$  material constant

vary with the tool geometry, cutting condition, and the work materials. A large shear angle is associated with continuous chip formation, good surface finish and low cutting forces. Over time, there have been many theoretical attempts to derive the shear angle relationships or, alternatively, chip compression relationships (see Table 3.1).

Many other shear zone angle solutions have been developed based on the assumption that the workpiece is isotropic and is a homogeneous continuum (Shaw 1984). No attention was paid to the effect of crystallographic anisotropy of the work material on the chip formation process. These early shear angle equations were very useful in qualitative analysis of problems encountered in conventional machining. However, they are incapable of explaining the variation of micro-cutting force with crystallographic orientations of workpiece materials in the diamond cutting processes. Therefore, a correct description of the relationship between the shear angle and the crystallographic cutting direction is much needed for a better understanding of the chip formation mechanism.

## References

- Acharya, A., & Bassani, J. L. (2000). Lattice incompatibility and a gradient theory of crystal plasticity. *Journal of the Mechanics and Physics of Solids*, 48, 1565.
- Arcona, C. (1996). Tool force, chip formation and surface finish in diamond turning. PhD thesis, North Carolina State University, p. 1.
- Bailey, J. A., & Boothroyd, G. (1968). Critical review of some previous work on the mechanics of the metal-cutting process. *Journal of Engineering for Industry*, 90, 54.
- Black, J. T. (1971). On the fundamental mechanism of large strain plastic deformation. *Journal of Engineering for Industry*.
- Boothroyd, G., & Knight, W. A. (1989). *Fundamentals of machining and machine tools*. New York: Marcel Dekker Inc.

- Burns, T. J., & Davis, M. A. (2002). On repeated adiabatic shear band formation during high-speed machining. *International Journal of Plasticity*, 18, 487–506.
- Calamaz, M., Coupard, D., & Girod, F. (2008). A new material model for 2D numerical simulation of serrated chip formation when machining titanium alloy Ti-6Al-4V. *International Journal of Machine Tools and Manufacture*, 48, 275–288.
- Calamaz, M., Limido, J., Nouari, M., Espinosa, C., Coupard, D., Salaün, M., et al. (2009). Toward a better understanding of tool wear effect through a comparison between experiments and SPH numerical modeling of machining hard materials. *International Journal of Refractory Metals & Hard Materials*, 27, 595–604.
- Carroll, J. T., & Strenkowschi, J. S. (1988). Finite element models of orthogonal cutting with application to single point diamond turning. *International Journal of Mechanical Science*, 30, 899.
- Ceretti, E., Fallbohmer, P., Wu, W. T., & Altan, T. (1996). Application of 2-D FEM to chip formation in orthogonal cutting. *Journal of Materials Processing Technology*, 59, 169.
- Chandrasekharan, H., & Thuvander, A. (1998). Tool stresses and temperature in machining. In *CIRP International Workshop on Modeling of Machining Operations*, pp. 2B/7-1.
- Chen, Y. P., Lee, W. B., To, S., & Wang, H. (2008). Finite element modeling of micro-cutting processes from crystal plasticity. *International Journal of Modern Physics B*, 22(31 & 32), 5943–5948.
- Chuzhoy, L., DeVor, R. E., Kappor, S. G., & Bammann, D. J. (2001). Microstructure-level modeling of ductile iron machining. In *Proceedings of ASME Manufacturing Engineering Division (MED-Vol. 12)*, ASME International Mechanical Engineering Congress and Exposition, NY, p. 125.
- Cundall, P. A. (1971). A computer model for simulation progressive, large-scale movements in blocky rock systems. In *Symposium of International Society of Rock Mechanics*, Nancy France 2, No. 2, pp. 11–19.
- Duan, C., & Wang, M. (2005). Some metallurgical aspects of chips formed in high speed machining of high strength low alloy steel. *Scripta Materialia*, 52, 1001–1004.
- Ernst, H., & Merchant, M. E. (1941). *Chip formation, friction, and high quality machined surfaces*. Surface Treatment of Metals, ASM, p. 299
- Fang, F. Z., Wu, H., & Liu, Y. C. (2005). Modeling and investigation on machining mechanism of nano-cutting monocrystalline silicon. *International Journal of Machine Tools and Manufacture*, 45, 1681–1686.
- Fang, F. Z., Wu, H., Zhou, W., & Hu, X. T. (2007). A study on mechanism of nano-cutting single crystal silicon. *Journal of Materials Processing Technology*, 184, 407–410.
- Fang, N. (2003a). Slip-line modeling of machining with a rounded-edge tool—Part I: New model and theory. *Journal of the Mechanics and Physics of Solids*, 51, 715–742.
- Fang, N. (2003b). Slip-line modeling of machining with a rounded-edge tool—Part II: Analysis of the size effect and the shear strain-rate. *Journal of the Mechanics and Physics of Solids*, 51, 743–762.
- Fang, N., & Dewhurst, P. (2005). Slip-line modeling of built-up edge formation in machining. *International Journal of Mechanical Sciences*, 47, 1079–1098.
- Finnie, I. (1956). Review of metal cutting analyses of the past hundred years. *Mechanical Engineering*, 78, 715.
- Fleck, N. A., & Hutchinson, J. W. (1993). A phenomenological theory for strain gradient effects in plasticity. *Journal of the Mechanics and Physics of Solids*, 41, 1825.
- Fleck, N. A., Muller, G. M., Ashby, M. F., & Hutchinson, J. W. (1994). Strain gradient plasticity: Theory and experiments. *Acta Metallurgica et Materialia*, 42(2), 475.
- Gao, H., Huang, Y., Nix, W. D., & Hutchinson, J. W. (1999). Mechanism-based strain gradient plasticity—I. Theory. *Journal of the Mechanics and Physics of Solids*, 47, 1239.
- Gingold, R. A., & Monaghan, J. J. (1977). Smoothed particle hydrodynamics—Theory and application to non-spherical stars. *Royal Astronomical Society, Monthly Notices*, 181, 375–389.

- Guduru, P. R., Ravichandran, G., & Rosakis, A. J. (2001). Observation of transient high temperature vertical microstructures in solids during adiabatic shear banding. *Physical Review E*, 64:036128.
- Guo, Y. B. (2004). A FEM study on mechanisms of discontinuous chip formation in hard turning. *Journal of Materials Processing Technology*, 155–156, 1350.
- Hück, H. (1951). Dissertation. Aachen T.H.
- Inamura, T., Shimada, S., Takezawa, M., & Makahara, N. (1997). Brittle/ductile transition phenomena observed in computer simulations of machining defect-free monocrystalline silicon. *Annals of the CIRP*, 46, 31–34.
- Iwata, K., Osakada, K., & Terasaka, Y. (1984). Process modeling of orthogonal cutting by the rigid-plastic finite element method. *ASME Journal of Engineering Materials and Technology*, 106, 132.
- Jaeger, J. C. (1942). Moving sources of heat and temperature at sliding contact. *Proceedings of Royal Society of New South Wales*, 76, 203.
- Jiang, M. Q., & Dai, L. H. (2009). Formation mechanism of lamellar chips during machining of bulk metallic glass. *Acta Materialia*, 57, 2730–2738.
- Johnson, G. R., & Cook, W. H. (1983). *A constitutive model and data for metals subjected to large strains, high strain rates and high temperatures* (pp. 541–547). Hague: Seventh International Symposium on Ballistics.
- Johnson, G. R., & Cook, W. H. (1985). Fracture characteristics of three metals subject to various strains, strain rates, temperatures and pressures. *Engineering Fracture Mechanics*, 21, 31–48.
- Kakino, Y. (1971). Analysis of the mechanism of orthogonal machining by the finite element method. *Journal of the Japan Society for Precision Engineering*, 37(7), 503.
- Kim, K. W., Lee, W. Y., & Sin, H. (1999a). A finite element analysis for the characteristics of temperature and stress in micro-machining considering the size effect. *International Journal of Machine Tools and Manufacture*, 39, 1507.
- Kim, K. W., Lee, W. Y., & Sin, H. C. (1999b). A finite element analysis of machining with the tool edge considered. *Journal of Materials Processing Technology*, 86, 45.
- Komanduri, R., Chandrasekaran, N., & Raff, L. M. (1998). Effect of tool geometry in nanometric cutting: A molecular dynamics simulation approach. *Wear*, 219, 84–97.
- Komanduri, R., Chandrasekaran, N., & Raff, L. M. (2000). M.D. simulation of nanometric cutting of single crystal aluminum—Effect of crystal orientation and direction of cutting. *Wear*, 242, 60–88.
- Komvopoulos, K., & Erpenbeck, S. A. (1991). Finite element modeling of orthogonal metal cutting. *ASME Journal of Engineering for Industry*, 113, 253.
- Lee, E. H., & Shaffer, B. W. (1951). The theory of plasticity applied to a problem of machining. *Journal of Applied Mechanics*, 73, 405.
- Lee, W. B. (2005). A personal reflection of mesoplasticity and its applications. *Journal of Materials Processing Technology*, 167, 151–160.
- Lee, W. B., To, S., & Chan, C. Y. (1999). Deformation band formation in metal cutting. *Scripta Materialia*, 40, 439–443.
- Lee, W. B., To, S., Sze, Y. K., & Cheung, C. F. (2003). Effect of material anisotropy on shear angle prediction in metal cutting—A mesoplasticity approach. *International Journal of Mechanical Science*, 45, 1739–1749.
- Lei, S., & Yang, B. (2005). Distinct element simulation of ceramic machining: Material removal mechanism. *Transactions of the North American Manufacturing Research Institution of SME*, 33, 485–492.
- Liang, Y., Moronuki, N., & Furukawa, Y. (1994). Calculations of the effect of material anisotropy on microcutting processes. *Precision Engineering*, 16, 132.
- Lin, Z. C., & Huang, J. C. (2004). A nano-orthogonal cutting model based on a modified molecular dynamics technique. *Nanotechnology*, 15, 510–519.
- Limido, J., Espinosa, C., Salaün, M., & Lacombe, J. L. (2007). SPH method applied to high speed cutting modelling. *International Journal of Mechanical Sciences*, 49, 898–908.

- Liu, X., DeVor, R. E., & Kapoor, S. G. (2004a). The mechanics of machining at the microscale: Assessment of the current state of the science. *Transaction of ASME, Journal of Manufacturing Science and Engineering*, 126, 666–678.
- Liu, X., Jun, M. B. G., DeVor, R. E., & Kapoor, S. G. (2004b). Cutting mechanisms and their influence on dynamic forces, vibrations and stability in micro-endmilling. In *Proceedings of the ASME Manufacturing Engineering Division (MED-15), ASME International Mechanical Engineering Congress and Exposition*, Anaheim CA, Paper no. IMECE2004-62416.
- Liu, K., & Melkote, S. N. (2004). A strain gradient based finite element model for micro/meso-scale orthogonal cutting process. In *Proceedings of 2004 Japan-USA Symposium on Flexible Automation*, Denver, Colorado.
- Mallock, A. (1881). The action of cutting tools. *Proceedings of the Royal Society of London*, 33, 127.
- Marusich, T. D., & Ortiz, M. (1995). Modelling and simulation of high speed machining. *International Journal of Numerical Methods in Engineering*, 38, 3675.
- Medyanik, S. N., Liu, W. K., & Li, S. (2007). On criteria for dynamic adiabatic shear band propagation. *Journal of the Mechanics and Physics of Solids*, 55, 1439–1461.
- Merchant, M. E. (1945). Mechanics of the metal cutting process. I: orthogonal cutting and A type 2 chip. *Journal of Applied Physics*, 16, 267.
- Miller, R., Ortiz, M., Phillips, R., Shenoy, V. B., & Tadmor, E. B. (1998a). Quasicontinuum models of fracture and plasticity. *Engineering Fracture Mechanics*, 61, 427–444.
- Miller, R., Tadmor, E. B., Phillips, R., & Ortiz, M. (1998b). Quasicontinuum simulation of fracture at the atomic scale. *Modelling and Simulation in Materials Science and Engineering*, 6, 607–638.
- Molinari, A., & Moufki, A. (2008). The Merchant's model of orthogonal cutting revisited: A new insight into the modeling of chip formation. *International Journal of Mechanical Sciences*, 50, 124–131.
- Ng, E.-G., Aspinwall, D. K., Brazil, D., & Monaghan, J. (1999). Modeling of temperature and forces when orthogonally machining hardened steel. *International Journal of Machine Tools and Manufacture*, 39, 885.
- Obikawa, T., Sasahara, H., Shirakashi, T., & Usui, E. (1997). Application of computational machining method to discontinuous chip formation. *Journal of Manufacturing Science and Engineering*, 119, 667.
- Pen, H., Bai, Q., Liang Y., & Chen, M. (2009). Multiscale simulation of nanometric cutting of single crystal copper—Effect of different cutting speeds. *Acta Metallurgica Sinica (English Letters)*, 22(6), 440–446.
- Piispanen, V. (1948). Theory of formation of metal chips. *Journal of Applied Physics*, 19, 876–881.
- Potyondy, D. O., & Cundall, P. A. (2004). A bonded-particle model for rock. *International Journal of Rock Mechanics & Mining Science*, 41, 1329–1364.
- Rakotomolala, R., Joyot, P., & Touratier, M. (1993). Arbitrary Lagrangian-Eulerian thermo-mechanical finite-element model of material cutting. *Communications in Numerical Methods in Engineering*, 9, 975.
- Recht, R. F. (1985). A dynamic analysis of high speed machining. *ASME Journal of Engineering for Industry*, 107, 309–315.
- Recht, R. F. (1964). Catastrophic thermoplastic shear. *Journal of Applied Mechanics*, pp 189–193.
- Rhim, S.-H., & Oh, S.-I. (2006). Prediction of serrated chip formation in metal cutting process with new flow stress model for AISI 1045 steel. *Journal of Materials Processing Technology*, 171, 417–422.
- Sato, M., Kato, K., & Tuchiya, K. (1978). Effect of material and anisotropy upon the cutting mechanism. *Transactions JIM*, 9, 530.
- Sekhon, G. S., & Chenot, S. (1993). Numerical simulation of continuous chip formation during non-steady orthogonal cutting. *Engineering Computations*, 10, 31.

- Shaw, M.C. (1968). Historical aspects concerning removal operations on metals. *Metal Transformations*, Gordon and Breach, NY, pp. 211.
- Shaw, M. C. (1984). Shear strain in cutting. In J.R. Crookall, & M. C. Shaw (Eds.), *Metal cutting principles*. Oxford: Clarendon Press, p. 168
- Shi, J., & Liu, C. R. (2004). The influence of material models on finite element simulation of machining. *ASME Journal of Manufacturing Science and Engineering*, 126, 849–857.
- Shih, A. J., & Yang, H. T. Y. (1993). Experimental and finite element predictions of residual stresses due to orthogonal metal cutting. *International Journal of Numerical Methods in Engineering*, 36, 1487.
- Shimada, S., Ikawa, N., Tanaka, H., Ohmori, G., Uchikoshi, J., & Yoshinaga, H. (1993). Feasibility study on ultimate accuracy in microcutting using molecular dynamics simulation. *Annals of the CIRP*, 42, 91–94.
- Shirakashi, T., & Usui, E. (1976). Simulation analysis of orthogonal metal cutting process. *Journal of the Japan Society for Precision Engineering*, 42, 340.
- Stabler, G. V. (1951). The fundamental geometry of cutting tools. *Proceedings of the Institution of Mechanical Engineers*, 165, 14–21.
- Strenkowski, J. S., & Carrol, J. T., III. (1985). A finite element model of orthogonal metal cutting. *ASME Journal of Engineering for Industry*, 107, 349.
- Sun, X., Chen, S., Cheng, K., Huo, D., & Chu, W. (2006). Multiscale simulation on nanometric cutting of single crystal copper. *Proceedings of the Institution of Mechanical Engineers, Part B: Journal of Engineering Manufacture*, 220, 1217–1222.
- Tadmor, E. B., Miller, R., Phillips, R., & Ortiz, M. (1999). Nanoindentation and incipient plasticity. *Journal of Materials Research*, 14, 2233–2250.
- Tadmor, E. B., Ortiz, M., & Phillips, R. (1996). Quasicontinuum analysis of defects in solids. *Philosophical Magazine A*, 73, 1529–1563.
- Tadmor, E. B., & Phillips, R. (1996). Mixed atomistic and continuum models of deformation in solids. *Langmuir*, 12, 4529–4534.
- Tan, Y., Yang, D., & Sheng, Y. (2008). Study of polycrystalline Al<sub>2</sub>O<sub>3</sub> machining cracks using discrete element method. *International Journal of Machine Tools and Manufacture*, 48, 975–982.
- Tan, Y., Yang, D., & Sheng, Y. (2009). Discrete element method (DEM) modeling of fracture and damage in the machining process of polycrystalline SiC. *Journal of the European Ceramic Society*, 29, 1029–1037.
- Teng, X., Wierzbicki, T., & Couque, H. (2007). On the transition from adiabatic shear banding to fracture. *Mechanics of Materials*, 39, 107–125.
- Tersoff, J. (1986). New empirical model for the structural properties of silicon. *Physical Review Letters*, 56 (6): 632–635.
- Tropov, A., & Ko, S.-L. (2003). Prediction of tool-chip contact length using a new slip-line solution for orthogonal cutting. *International Journal of Machine Tools and Manufacture*, 43, 1209–1215.
- Ueda, K., & Manabe, K. (1993). Rigid-plastic FEM analysis of three-dimensional deformation field in chip formation process. *Annals of the CIRP*, 42(1), 35.
- Ueda, K., Manabe, K., & Nozaki, S. (1996). Rigid-plastic FEM of three-dimensional cutting mechanism (2nd report)—Simulation of plain milling process. *Journal of the Japan Society for Precision Engineering*, 62(4), 526.
- Wang, H., To, S., Chan, C. Y., Cheung, C. F., & Lee, W. B. (2010). A theoretical and experimental investigation of the tool-tip vibration and its influence upon surface generation in single-point diamond turning. *International Journal of Machine Tools and Manufacture*, 50, 241–252.
- Xiao, G., To, S., & Zhang, G. (2015). Molecular dynamics modelling of brittle-to-ductile cutting mode transition: Case study on silicon carbide. *International Journal of Machine Tools and Manufacture*, 88, 214–222.



- Yen, Y. C., Jain, A., & Altan, T. (2004). A finite element analysis of orthogonal machining using different tool edge geometries. *Journal of Materials Processing Technology*, 146, 72.
- Zhang, B., Tokura, H., & Yoshikawa, M. (1988). Study on surface cracking of alumina scratching by single-point diamonds. *Journal of Materials Science*, 23, 3214–3224.
- Zhou, Y., Zeng, Y., He, G., & Zhou, B. (2001). The healing of quenched crack in 1045 steel under electropulsing. *Journal of Material Research*, 16, 17–19.
- Zienkiewicz, O. C. (1971). *The finite element method in engineering science*, 2nd edn. Chapter 18. London: McGraw-Hill.
- Zhang, J. H. (1986). *Theory and technique of precision cutting*. Pergamon Press.

**Part II**  
**Materials Characterisation**  
**in Ultra-Precision Diamond**  
**Turning**

# Chapter 4

## Machinability of Single Crystals in Diamond Turning

**Abstract** Machinability refers to the relative ease with which a material can be cut successfully. The criteria to measure a successful cut are plentiful. Some commonly accepted measures include the surface roughness, the ease of removal of the chip, the amount of tool wear, the cutting force and the power consumption. These factors are often related to one another. This chapter showcases the material characterisation methods and the in-depth study on the machinability of single crystal materials in a series of delicate diamond turning experiments undertaken by the authors and their colleagues.

### 4.1 Key Aspects in Diamond Turning of Single Crystals

#### 4.1.1 *The Ultra-Precision Machine*

Our cutting experiments were performed on a two-axis CNC contouring lathe from Taylor Hobson Pneumo. The machine utilises a precision dovetail slide and a high speed air bearing spindle with an integral AC drive motor. The slide is mounted on natural granite. The spindle rotation is infinitely variable from 3000 to 10,000 rpm with acceleration and deceleration times of less than 5 s. The workpiece was mounted by an air-actuated collet mechanism within the air bearing spindle. A photo and the schematic diagram of the machine (Optoform 30) used in diamond turning the single crystal are illustrated in Figs. 4.1 and 4.2 respectively. Table 4.1 shows the property parameters of the ultraprecision machine.

#### 4.1.2 *Diamond Tools*

High quality diamond tools that can produce very fine chips are essential for the study of the chip formation mechanism. As the single crystal diamond tool has low affinity with those materials used in ultraprecision cutting and is able to be made

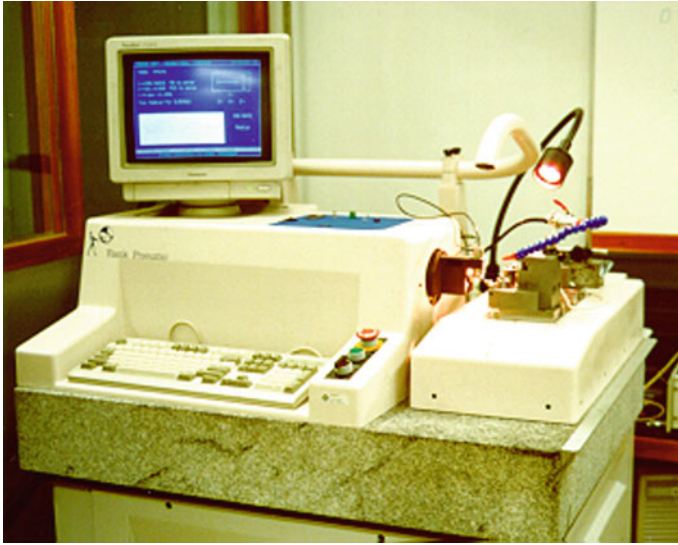


**Fig. 4.1** Photo of the ultraprecision machine (Optoform 30)

**Fig. 4.2** Schematic diagram of the diamond turning machine

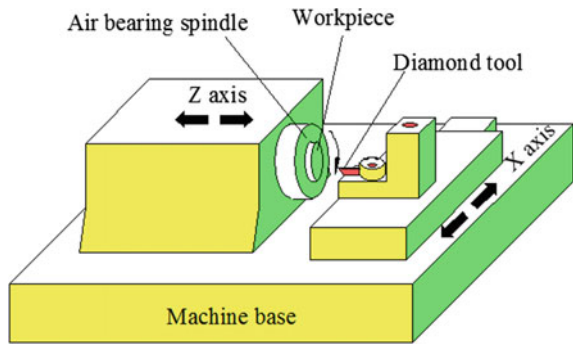


**Table 4.1** Property parameters of ultraprecision machine (Optoform 30)

Workspindle	Design	Air bearing
	Speed range	3000–10,000 rpm
	Acceleration time	Less than 5 s
Slide ways	Design	Precision contacting way
	X travel	150 mm
	Z travel	100 mm
	Velocity	0.25–1500 mm min <sup>-1</sup>
Feedback system	Linear glass scales	
Feedback resolution	0.02 μm	
Form accuracy	0.5 μm	

**Fig. 4.3** Photo of single-point diamond tool

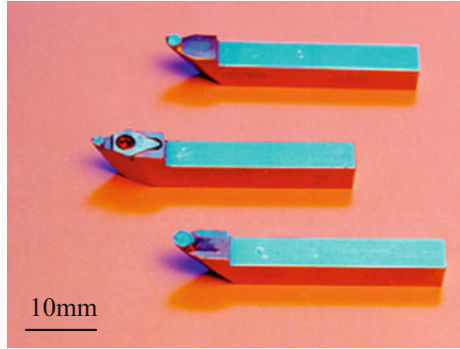
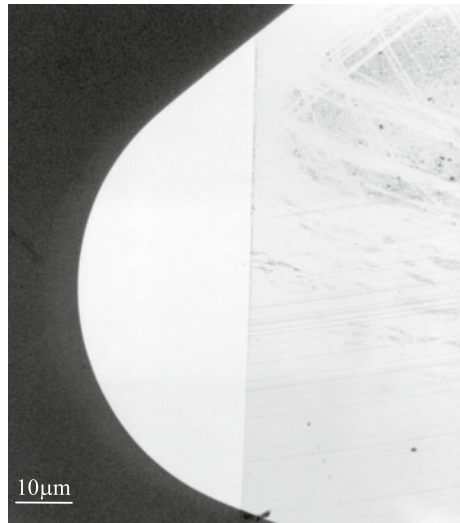


**Fig. 4.4** Micrograph of the outline curve of cutting edge of diamond tool



with a very sharp cutting edge, it is recognised to be an ideal ultraprecision cutting tool (To et al. 1997, 1999, 2002, 2003, 2013; To and Lee 2001). Diamond cutting tools used for producing extremely precise contoured surfaces are themselves highly accurate devices. The design, manufacturing and proper use of diamond tools are among the key elements of the single-point diamond turning (SPDT) technique. A single crystal diamond tool has the greatest hardness, wear resistance and thermal conductivity of all cutting tool materials. In diamond cutting, generation of heat is very small.

Natural single-point diamond tools used in the cutting experiments were made by Contour Fine Tooling Company of the UK. The diamond tool's outline and nanometric sharpness are shown in Figs. 4.3 and 4.4, respectively.

### 4.1.3 Measurement of Surface Roughness

A machined surface inherits characteristic irregularities on the surface caused by the cutting tool. The direction of the predominant surface pattern (known as the lay) in turning lies in the feed direction of the cutting tool. The commonly used roughness parameters used to create a desirable roughness profile (Fig. 4.5) are as follows:

- Peak-to-valley roughness  $R_t$  which is the difference between the highest peak and the lowest valley over the sampling length.
- Arithmetic average roughness  $R_a$  which is obtained by measuring the mean deviation of the peaks from the centre line of a profile trace.
- RMS value which gives the root-mean-square deviation defined relative to a mean line. (RMS =  $0.9R_a$  for a sine wave).

The characterisation of the surface by a high-order probability function such as power spectral density (PSD) is finding increasing use. The variation of the surface characteristics and micro-cutting forces is analysed by power spectrum analysis technique. The power spectrum of the cutting force signal is determined by discrete Fourier transformation (DFT) computing with a fast Fourier transformation algorithm (Proakis and Manolakis 1996). As the cutting force signal is denoted by  $F(k)$  with  $k = 0, 1, 2, \dots, N - 1$ , where  $N$  is the number of samples in the force signal, the power spectrum of the force signal is defined as:

$$Z(f_n) = \frac{1}{N} \sum_{k=0}^{N-1} F(k) \exp\left(\frac{-2\pi j}{T} k f_n\right), \quad (4.1)$$

where  $n$  is an integer number; and  $f_n$  is a frequency component of the cutting force signal which represents the number of waves with a wavelength of  $\lambda_n$  within a unit period of time.

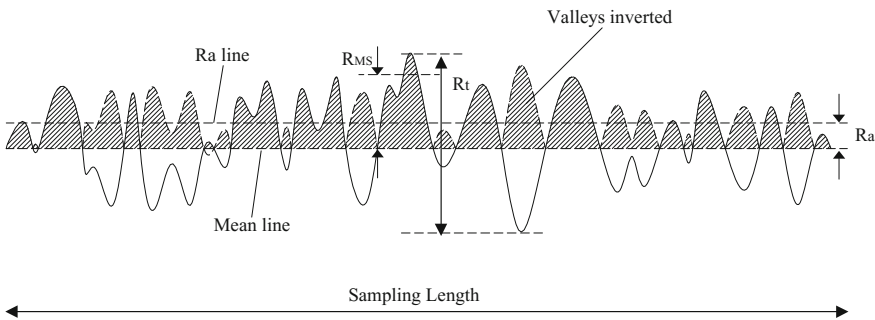


Fig. 4.5 Description of surface parameters

$$\lambda_n = \frac{1}{f_n} = \frac{T}{n} \quad (4.2)$$

$N$  is the total number of samples with spacing  $\Delta t$  taken within the measured time period  $T$  of the force signal, i.e.

$$N = \frac{T}{\Delta t} \quad (4.3)$$

In order to prevent aliasing distortion (Mulgrew et al. 1999), the sample rate  $f_{\text{sample}}$  must be chosen to be at least twice that of the highest nonzero frequency component  $f_{\text{max}}$  contained in cutting force signal according to the sampling theorem or Nyquist criterion, i.e.

$$f_{\text{sample}} \geq 2f_{\text{max}} \quad (4.4)$$

In terms of the sample spacing  $\Delta t$ , it should be:

$$\Delta t \leq \frac{1}{2f_{\text{max}}} \quad (4.5)$$

$\Delta t$  is commonly chosen to be 0.0004 s which ensures an accurate representation of the cutting force signal with frequency content up to 1,250 Hz.

The PSD is determined directly from the DFT. The periodogram  $|Z(f_n)|^2$  is obtained by transforming the real data. This yields  $N$  transformed points corresponding to  $N$  real data points. To minimise the distortion of the true spectrum due to Gibb's phenomenon, the spectral window corresponding to the Hanning lag window is applied to get the PSD (Proakis and Manolakis 1996). The Hanning window is operated on the frequency data by means of convolution, i.e.

$$\text{PSD}(f_o) = 0.25(Z(f_p))^2 + 0.50(Z(f_o))^2 + 0.25(Z(f_s))^2, \quad (4.6)$$

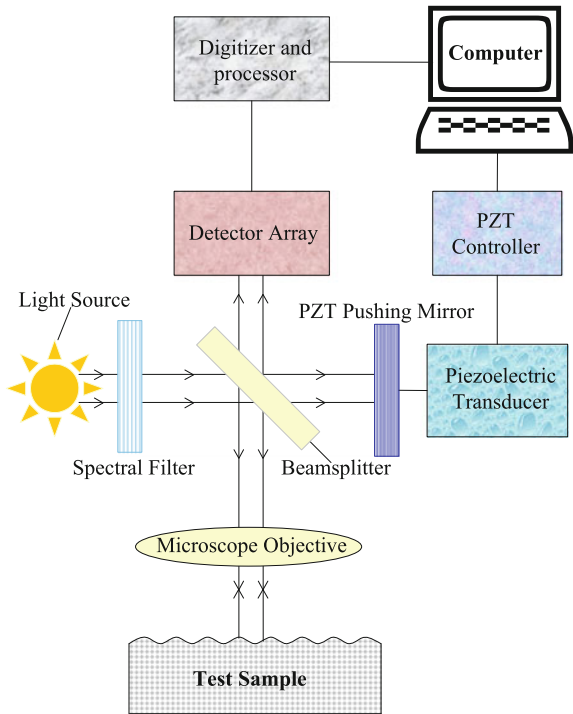
where  $\text{PSD}(f_o)$  is the PSD at a particular frequency  $f_o$ ,  $f_p$  and  $f_s$  are the preceding and the succeeding frequencies for  $f_o$ , respectively. A force analysis program is made for the determination of the power spectrum of the measured cutting force signals.

Two methods of surface roughness measurement are used: the interferometric method and the stylus method. A WYKO noncontact phase shift interferometry measurement system (Fig. 4.6) is used to determine a 3-D surface topography of the diamond turning surface. Surface roughness down to below 0.1 nm can be measured with no contact and no damage to the surface being tested; the sampling area measured is 0.3 by 0.3 mm. Phase measurement interferometry has been known for several years (Selberg 1987), and various implementations of interferometry have been used to measure the microsurface roughness (Azzazy 1989; Reid and Rixon

**Fig. 4.6** Wyko noncontact microsurface measurement system



**Fig. 4.7** Phase shift interferometer microscope for measuring phase and sending data to computer for the phase calculation



1986). A typical interferometric microscope consists of a phase-shifting interferometer, the electronic interface unit and the computer as shown in Fig. 4.7. The optical data used to construct topography of the sample surface are created from phase interferometer. Both the paths of light reflecting off the workpiece surface



**Fig. 4.8** Form Talysurf laser interferometric surface texture measuring system



and the path of light reflecting off the reference surface are combined inside the magnification head to produce fringes which are digitised and processed to give 3D surface topography.

Another method is used to measure the surface roughness profile by the Form Talysurf System (Fig. 4.8). It is a contact type measuring system used to measure the surface texture, waviness, dimension and the form of the diamond-turned surface with a resolution down to 10 nm. The Form Talysurf instrument was designed and built by Taylor–Hobson Pneumo Limited, who developed the first such profile machine (Talysurf) in 1941. Figure 4.9 illustrates a diagram showing the chief constituents of a stylus type surface texture measuring instrument. The stylus traverses across the surface and the gauge converts its vertical movements into an electrical signal which is amplified and used to operate a recorder. The  $R_a$  (arithmetic roughness) value is derived from this filtered signal which is displayed on a

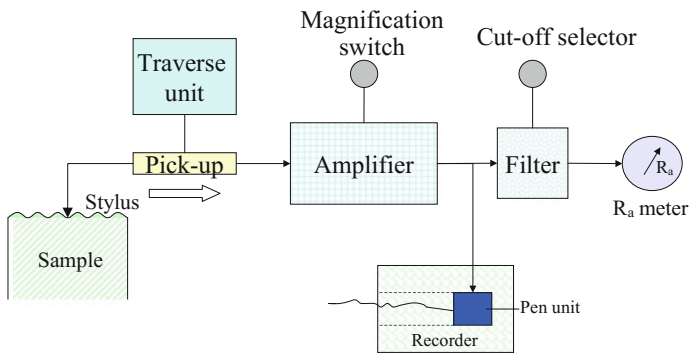


**Fig. 4.9** Diagram showing the chief constituents of the Form Talysurf

printer. The instrument is operated with a  $0.6\ \mu\text{m}$  radius conical diamond tip and 120 mm traverse unit.

#### 4.1.4 Measurement of Cutting Force

In our research testing, the main cutting force was picked up by a force sensor mounted underneath the tool. A dynamic spectrum analyser (HP 3562 A) was used to analyse the characteristics of the raw signals. The results of feature signals were subsequently digitised by an A/D converter and then fed into a PC-586 compatible computer for further processing. The outputs from the charge amplifier were recorded by a seven-channel cassette tape recorder. The main cutting forces were captured approximately at the midway point of the tool travel between the periphery and the centre of the workpiece. Since the captured time length (0.2 s) is relatively small compared with the overall cutting cycle (19 s), it is assumed that the mean cutting forces were quasi-static in the measuring range. The direction of main cutting force is shown in Fig. 4.10. The main parts of the experimental set-up are shown in Fig. 4.11.

#### 4.1.5 Work Materials and Cutting Conditions

We conducted a series of face cutting experiments on copper and aluminium single crystals with different crystallographic orientations. The crystals were obtained from Gold Company, UK. The cutting was performed on the basal plane of the

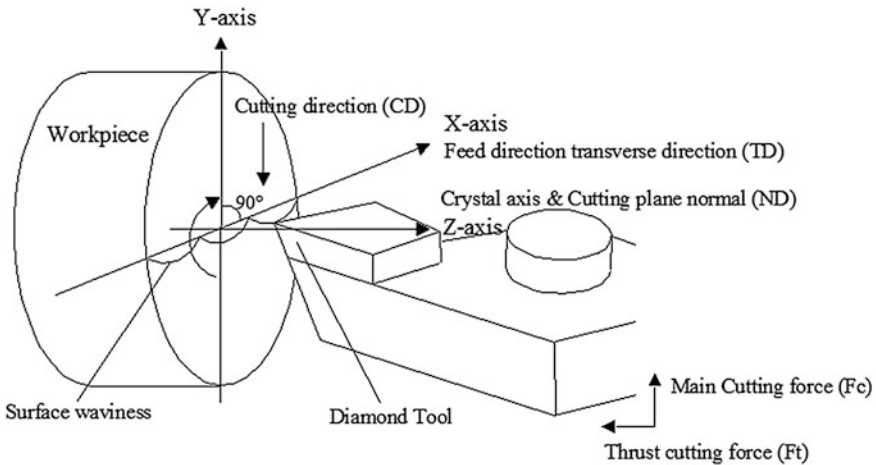
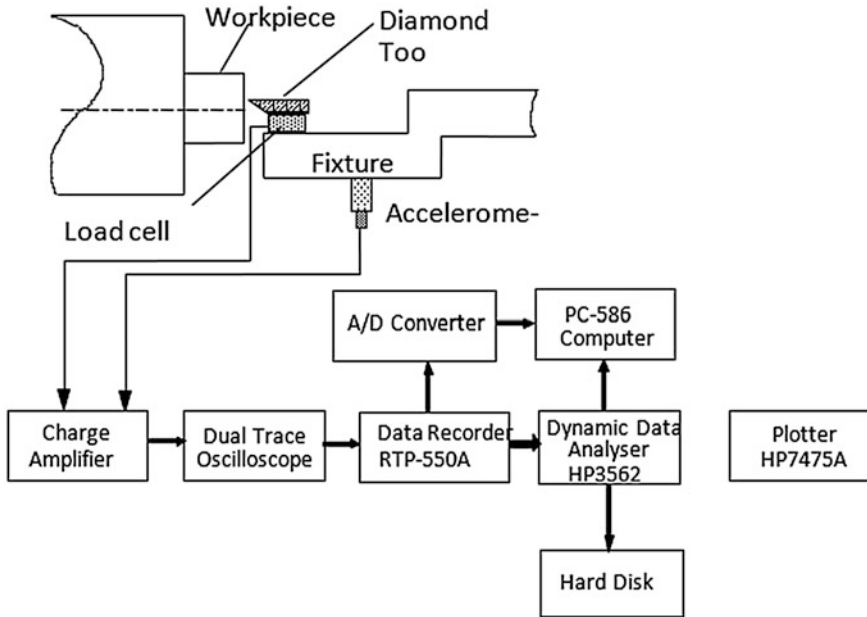


Fig. 4.10 Schematic diagram of facing turning



**Fig. 4.11** Experimental set-up for measuring of cutting force

cylindrical specimens with a diameter of 12.7 mm and length of 15 mm. Prior to machining, the samples were first ground by using a silicon carbide grinding paper of grit size 600 and then polished with 6 and 1  $\mu\text{m}$  diamond polishing compounds. Finally, the workpieces were electropolished with 10%<sub>vol</sub> perchloric acid (70%) and 90%<sub>vol</sub> absolute ethanol for the aluminium single crystals and 98% sulphuric acid for the copper single crystals to remove the surface deformed layer. For single crystal specimens, the basal plane normal of the specimens was aligned with the crystallographic plane normal of the crystals. The initial crystallographic orientation of the single crystal specimens was examined by a standard reflection technique on an X-ray diffractometer prior to the cutting tests.

The cutting experiments were divided into four groups, i.e. Groups I, II, III and IV. Group I included those cutting tests for studying the optical surface patterns of the workpiece. The Group II dealt with the effects of crystallographic orientation on the surface roughness investigated under various feed rate conditions. The chip formation was studied in Group III. The Group IV experiment deals with the measurement of cutting. Tables 4.2 and 4.3 summarises the cutting conditions and materials used in the cutting experiments.

**Table 4.2** Cutting condition for the cutting tests

Conditions	Experimental Group			
	I	II	III	IV
Spindle speed (rpm)	8000	4000	8000	8000
Feed rate (mm min <sup>-1</sup> )	20	40, 60, 80, 100	10, 30, 50	20
Depth of cut (μm)	10	10	1, 3, 5, 7	5, 10
Tool rake angle	5°	0°	0°	0°
Tool nose radius (mm)	0.653	0.5329	0.5329	0.5329

**Table 4.3** Specifications of workpiece materials

Specimen no.	Specification of workpiece materials
1	Aluminium single crystal with (001) as the cutting plane and the crystallographic orientation (001) [010] as the initial direction
2	Aluminium single crystal with (011) as the cutting plane and the crystallographic orientation ( $\bar{1}01$ ) [ $1\bar{1}1$ ] as the initial direction
3	Aluminium single crystal with (111) as the cutting plane and the crystallographic orientation ( $1\bar{1}1$ ) [ $0\bar{1}1$ ] as the initial direction
4	Copper single crystal with (001) as the cutting plane and the crystallographic orientation (001) [010] as the initial direction
5	Copper single crystal with (011) as the cutting plane and the initial crystallographic orientation (101) [ $1\bar{1}2$ ] as the initial direction
6	Copper single crystal with (111) as the cutting plane and the crystallographic orientation ( $1\bar{1}1$ ) [ $0\bar{1}1$ ] as the initial direction

## 4.2 Effect of Crystallography on Surface Roughness

Optical surfaces can be machined directly by ultraprecision machines on ductile materials under optimal cutting conditions. The surface roughness is affected by the depth of cut, feed rate, spindle revolution speed, tool rank angle and lubricants, as well as by the crystallographic orientation of the material being cut (To et al. 1994a, b). To investigate the effects of crystallographic orientation on the surface roughness formation in ultraprecision diamond turning of single crystal materials, a series of cutting experiments on single crystal aluminium and copper was carried out in different crystallographic directions using an ultraprecision diamond turning machine.

### 4.2.1 Surface Features with Crystallographic Orientation

Optical micrographs were taken using a microscope with Nomarski and Polariser functions. The surface was diamond-turned at a depth of cut of 10 μm and at a feed rate of 20 mm min<sup>-1</sup> by the diamond turning machine. Figures 4.12 and 4.13 show

the micrographs and the schematic representation of (100), (110) and (111) aluminium and copper single crystals surfaces, respectively. It is observed that there are threefold and fourfold patterns formed on the surface topographies of aluminium and copper single crystal. Comparing Fig. 4.12 with 4.13, a cloudy surface is more pronounced in the copper single crystal than in the aluminium crystal. On the (001) plane of both aluminium and copper crystals, a cyclic variation on the surface morphology having a quadruple rotation frequency (Figs. 4.12a and 4.13a) is observed. All four sectors of the cloudy surface are similar in size and symmetrical, and cover areas between  $\langle 001 \rangle$  and  $\langle 110 \rangle$  cutting directions. On the (110) cutting plane, there are also four sectors of cloudy surface in the form of twofold symmetry (Figs. 4.12b and 4.13b). In aluminium, the shear region lies

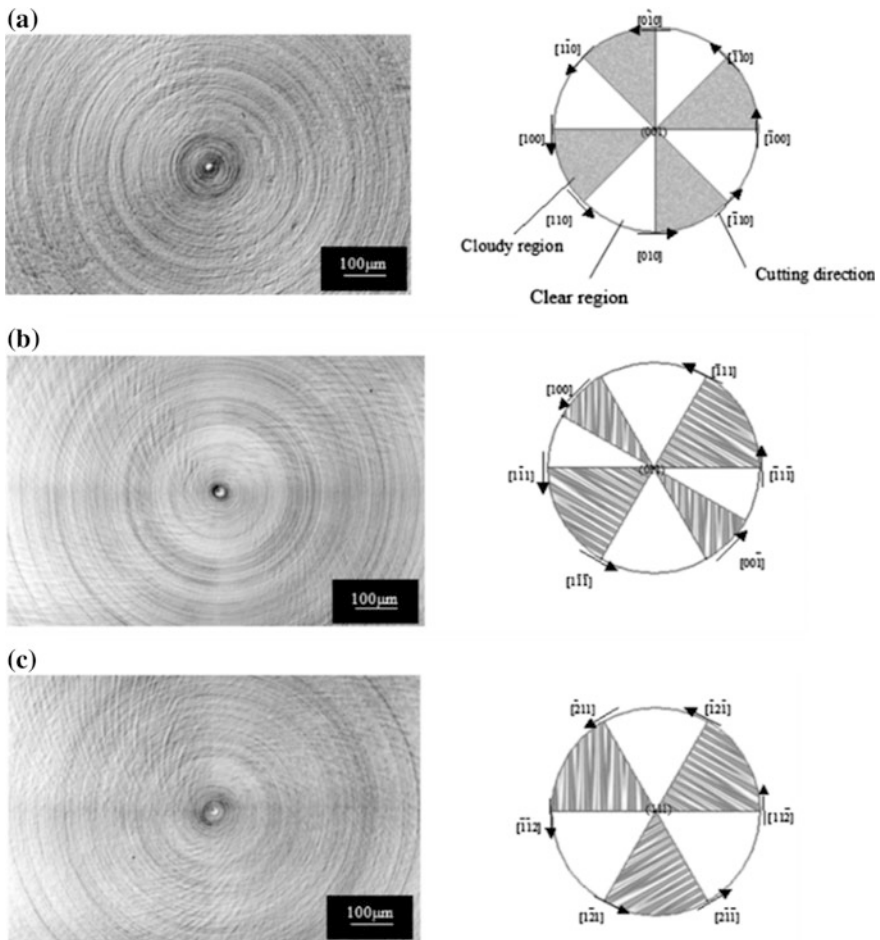


**Fig. 4.12** Optical micrographs and schematic representation of (100), (110) and (111) aluminium single crystal

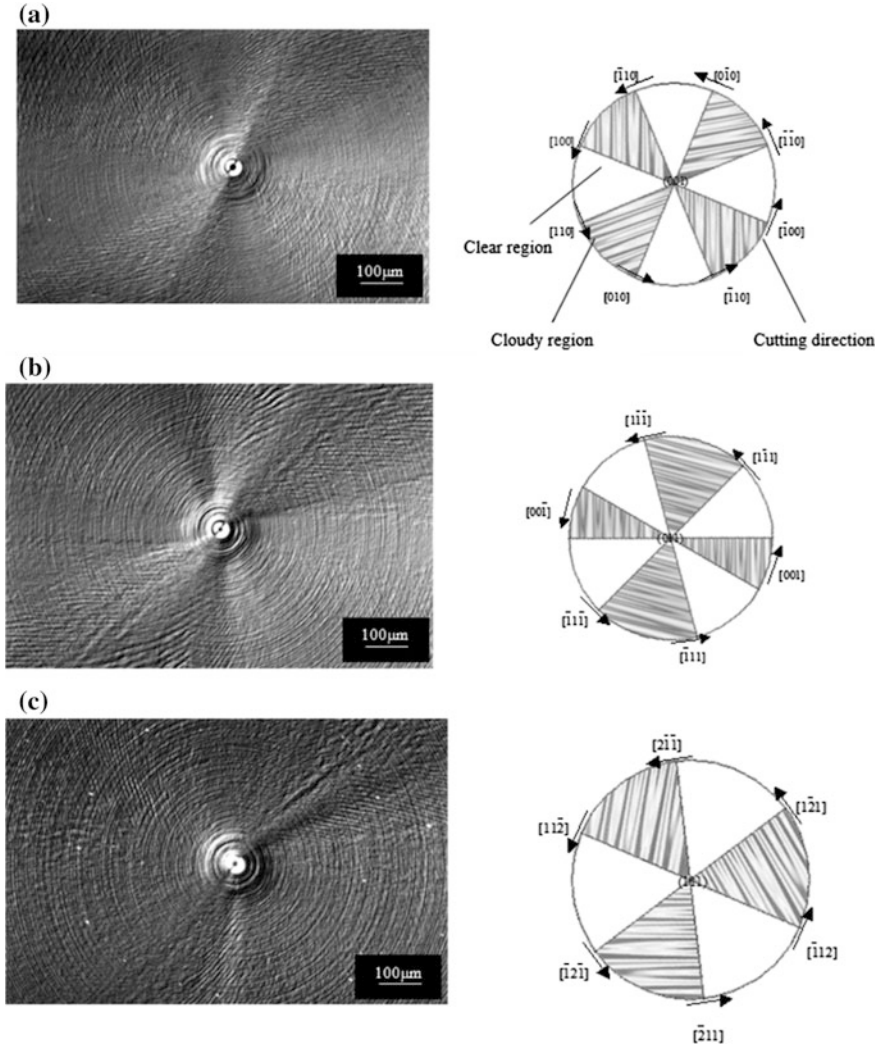


**Fig. 4.13** Optical micrographs and schematic representation of **a** (100), **b** (110) and **c** (111) copper single crystal

between the  $[\bar{1}11]$  and  $[\bar{1}\bar{1}\bar{1}]$ ,  $[1\bar{1}\bar{1}]$ , and  $[1\bar{1}\bar{1}]$  cutting direction. In (110) copper crystal, the cloudy areas between  $[1\bar{1}\bar{1}]$  and  $[1\bar{1}\bar{1}]$ ,  $[\bar{1}\bar{1}\bar{1}]$  and  $[\bar{1}\bar{1}\bar{1}]$  are found to be bigger than those along  $[00\bar{1}]$  and  $[001]$  cutting directions. On the (111) aluminium and copper surface, three sectors of shear region are observed between  $[1\bar{2}\bar{1}]$  and  $[2\bar{1}\bar{1}]$ ,  $[1\bar{1}\bar{2}]$  and  $[\bar{1}\bar{2}\bar{1}]$ ,  $[\bar{2}\bar{1}\bar{1}]$  and  $[\bar{1}\bar{1}\bar{2}]$  cutting directions. The surface morphology had less shear damage in other regions. In general, the surface patterns for the (100) and (111) cutting planes in both crystals are similar, whereas there is little variation observed on the (110) plane. Three-dimensional surface plots of the

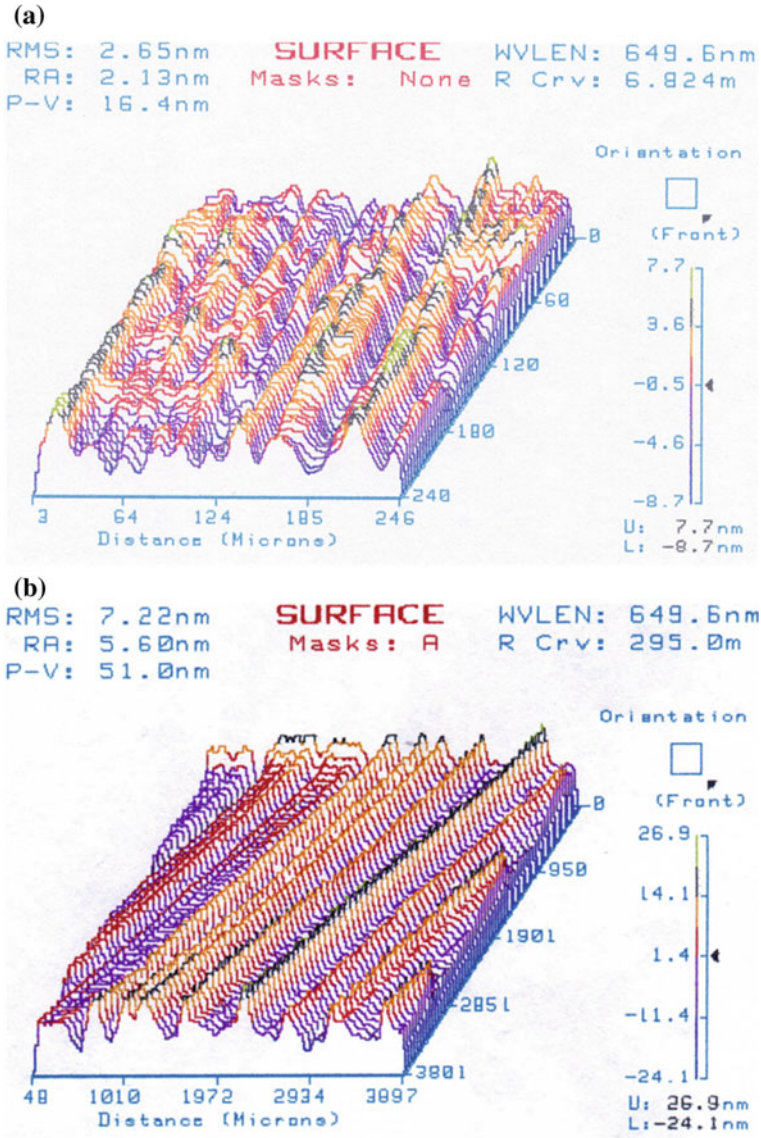


**Fig. 4.14** 3-D plot of diamond-turned surface with a cutting depth 10  $\mu\text{m}$  of copper single crystal **a** clear region, **b** cloudy region of Fig. 4.13a

phase shift interferometric pattern of the diamond-turned surface were taken at the position cloudy region and the clear region of the (001) copper single crystal (Fig. 4.14). A high roughness value (rms = 7.22 nm) was found in the cloudy region while that for the clear region was smaller (rms = 2.65 nm).

### 4.2.2 Surface Roughness Profiles Along Radial Sections

The surface roughness profiles at 12 equally angular spaced radial sections (i.e.  $m = 1-12$ ) in Fig. 4.15 on the diamond-turned surface were measured by a Form Talysurf system equipped with the rotary table with a resolution of 0.017. Measurements were started at the initial orientation of the workpiece (see Table 4.3). A measured length of 1.75 mm and a cutoff length of 0.25 mm were used throughout the experiments.

Figures 4.16 and 4.17 show the variation of the surface roughness at different radial sections of the diamond-turned aluminium and copper single crystals. The surface roughness is found to vary systematically with the crystallographic orientation of the materials being cut. Greater variation is observed on the (110) crystal plane than the (111) plane, and is the smallest on the (001) plane. There appears to be a periodic variation of surface roughness during one revolution of cut. The cyclic frequency of variation of arithmetic roughness is estimated to be four, two and three for (001), (011) and (111) planes, respectively.

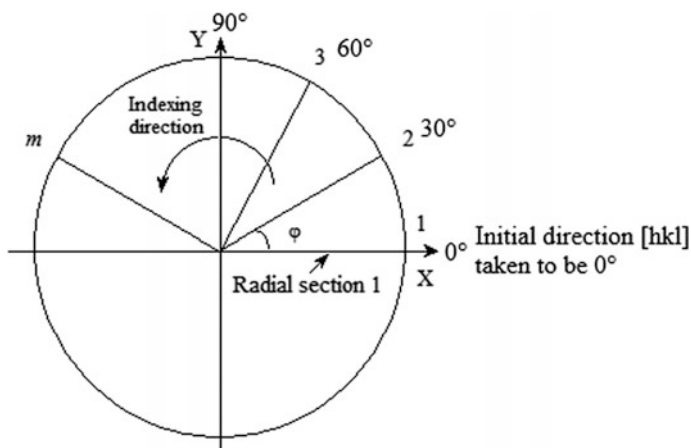


Fig. 4.15 Graphical illustration of the surface roughness measurement

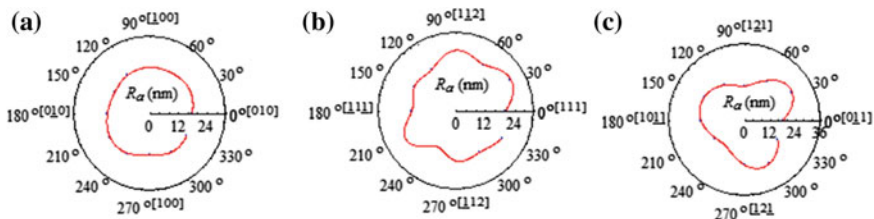


Fig. 4.16 Variation of surface roughness in diamond turning of aluminium single crystals with **a** (001) plane, **b** (110) plane and **c** (111) plane as the cutting plane



### 4.2.3 Degree of Roughness Anisotropy (DRA)

To measure quantitatively the local variation of surface roughness, a parameter named degree of roughness anisotropy (DRA) is used which is defined as the ratio of the standard deviation to the mean of the arithmetic roughness values at a finite number of equally angular spaced radial sections of the machined surface (Lee et al. 2000), i.e.

$$DRA = \frac{\sigma_{R_a}}{\bar{R}_a} = m \sqrt{\frac{\sum_{i=1}^m R_{a,i} - \bar{R}_a}{\sqrt{m-1} \sum_{i=1}^m R_{a,i}}} \quad (4.7)$$

where  $R_{a,i}$  is the arithmetic roughness value at  $i$ th radial section of the workpiece;  $\bar{R}_a$  and  $\sigma_{R_a}$  are the mean and the standard deviation of the arithmetic roughness values for the  $m$  radial sections on the surface. The parameter (DRA) provides a measure of the normalised variation of the surface roughness over the diamond-turned surface. A large value of DRA implies a high anisotropy of surface roughness.

To characterise the variation of surface roughness, the DRA of the parameter of the copper single crystal on the three cutting planes (001), (110) and (111) was calculated and is shown in Table 4.4. The observation of the surface roughness variation of Fig. 4.17 confirms the quantitative indicator as expressed by the DRA parameter. The DRA obtained for (001) plane is significantly lower than the DRA on other planes. This gives a good indication of the roughness variation.

To further illustrate the use of DRA, the effects of crystallographic orientation on the surface roughness were investigated under various feed rate conditions (i.e. 40, 60, 80 and 100 mm min<sup>-1</sup>), Fig. 4.18 shows the effect of feed rate on the variation of arithmetic roughness with cutting performed on single crystal copper with (001), (110) and (111) as the cutting planes, respectively. Similar to Fig. 4.17, systematic variation of surface roughness for the specimens is observed under various feed rates. As the feed rate increases, the arithmetic roughness for the diamond-turned crystals is found to increase (see Fig. 4.19). However, it appears that the extent of surface roughness variation changes with increasing feed rate. Figure 4.20 shows the relationship between the DRA and the feed rate. In all three crystals being

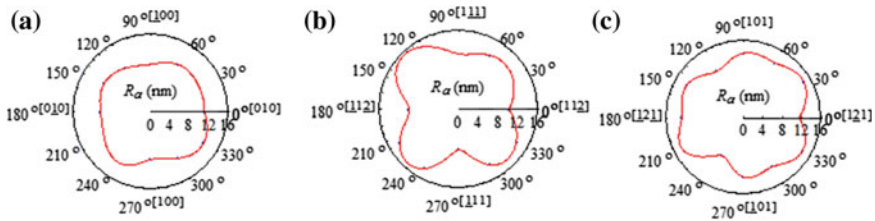


**Fig. 4.17** Variation of surface roughness in diamond turning of copper single crystals with **a** (001) plane, **b** (110) plane and **c** (111) plane as the cutting plane

**Table 4.4** Results of surface roughness measurement on copper single crystal

Specimen	Arithmetic roughness $R_a$ (nm)		
	Range	Mean	Degree of roughness anisotropy
(001)	9.75–12.55	10.97	0.075
(110)	8.15–14.65	12.13	0.167
(111)	9.05–14.35	12.44	0.120

**Fig. 4.18** Effect of feed rate on the variation of surface roughness ( $R_a$ ) in diamond turning of (001), (011) and (111) copper single crystal

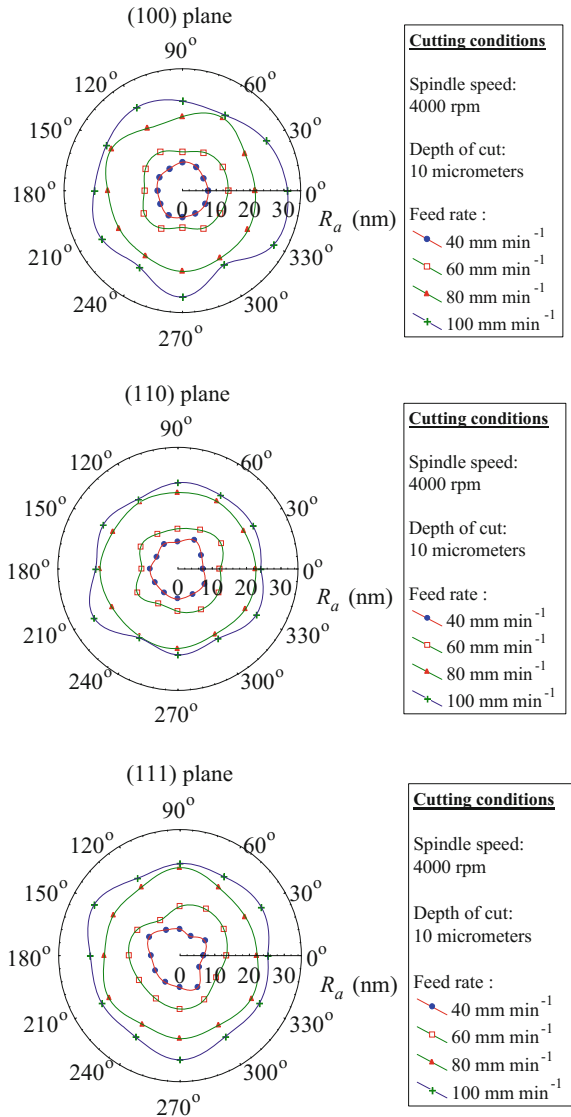


**Fig. 4.19** Effect of feed rate on the variation of surface roughness ( $\bar{R}_a$ ) measured in direction of feed (depth of cut at 10  $\mu\text{m}$ )

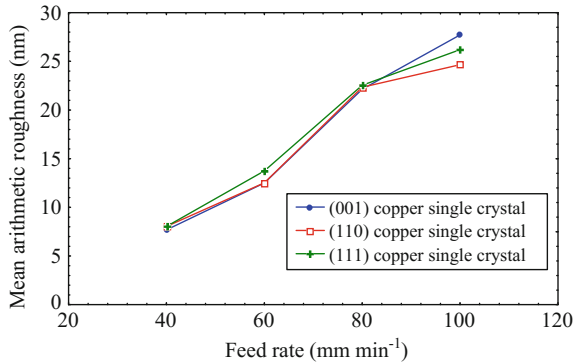
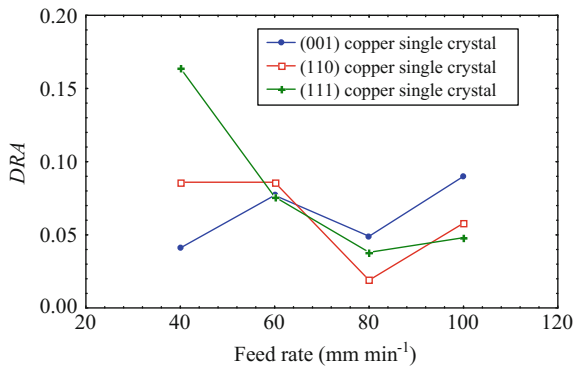


**Fig. 4.20** Relationship between degree of roughness anisotropy and feed rate of copper single crystal (depth of cut at 10  $\mu\text{m}$ )



investigated, although the mean arithmetic roughness increases with the feed rate, there exists an optimum feed rate (i.e. 80 mm min<sup>-1</sup>) at which the variation of the local surface roughness is at a minimum. This finding provides an important means for the improvement of surface quality in diamond turning of crystalline materials.

### 4.3 Variation of Cutting Force

#### 4.3.1 Effect of Feed Rate on the Cutting Force

Real-time measurement of the cutting force was carried out at various depths of cut. The spindle speed was set at 8,000 rpm whilst feed rates of 10, 30, or 50 mm min<sup>-1</sup> were used. Figure 4.21 shows the relationship between the main cutting force and the depth of cut at various feed rates in turning the (110) plane of an aluminium single crystal. The main cutting force was found to increase with the depth of cut, but the cutting force did not increase or decrease monotonically with the feed rate. When the depth of cut increased initially from 1 to 3  $\mu\text{m}$ , the difference in the cutting forces was small for the three curves.

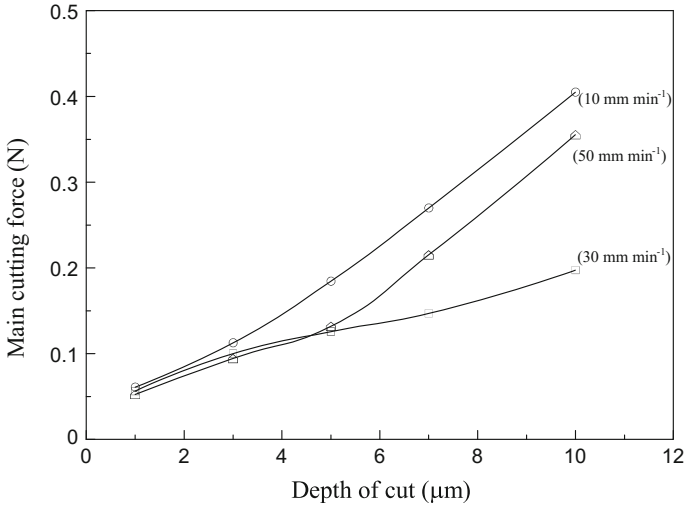


**Fig. 4.21** Effect of the feed rate on the main cutting force in cutting the (110) plane of aluminium single crystal

However, when the depth of cut was increased beyond  $5 \mu\text{m}$ , the curves started to diverge and it was found that the cutting forces were the smallest at the intermediate feed rate (i.e.  $30 \text{ mm min}^{-1}$ ) used in the experiments. This can be explained by a stick-slip motion possibly occurring at too small a feed rate. In ultraprecision diamond turning, the cutting force will increase if the feed rate is smaller than a particular critical value, and there is an optimum value of the feed rate to obtain an overall good surface finish. In turning an aluminium alloy, it has been reported by To and Lee (1995) that a good mirror surface roughness was obtained at a feed rate between  $25$  and  $30 \text{ mm min}^{-1}$ . When the feed rate was increased beyond  $30 \text{ mm min}^{-1}$ , the surface roughness rapidly increased.

### 4.3.2 Effect of Depth of Cut on the Cutting Force

The effect of cutting depth on the main cutting force of the aluminium and copper single crystals is shown in Figs. 4.22 and 4.23 respectively. At a depth of cut of  $1 \mu\text{m}$ , the cutting forces were almost the same for both materials. This observation is in agreement with the results reported by Moriwaki et al. (1993). When the depth of cut is greater than  $1 \mu\text{m}$ , all the crystals show a monotonic increase in the main cutting force with depth of cut, a size effect which has been discussed by Sato et al. (1983). In machining aluminium and copper single crystals, the (111) crystals had a relatively lower value of cutting force, as compared with those of (001) and (110) crystals. It is of interest to note that the difference in the cutting forces on the (110) and (111) planes in a single copper crystal are small.

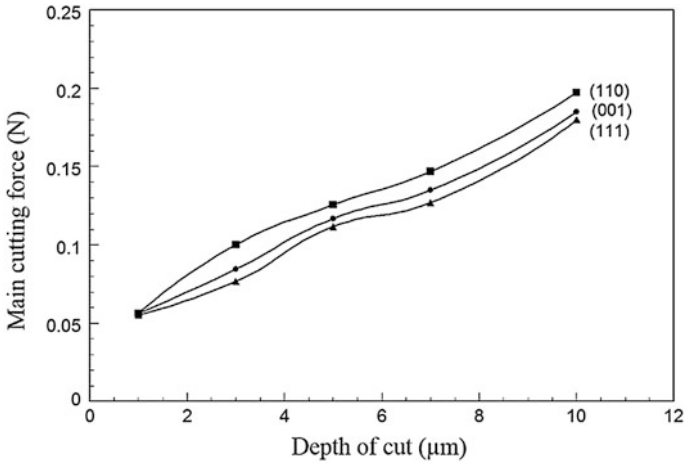


Fig. 4.22 Effect of cutting depth on the main cutting force in three aluminium single crystals

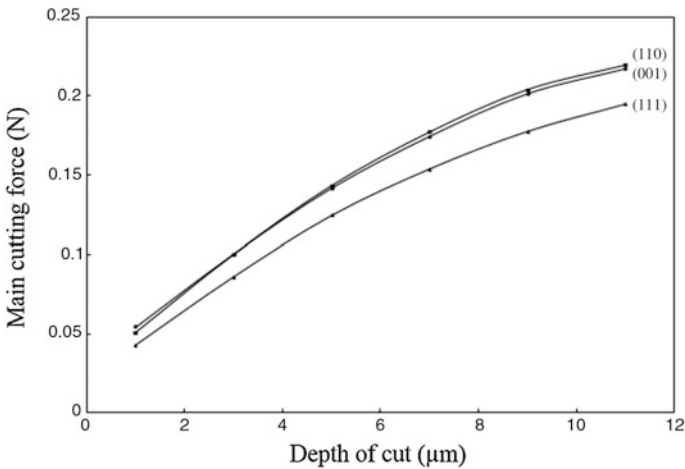


Fig. 4.23 Effect of cutting depth on the main cutting force in three copper single crystals

### 4.4 Observation on Chip Formation

The process of chip formation plays an important role in cutting mechanics. In ductile machining, plastic deformation is involved. The chip is formed through shear in a thin region (the primary deformation zone) from the tip of the tool to the free surface of the workpiece. The angle at which this shearing occurs with respect to the cutting direction is called the shear angle  $\phi$  (Fig. 4.24). Fluctuation of the shear angle manifests itself in the variation of the chip thickness. Most of the studies

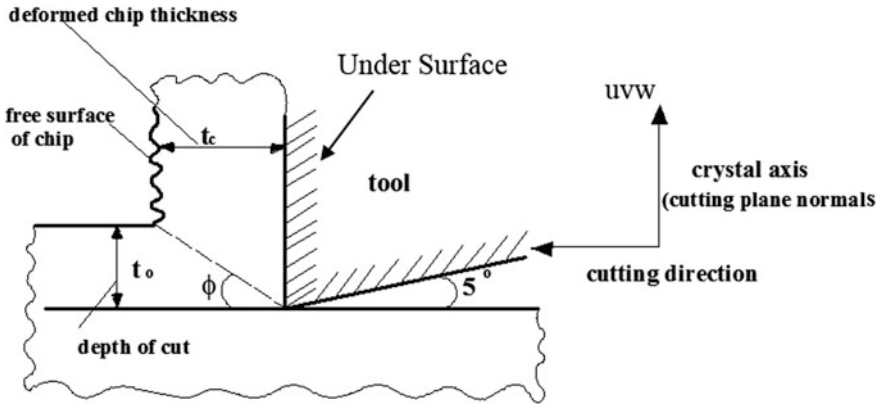


Fig. 4.24 The cutting geometry of the single crystal in diamond turning (tool rake angle = 0)

on chip formation were associated with conventional machining, although there have been a few studies on the chip formation in diamond turning (Arcona 1996). In this section, our experimental study on chip formation in aluminium and copper single crystals is reported.

Aluminium and copper single crystals with (001), (011) and (111) cutting planes were turned at a spindle speed of 8000 rpm, a feed rate of  $20 \text{ mm min}^{-1}$ , and depths of cut of 5 and  $10 \text{ }\mu\text{m}$ . Continuous chip formation occurred under all cutting conditions in the aluminium and copper single crystals. High magnification SEM photography of a typical aluminium chip is shown in Fig. 4.25. A lamellar structure was observed on the free surface of all the chips examined which was indicative of the nature of inhomogeneous strain distribution in the chip (Fig. 4.26a). The surface underneath that in contact with the tool was found to be smoother, and had long scratch marks on it similar to those found on a freshly machined surface (Fig. 4.26b). The lamellar spacings of the chip from the (011), (001) and (111) cutting planes were determined from the micrographs of Fig. 4.27a–c, which were 1.5, 0.8 and  $0.5 \text{ }\mu\text{m}$ , respectively. The lamellar spacing indicates the distance between the shear fronts. When the flow in the chip is much more homogeneous, the lamellar spacing decreases and the cutting face is expected to be lower (Williams and Gare 1977). Such observation is consistent with the result from experiments on cutting force that the cutting force in aluminium is higher on (011) plane, followed by (001) plane and lowest on (111) plane (Fig. 4.22).

Figures 4.28 and 4.29 show the SEM photographs of deformed chips in diamond-turned aluminium and copper crystals at a depth of cut of 5 and  $10 \text{ }\mu\text{m}$ , respectively. The chips were sheared off in different crystallographic directions during one revolution of the workpiece. A detailed examination of the cross sections of the chip under the SEM reveals significant fluctuation in the chip thickness.

From the classical work of Merchant (1945a), the deformed chip thickness  $t_c$  is given by:

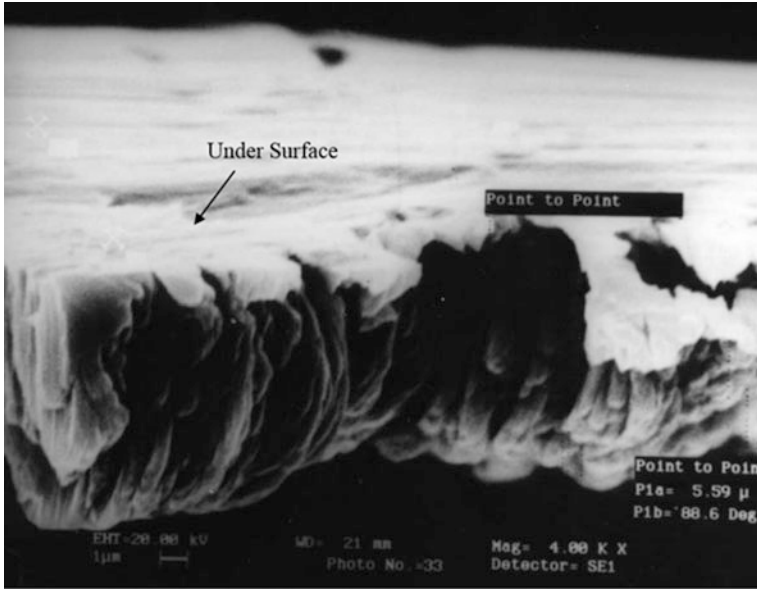


Fig. 4.25 SEM photography of an aluminium chip

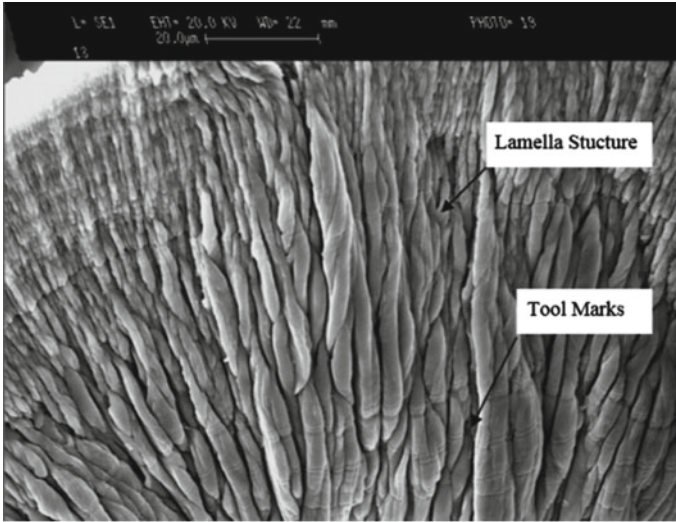
$$t_c = t_0 / \left( \frac{\cos \alpha}{\tan \phi} + \sin \alpha \right) \quad (4.8)$$

where  $\phi$  is the shear angle,  $\alpha$  is the rake angle and  $t_0$  the depth of cut. It can be noted that when the rake angle  $\alpha$  is zero, the Eq. (4.8) is simplified as:

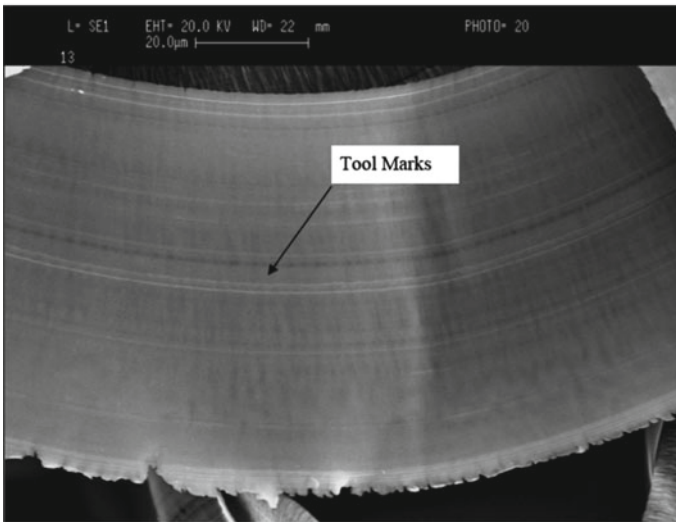
$$t_c = t_0 \cot \phi \quad (4.9)$$

Considerable variation in the chip thickness is observed as the cutting direction changes with respect to the crystal axis during one revolution of cut. An estimation of the shear angle based on the empirical Eq. (4.9) is from  $29^\circ$  to  $48^\circ$ . Such a varying chip thickness as a result of the fluctuation of shear angle will give rise to changes in the cutting force (Albrecht 1965).

To sum up, the effect of crystallographic orientation on the machinability of single crystals has been experimentally studied with respect to the change in surface roughness, cutting force and chip formation. There clearly exists an orientation dependence on the machinability parameters being studied. Among the three crystallographic cutting planes, the mean arithmetic roughness is lower on the (001) plane and higher on the (110) and (111) planes. The roughness value  $R_a$  measured along the radial dimension on the turned surface in one complete cycle shows a cyclic pattern which can be correlated with the crystallographic plane being cut, i.e. a periodicity of four, two and three is associated with (001), (110) and (111) cutting planes, respectively.



(a) Free surface



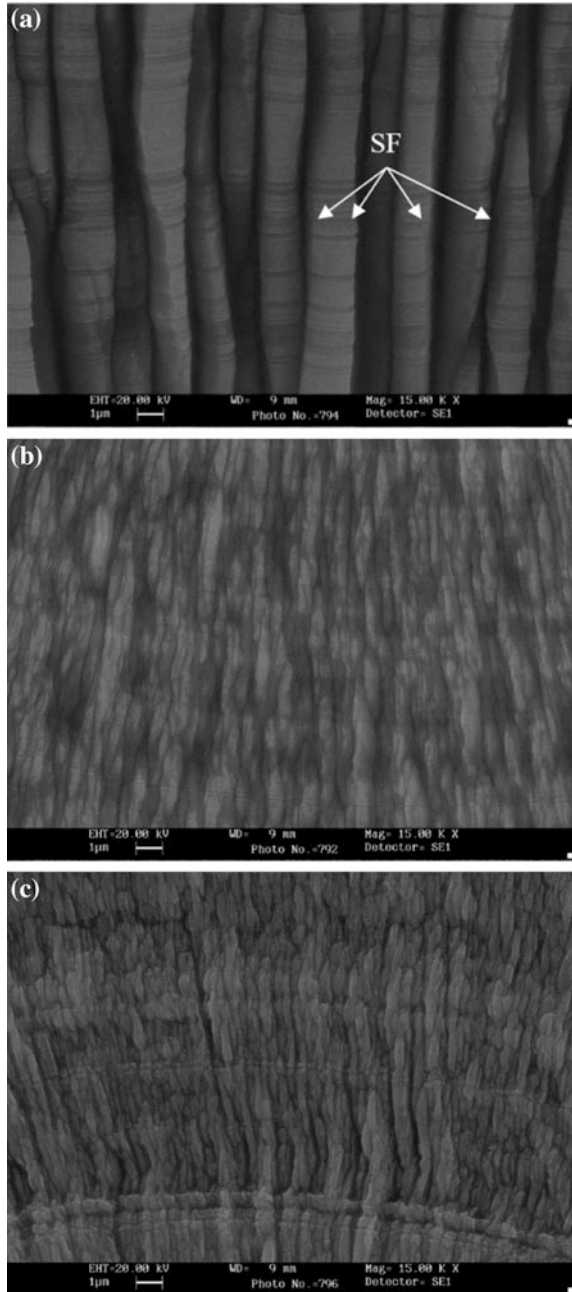
(b) Under surface

**Fig. 4.26** Lamellar structure at **a** the cutting free surface and **b** the under surface of the chip of (011) aluminium crystal

To compare the extent of the variation of roughness data on different crystallographic planes, a parameter called the degree of roughness anisotropy (DRA) is introduced which measures quantitatively the local variation of surface roughness. The greatest variation is observed on the (110) cutting plane, less on the (111) plane and is the smallest on the (001) plane. An increase in the feed rate increases the

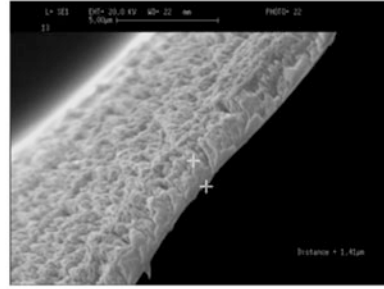


**Fig. 4.27** Scanning electron micrography of the free surface of chips from an aluminium single crystal on various planes **a** (011), **b** (001) and **c** (111) at depth of cut  $-10\ \mu\text{m}$

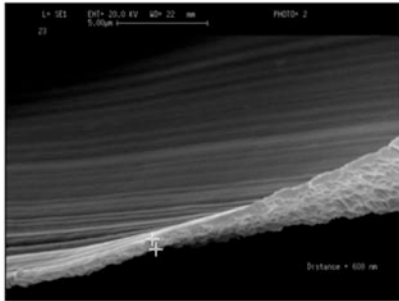




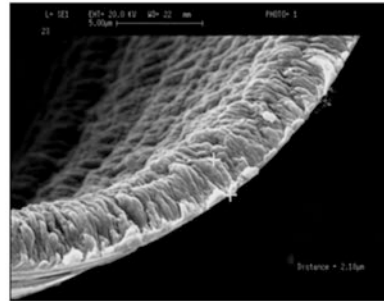
(a) (001) cutting plane; Depth of cut = 5  $\mu\text{m}$



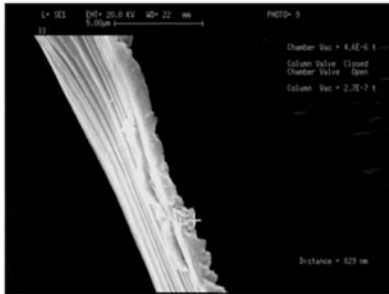
(b) (001) cutting plane; Depth of cut = 10  $\mu\text{m}$



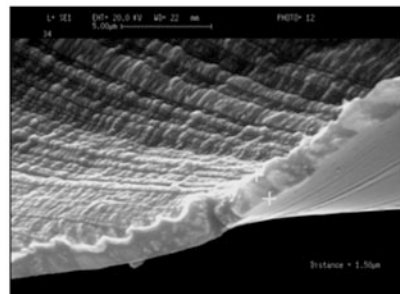
(c) (011) cutting plane; Depth of cut = 5  $\mu\text{m}$



(d) (011) cutting plane; Depth of cut = 10  $\mu\text{m}$



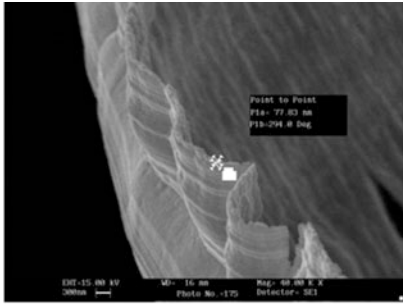
(e) (111) cutting plane; Depth of cut = 5  $\mu\text{m}$



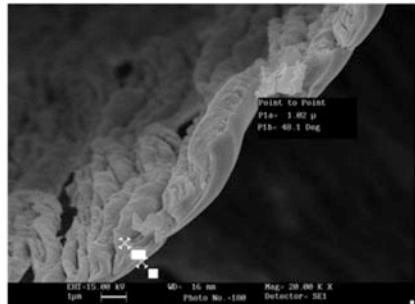
(f) (111) cutting plane; Depth of cut = 10  $\mu\text{m}$

**Fig. 4.28** SEM photographs of deformed chips of aluminium single crystal

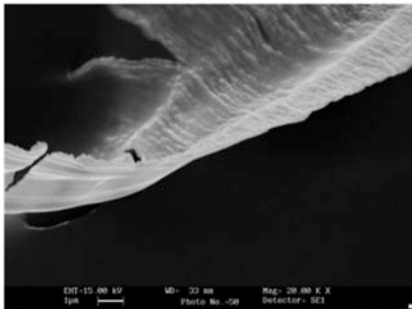
mean arithmetic roughness measured in the direction of feed. This is expected because the roughness measured in the feed direction is dictated mostly by the tool radius and feed rate. The roughness measured for each of the cutting planes is the smallest at a feed rate of 80 mm min<sup>-1</sup>. The actual surface roughness is higher than



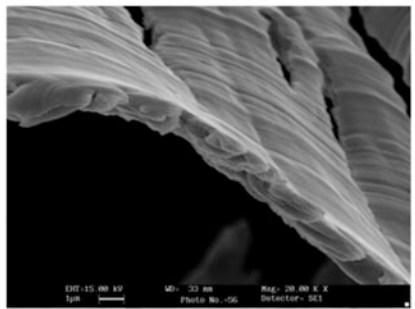
(a) (001) cutting plane; Depth of cut = 5  $\mu\text{m}$



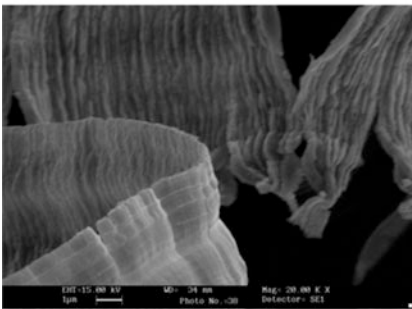
(b) (001) cutting plane; Depth of cut = 10  $\mu\text{m}$



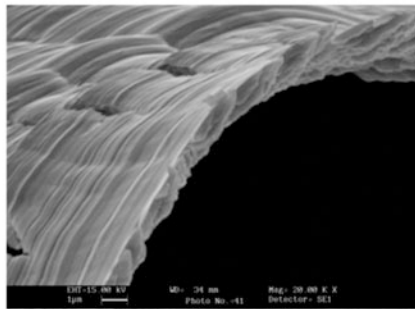
(c) (011) cutting plane; Depth of cut = 5  $\mu\text{m}$



(d) (011) cutting plane; Depth of cut = 10  $\mu\text{m}$



(e) (111) cutting plane; Depth of cut = 5  $\mu\text{m}$



(f) (111) cutting plane; Depth of cut = 10  $\mu\text{m}$

**Fig. 4.29** SEM photo of deformed chips of copper single crystal

the values obtained from the theoretical roughness which takes into account the feed rate and nose radius only.

The metal chip has a lamellar structure on the free surface which reveals the inhomogeneous nature of plastic deformation in the shearing process. The lamellar

spacing varies with the crystallographic orientation of the cutting plane and a small spacing is associated with a lower cutting force, and vice versa. The chip thickness varies along its length in face turning as the orientation of the cut changes continually in one revolution of cut. Variation in the chip thickness caused by the fluctuation in the shear angle will induce changes in the cutting force and hence the surface roughness.

## References

- Albrecht, P. (1965). Dynamics of the metal cutting process. *Engineering for Industry*, 87, 429.
- Arcona, C. (1996). *Tool force, chip formation and surface finish in diamond turning*, PhD thesis, North Carolina State University, p.1.
- Azzazy, M. (1989). Surface topography using diffuse point differential interferometry. *Optics and Lasers in Engineering*, 10, 81.
- Merchant, M. E. (1945). Mechanics of the metal cutting process. I: Orthogonal cutting and A type 2 chip. *Journal of Applied Physics*, 16, 267.
- Moriwaki, T., Okuda, K., & Shen, J. G. (1993). Study of ultraprecision orthogonal microdiamond cutting of single crystal copper. *JSME International Journal Series C*, 36(3), 400.
- Mulgrew, B., Grant, P. & Thompson, J. (1999). Multirate signal processing. In *Digital Signal Processing* (pp. 299–326). Macmillan Education UK.
- Proakis, J. G., & Manolakis, D. G. (1996). *Digital signal processing: Principles, algorithm, and applications* (3rd ed.). New York: Prentice Hall.
- Reid, G. T., & Rixon, R. C. (1986). Optical testing of large SPDT mirrors using visible and IR interferometry. In *SPIE* (Vol. 665, p. 162). *Optical Techniques for Industrial Inspection*.
- Sato, M., Kato, Y., & Aoki, S. (1983). Effects of crystal orientation on the cutting mechanism of the aluminium single crystal. *Bulletin of JSME*, 26, 890.
- Selberg, L. A. (1987). Interferometer accuracy and precision. *SPIE Proceedings*, 749, 8.
- To, S. & Lee, W. B. (1995). A study of the surface microtopography of aluminium alloys in single point diamond turning. In *American society of precision engineering (ASPE)* (p. 124), October 15–20, 1995.
- To, S., & Lee, W. B. (2001). Deformation behavior of aluminium single crystals in ultraprecision diamond turning. *Journal of Materials Processing Technology*, 133, 296–300.
- To, S., Lee, W. B., & Chan, C. Y. (1997). Ultraprecision diamond turning of aluminium single crystals. *Journal of Materials Processing Technology*, 63(1–3), 157–162.
- To, S., Lee, W. B., & Chan, C. Y. (1999). Effect of machining velocity on the crystallographic texture in a diamond turned aluminium single crystal. *Textures and Microstructures*, 31(4), 249–261.
- To, S., Lee, W. B., & Cheung, C. F. (2003). Orientation changes of aluminium single crystals in ultra-precision diamond turning. *Journal of Materials Processing Technology*, 140(1–3), 346–351.
- To, S., Lee, W. B., & Ralph, B. (1994a). Deformation and recrystallization in cross-rolled Al–Cu precipitation alloys. *Journal of Materials Science*, 29, 269–275.
- To, S., Lee, W. B., & Ralph, B. (1994b). Recrystallization textures of a cross-rolled aluminium alloy. *Textures and Microstructures*, 157–162, 327–332. Part 2.
- To, S., Lee, W. B., & Zhu, Y. H. (2002). Ultra-precision-machining induced surface structural change of Zn–Al alloy. *Materials Science and Engineering A*, A325, 497–502.

- To, S., Wang, H., & Jelenković, E. V. (2013). Enhancement of the machinability of silicon by hydrogen ion implantation for ultra-precision micro-cutting. *International Journal of Machine Tools and Manufacture*, 74, 50–55.
- Williams, J. A., & Gare, N. (1977). Some observations on the flow stress of metals during metal cutting. *Wear*, 42, 341.
- Lee, W. B., To, S., & Cheung, C. F. (2000). Effect of crystallographic orientation in diamond turning of copper single crystals. *Scripta Materialia*, 42(10), 937–945.

# Chapter 5

## Materials Deformation Behaviour and Characterisation

**Abstract** Ultraprecision diamond turning can produce advanced components with not only a high-dimensional accuracy but also with a good surface integrity such as a small surface roughness and low-residual stress. In this chapter, an experimental study on diamond-turned surface layers was conducted by machining single crystals with different crystallographic planes. The influences of the depth of cut and the initial crystal orientation on the plastic properties were studied from the changes in dislocation density, the microstrain, the microhardness of the machined surface layer and the deformed structure. The block size, microstrain and dislocation density in the deformation layer were derived from the X-ray diffraction (XRD) line profile analysis method. The elastic modulus and the recovery behaviour were measured by nano-indenter testing. Transmission electron microscopy (TEM) was used to characterise the dislocation structure of the diamond-turned surface at various depths of cut.

### 5.1 Techniques for Materials Characterisation

#### 5.1.1 X-ray Diffraction

A practical guide for exploring the deformation layer caused by of diamond turning is given for use with a Philips X'PERT X-ray diffractometer (PW3710) with Cu  $K_\alpha$  radiation source ( $\lambda = 1.54$ ) (Fig. 5.1). Parallel beam optics for thin film geometry were employed. In this mode, the incident X-ray beam is directed to shine on the surface with a small grazing angle of  $0.75^\circ$ , so as to increase the interaction path between the beam and the deformation layer. The detector is driven to scan from  $2\theta = 35^\circ\text{--}75^\circ$ . If there are grains in the samples having lattice planes with a separation of  $d$ , the angles  $\theta_1$  and  $\theta_2$  shown in Fig. 5.1 are equal ( $=\theta$ ), and the Bragg condition, as in Eq. (5.1), is satisfied, then constructive interference occurs and a strong diffraction peak is observed.

$$\lambda = 2d \sin \theta \quad (5.1)$$

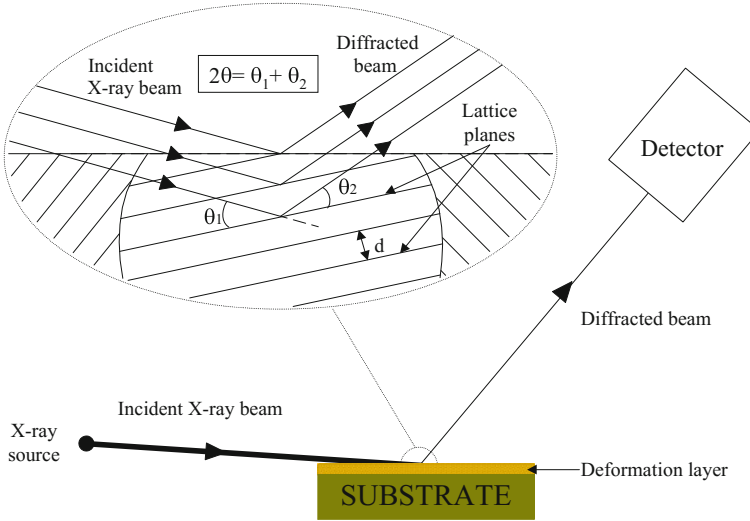


**Fig. 5.1** The basic feature of the  $2\theta$  scanning mode of XRD experiment

The intensity distribution function of X-ray diffraction,  $h(x)$ , can be expressed as

$$h(x) = \int_{-\infty}^{\infty} g(y)f(x-y)dy \quad (5.2)$$

where  $g(y)$  is of the intensity function of the geometric broadening function and  $f(x)$  is the intensity distribution function of the physical broadening function. The true (physical) broadening,  $\beta$ , is given by

$$\beta = \frac{m_{hkl}n_{hkl}}{\int_{-\infty}^{\infty} M(x)N(x)dx} \quad (5.3)$$

where  $m_{hkl}$  and  $M(x)$  are, respectively, the part of the broadening and the intensity distribution function corresponding to the dispersion of the blocks,  $n_{hkl}$  and  $N(x)$ , being the same for the microstrains (strains of scale comparable with the grain size). When  $M(x)$  and  $N(x)$  are the Lorentzian and Gaussian functions, respectively, then

$$H = \int_{-\infty}^{\infty} L(x)G(x)dx \quad (5.4)$$

where  $L(x) = (1 + \alpha_L x^2)^{-1}$  and  $G(x) = \exp(-\alpha_G x^2)$ . The block size is deduced from the broadening using (Cullity 1956)

$$D_{hkl} = \frac{K\lambda}{m_{hkl} \cdot \cos \theta_{hkl}} \quad (5.5)$$

where  $K$  is a constant dependent on the block shape,  $\lambda$  is the X-ray wavelength, and  $M_{hkl}$  is as above. The microstrains are deduced from the line broadening as:

$$\varepsilon_{hkl} = \frac{\Delta d_{hkl}}{d_{hkl}} = \frac{n_{hkl} \cos \theta}{4} \quad (5.6)$$

where  $d_{hkl}$  is the interplanar distance and  $n_{hkl}$  is the part of broadening associated with these strains. The minimum dislocation density is calculated by the Voigt function. The  $\rho_{hkl}$  values are based on the block size as determined in one of the above ways from the line intensities, and line widths. The minimal dislocation density is given by

$$\rho_{hkl} = \frac{3}{D_{hkl}^2} \quad (5.7)$$

X-ray diffraction (XRD) line profiles were measured by a diffractometer with Cu  $K_\alpha$  radiation. The diffraction peaks (001), (011) and (111) of the aluminium single crystal were used for analysis. The strong line profile from diffraction was recorded by step scanning in  $2\theta$  steps of  $0.04^\circ$ , with RS =  $0.5^\circ$  and DS/SS =  $1^\circ$ . RS is the receiving slit, DS is the divergence slit and SS is the scattering slit, at an X-ray tube voltage of 40 kV and current of 35 mA.

### 5.1.2 Nano-indentation Measurements

A Nanoindenter (Nano Instruments Inc., Model IIs) was used for testing the hardness of the deformation layer. A highly accurate result can be obtained as the load of this instrument can be maintained as low as 500  $\mu\text{N}$ , and the resolution of the penetration depth is 0.04 nm.

In practice, the nanoindenter has a Berkovich indenter head (a 3-sided pyramidal diamond tip). The normal load of the indenter is controlled by a current passing through a coil. A magnetic field is generated to interact with a permanent magnet, which is attached to the indenter shaft. The displacement of the indenter is converted to a voltage signal by a capacitance displacement gauge. The electrical signal from the gauge is then amplified and recorded by a computer. The schematic representation of the Nano Indenter II system is shown in Fig. 5.2. The relationship of the indenter proper to the indenter head is illustrated. The coil and magnet move



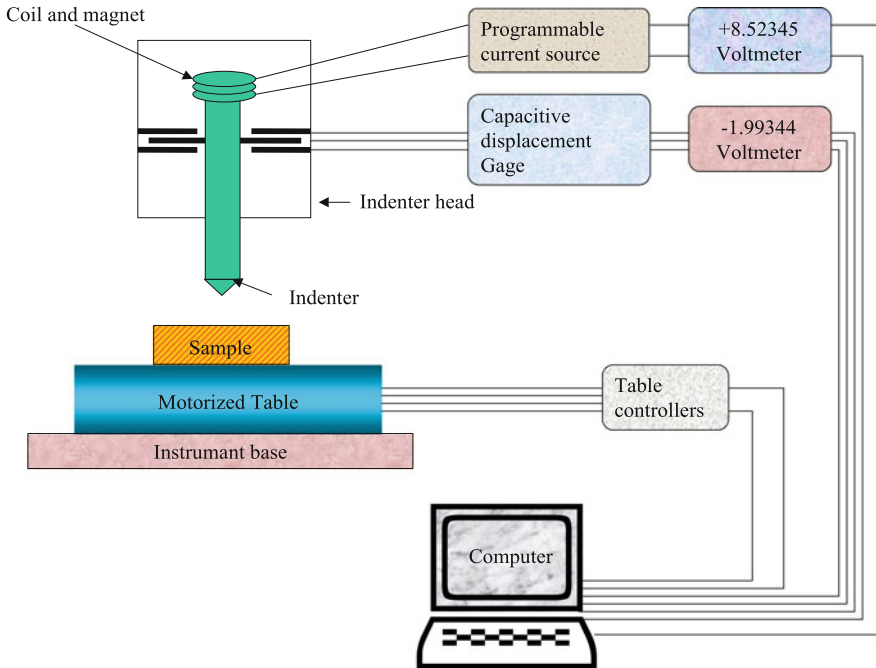


**Fig. 5.2** Schematic representation of the Nano Indenter II system

the indenter only. Gross motion of the specimen in the  $z$  direction is accomplished by the motorised table, which is capable of motion in all three directions.

In order to calibrate the area function  $A(h_c)$  of the diamond tip and the load frame stiffness  $S$  of the indenter, the procedures which were proposed by Oliver and Pharr (1992) were followed firstly. Indentation tests with different maximum loads were then made. Each indentation cycle consists of a loading curve and an unloading curve (Fig. 5.3), showing the displacement of the tip when the normal load is increased and reduced, respectively.

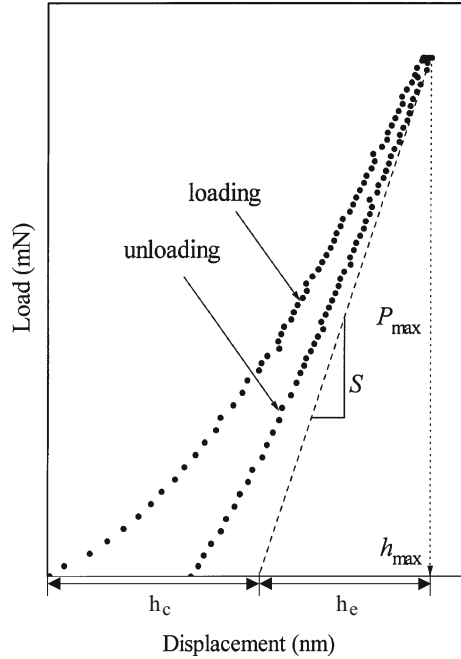
The unloading curve is then fitted using a power law function:

$$P = K(h - h_f)^m \quad (5.8)$$

where  $P$  and  $h$  are the instant applied normal load and displacement of the diamond tip,  $K$  and  $m$  are constants and  $h_f$  is the depth of indent after the normal load is removed.  $K$ ,  $h_f$  and  $m$  are determined from the least-squares-fit method, by using 90% of the data in the unloading curve.

It is assumed that during indentation, both elastic deformation and plastic deformation are generated. When the normal load is removed, the elastic deformation recovers. The elastic deformation at maximum load is then characterised by

**Fig. 5.3** A typical pattern of loading/unloading curves of a nano-indentation



a depth  $h_c$  (Fig. 5.3). Before determining the value of  $h_c$ , the stiffness  $S$  at maximum load  $P_{\max}$  is first attained and is equal to the slope of the unloading curve at  $P_{\max}$  (see Fig. 5.3).  $h_c$  is thus determined as:

$$h_c = \varepsilon \frac{P_{\max}}{S} \quad (5.9)$$

where  $\varepsilon$  is set to 0.75, assuming that the indenter head has an X-ray diffraction parabolic revolution geometry. The plastic displacement (contact depth)  $h_c$  is determined as:

$$h_c = h_{\max} - h_e \quad (5.10)$$

where  $h_{\max}$  represents the maximum displacement of the diamond tip (see Fig. 5.4). The contact area can be determined from  $h_c$  and the area function  $A(h_c)$ . The deformation hardness  $H$  is then calculated as:

$$H = \frac{P_{\max}}{A(h_c)} \quad (5.11)$$

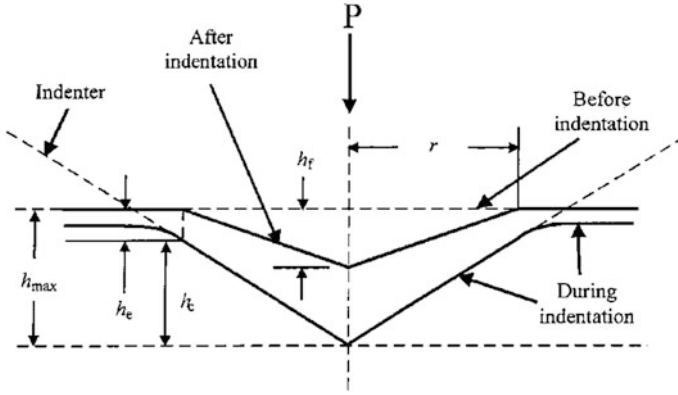


**Fig. 5.4** Deformation generated during indentation.  $R$  is the radius of the contact circle (Oliver and Pharr 1992)

In addition, the reduced elastic modulus  $E_r$  is determined from the formula:

$$S = \frac{2}{\sqrt{\pi}} E_r \sqrt{A(h_c)} \quad (5.12)$$

where  $E_r$  is given by:

$$E_r = \left[ \frac{1 - \nu_i^2}{E_i} + \frac{1 - \nu_s^2}{E} \right] \quad (5.13)$$

In Eq. (5.13),  $\nu_i$  ( $=0.07$ ) and  $E_i$  ( $=1,141$  GPa) are the Poisson's ratio and the elastic modulus of the diamond, and  $\nu_s$  represents the Poisson's ratio of the test material and is assumed to be 0.25 for our samples.  $E$ , the elastic modulus of the testing material, can thus be calculated accordingly.

For each sample, twelve indentations were made at different points in the form of a 3 by 4 matrix. Each experiment was repeated four times to get the average values of  $H$  and  $E$ . The range of load used in the experiment was from 0.07 to 300 mN.

### 5.1.3 Nanoscratch Testing

Nanoscratch tests were carried out with the nanoindenter operated in the scratching mode, using another Berkovich diamond tip. Aluminium single crystals with (001), (011) and (111) orientations were selected for the study. A typical nanoscratch test consists of two segments, the scratch segment and the post scan segment. In the scratch segment, the diamond tip is programmed to travel a distance of 500  $\mu\text{m}$  on the sample surface with a constant speed of 5  $\mu\text{m s}^{-1}$ . The normal load is either fixed at one of the four values of 0.2, 0.4, 0.7 and 2.5 mN (Fig. 5.5).

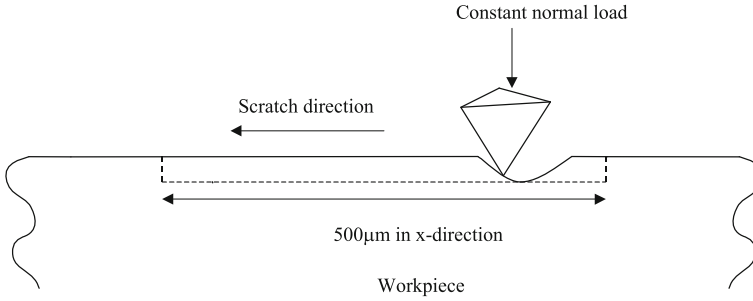


**Fig. 5.5** Scratching with constant normal load

The indenter head has two proximity sensors, which are used to record the components of the frictional force generated in the two perpendicular directions during scratching. The resultant frictional force is thus obtained. The friction coefficient  $\mu$  of the sample along the scratch track can then be determined.

#### 5.1.4 Transmission Electron Microscopy (TEM)

An electron beam passing through a crystalline specimen, sufficiently thin so that absorption may be considered negligible, is in part transmitted without deflection and in part diffracted by the crystal planes. Bragg's Law applies to the diffracted beam where  $\lambda$  is the wavelength of the electrons given by the modified De Broglie relation ( $h$  denotes the Planck constant in Eq. (5.14) only)

$$\lambda = \frac{h}{[2m_0eV(1 + (eV/2m_0c^2))]^{1/2}} \quad (5.14)$$

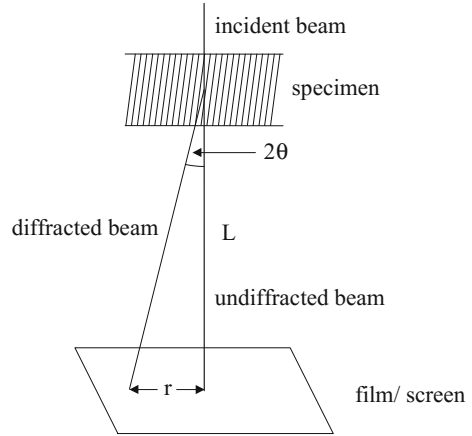
with  $E_{\text{kin}} = eV$  being the kinetic energy of an electron accelerated by an electric potential  $V$ .  $d_{hkl}$  is the spacing between planes and for the cubic lattice is given in terms of the Miller Indices  $hkl$  as:

$$d_{hkl}^2 = a_0^2 / (h^2 + k^2 + l^2) \quad (5.15)$$

where  $a_0$  is the lattice parameter. By convention (Goodhew and Humphreys 1992) the order of reflection,  $n$ , is set to unity and higher order reflections are defined as  $n = 1$  reflections from the higher order plane.

The diffraction mode in the TEM allows these diffracted beams to be imaged on a phosphor screen, as shown simplistically in Fig. 5.6, forming a pattern of spots with each representing diffraction from a particular set of  $\{hkl\}$  planes. The

**Fig. 5.6** Simplified electron diffraction



separation  $r$  between the transmitted spot and a diffracted spot is given in terms of the camera length  $L$  and the Bragg angle  $\theta$  as:

$$r = 2\theta L \quad (5.16)$$

and so by combining this with Eqs. (5.1) and (5.12), the diffraction planes and interplanar spacings can be inferred from the relationship

$$r = \frac{L\lambda}{d_{hkl}} = \frac{L\lambda}{a_0} \sqrt{h^2 + k^2 + l^2} \quad (5.17)$$

The diffraction conditions are often represented by the Ewald sphere construction (Goodhew and Humphreys 1992) in which the crystal is drawn in terms of its reciprocal lattice. From the undiffracted primary beam spot, the incident electron beam is drawn parallel to its direction in real space and of length  $1/\lambda$  and then the Bragg condition is then equivalent to a circle of radius  $1/\lambda$  intersecting both the primary spot and another reciprocal lattice point.

Diffraction from a crystal may be represented by a Kikuchi map where the major axes are plotted in similar fashion to stereographic projection, hence tilting of the specimen results in translation within the Kikuchi map. The major axes are connected by Kikuchi lines which are the result of the elastic scattering of previously elastically scattered electrons (Goodhew and Humphreys 1992).

The structure of a diamond-turned surface was examined by transmission electron microscope (Model H-800 from Joel). In order to achieve a fresh diamond-turned surface, an aluminium single crystal of about 0.3 mm thickness was cut by a diamond saw. The sample was put on the sample holder, and then both sides of the sample were diamond turned at different depths of cut until the thickness of the sample was about 30  $\mu\text{m}$ , and it then thinned by single-jet electrolytic polishing. Examination of the diamond-turned surface structure was performed by the methods of dark and bright field images.

## 5.2 Characterisation of the Diamond-Turned Surface Layer

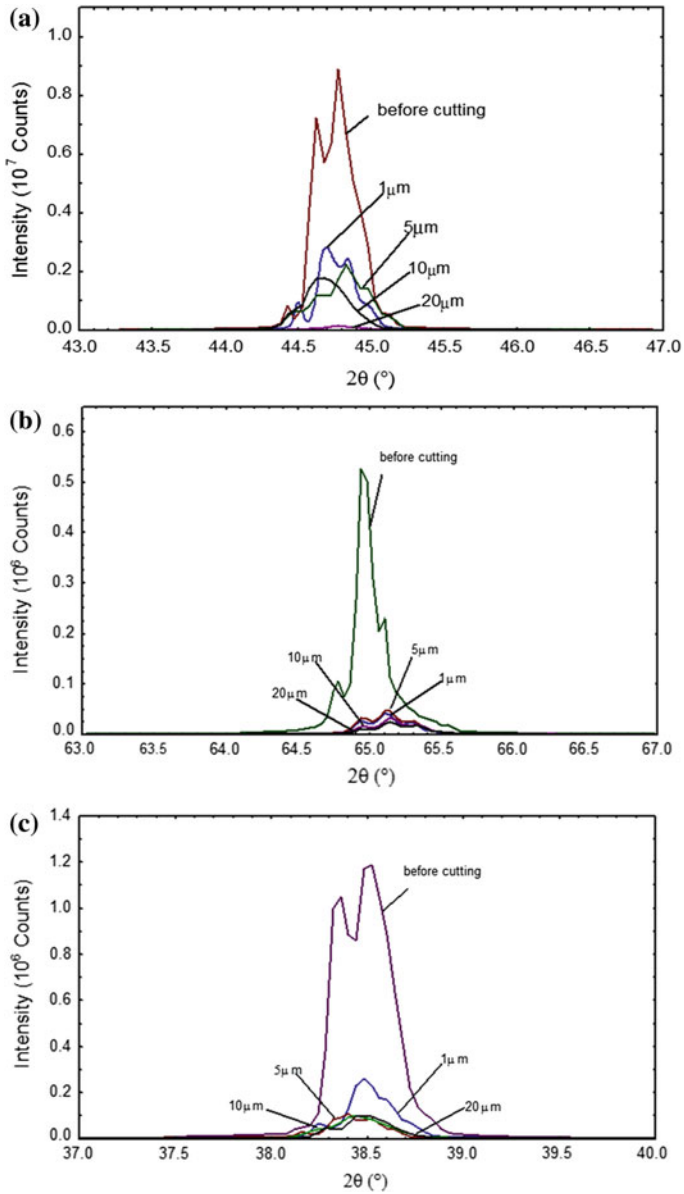
### 5.2.1 X-ray Diffraction Line Profile Analysis

Figure 4.7a, b and c show the typical X-ray diffraction line profiles of diamond-turned surfaces of (001), (011) and (111) aluminium single crystals. Bragg reflections of the diamond-turned surface with different depths of cut are compared with the line profile recorded from an aluminium single crystal before machining. The intensity of the line profile from a diamond-turned surface layer is decreased significantly compared with an uncut surface. A deformation layer clearly exists after diamond turning although the depth of cut is very small, from 1 to 20  $\mu\text{m}$ . The intensity of line profile decreases with an increase in the depth of cut in aluminium single crystals (001), (011), and (111) (Fig. 5.7).

Mean values of the block size, microstrains and dislocation density obtained from the modified Voigt function method based on the X-ray diffraction line profile broadening analysis are listed in Table 5.1. It is found that the microstrains are the same at different depths of cut. The microstrains of (011) single crystal are lower than those of (001) and (111) single crystals. The block size of the machined surface decreases with increases in the depth of cut. It drops very quickly in (001) and (011) aluminium single crystals. However, the block size varies very little in the (111) aluminium single crystal (Fig. 5.8a). The dislocation density below the machined surface increases with increases in the depth of cut. Up to 10  $\mu\text{m}$  depth of cut, the dislocation density is the highest in {111} crystal plane. Beyond 10  $\mu\text{m}$ , the highest dislocation density is found in the {001} plane. A high-dislocation density implies higher plastic deformation on the cutting plane.

### 5.2.2 Microhardness and Elastic Modulus of Machined Surface

The microhardness and the elastic modulus of the machined surface of three aluminium single crystals were measured by the nanoindenter. The microhardness ( $H$ ) and the elastic modulus ( $E$ ) of a diamond-turned aluminium single crystal surface layer with a depth of 10  $\mu\text{m}$  at various penetration depths are shown in Figs. 5.9 and 5.10, respectively. When the indentation depth was increased to 200 nm, the microhardness of the machined surface rapidly decreased. When the indentation depth was beyond 300 nm, there was no significant change in the microhardness. The deformation layer at a cutting depth of 10  $\mu\text{m}$  can be estimated from Fig. 5.9, and the thicknesses of the deformation layers were estimated to be 172, 124, and 196 nm on the (001), (011), and (111) cutting planes, respectively. The mean depth of the deformation layer in diamond turning lies in the range from 100 to 400 nm. Typical load-displacement curves during indentation of the



**Fig. 5.7** Typical X-ray diffraction line profile from diamond-turned surface layer of Al single crystal in different depth of cut **a** (001) Al single crystal **b** (011) Al single crystal **c** (111) Al single crystal

**Table 5.1** Block size ( $D$ ), dislocation density ( $\rho$ ) and microstrain ( $\epsilon$ ) of the aluminium single crystal with different cutting depth

Orientation	Depth of cut ( $\mu\text{m}$ )	Block size, $D$ (nm)	Dislocation density, $\rho$ ( $\text{N}/\text{cm}^2$ ) $\times 10^{10}$	Microstrain, $\epsilon(\Delta d/d\%) \times 10^{-8}$
Al (001)	1	182.4	1.6	6.0
Al (001)	5	137.9	3.6	6.0
Al (001)	10	54.6	10	6.0
Al (001)	20	30.2	32	6.0
Al (011)	1	153.6	1.2	3.9
Al (011)	5	149.9	1.3	3.9
Al (011)	10	60.7	8.1	3.9
Al (011)	20	43.2	16	3.9
Al (111)	1	50.5	11	7.1
Al (111)	5	50.0	12	7.1
Al (111)	10	40.6	18	7.1
Al (111)	20	38.1	20	7.1

aluminium single crystals on different cutting planes are shown in Fig. 5.11. Among the three cutting plane, the hardness and elastic modulus are highest on (110) plane and lowest on (111) plane. The elastic displacement and plastic displacement of three aluminium single crystals are also shown in Figs. 5.11 and 5.12.

For the purpose of comparison, the elastic and plastic displacement curves of copper are shown in Figs. 5.13 and 5.14, respectively. In both crystals, the amount of elastic and plastic deformation varies with the crystal plane. In aluminium, the elastic deformation is the highest on (110) and the smallest on (111), whereas in a copper crystal, the highest is on (110) but smallest on (001) plane. The plastic deformation increases in the ascending order of (110), (100) and (111) in aluminium, whereas in copper the difference among the three orientations is small. Comparing the two crystals, the hardness and elastic modulus are higher in copper than those in aluminium. However, the difference in elastic deformation between the materials is small for a given load. The load-displacement curves of the aluminium and copper single crystals are reconstructed from the test data and are shown in Fig. 5.15. The difference in the deformation characteristics of the aluminium and copper single crystal is clear.

### 5.2.3 Friction Coefficient

The change of the coefficient of friction determined from the scratch test with various applied loads is shown in Fig. 5.16 for different crystal planes. The data is tabulated in Table 5.2. The coefficient of friction is highest on {011} plane and the lowest on {111} plane. However, the difference in the coefficient is small (i.e. in the range of 0.32–0.47). The value determined from the nanoindenter is higher than



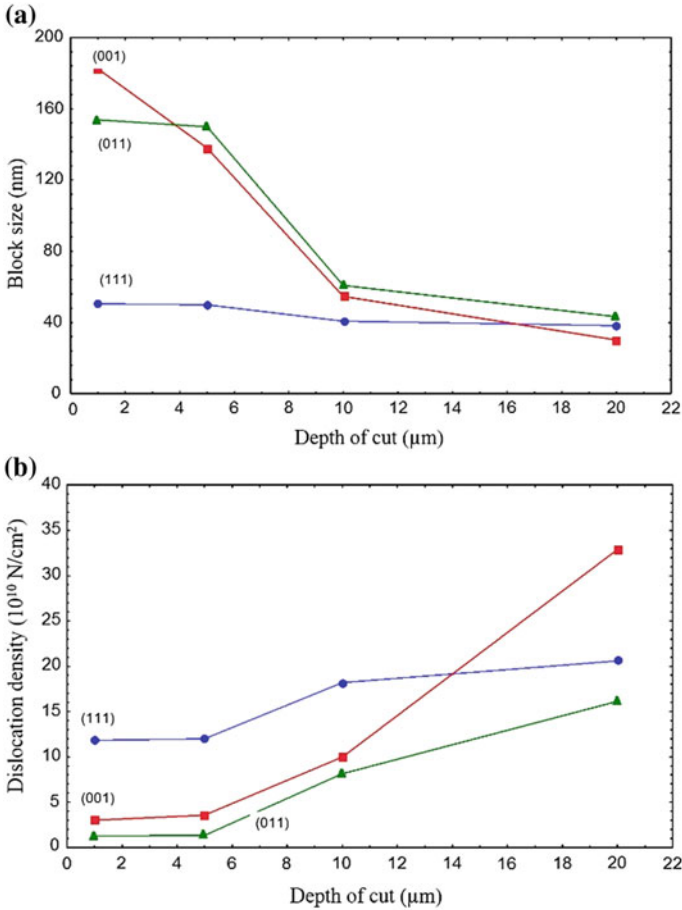


**Fig. 5.8** Effect of depth of cut on **a** block size, **b** dislocation density in (001), (011) and (111) aluminium single crystal

those reported in the literature on diamond turning (Yuan et al. 1996) and is different from those obtained in sliding tests or cutting tests.

### 5.2.4 Dislocation Density and Structure of Diamond-Turned Surface Layers

The density of the dislocations is a criterion of the cutting deformation of the machined surface layer, which affects the mechanical and physical properties of the metal. The microstructure of the deformed surface layer under various depths of cut is shown in the TEM micrographs from Figs. 5.17, 5.18, 5.19, 5.20 and 5.21.

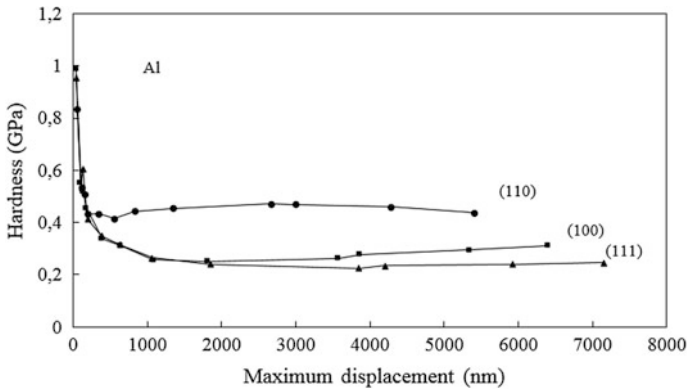


Fig. 5.9 Nano-indentation measurements of hardness of a diamond-turned aluminium single crystal on different crystallographic planes

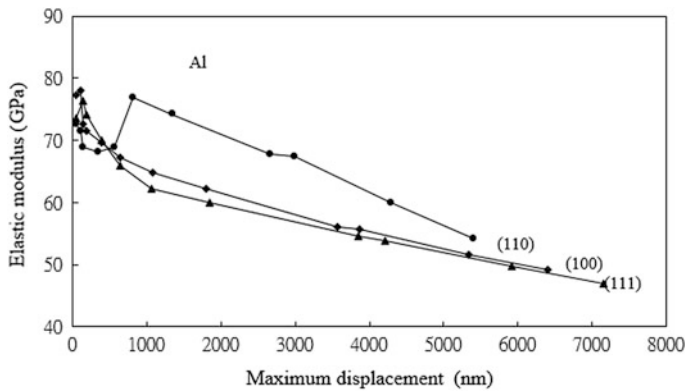


Fig. 5.10 Nano-indentation measurements of modulus of elasticity of aluminium single crystal

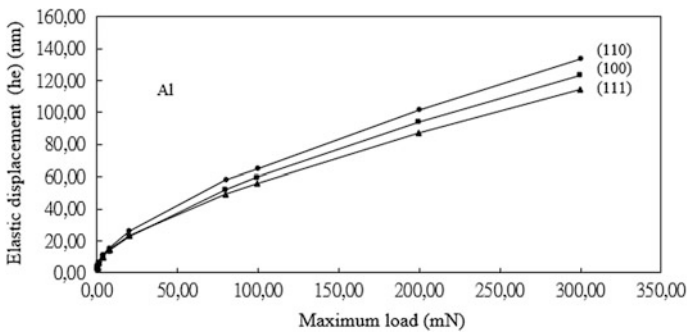
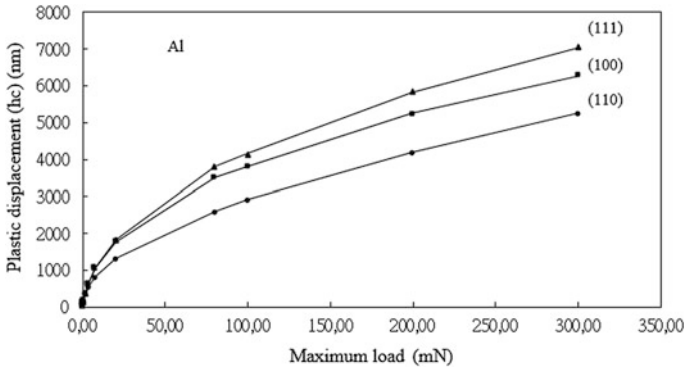
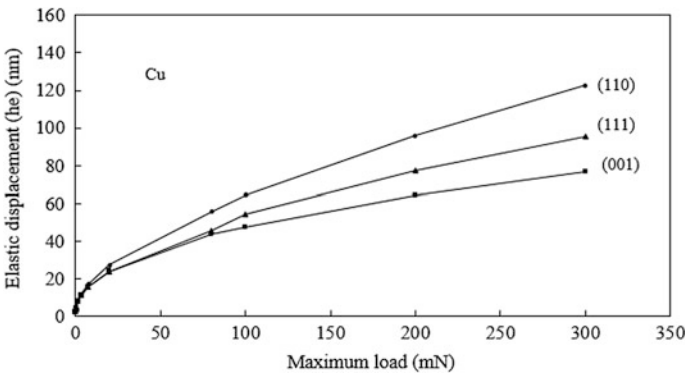


Fig. 5.11 Elastic displacement ( $h_e$ ) of three aluminium single crystals in nano-indentation testing under various maximum indentation load ( $P_{max}$ )



**Fig. 5.12** Plastic displacement ( $h_c$ ) of three aluminium single crystal in nano-indentation testing under various maximum indentation load ( $P_{max}$ )



**Fig. 5.13** Elastic displacement ( $h_e$ ) of three copper single crystals in nanoindentation testing under various maximum indentation load ( $P_{max}$ )

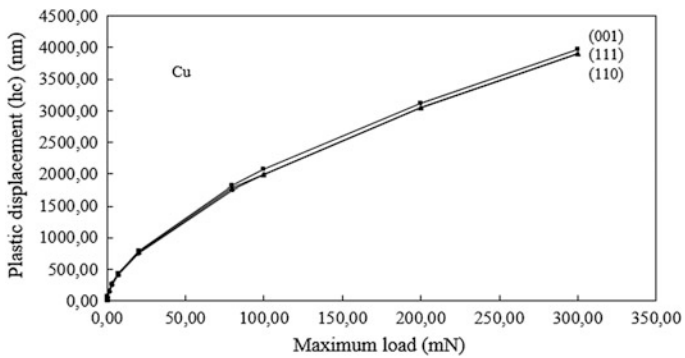


**Fig. 5.14** Plastic displacement ( $h_c$ ) of three copper single crystals in nano-indentation testing under various maximum indentation load ( $P_{max}$ )

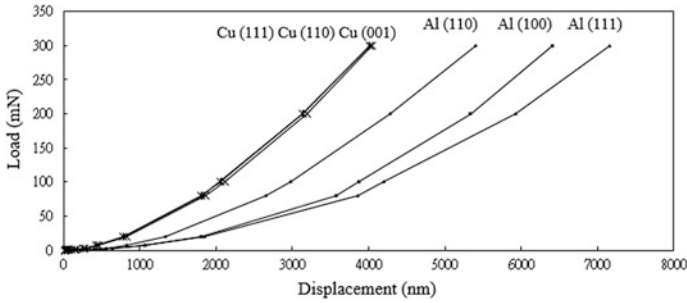


**Fig. 5.15** Load-displacement curves of aluminium and copper single crystals in nano-indentation testing

**Fig. 5.16** Friction coefficient of three aluminium single crystals

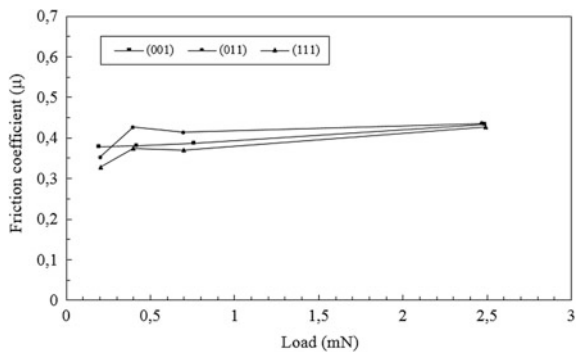


**Table 5.2** Friction coefficient of aluminium single crystal

Load (mN)	Friction coefficient		
	(001)	(011)	(111)
0.2	0.379	0.353	0.329
0.4	0.381	0.427	0.375
0.7	0.387	0.414	0.369
2.5	0.433	0.435	0.427

Figures 5.17, 5.18 and 5.19 show the TEM photographs of the cutting surface layer machined with diamond tools at different cutting depths and on different cutting planes. A dislocation line is present at a depth of cut of 1 μm. Some dislocation cells start to appear at a cutting depth of 5 μm. When the depth of cut increases to 10 μm and higher, more complex dislocation structures start to form. The dislocation cells appear gradually, and the dislocation density become higher as the depth of cut increases. The TEM observation agrees with the findings obtained by X-ray diffraction line profile analysis.

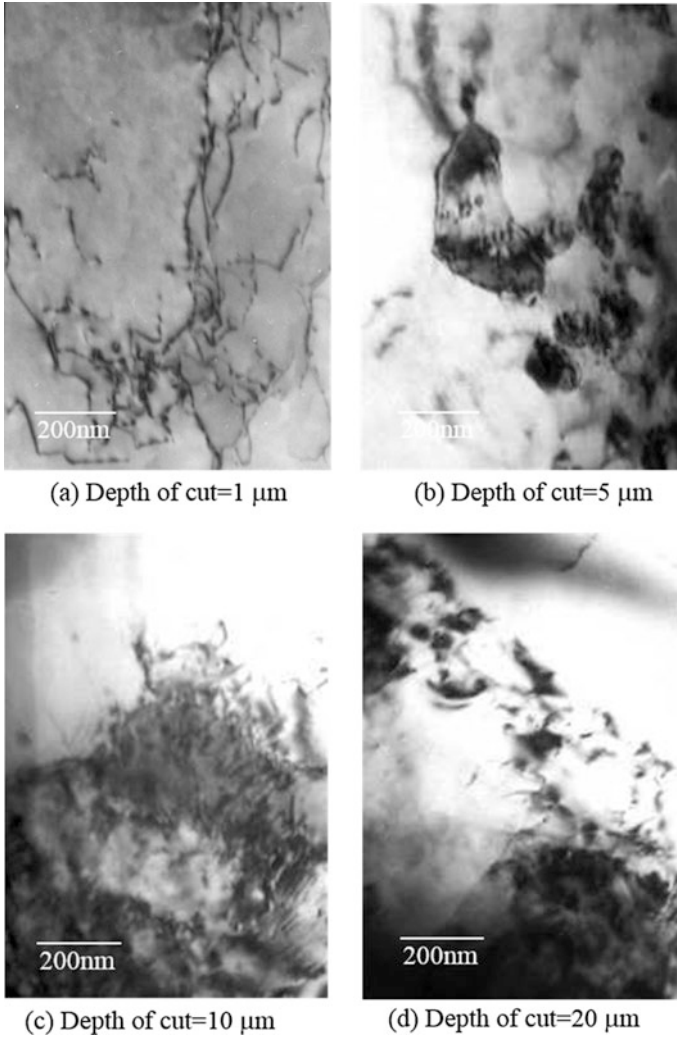


**Fig. 5.17** TEM micrograph of dislocations dispersed in diamond-turned surface layer of single crystal aluminium (001) at different depths of cut

An enlarged electron micrograph of the deformed microstructure of the (111) cutting plane is shown in Fig. 5.20. Regions relatively free of dislocations and walls of dense dislocations are clearly revealed. The cellular structure resembles the deformed structure of cold-rolled high-stacking fault f.c.c. materials (Hansen 1990), which are formed by a relaxation process (Maser et al. 1963) at early stages of homogenous slip when dislocations are free to arrange themselves. The cell wall thickness decreases with strain while the cell interiors appear

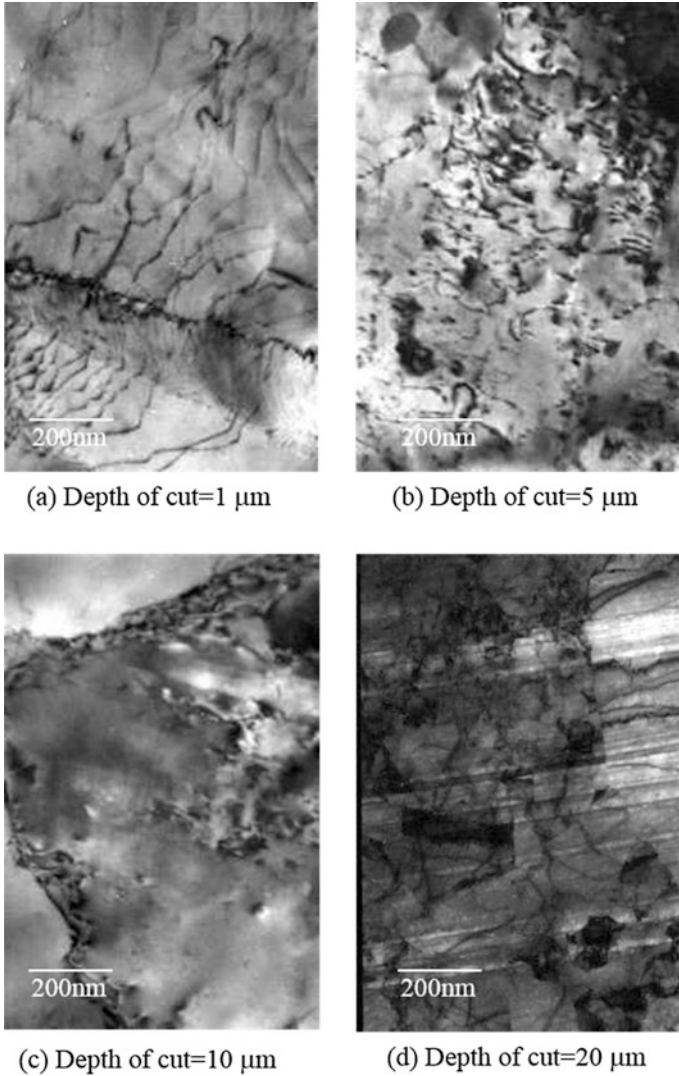


**Fig. 5.18** TEM micrograph of dislocations dispersed in diamond-turned surface layer of single crystal aluminium (011) at different depths of cut

progressively cleaner. Once a cell structure is developed, the cell walls block the cross-slip and create the dislocation cell. When the deformation increases, the slip process that leads to the development of the cell structure ceases. Another feature known as a microband (MB) (Malin and Hatherly 2013) starts to develop. Microbands are elongated plate-like regions of material bounded by

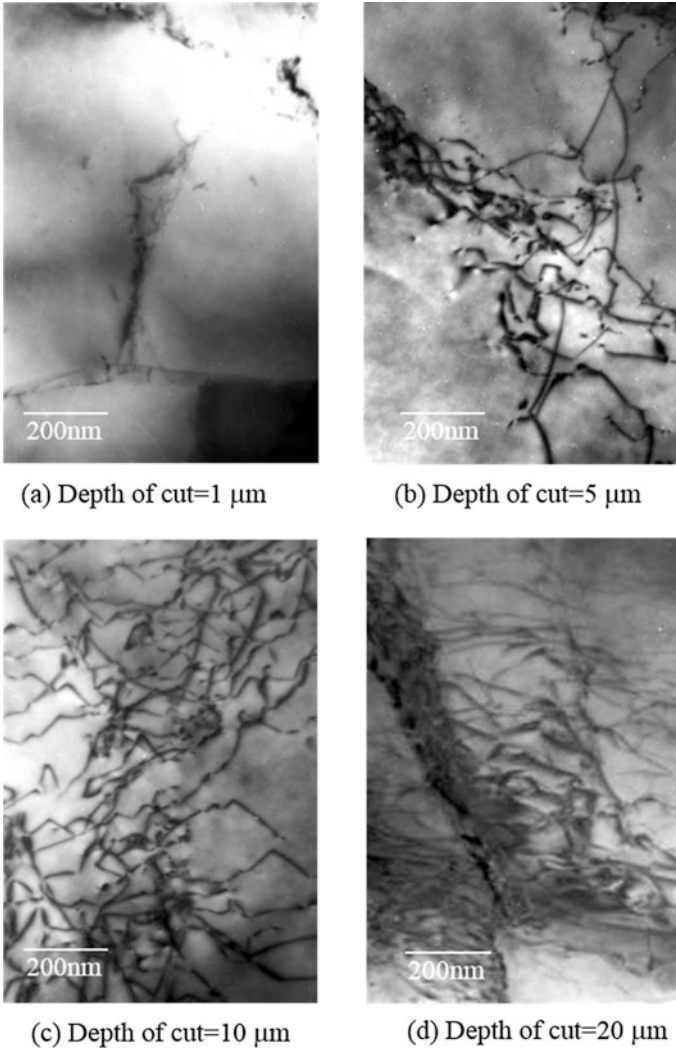


**Fig. 5.19** TEM micrograph of dislocations dispersed in diamond-turned surface layer of single crystal aluminium (111) at different depths of cut

dislocation boundaries and have a high-dislocation density. Such an MB feature can be found in Fig. 5.21 of the (110) aluminium crystal machined at a large depth of cut at 20  $\mu\text{m}$ . An interesting feature is that the MB lies parallel with traces of the diamond turning as marked on the micrograph, and the alignment is almost perfect.

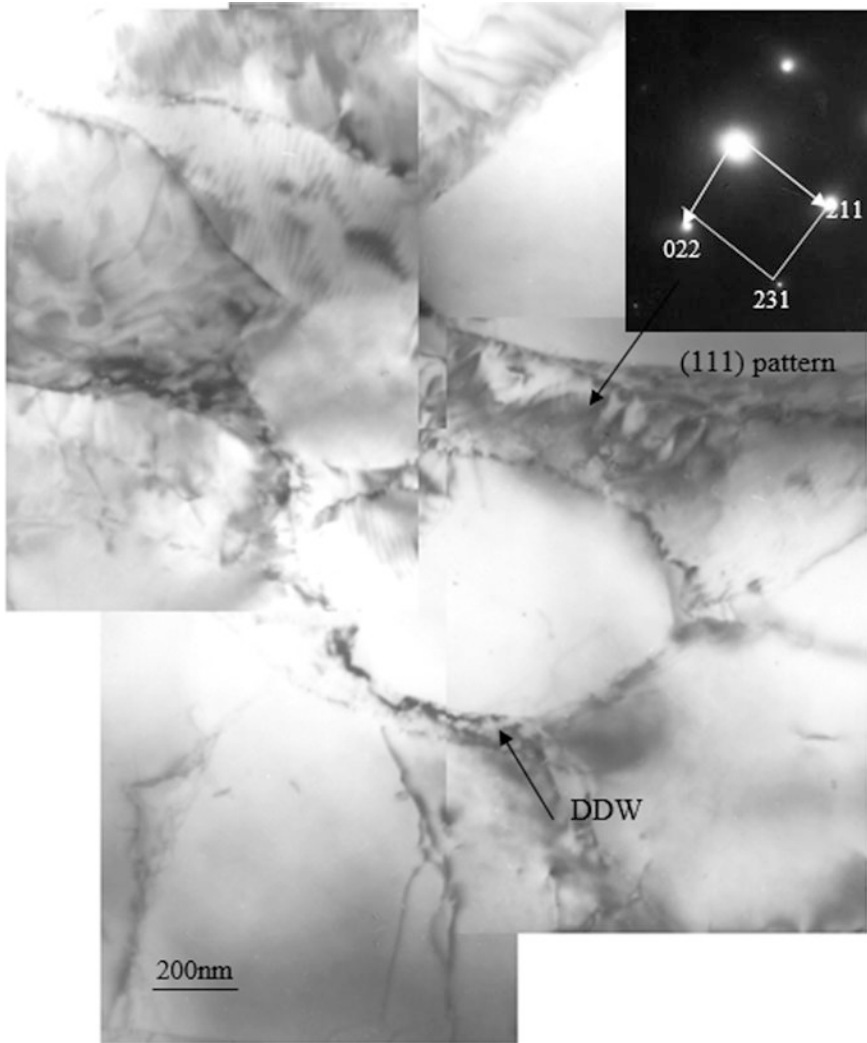


**Fig. 5.20** TEM microstructure of dislocation density on (111) oriented plane aluminium single crystal with 1  $\mu\text{m}$  depth of cut. Dense dislocation wall is marked with an *arrow*

## 5.3 Influences of Material Swelling upon Surface Roughness

### 5.3.1 Materials Swelling Effect

In ultraprecision diamond turning, the quality of the machined surface plays an essential role in the functional performance of a product, especially in optical



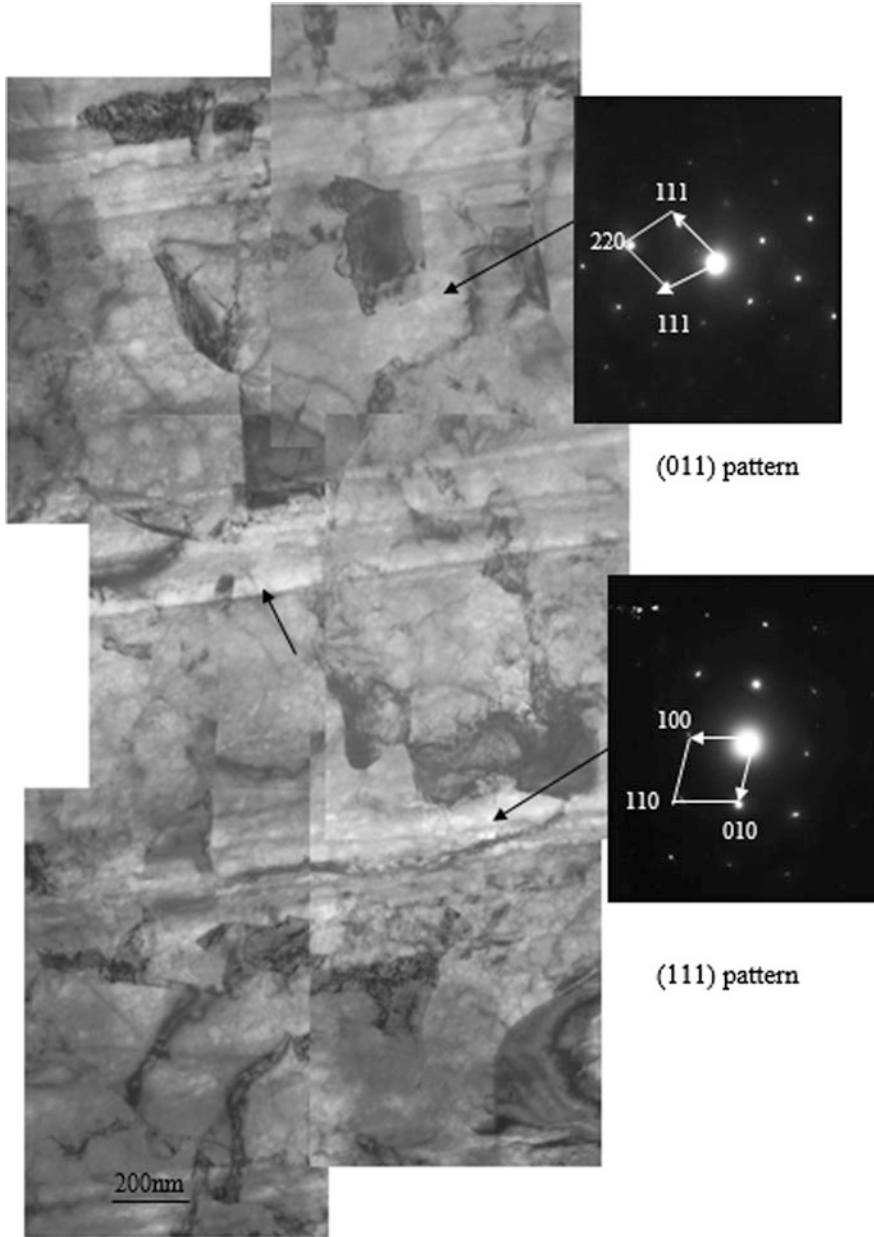


**Fig. 5.21** Plan view of TEM microstructure of diamond-turned surface aluminium (011) single crystal in cutting depth of 10  $\mu\text{m}$  (diamond turning trace is marked with *arrows*)

applications (Ikawa et al. 1991). Among the various attributes of the surface quality, surface roughness in machining has been most extensively studied. The difference between conventional turning and single point diamond turning lies not only in the relative magnitude of the influence of these factors affecting the surface roughness formation, but also on the material behaviour of material at the submillimetre depth of cut.

In lathe turning, there are two types of surface that are produced, one produced by the primary cutting edge (also known as tool edge cut surface) and the other produced by the secondary cutting edge (also known as the tool nose cut surface), as shown in Fig. 5.22. In diamond turning, cutting is done at high speed and there is no built-up edge. In the absence of machine tool vibration, spindle motion error and tool wear, the roughness of a tool edge cut surface should correspond to the edge roughness of the cutting tool, and is identical to the tool shape and cutting conditions (Sata 1964). On the other hand, the component of the surface roughness due to the nose geometry can be calculated readily from Fig. 5.23 as

$$R_t \cong \frac{f_t^2}{8R} \quad (5.18)$$

where  $R_t$  is the peak-to-valley roughness and  $f_t$  is the feed rate and  $R$  is the tool radius. Equation (5.18) is also known as the theoretical surface roughness equation, in which  $v$  is the greatest in a direction perpendicular to the cutting direction.

Most of the research on surface metrology in metal cutting focused on the geometrical and process aspects (Takasu et al. 1985). The most comprehensive study of the roughness profile of tool-nose cut surface was conducted by Sata (1964) and Sata et al. (1985), who first pointed out that during machining, the workpiece swells causing more tool marks and higher surface roughness than that given by the Eq. (5.19), i.e. the peak has a greater height than the theoretical peak.

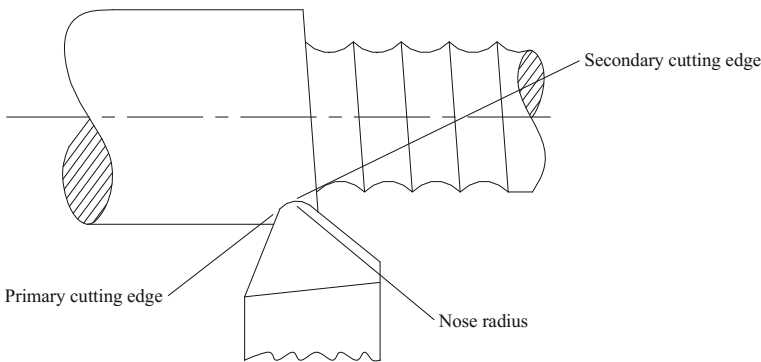


**Fig. 5.22** Diagrammatic sketch of axial turning operation showing primary and secondary cutting edges (after Shaw 1984)

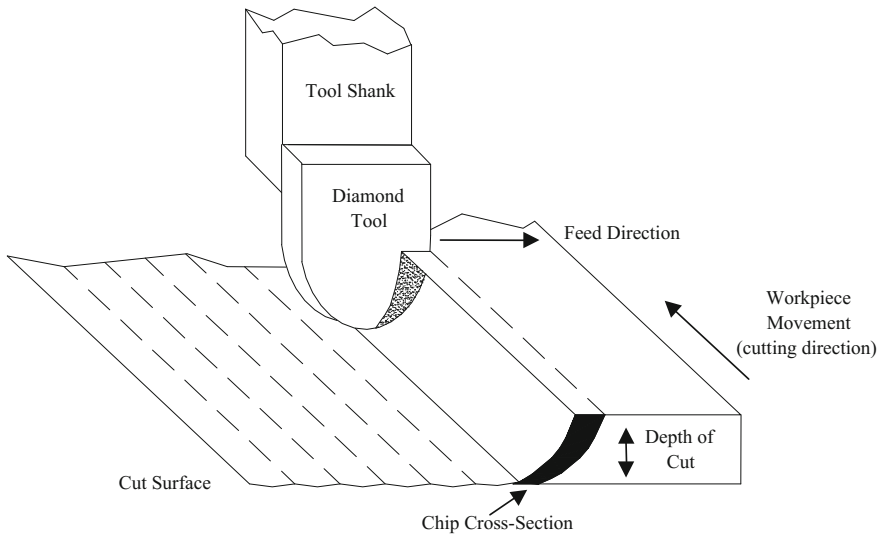


**Fig. 5.23** Theoretical tool-nose surface roughness in the feed direction

The roughness  $R$  for the tool nose cut surface has four components, the theoretical component  $R_t$ , a swelling term  $R_s$ , a vibration term  $H_v$  and a tool-wear term  $H_w$ , i.e.

$$R = R_t + R_s + H_v + H_w \quad (5.19)$$

The swelling is thought to occur as the cutting force normal to the cutting surface pushes the work material near the tool nose causing it to flow to the free surface (i.e. deep swelling). When the metal at the trailing edge of the tool, which is subjected to unusually high normal stress, flows to the side to relieve the stress, and this is referred to as side flow (i.e. side swelling). Swelling adds to the roughness (Shaw 1984; Whithouse 1994). Soft and ductile materials were observed to have more swelling than hardened and brittle materials.

In this section, the effect of the crystallographic orientation on the roughness in two different single crystals is investigated. A power spectrum analysis of the surface roughness profile is carried out to assess the contributing factors in Eq. (5.19), and a non-dimensional measure is proposed to quantify the effect of material swelling in diamond turning. The material behaviour of the two single crystals is discussed.

Face cutting experiments were performed on the “basal plane” of the cylindrical aluminium single crystal and copper single crystal with two crystallographic orientations. The surface roughness of the machined surfaces was measured by a Form Talysurf system and analysed by a Fast Fourier Transform (FFT) spectrum analysis programme developed for the study.

Figure 5.24 shows a schematic diagram of the data acquisition system. The roughness was measured along the radial direction on the cutting plane that is, the

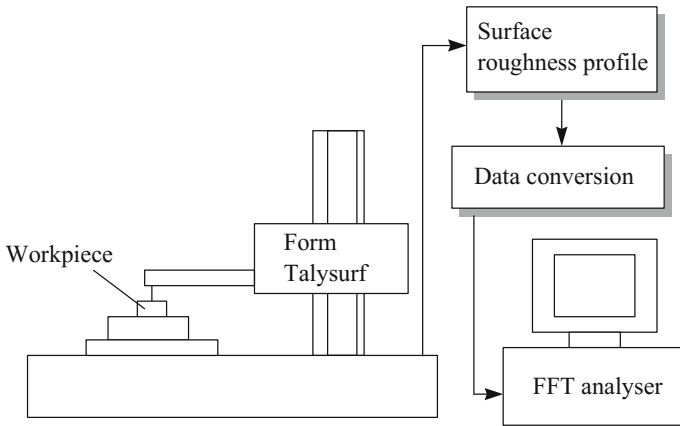


**Fig. 5.24** Schematic diagram of the data acquisition system

**Table 5.3** Specifications of the workpiece materials

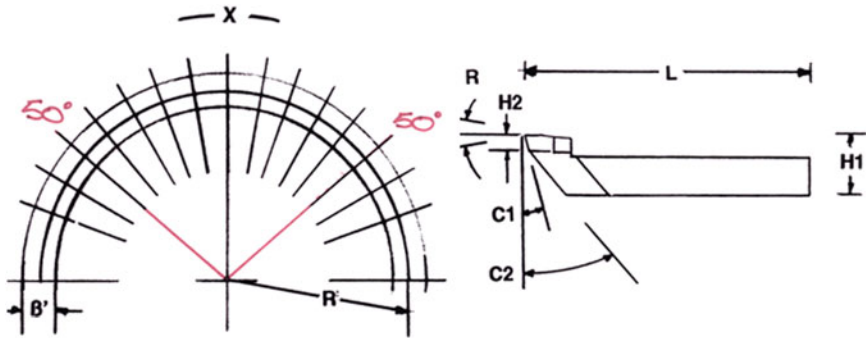
Specimen no.	Descriptions
1	Aluminium single crystal with (001) as the cutting plane
2	Aluminium single crystal with (011) as the cutting plane
3	Copper single crystal with (001) as the cutting plane
4	Copper single crystal with (011) as the cutting plane

**Table 5.4** Cutting conditions for the cutting tests

Spindle rotational speed	2000 rpm
Feed rate	20 mm min <sup>-1</sup>
Depth of cut	5 μm
Front clearance angle	12.5°
Tool nose waviness	0.5 μm
Tool rake angle	0°
Tool nose radius	2.0 mm

tool-nose cut surface. Tables 5.3 and 5.4 summarise the specifications of the work materials and the cutting conditions used in the investigation. All cutting tests were performed on a two-axis CNC ultraprecision machine (Nanoform 300 from Taylor Hobson Pneumo Co.). In order to minimise the effect of tool nose waviness on the surface roughness profile, controlled waviness diamond cutting tools were used throughout the experiments.

Figure 5.25 shows the geometry of the diamond cutting tools used in the study. In order to minimise the effect of tool wear on the results of the analysis, fresh diamond tools with controlled waviness, tool nose radius of 2.0 mm and zero rake angle were used. A new cutting tool was used for each different single crystal and for each cut. In addition, the cutting edge of the tool was inspected before and after



Tool nose radius,  $R$ : 2.0 mm

Arc of the tool nose,  $X$ :  $100^\circ$

Tool nose waviness,  $B$ :  $< 0.5 \mu\text{m}$

Cutting height,  $H1$ : 10.57 mm

Primary clearance height,  $H2$ : 1.08 mm

Rake angle,  $R$ :  $0^\circ$

Primary clearance angle,  $C1$ :  $12.5^\circ$

Secondary clearance  $C2$ :  $39^\circ$

Length,  $L$ : 50.8 mm

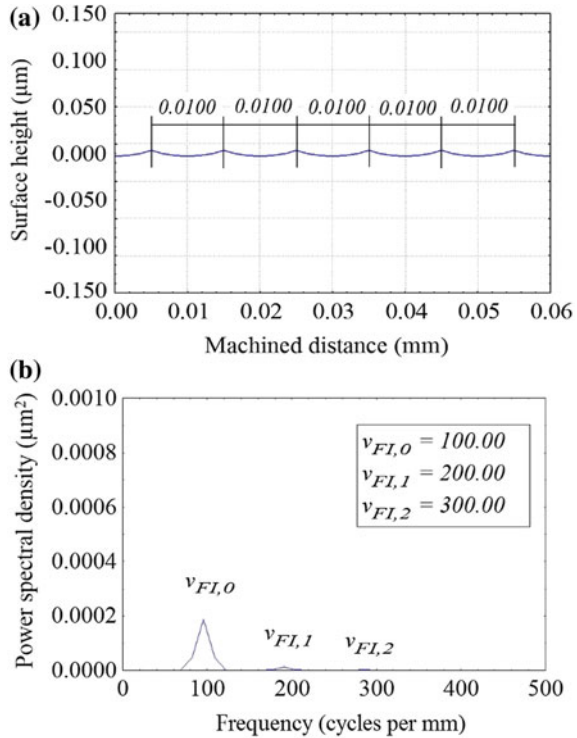
**Fig. 5.25** Geometry and specifications of the diamond cutting tool

machining to make sure the waviness of the tool nose was controlled within  $0.5 \mu\text{m}$  and there were no worn edge. The crystallographic orientation ( $hkl$ ) of the “basal plane” of the cylindrical single crystals was checked by an X-ray diffraction technique on a texture goniometer (Philips PW3710). Before and after diamond turning, the crystallographic orientation of the cutting plane of the aluminium and copper crystal were also measured.

The surface roughness profile and its spectrum for an ideal crystal surface are given in Fig. 5.26. The measured roughness profiles for the specimens are depicted in Fig. 5.27a, 5.28, 5.29 and 5.30a. The surface roughness of the machined surfaces was not found to be an exact replica of the profile of the cutting tool. The width of the tool marks formed on the specimens was found to be slightly larger than the ideal profile. The copper single crystal made deeper tool marks than the aluminium single crystal. The tool marks were found to be slightly wider for the aluminium single crystal than that of the copper single crystal. The power spectrums clearly show the presence of swelling as can be seen in Fig. 5.27b, 5.28, 5.29 and 5.30b. The PSD for the feed component ( $\nu_{FM,0}$ ) and its harmonics ( $\nu_{FM,1}, \nu_{FM,2}$ ) are found to vary with the material being cut.

This variation agrees well with the ideal spectrum profile of the tool marks distorted by the presence of the swelling effect. An increase in PSD at the fundamental frequency corresponds to an increase in the depth of the basic form of the tool marks, while an increase of PSD in the harmonics induces ripples on the profile of the tool marks. The induced ripples cannot be explained by the tool wear, the

**Fig. 5.26** **a** Surface roughness profile and **b** its spectrum for the ideal crystal surface



relative tool-work vibration and the tool nose waviness for a number of reasons. First, the waviness of the tool nose is controlled within 0.5 µm, which is far greater than that of the observed ripples (less than 0.02 µm, peak-to-peak). Second, the wavelength of the waviness (greater than 30 µm) due to the relative tool-work vibration, i.e. the component  $v_{TW,1}$ , is much longer than that of the ripples (wavelength < 3 µm). In addition, the cutting tests were performed under identical cutting conditions and virgin diamond cutting tools with perfectly sharp cutting edges were used for each cutting test.

### 5.3.2 Characterisation Techniques

A graphical illustration of the influence of material swelling on the surface roughness formation is shown in Fig. 5.31. Basically, there are two types of swelling that can occur in the machining process, namely side swelling and deep swelling. The former is due to the plastic side flow (Shaw and Crowell 1965) in which the metal left behind on the cutting edge is subjected to sufficiently high pressure to cause the metal to flow to the side of the active cutting edge.

**Fig. 5.27 a** Surface roughness profile and **b** its spectrum for (001) aluminium single crystal

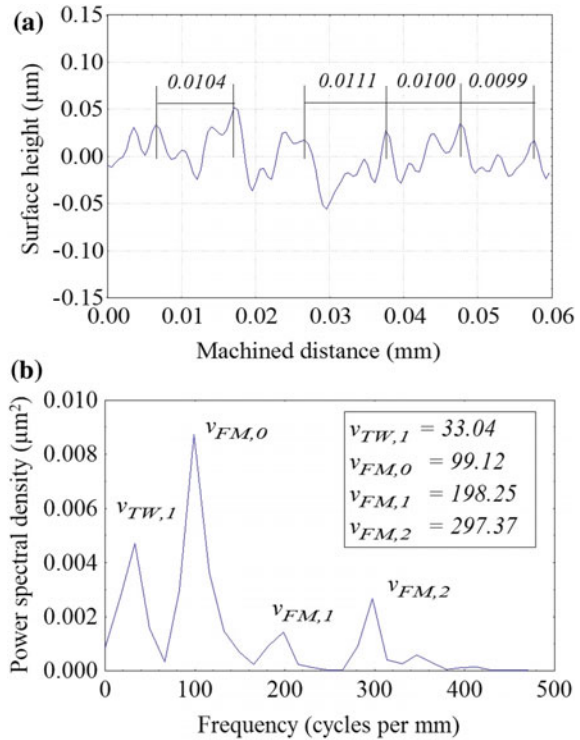


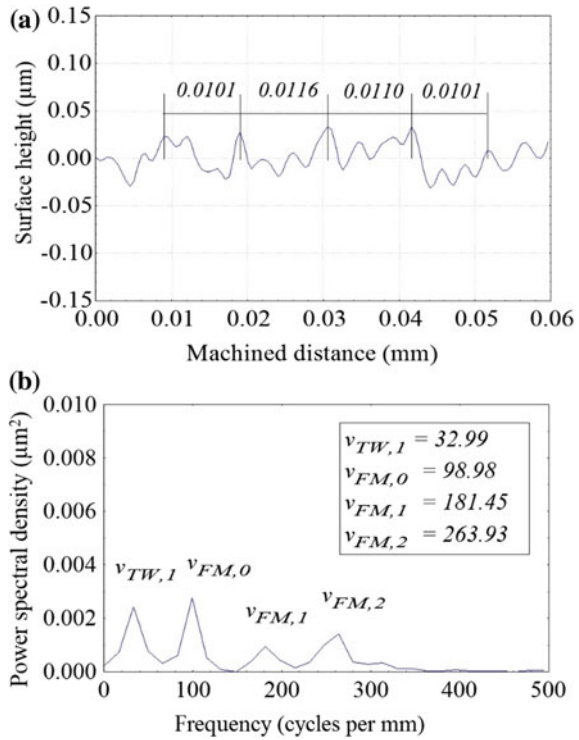
Figure 5.31a, b show the resulting profile in the absence and in the presence of side flow, respectively. The width of cut marks is seen to be slightly larger when side swelling is present. The formation of deep swelling, on the other hand, is caused by the cutting force along the main cutting edge of the tool ( $F_z$  in Fig. 5.31) which pushes aside the work material near the tool nose causing it to flow to the free surface (Whitehouse 1994). This results in a deeper tool mark being formed on the surface. The side swelling together with the deep swelling causes greater and wider tool marks and hence greater surface roughness.

Two proxy parameters are used to characterise the swelling of a work material: the coefficient of side swelling (COSS) and the coefficient of deep swelling (CODS). The COSS is defined as the ratio of the mean width of the tool marks (see Fig. 5.21) and the feed rate per workpiece revolution,  $s$ , i.e.

$$COSS = \frac{1}{N_S} \sum_{i=1}^{N_S} \frac{W_i}{s}, \tag{5.20}$$

where  $W_i$  is the width of  $i$ -th tool marks on the surface roughness profile and  $N_S$  is the number of tool marks being measured. It is used to determine the combined effect of side swelling and recovery of the active cutting edge after cutting. The

**Fig. 5.28** **a** Surface roughness profile and **b** its spectrum for (011) aluminium single crystal



CODS is used to measure the combined effect of deep swelling and the elastic recovery of the tool marks formed on a work surface. It is defined as the square root of the sum of rate of change of the measured power spectral density (PSD) for the feed components and its harmonics with respect to those for the ideal roughness spectrum. Thus,

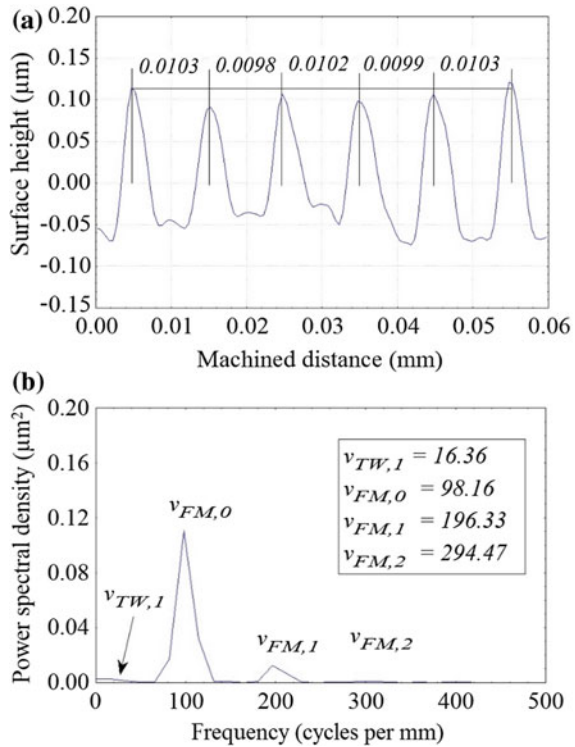
$$CODS = \sqrt{\sum_{j=0}^{N_D} \left\{ \frac{PSD(v_{FM,j}) - PSD(v_{FL,j})}{PSD(v_{FL,j})} \right\}}, \quad (5.21)$$

where  $N_D$  is the number of feed components being observed on the measured roughness spectrum;  $v_{FL,j}$  and  $v_{FM,j}$  are the frequencies of the  $j$ -th harmonics of the feed components for the ideal and the measured roughness spectra, respectively;  $PSD_j(v_{FL,j})$  and  $PSD_j(v_{FM,j})$  are their corresponding power spectral densities, respectively.

The CODS is defined based on the fact that the profile of the tool marks contributes to the peaks of the feed component and its harmonics in the roughness spectrum. An ideal roughness profile can be treated as being composed of the undeformed tool marks, i.e. no swelling and no elastic recovery. Any deviations of the geometry of the tool marks from that for an ideal roughness profile could be due



**Fig. 5.29** **a** Surface roughness profile and **b** its spectrum for (001) copper single crystal



to the combined effect of lattice dislocations, plastic deformation and elastic recovery of the crystals during cutting. These deviations ought to be reflected in the power spectrum density (PSD) of the feed components. Hence, the total rate of change of PSD of the feed components of the roughness profile measured against the ideal profile can provide a proxy measure of the combined effect of deep swelling and recovery of a work material. For a material with no deep swelling and recovery, CODS should be zero.

The COSS and CODS can be used as proxy measures of the effect of material swelling and recovery after machining. Since both of the COSS and CODS are determined after machining, they could also be treated as proxy measures of the resultant plastic and elastic deformation in the machined surfaces.

Table 5.5 tabulates the calculated COSS and CODS for the materials being studied. The COSS is shown to be close to 1, which infers that the side swelling effect is slight. Remarkably, high CODS are found for all specimens. There is a good agreement between the surface roughness and the coefficient of deep swelling. A large CODS is found to correspond to a high surface roughness. Figure 5.32 depicts the relationship between the coefficient of deep swelling (CODS) and the maximum peak-to-valley height  $R_t$ , and that for the arithmetic roughness  $R_a$  is shown in Fig. 5.33. Irrespective of the materials being cut, CODS is shown to vary

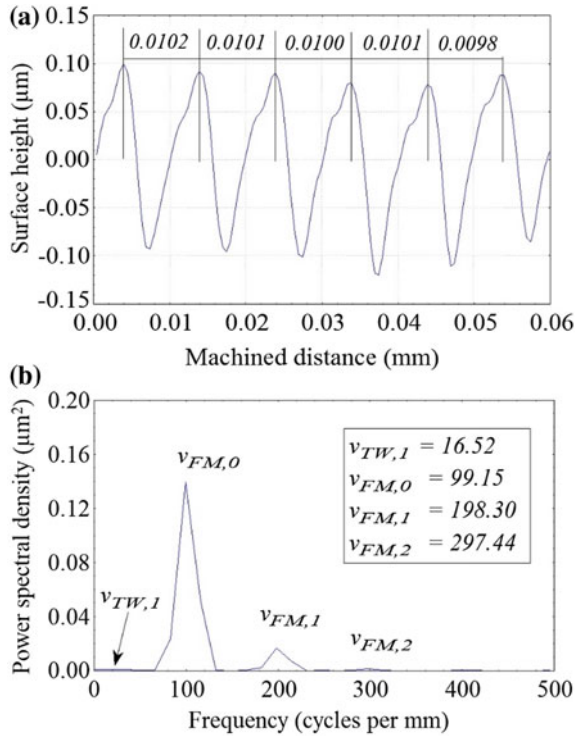


Fig. 5.30 a Surface roughness profile and b its spectrum for (011) copper single crystal

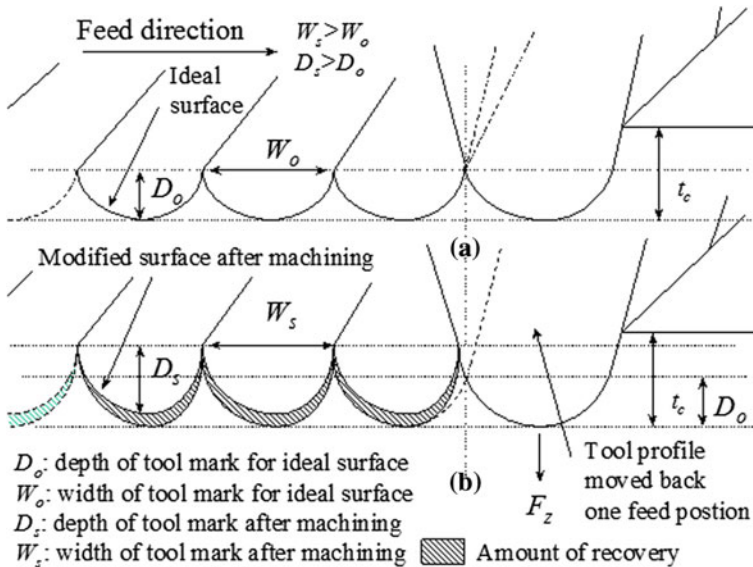
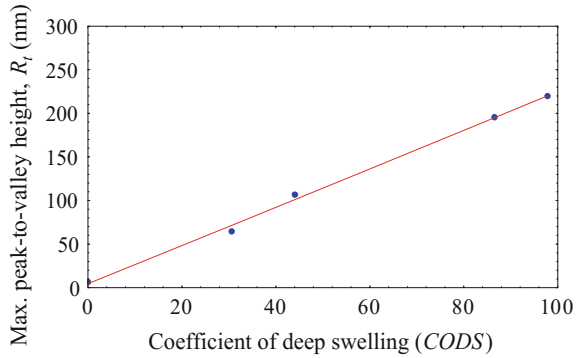


Fig. 5.31 Illustration of material swelling

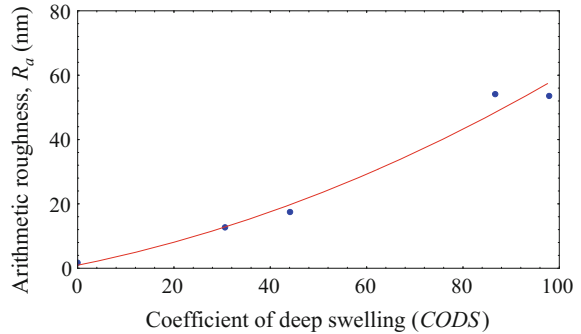
**Table 5.5** Summary of the results of analysis

Material orientation	Coefficient of side swelling, COSS	Coefficient of deep swelling, CODS	Arithmetic roughness, $R_a$ (nm)
Al (001)	1.035	7.086	15.59
Al (011)	1.070	4.430	14.55
Cu (001)	1.010	27.67	54.36
Cu (011)	1.004	27.10	48.38

**Fig. 5.32** Relationship between coefficient of deep swelling and maximum peak-to-valley height



**Fig. 5.33** Relationship between coefficient of deep swelling and arithmetic roughness



linearly with the  $R_t$  values. The  $R_a$  value is found to increase with increasing CODS. This indicates that material swelling directly correlates with surface roughness. When the amount of plastic deformation of the material in different orientations is compared, there is a good agreement with the CODS value. In aluminium crystals, the larger difference in the extent of plastic deformation is reflected in a large difference in the amount of deep swelling, whereas in copper, the amounts of plastic deformation for different orientations are close to each other, and this is reflected in similar amounts of deep swelling as determined from the roughness profile.

### 5.3.3 Formation of Surface Roughness in Machining

The foregoing machining tests also revealed that radically different machined surface roughness profiles were produced by different materials even when identical tools and cutting conditions were used. There are particularly different profiles for the copper compared to the aluminium samples. This can only be accounted for by the difference in the nature of the materials. The process of the formation of a machined surface is shown in Fig. 5.34. When plastic deformation is involved and the cutting tool is perfectly sharp (i.e. zero radius of cutting edge), the layer to be cut (i.e.  $t_c$ , the chip thickness) will separate sharply or will fracture along the line OA and shear off in the direction OS to become the chip (Fig. 5.34a). The freshly machined surface will be at the same level as the baseline OA and the tool edge cut surface is smooth. The tool nose cut surface is given by a theoretical prediction. As the cutting tool always processes a radius at the cutting edge, the workpiece material will be separated along the line LM instead of OA. The part of the undeformed chip with thickness of  $\Delta t_c$  will be elastically and plastically compressed and extruded (or burnished) under the round cutting edge to become the machined surface (Fig. 5.34b). The actual profile of the machined surface deviates from the tool marks as described by Eq. (5.18). Such a thin layer of plastically deformed material will undergo an elastic recovery behind the cutting edge to form the freshly cut surface (Fig. 5.34b). The amount of recovery depends on the extent of plastic deformation and Young's modulus of the substrate material. Figure 5.34b shows the formation of the machined surface for a ductile metal with both elastic and plastic deformation.

The crystal's elastic modulus varies with direction and therefore the elastic displacement upon unloading was found to vary with the crystallographic plane. In general, the higher the modulus, the smaller the elastic recovery will be. This explains the relatively flat tool marks observed in aluminium compared to copper. The difference in Young's modulus between aluminium and copper is larger than that between the (001) and (011) crystallographic plane and is reflected in the degree of deviation from the ideal surface roughness profile. Since the hardness and Young's modulus are different for different grain orientations, it is also expected that different crystallographic orientations will produce different recovery effects and also a difference in the height levels of the surface. Such spring back might reduce the additional roughness caused by the swelling effects, although the recovery effect will be more pronounced.

Plastic deformation, on the other hand, is non-linear and is more complex. The swelling of material produced in the front of the indenter under scratching was studied by Kobayashi et al. (1996) in a Cu–Al single crystal. The microscopic origin of the swelling was clearly shown on the {111} crystal planes. The width of the scratched area was found to be narrower than that at the indenter point and is orientation dependent. These findings are in line with the earlier reports on the sensitivity of the track width to orientation in the scratching of various f.c.c., b.c.c.

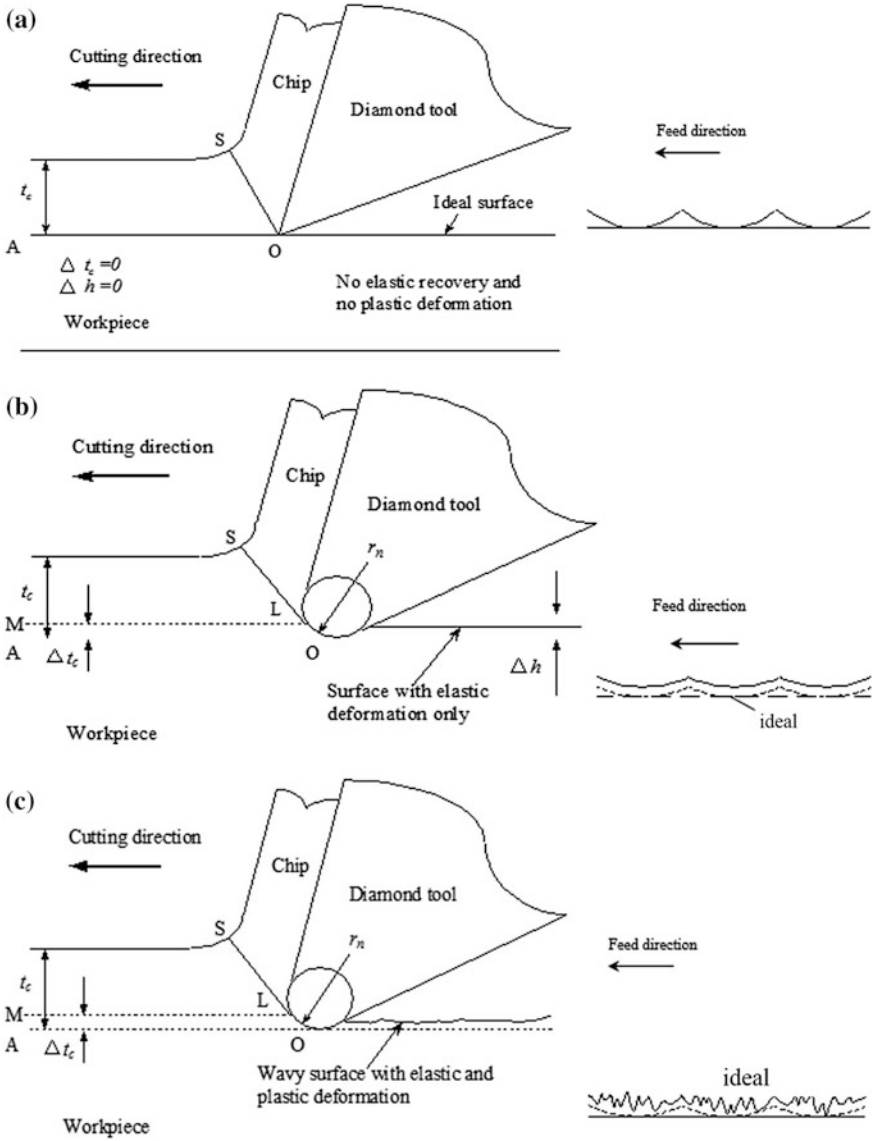


Fig. 5.34 Formation of diamond-turned surface a no deformation of surface, b elastic deformation only c elastic and plastic deformation

and h.c.p. materials, with extensive ploughing occurring (Steijn 1964). The swelling of a diamond-turned surface bears a close resemblance to the swelling produced in a scratching test.

Depending on the substrate material and its crystallographic orientation, the as-machined surface can appear flat or wavy. Indirect evidence of large plastic

deformation was also shown in the compression texture detected for the diamond-turned surface of an aluminium single crystal (Proakis and Manolakis 1996). Their initial orientations were the same (i.e.  $\{001\}\langle 100\rangle$ ). After machining, there was a substantial weakening of the  $\{001\}$  intensity and a spread of the  $\{001\}$  components towards other orientations. In the aluminium sample, the major texture components were  $\{102\}\langle 231\rangle$  (21%),  $\{104\}\langle 401\rangle$  (14%),  $\{001\}\langle 610\rangle$  (13.6%) and  $\{001\}\langle 010\rangle$  (6.6%), whereas in the copper sample, the major components were  $\{100\}\langle 013\rangle$  (27.7%),  $\{012\}\langle 321\rangle$  (12.5%),  $\{416\}\langle 121\rangle$  (8.2%) and  $\{110\}\langle 115\rangle$  (14.8%). A significant proportion of  $\{110\}$  components (i.e. 14.8%) found in the copper sample was absent in the aluminium one.

Although the initial orientation and machining conditions were the same for the aluminium and copper crystals, the difference in the ODF clearly revealed the operation of different slip systems, and hence different rotation paths in these two materials. The difference in the plastic behaviour of the copper and aluminium samples could arise from the difference in the stacking fault energy, dynamic recovery, ease of dislocation generation and cross-slip, direction of the shear plane and the value of resolved shear stress that acts on that plane. A better understanding of the underlying plastic deformation mechanisms that leads to the external shape change in these two crystals is needed to predict the swelling effect of the machined surface.

From the above findings, it is clear that the swelling effect distorts the tool marks formed on the machined surface and induces additional surface roughness from that calculated from the theoretical value alone. Although the swelling effect is not significant in conventional machining, it is pronounced in diamond turning and affects the fidelity of the reproduction of the tool profile on the diamond-turned surface. Unlike conventional machining, high rotation speed together with a fine feed rate is usually adopted in ultraprecision diamond turning. Under this condition, a phenomenon called tool interference occurs in which the preceding movement of the tool has already removed the chip which is then cut away by the succeeding tool movements. Better surface finish can be expected when interference of the tool occurs. However, the influence of the tool interference is overwhelmed by other factors such as material swelling.

## References

- Cullity, B.D. (1956), *Elements of X-Ray Diffraction*, Addison-Wesley Publishing Company, Inc. Reading, Massachusetts.
- Goodhew, P. J., & Humphreys, F. J. (1992). *Electron microscopy and analysis*. London: Taylor and Francis.
- Hansen, N. (1990). *Materials Science and Technology*, 6, 1039.
- Ikawa, N., Donaldson, R. R., Komanduri, R., König, W., Aachen, T. H., McKeown, P. A., et al. (1991). Ultraprecision metal cutting—The past, the present and the future. *Annals of the CIRP*, 40, 587–594.

- Kobayashi, S., Kawata, M., & Mori, K. (1996). Deformation mechanism in Cu–Al single crystals and bicrystals under scratching with pyramidal indenter. *Journal of Materials Science*, 31, 5797.
- Malin, A. S., & Hatherly, M. (2013). Microstructure of cold-rolled copper. *Metal Science*, 13(8), 463–472.
- Maser, S., Seeger, A., & Theieringer, H. (1963). *Philosophical Magazine*, 22, 515.
- Oliver, W. C., & Pharr, G. M. (1992). An improved technique for determining hardness and elastic modulus using load and displacement sensing indentation experiments. *Journal of Material Research*, 7, 1564.
- Proakis, J. G., & Manolakis, D. G. (1996). *Digital signal processing: principles, algorithm, and applications* (3rd ed.). Englewood Cliffs: Prentice Hall.
- Sata, T. (1964). Surface finish in metal cutting. *Annals of the CIRP*, 12, 190.
- Sata, T., Li, M., Takata, S., Hiraoka, H., Li, C. Q., Xing, X. Z., et al. (1985). Analysis of surface roughness generation in turning operation and its applications. *Annals of the CIRP*, 34(1), 473.
- Shaw, M. C., & Crowell, J. A. (1965). Finish machining. *CIRP ANN*, 13(1), 5–22.
- Shaw, M.C. (1984). Shear strain in cutting. In J.R. Crookall & M.C. Shaw (Eds.), *Metal Cutting Principles* (p. 168). Oxford: Clarendon Press.
- Steijn, R. P. (1964). “Friction and wear of single crystal. In P. J. Bryant (Ed.), *Mechanisms of solid friction*. New York: Elsevier Publishing Company.
- Takasu, S., Masuda, M., & Nishiguchi, T. (1985). Influence of steady vibration with small amplitude upon surface roughness in diamond machining. *Annals of the CIRP*, 34(1), 463.
- Whitehouse, D. J. (1994). *Handbook of surface metrology*. Bristol: Institute of Physics Publishing.
- Yuan, Z. J., Zhou, M., & Dong, S. (1996). Effect of diamond tool sharpness on minimum cutting thickness and cutting surface integrity in ultraprecision machining. *Journal of Materials Processing Technology*, 62, 327.

# Chapter 6

## Material Electropulsing Treatment and Characterisation of Machinability

**Abstract** The machinability of metals and alloys is well known for being affected by the cutting conditions, cutting tools and material properties. A very high-quality surface finish can be obtained by the use of advanced machine tools based on single point diamond turning (SPDT). However, no matter how accurate the machining system is, the limit of performance is determined by the tool/workpiece interaction during the chip removal process at the micro- and nano-scales. In particular, the dimensional accuracy and stability of the machined surface depend on the metallurgical properties of the surface before and after machining, such as the plastic deformation, microstructural changes, phase transformation. This chapter introduces the electropulsing treatment (EPT), as an alternative to traditional thermal and mechanical processes, to enhance the machinability of the difficult-to-machine materials for ultraprecision machining.

Good surface finish and low-cutting force are associated with a high-shear angle, which is characterised by continuous chip formation and is intimately related to the properties of the workpiece materials. The chip formation process involving the dynamic interaction of the cutting tool and microstructural state of the workpiece is decisive in determining the surface quality and integrity of an ultraprecision-machined surface. Material properties also play a critical role in achieving a high-quality machined surface; thus, different material treatments have been applied on the workpiece materials before machining.

As an alternative to traditional thermal and mechanical processes, electropulsing treatment (EPT) has been widely applied to materials processing to improve the mechanical properties by means of inducing microstructural changes, refining grain size, improving dislocation distributions, etc. (To et al. 2009; Zhu et al. 2009a, b). In EPT, critical electric current pulses can be applied to pass through the materials with a high-current density. The treatment can be done so efficiently that only one thousandth of the energy is needed and as little as one thousandth of the time is taken compared with a conventional furnace treatment. The electropulsing treated materials are expected to have better ductility, finer grain microstructure and better machinability in terms of the achievable surface finish by ultraprecision diamond turning.



## 6.1 Basics of Electropulsing Treatment

### 6.1.1 Development of Electropulsing Treatment

The electropulsing effect is a phenomenon which alters the properties of materials, including metals, ceramics, superconductors and metallurgic powders, through applying high-density current pulses. The EPT effectively decreases the drawing force and the ultimate tensile strength and simultaneously improves the plasticity and the elongation ratio significantly. As an alternative to traditional thermal and mechanical processes, EPT has been recognised for its high efficiency and low cost. In recent years, the influence of an electric current on the solid-state transformations in metals has been studied to solve the critical problems of interfacial reactions leading to inter-metallic compound formation, precipitation (ageing) of substitutional and interstitial solutes, crystallisation of amorphous alloys, recrystallisation and grain growth following cold working.

The electropulsing effect was first found in the 1960s by a soviet scientist in experiments in drawing a Zn single crystal with electron radiation. It was found that with the radiation of the electrons, the drawing stress was decreased (Troitskii and Likhtman 1963). It later became a subject of greater interest. Okazaki et al. (1967) reported that under constant-strain-rate conditions, stainless steel wires subjected to current pulses varying in intensity between zero and  $8000 \text{ A/mm}^2$  experienced stress relaxation during the pulses. The applications of EPT boomed in the materials science and engineering fields, such as electroplasticity (Yang and Conrad 2001), electromigration (Lloyd 1999), enhanced powder densification (Mishra and Likhtman 2000), recrystallization (Xiao et al. 2002) and healing cracks and damage (Zhou et al. 2004). In recent years, more work has been conducted in this field, and simultaneously many more problems have been confronted. Research on the effect of EPT on material properties in ultraprecision machining is an area full of challenges and is of great significance.

EPT is enabled by an alternating current (AC) generator used to provide high-frequency electropulses as shown in Fig. 6.1, by controlling current frequency and voltage values. The surface temperature of the specimens during the electropulsing process can be measured by a contact thermocouple (Fig. 6.2). Accurate electropulsing parameters were found using a Hall effect sensor (HDC3000H as in Fig. 6.3) connected to an oscilloscope (Tekronix-TDS 1002 as in Fig. 6.4). By monitoring the wave pattern, accurate frequency, amplitude and the root-mean-square (RMS) values, the electropulsing current can be controlled.

### 6.1.2 Theory of Electropulsing Treatment

A wealth of research has been reported on the electropulsing effect (EPE) mechanism from different aspects of the respective theoretical basis, such as

**Fig. 6.1** AC electropulsing generator



**Fig. 6.2** Contact thermocouple





**Fig. 6.3** Hall effect sensor (HDC3000H)

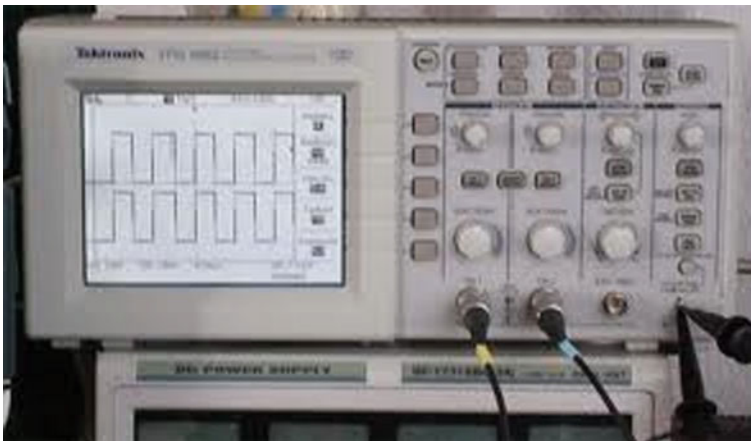


**Fig. 6.4** Oscilloscope (Tektronix-TDS 1002)

the work done by Troitskii and Likhtman (1963) in drawing a single Zn crystal, and Conrad et al. (1989a, b) on the recrystallisation of copper associated with EPT. The well-received theories of EPE are the electric wind force and the magnetic field effect: (i) in drawing a Zn single crystal with electron radiation, it was found that the drawing stress was decreased. Troitskii and Savenko (1986) claimed that when the electrons were introduced into the wire-drawing process, the electrons gave a force to the dislocations, which led to the movement of the dislocations and their homogeneous distribution. The explanation was that with the introduction of current pulses, the electrons would exert a force named “electric wind force” on the

dislocations and enhance their movement so as to scatter the tangles of dislocations, thus leading to an increase in the plasticity of the material; and (ii) when current pulses were introduced into the process of metal wire drawing, the motion of dislocations was hindered by a pinning centre of paramagnetic character, and the depinning rate was strongly affected by the magnetic field induced by the current. Such a model was established on the assumption that the principal cause of the electro-plastic effect was the increase in the length of the free dislocation segments in the current induced magnetic field, and the paramagnetic character of the pinning centre was another important assumption.

EPT is the key technique in the manufacture of high-quality metal parts. The state-of-the-art research finds a wealth of experiments done on drawing zinc, copper single crystal, dual-phase austenite and martensite, and stainless steel wires. Since the electropulsing effect (EPE) was found, it has been explored and applied in the metalworking of sundry materials of poor workability. Tang et al. (1998) investigated the application of electro-plastic processing technology for the cold drawing of steel wires, mainly focusing on the properties of  $\text{Cr}_{17}\text{Ni}_6\text{Mn}_3$  and 4J42 alloys in the process. It was found that the drawing stress decreased by about 20–50% with the application of electric current pulses. For  $\text{Cr}_{18}\text{Ni}_9$ , the drawing stress decreased to about 50% compared with the conventional wire-drawing process. Simultaneously, the plasticity of the material was significantly improved. Due to the application of electric current pulses, a better surface quality than that drawn in the conventional process is expected. When a density of approximately  $10^3 \text{ A/mm}^2$  for about 20  $\mu\text{s}$  current pulse was applied to the drawing process of  $\text{Cr}_{17}\text{Ni}_6\text{Mn}_3$  and 4J42, the drawing force and the ultimate tensile strength decreased, the plasticity of the wire and the elongation ratio improved significantly. Moreover, there was an increased velocity of  $\text{Cr}_{17}\text{Ni}_6\text{Mn}_3$  from 9 to 60 m/min, which was the velocity used in the actual production process in the factory.

To date, the main fields of research include paramagnetic or ferromagnetic metals, dual-phase crystals or single crystals, superconductive materials and application of EPT in producing accurate parts for aerospace industry. The influence of an electric current on the solid-state transformations in metals is considered to be the crucial part of such studies, including inter-metallic compound formation and growth in diffusion couples, precipitation, crystallisation of amorphous alloys, and recrystallisation and grain growth of cold worked metals.

The formation and growth of intermetallic compounds are in qualitative accord with electro-migration theory. Regarding precipitation, an electric current can either enhance or retard the precipitation rate, depending on the alloy, the current density and its frequency. Although electromigration plays a major role in the phase transformation process, many factors including the quenched-in vacancies to various sinks and the local internal stress are also important considerations. Both a continuous direct current (DC) and high-current density electropulsing enhance the crystallisation rate of amorphous alloys. The effects are greater than can be explained by simple electro-migration theory and suggest the cooperative motion of a larger number of atoms. Electro-pulsing enhances the recrystallisation rate of cold worked metals, but retards subsequent grain growth (Conrad 2000).

Research on microstructural changes under electropulsing was also conducted on amorphous materials. It was reported that amorphous  $\text{Fe}_{78}\text{Si}_9\text{B}_{13}$  ribbons were nano-crystallised by using high-current density electropulsing instead of the common annealing treatment (Teng et al. 1996). Crystallisation under electropulsing suggested that a resonant collective motion of many atoms and modification of the thermodynamic parameters in amorphous alloys would occur (Mizubayashi et al. 2001). The maximum stress impedance ratio of 350% was obtained in amorphous  $\text{Fe}_{73.5}\text{Cu}_1\text{Nb}_3\text{Si}_{13.5}\text{B}_9$  ribbons in optimal conditions of current annealing. Electropulsing would also induce many factors which would cause nanostructure transitions, such as high-rate heating, rapid cooling, thermal stress, reduced thermodynamic energy barrier, high-rate electron impacting and accompanying phase transformation (Zhang et al. 2003). The dominant factor determining the microstructural changes depends on the material and experimental conditions.

As an alternative to traditional thermal and mechanical processes, EPT has been recognised for its high efficiency and low cost. Extensive studies have been carried out in the areas of precipitation diffusion, recrystallisation and dislocation movements, crack healing, nucleation rate changes, nanostructure formation and electroplastic effects.

Campbell and Conrad (1994) reported that with precise frequency control it was possible to completely suppress carbon precipitation in the quench ageing process of low carbon steel. By applying EPT of 1000 A/cm<sup>2</sup> current at 100 Hz, the age hardening behaviour could also be reduced. This phenomenon was attributed to the fact that when the frequency of the pulsed current matches the carbon atom jump frequency towards a vacancy, precipitate nucleation in the iron would be under scrutiny. Li et al. (1998) also reported that the electric current would help the segregation of impurity atoms at the grain boundaries. In 2004, it was found that electric current improved long range diffusion of  $\beta$ -phase precipitation in Cu-Zn alloys (Zhou et al. 2004). Classical electro-migration theory failed to explain the order of the increased diffusion rate needed for supporting the formation of the microstructure. The assumption of the dramatic increment in the diffusion coefficient and the decrease in the activation energy was used to explain the phenomena.

The effects of electropulsing on dislocation movement and recrystallisation were first reported by Conrad et al. (1983). It was found that the application of DC electropulsing on cold worked copper would result in a refined microstructure. Short treating time, high-heating rate, accelerated nucleation and lower final dislocation density under electropulsing conditions might cause this phenomenon. The dislocation structure in an electropulsed specimen was also found to be vastly different from that of a thermally treated one. It was proposed that the movement of dislocation enhancement by EPT was caused by (1) the electron wind effect, (2) localised atomic scale heating, (3) the increment of the dislocation vibration frequency and (4) improvement of the sub-grain coalescence. It was also found that a recrystallised nucleus would form in the lower dislocation density region, while boundaries would form in the higher dislocation density region when the

dislocation density gradient accumulated to a certain level. The nucleation rate in recrystallisation under EPT was reported to be  $10^4$  times higher than in the conventional treatment methods.

The crack healing effect by EPT was firstly reported by Conrad et al. (1991). The voids or cavities of 7475 aluminium alloy were healed by using EPT. Yao et al. (2001a, b) also reported the improvement of surface finishing, scratch healing and micro-crack healing by using electric current. Qin and Su (2002) developed a rigorous theory towards understanding the healing effect of EPT. The thermodynamic driving force for healing cracks was calculated and was found to be proportional to the square of current density. For better crack healing, the EPT should be controlled considering the following factors: (1) the temperature rise by Joule heating should be lower than the structural transformation temperature in the bulk material, but higher than the melting temperature at the crack region (2) the electric current should be above certain value (300–600k A/m<sup>2</sup>, depending on the material).

The effect of electropulsing on the nucleation rate has drawn attention ever since the 1980s. Conrad et al. (1984) reported that the colony size of a cast tin lead alloy under electropulsing was reduced significantly under EPT. Qin (1998) developed a quantitative relationship between the nucleation rate and applied electropulsing parameters. The excess free energy for a spherical nucleus under electropulsing was calculated, and it was found that the application of a low-electric pulse of about  $10^3$  A/cm<sup>2</sup> would reduce the grain size. However, the influence of the pinch force and Joule heating was ignored in the theory, which could play an important role in a high-current density situation. High-current density electropulsing experiments with  $1.05 \times 10^{10}$  A/m<sup>2</sup> and of 130  $\mu$ s duration were made on low-carbon steel, and the results showed dramatic changes in the microstructure. Application of electropulsing with current density up to  $10^{10}$  A/m<sup>2</sup> was used on some metallic alloys too. For cold worked H52 Cu–Zn alloy, the randomly oriented grains were three orders of magnitude smaller than the original size.

The electro-plastic effect is the application of electric current on metals that reduce deformation resistance and strain hardening, while increasing the materials' plasticity. Li and Conrad (1998) reported softening behaviour of Zn 5wt%-Al alloy with reduced flow stress, decreased creep rate, increased strain hardening rate and a strengthening property by using an electric current. Cao et al. (1990) also reported that high-electric current would improve the hardening ability of 4030 steel during quench casting, and at the same time reduce defects and micro twins in the material. For Cr<sub>18</sub>Ni<sub>9</sub> austenitic steel, decreases of ultimate tensile strength and increases of elongation were found by using EPT (Tang et al. 2000). It was assumed that the excess energy in the electropulsing process provided activation energy for the dislocations to overcome obstacles and thus reduce internal friction resistance. Livesey et al. (2001) conducted electropulsing experiments in silicon steel, and found the hardness decreased linearly with increasing current density. Noticing that an optimal frequency existed for the phenomena, Tang and Zhang (2003) suggested that when the frequency of the input pulses approached the substance wave in the material, an intensive elastic vibration of waves with the same frequency would occur, thus enabling the movement of the dislocations in the material along the flow

direction at a high speed. This hypothesis was later proven to be deficient, as the atomic vibration frequency is of much higher order than the pulse frequency. In the sense that the EPT process can reduce the deformation resistance and improve the surface quality of materials, EPT is also expected to be a promising material treatment method that can be implemented in ultraprecision machining technology for producing optical quality components with submicron form accuracy and surface roughness within tens of nanometres.

## 6.2 Effect of Electropulsing Treatment on Microstructural Changes

The electropulsing effect involves a high-density current pulse being applied to improve the properties of materials, including metals, ceramics, superconductors and metallurgic powders. Compared with traditional thermal and mechanical processes, EPT stands out for its high efficiency and low cost. Studies on the effect of EPT have been conducted to explore the characteristics and mechanisms of EPT, such as electroplasticity, recrystallisation, crack healing, phase transformations and dislocation movements (Conrad et al. 1991; Yao et al. 2001a; Qin and Su 2002; Li and Conrad 1998; Cao et al. 1990). Two practical types of EPT methods have been developed: static electropulsing and dynamic electropulsing. Static EPT combines a thermal process and electropulsing, whilst dynamic EPT is a complex thermal process, which performs EPT and plastic deformation simultaneously. Research and industrial applications for magnesium alloys are booming nowadays thanks to their excellent properties. Mg alloys are reportedly used in aerospace and automobile industries in light of their comprehensive properties, such as low density, high-specific strength and stiffness, excellent machinability and good castability. As one of the most widely and commercially used Mg alloys, AZ91 alloy with nominal composition of Mg–9Al–1Zn, known for its low density, high-specific strength and stiffness, and improved castability, is widely used as an ideal material for light-weight construction. It is one of the most popular cast magnesium alloys. The AZ91 alloy outshines other conventional wrought magnesium alloys such as AZ31 and AZ61 by the combination of castability, plasticity and cost advantage (Jiang and Dai 2009). In this section, the effects of static EPT and dynamic EPT on microstructural changes and phase transformations are elaborated for AZ91 magnesium alloy.

### 6.2.1 Technical Aspects of Electropulsing Treatment

A series of experiments were conducted on the commercial magnesium alloy AZ91 (9.1 wt%Al, 0.9 wt%Zn, 0.2 wt%Mn, balance Mg). The material was homogenised at 693 K in a graphite crucible electric resistance furnace for 16 h, and

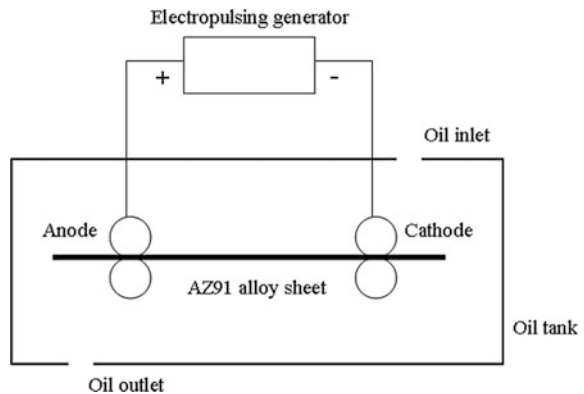
subsequently poured into a preheated iron mould at 593 K, which provided cuboid shaped specimens of thickness 1.9 mm and width 4 mm, and was then extruded into a strip of 2.90 mm width and 1.45 mm thickness. Differing in the preparation methods and electropulsing styles, the AZ91 alloy prepared for the present study can be divided into three groups: as-tempered specimens for static EPT, cold-rolled specimens for static EPT and rolling specimens with dynamic EPT.

### 6.2.1.1 Static Electropulsing Treatment

For the as-tempered specimens, the strip was electropulsing-rolled to a thickness of 1.0 mm. Multiple positive electropulses were applied while the strip was moving at a speed of 2 m/min over a distance of 225 mm between the two roller electrodes. The pressure between the electrodes and strips was adjusted to keep good electrical contact without causing deformation of the strip.

The rolled strip was tempered at 493 K for 12 h, followed by natural cooling in air. The tempered strip was cut into pieces 80 mm long, and subjected to EPT. During the process, a jet-type oil cooling system was used to cool and protect the surface of the specimen. The duration time of electropulsing was controlled to 10 s. The current amplitude, root-mean-square value, frequency and duration time were monitored by an oscilloscope connected to a Hall effect sensor. A schematic illustration of the EPT system is presented in Fig. 6.5. Various electropulsing operational parameters, such as pulse frequency, root-mean-square value of current density, amplitude of current density and temperature are listed in Table 6.1. It was found that the temperature of the EPT specimen increases gradually with the frequency of electropulsing. The higher frequency contributes to larger RMS values of current density, which results in a larger Joule heating effect. Longitudinal cross-sections of the four specimens under various frequencies of EPT were polished and then examined using backscattered electron microscopy (JSM-6490

**Fig. 6.5** The Schematic illustration of the static EPT system for as-tempered specimens



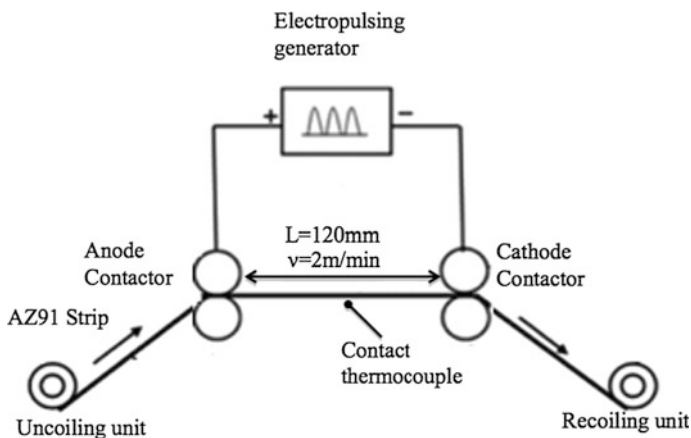


**Table 6.1** Experimental parameters of as-tempered specimens under static EPT

Specimen no.	Frequency (Hz)	RMS (A)	Amplitude (A/mm <sup>2</sup> )	Temperature (K)
EPT 1	Non-EPT	–	–	293
EPT 2	120	177.7	45.33	323
EPT 3	183	204.35	58.10	385
EPT 4	252	61.33	204.35	407

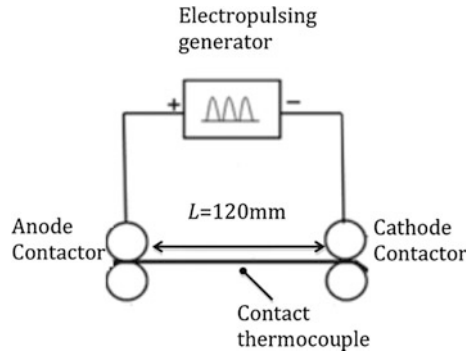
BSEM). These phases were also identified by an X-ray diffractometer (Bruker D8 Discover XRD). Examination of the specimens was carried out using transmission electron microscopy (JEOL 2010 TEM).

In the second group, the extruded strip was cut to a 300 mm length, and then cold-rolled to 1.15 mm thick. During the rolling process, the strip was moving at a speed of 2 m/min. A schematic illustration of the cold-rolling system is shown in Fig. 6.6. The middle parts of the cold-rolled strips with length of 120 mm were selected to undergo static EPT. A self-made electropulsing generator was applied to discharge positive direction multiple pulses with various current parameters for 10 s. Multiple electropulses were applied with two electrical contactors on the two sides of the strips. During the electropulsing process, the electropulsing parameters, including frequency, root-mean-square current (RMS), amplitude current and duration of the multiple pulses were monitored by an oscilloscope connected to a Hall effect sensor, as listed in Table 6.2. The EPT process is schematically shown in Fig. 6.7. BSEM (Hitachi-S4800 ultra-high resolution field emission scanning electron microscopy) examination was carried out to observe the longitudinal cross-sections of the specimens under various frequencies of EPT. An X-ray diffractometer (Bruker D8 Advance) was used to identify the phases. The

**Fig. 6.6** A schematic view of dynamic electropulsing process

**Table 6.2** Experimental parameters of cold-rolled specimens under static EPT

No.	Frequency (Hz)	RMS (A)	Amplitude (A/mm <sup>2</sup> )	Temperature (K)
EPT 1	Non-EPT	–	–	293
EPT 2	151	71.62	274.2	335
EPT 3	209	79.81	265.1	346
EPT 4	253	104.57	319.84	428
EPT 5	294	121.52	347.26	507

**Fig. 6.7** A schematic illustration of the EPT process

metallurgical structure was observed by inverted microscopy (Olympus GX51). TEM examination was carried out using transmission electron microscopy (JEOL 2010).

### 6.2.1.2 Dynamic Electropulsing Treatment

In the dynamic electroplating process, the extruded strip was rolled under electroplating. During the rolling, the strip was moving at a speed of 2 m/min between two electrodes spaced at a distance of 225 mm. A self-made electroplating generator was continuously used to discharge multiple positive pulses with various current parameters on the rolling material, and it took about 10 s for the strip to pass the electrodes. The pressure between the electrodes and the strip was adjusted to keep good electrical contact without causing deformation of the strip. During the dynamic electroplating, the current parameters including frequency, root-mean-square current (RMS), amplitude current and duration of multiple pulses were monitored by an oscilloscope, and are listed in Table 6.3. The longitudinal cross sections of the specimens under various frequencies of EPT were examined by a BSEM (Hitachi-S4800 ultra-high resolution field emission scanning electron microscope). The phases were identified by an X-ray diffractometer (Bruker D8 Advance XRD), and a range of diffraction from 25° to 65° was selected. The scanning speed was 1 °/min, with increments of 0.03. The metallurgical structure of

**Table 6.3** Experimental parameters of dynamic EPT

No.	Frequency (Hz)	RMS (A)	Amplitude (A/mm <sup>2</sup> )	Temperature (K)
EPT 1	Non-EPT	–	–	293
EPT 2	126	52.00	211.2	316
EPT 3	204	63.05	237.6	349
EPT 4	265	89.53	256.5	359
EPT 5	309	100.19	271.6	390

the specimens was observed by an Inverted Microscopy (Olympus GX51), after the specimens were etched by using the customised solution. Examination of TEM was carried out using a TEM (JEOL 2010 transmission electron microscope).

### 6.2.2 Phase Transformation and Microstructural Changes

The phases in the specimen are identified by a Bruker D8 Discover X-ray diffractometer. The XRD patterns for the specimens under different parameters of EPT are shown in the Fig. 6.8, with a range of diffraction from 25° to 85°. The non-EPT specimen has typically a primary  $\alpha$ -Mg phase matrix and a  $\beta$ -Mg<sub>17</sub>Al<sub>12</sub> phase. As the frequency of the EPT increases from 120 to 183 Hz, the peaks of the  $\beta$ -Mg<sub>17</sub>Al<sub>12</sub> phase increase, which implies that precipitation of the  $\beta$  phase has taken place; and as the frequency continues to increase from 183 to 252 Hz, the peak of the  $\beta$  phase decreases, which implies that a reverse phase transformation occurred.

The microstructural changes are observed by BSEM. It is noticed that a phase transformation occurred in the specimens after EPT at various frequencies. The microstructure of the non-EPT specimen is shown in Fig. 6.9a. The  $\beta$ -Mg<sub>17</sub>Al<sub>12</sub> phase appeared as lamellar clusters shown in circles, when the frequency of EPT increases from non-EPT to 120 and 183 Hz, the amounts of the  $\beta$  phase increase. The microstructures of specimens after EPT, with frequencies of 120 and 183 Hz, are shown in Fig. 6.9b, c. It is interesting to observe that the amounts of the  $\beta$  phase decrease after EPT at 252 Hz. This is in agreement with the XRD patterns shown in Fig. 6.8. The decomposition process of the  $\beta$  phase is defined as a way of up-quenching, and the precipitation process of the  $\beta$  phase is defined as a way of quenching in EPT. Further details of the phase transformations induced by the EPT are studied by TEM observation. The thin-foil specimens of non-EPT, 120 Hz frequency of EPT, 183 Hz frequency of EPT and 252 Hz frequency of EPT specimens are mechanically polished and produced using precision ion polishing system (PIPS).

The TEM bright field of the non-EPT specimen is shown in Fig. 6.10a. Together with the indexed selected area diffraction pattern (SADPs) from the  $[\bar{1}21\bar{3}]$  zone of the hcp  $\alpha$  phase and from the [001] zone of the bcc  $\beta$  phase particle, the dark field

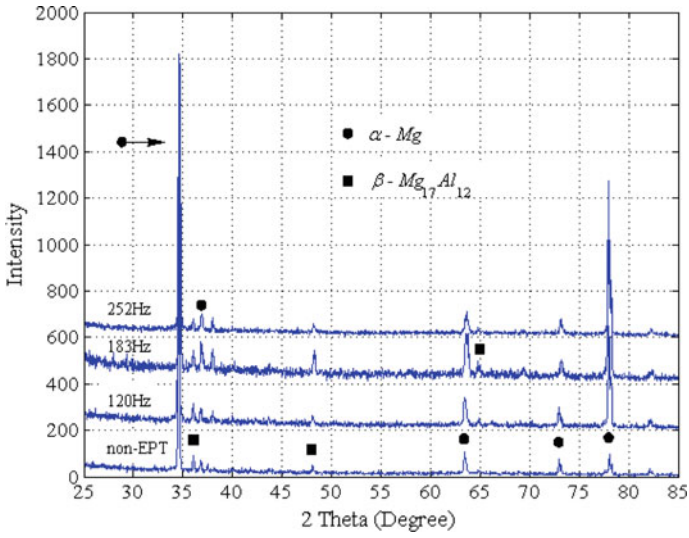


Fig. 6.8 XRD patterns for as-tempered specimens under various frequencies of static EPT

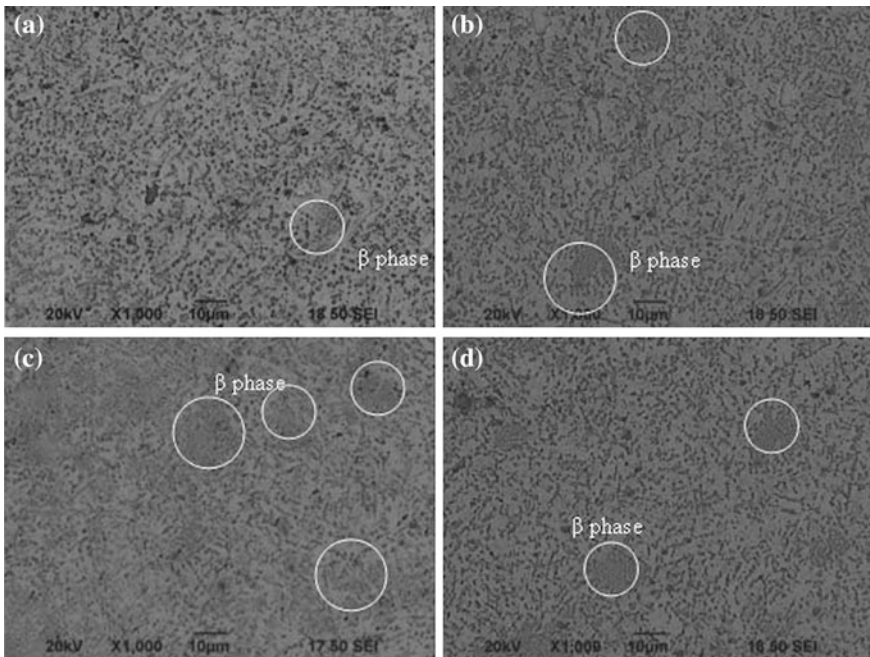
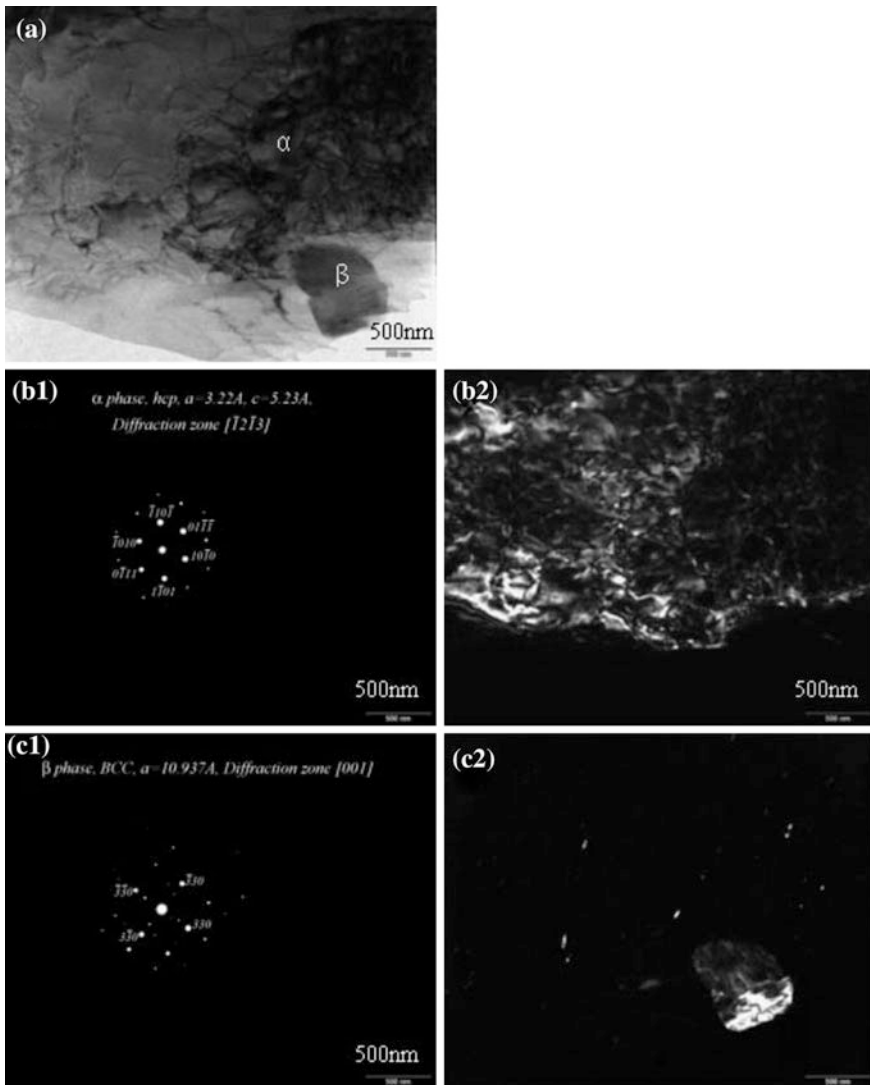
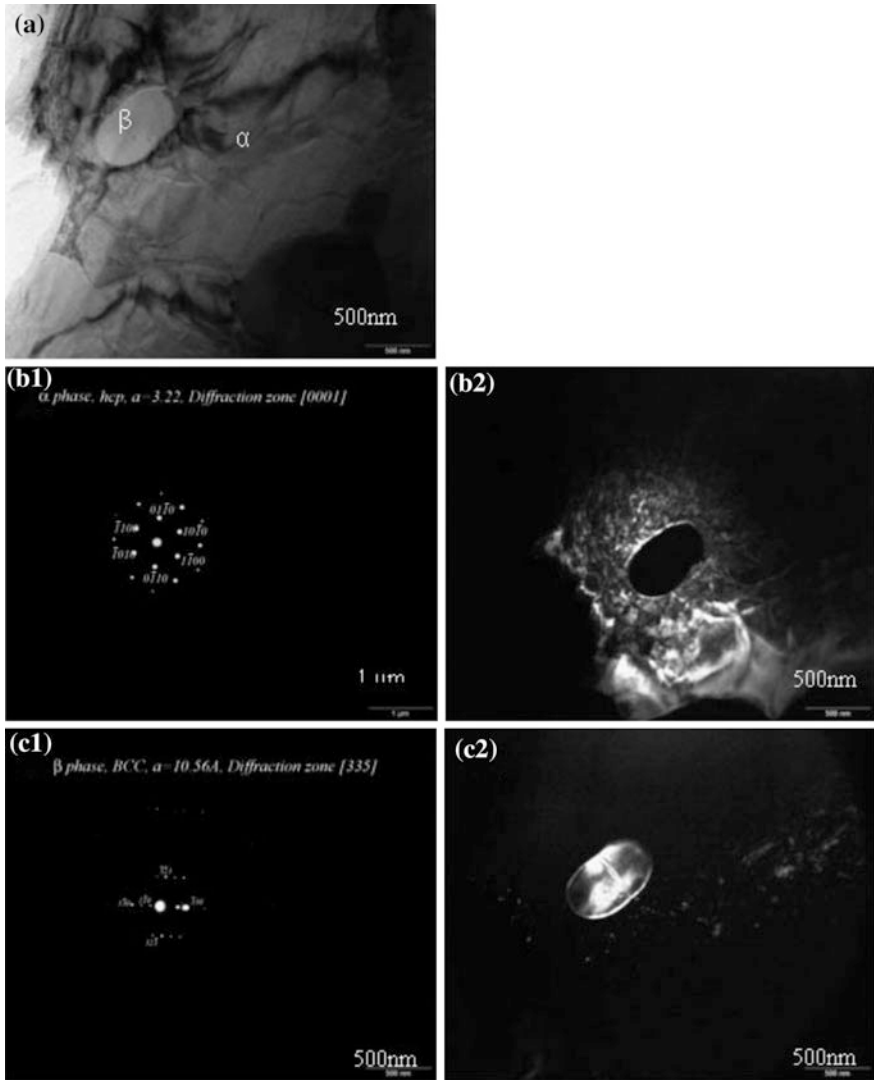


Fig. 6.9 SEM micrographs of the as-tempered specimens under a non-EPT, b 120 Hz frequency of EPT, c 183 Hz frequency of EPT, d 252 Hz frequency of EPT



**Fig. 6.10** TEM images of non-EPT **a** bright field image; **b2** dark field image of  $(\bar{1}10\bar{1})$  reflection together with **b1** diffraction pattern from  $B = [\bar{1}21\bar{3}]$  of the  $\alpha$  phase; **c2** dark field image of  $(3\bar{3}0)$  reflection together with **c1** diffraction pattern from  $B = [001]$  of the  $\beta$  phase

images using  $(\bar{1}10\bar{1})$  and  $(3\bar{3}0)$  reflections of these two phases are shown in Figs. 6.10b2 and 6.7c2, respectively. The lattice parameters of the  $\alpha$  phase are  $a = 0.322$  nm,  $c = 0.523$  nm and  $c/a = 1.624$ ; the lattice parameters of the  $\beta$  phase is  $a = 1.0937$  nm.  $\beta$  phase particles are also examined inside the  $\alpha$  lamella matrix in the 252 Hz-EPT specimen, as shown in Fig. 6.11. According to the identification,



**Fig. 6.11** TEM images of 252 Hz-EPT **a** bright field image; **b2** dark field image of  $(\bar{1}010)$  reflection together with **b1** diffraction pattern from  $B = [0001]$  of the  $\alpha$  phase; **c2** dark field image of  $(32\bar{3})$  reflection together with **c1** diffraction pattern from  $B = [335]$  of the  $\beta$  phase

the  $\beta$  phase particle is about 520 nm in diameter. Both the  $\alpha$  and  $\beta$  phases are marked in Fig. 6.11a. The indexed diffraction patterns and the dark field images reflected from  $[0001](\bar{1}010)$  of the  $\alpha$  phase and  $[001](330)$  of the  $\beta$  phase are shown in Fig. 6.11b1, b2, c1, c2.

The evolution of the  $\beta$  phase particles can also be observed in the TEM micrographs. In Fig. 6.12a, few precipitations of the  $\beta$  phase can be found in the TEM bright field of the non-EPT specimen, and as the frequency of EPT increases to 120 Hz, the amounts of the precipitates of the  $\beta$  phase increase, as shown in Fig. 6.12b. In Fig. 6.13c, the bright field of the 183 Hz frequency of EPT shows that the amount of  $\beta$  phase particles reaches a high level. It is in agreement with the XRD results shown in Fig. 6.8 and the SEM results shown in Fig. 6.9 in which the precipitates of the  $\beta$  phase occur in a few seconds under electropulsing. In short, there is a phase transformation by quenching in this first stage of EPT (To et al. 2009, 2011). Upon the frequency of EPT increasing to 252 Hz, the amount of  $\beta$  phase particles decreases as shown in Fig. 6.12d. This means that dissolution of the  $\beta$  phase occurs when further increasing the frequency of EPT. The decomposition of the  $\beta$  phase appears as a reverse transformation of the precipitate in a way of up-quenching.

The XRD patterns for the as-rolled specimen of non-EPT, the 151 Hz-EPT and 294 Hz-EPT specimens are shown in Fig. 6.13. The non-EPT specimen consists of mainly two phases, an  $\alpha$ -Mg phase and a  $\beta$ -phase ( $\text{Mg}_{17}\text{Al}_{12}$ ). As the frequency of EPT increases to 151 Hz, the peaks of the  $\beta$  phase weaken, which implies that the amounts of the  $\beta$  phase decrease and transform. Upon increasing the frequency of electropulsing to 294 Hz, the peaks of the  $\beta$  phase increase, compared to that of 151 Hz-EPT. This means that precipitation of the  $\beta$  phase increases with increasing frequency of electropulsing.

The BSEM images and TEM bright field images of the specimens at different frequencies of electropulsing are shown in Fig. 6.14. The microstructure of the non-EPT specimen mainly consists of the matrix  $\alpha$  phase and precipitates of the  $\beta$  phase, as shown in Fig. 6.14a1. Large amounts of  $\beta$  precipitates are observed in the cold-rolled specimen. After electropulsing with 151 Hz for 10 s, the amounts of the  $\beta$  phase decrease, as shown in Fig. 6.14a2, implying that the decomposition of the  $\beta$  phase is accelerated with increasing frequency. Previous studies reported that decomposition of the  $\beta$  phase occurred after 20 h of ageing at 673–693 K (Jiang and Dai 2009). It is obvious that under electropulsing the decomposition of the  $\beta$  phase is tremendously accelerated in the way of up-quenching. Upon the frequency of electropulsing further increasing to 294 Hz, the  $\beta$  phase amount increases in the way of quenching, as shown in Fig. 6.14a3. TEM examination confirms the aforementioned phase transformations. The TEM bright field images of (b1) non-EPT, (b2) 151 Hz-EPT and (b3) 294 Hz-EPT are shown in Fig. 6.14. Both the SEM results and TEM observations are in good agreement with the XRD patterns.

Moreover, it is noticed in the TEM bright field images that the amounts of dislocation are influenced by electropulsing. For the non-EPT specimen, arrays and blocks of dislocations are observed, as shown in Fig. 6.14b1. After 151 Hz-EPT for 10 s, the dislocation arrays decrease, as shown in Fig. 6.14b2. When the frequency of electropulsing increases to 293 Hz, the amount of the dislocation is further reduced, as shown in Fig. 6.14b3. It is assumed that under electropulsing, electron wind is formed and pushes the defects, including dislocations and vacancies, towards the grain boundaries, where accumulation and annihilation of the

**Fig. 6.12** TEM bright field images of **a** non-EPT, **b** 120 Hz frequency of EPT, **c** 183 Hz frequency of EPT and **d** 252 Hz frequency of EPT

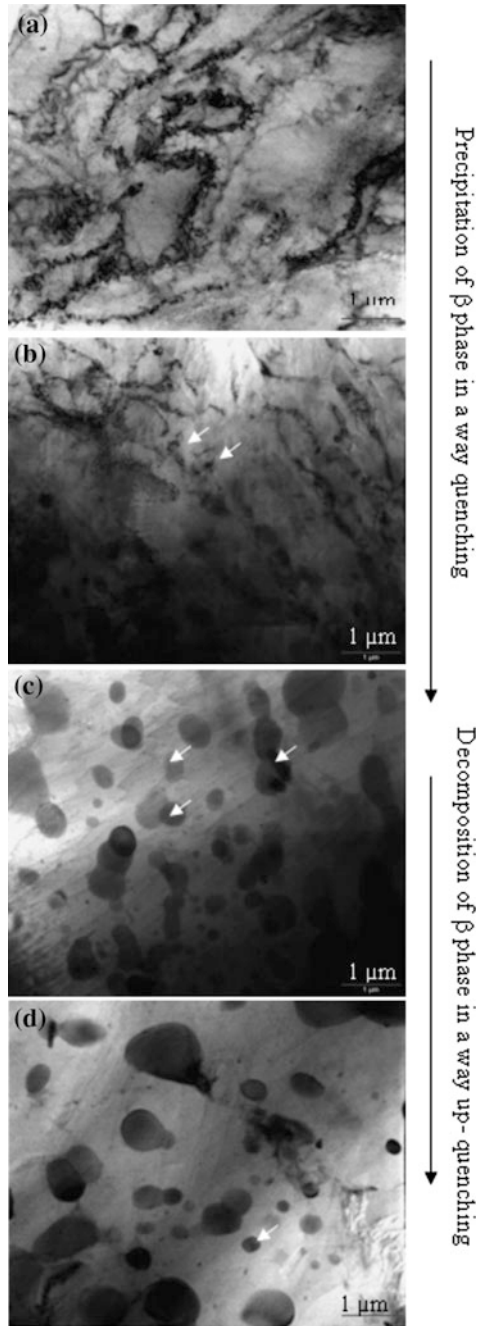
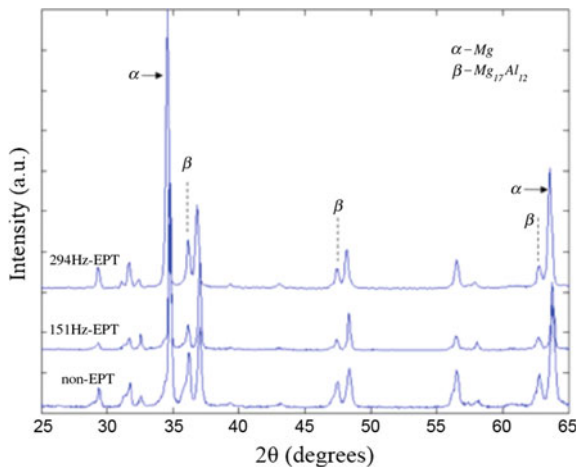




**Fig. 6.13** XRD patterns for cold-rolled specimens under various frequencies of EPT



dislocation occur simultaneously. When the frequency of electropulsing increases, both the accumulation and the annihilation are enhanced and maintain an adequate balance, which results in decreasing of the dislocation density.

The optical micrographs of the non-EPT specimen and the EPT specimens with various frequencies of electropulsing are shown in Fig. 6.15. For the cold-rolled specimen (non-EPT specimen) in Fig. 6.15a, many deformation twins inside the grains are observed, and the average size of the grains is about 77  $\mu\text{m}$ . With increasing the frequency of electropulsing, the amount of twins is decreased. The average grain size reduces from 68, 63 to 35  $\mu\text{m}$  in the 209, 253 and 294 Hz-EPT specimens, as shown in Fig. 6.15b–d, respectively. A relatively homogeneous microstructure of equiaxed grains is observed after 294 Hz-EPT for 10 s, implying that electropulsing greatly accelerates recrystallisation of the cold-rolled alloy specimens.

Figure 6.16 shows the X-ray diffractograms of the as-rolled (non-EPT) specimen and the dynamic EPT specimens. The non-EPT specimen consists of mainly two phases, the  $\alpha$ -Mg phase and the  $\beta$  phase ( $\text{Mg}_{17}\text{Al}_{12}$ ). When the frequency of electropulsing increases to 204 Hz, the XRD intensity of  $\beta$  phase reduces. Upon further increasing the frequency to 309 Hz, the XRD intensity of the  $\beta$  phase further reduces. This implies that the decomposition of the  $\beta$  phase is accelerated when the frequency of electropulsing increases during dynamic electropulsing.

The BSEM images and TEM bright field images of specimens under different frequencies of dynamic EPT are shown in Fig. 6.17. The matrix shows an  $\alpha$ -Mg phase, while the precipitates are of  $\beta$  phase ( $\text{Mg}_{17}\text{Al}_{12}$ ). For the as-rolled specimen, numerous  $\beta$  phase precipitates can be seen in Fig. 4.17a1; as the frequency of dynamic electropulsing increases to 204 Hz, the amount of the  $\beta$  phase precipitates decreases as shown in Fig. 6.17a2, When the frequency of electropulsing increases to 309 Hz, even fewer precipitates could be observed in Fig. 6.17a3. TEM bright field images of these specimens confirmed the same microstructural changes as

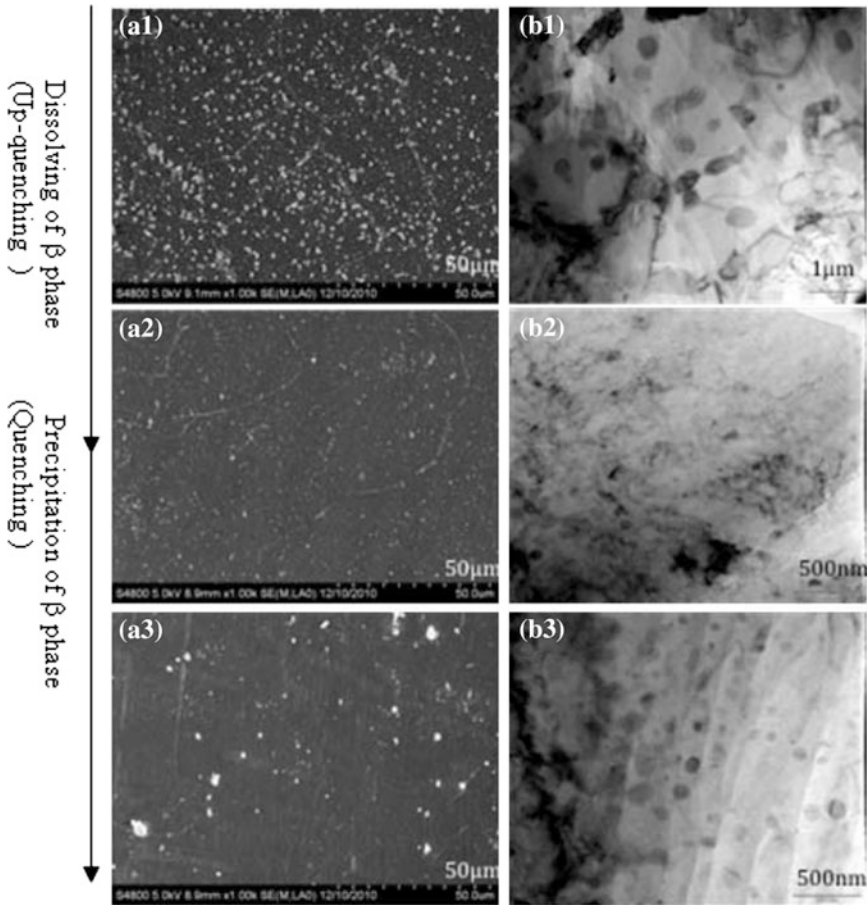


**Fig. 6.14** BSEM images of **a1** non-EPT, **a2** 151 Hz-EPT, **a3** 294 Hz-EPT and TEM bright field images of **b1** non-EPT, **b2** 151 Hz-EPT, **b3** 294 Hz-EPT, showing  $\beta$  phase precipitates changes with various frequency of EPT

shown in Fig. 6.17b1–b3. As the frequency of electropulsing increases, the amount of the precipitates marked by the white arrows decreases significantly, meaning that the decomposition of the  $\beta$  phase occurs simultaneously in the way of up-quenching. Both the SEM results and TEM observations are in good agreement with the XRD patterns shown in Fig. 6.16.

To identify the phases during the process, TEM examination of the dynamic electropulsing treated specimens is shown in Fig. 6.18. The bright field of the 204 Hz-EPT specimen is shown in Fig. 6.18a. Together with the indexed SADPs shown in Fig. 6.18b1 and c1, the dark field images reflected from  $[\bar{1}2\bar{1}3](10\bar{1}0)$  of the hcp  $\alpha$  phase, and  $[\bar{1}11](110)$  of the bcc  $\beta$  phases are shown in Fig. 6.18b2, c2, respectively. The lattice parameters of the  $\alpha$  phase are  $a = 3.22 \text{ \AA}$ ,  $c = 5.23 \text{ \AA}$  and  $cla = 1.624$ ; the lattice parameter of the  $\beta$  phase is  $a = 10.690 \text{ \AA}$ .

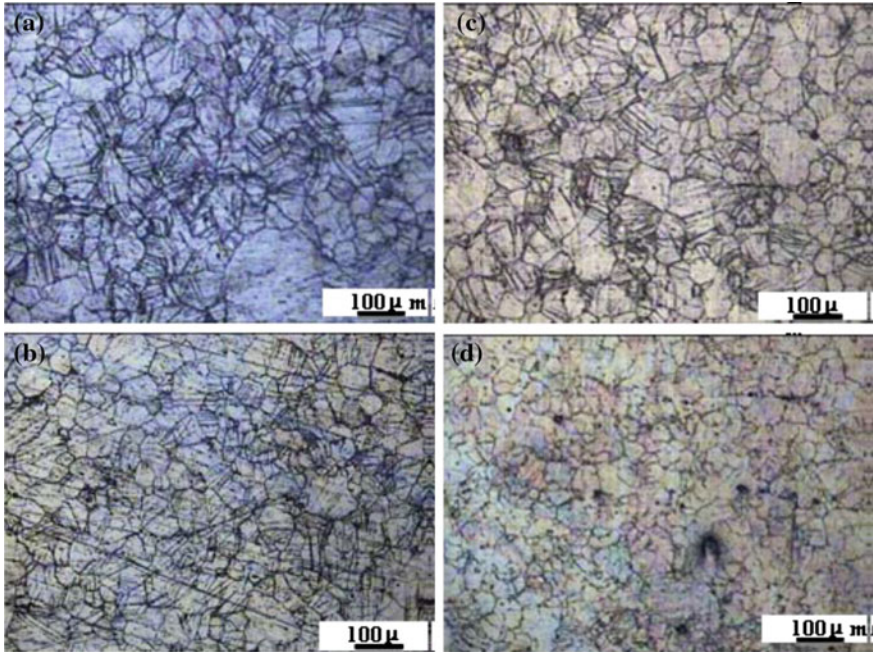
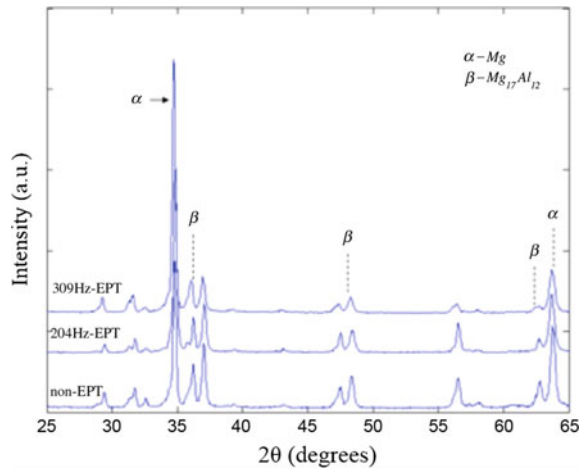


**Fig. 6.15** Optical micrographs of **a** non-EPT, **b** 209 Hz-EPT, **c** 253 Hz-EPT and **d** 294 Hz-EPT

**Fig. 6.16** XRD patterns for the specimens under various frequencies of dynamic EPT



For comparison, the AZ91 strips are statically electropulsing treated for various parameters. The BSEM images and TEM bright field images of the static EPT specimens are shown in Fig. 6.14. With increasing frequency of electropulsing, decomposition and precipitation of the  $\beta$  phase are tremendously accelerated

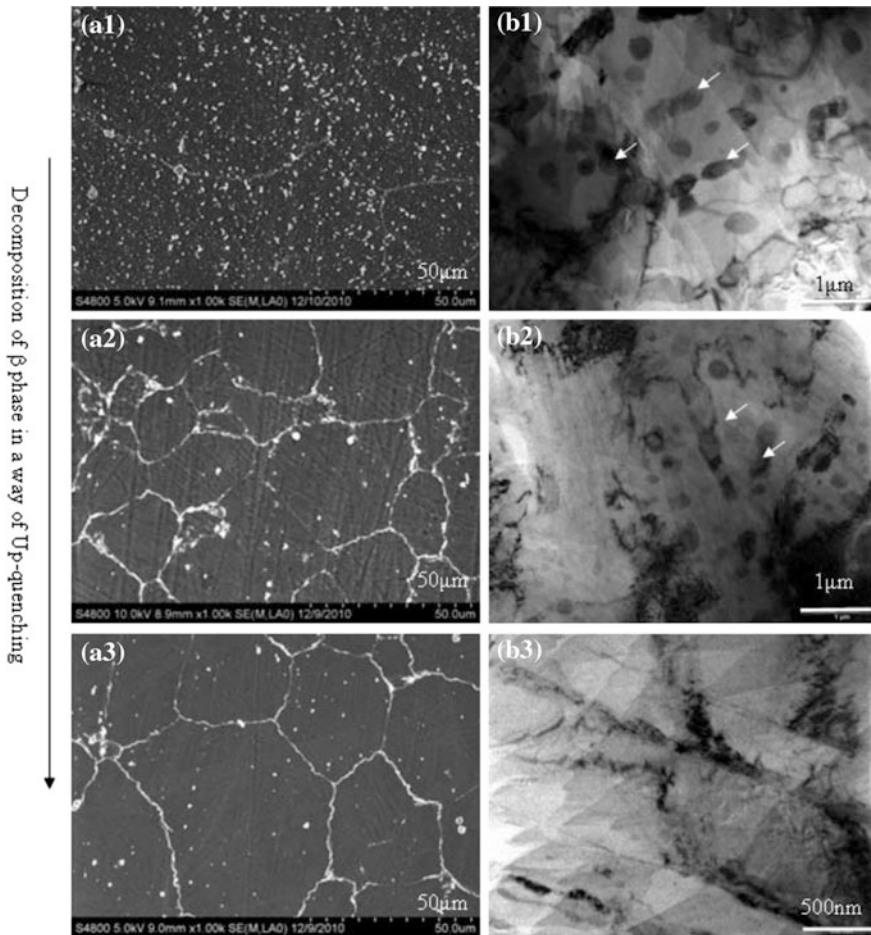


**Fig. 6.17** BSEM images of **a1** non-EPT, **a2** 204 Hz-EPT, **a3** 309 Hz-EPT and TEM bright field images of **b1** non-EPT, **b2** 204 Hz-EPT, **b3** 309 Hz-EPT, showing  $\beta$  phase precipitates changes with various frequency of EPT

sequentially, as shown in Fig. 6.14. While in the dynamic EPT specimens, only the decomposition of the  $\beta$  phase in the way of up-quenching occurs, as shown in Fig. 6.17. For the decomposition to be completed under the conventional thermal process of the AZ91 strips, about 20 h of ageing in the range of 673–693 K is required. This implies that electropulsing tremendously accelerates the phase transformations of the AZ91 alloy at a relatively lower temperature (349–390 K) within only a few seconds.

The optical micrographs of the non-EPT and the dynamic EPT specimens for various frequencies are shown in Fig. 6.19. For the non-EPT specimen, many deformation twins are observed inside the grains, as shown in Fig. 6.19a. When the

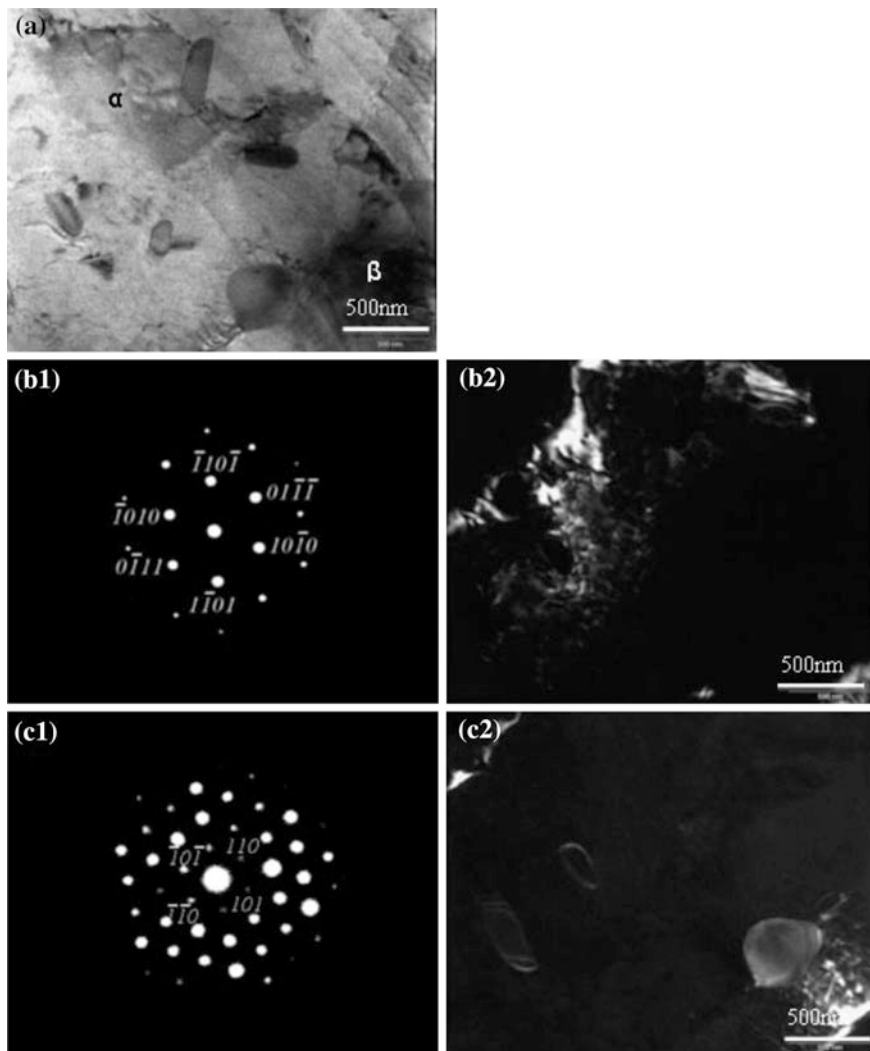


**Fig. 6.18** TEM images of 204 Hz-EPT **a** bright field image; **b2** dark field image of (1010) reflection together with **b1** diffraction pattern from  $B = [1213]$  of the  $\alpha$  phase; **c2** dark field image of (110) reflection together with **c1** diffraction pattern from  $B = [111]$  of the  $\beta$  phase

frequency of the dynamic electropulsing increases to 126 Hz, the twins inside the grains are rarely observed, as shown in Fig. 6.19b. Upon further increasing the frequency to 309 Hz, a relatively homogeneous microstructure of equiaxed grains is obtained, as shown in Fig. 6.19c–e. This is because, under the dynamic electropulsing, the external stress resulting from the plastic deformation is reduced

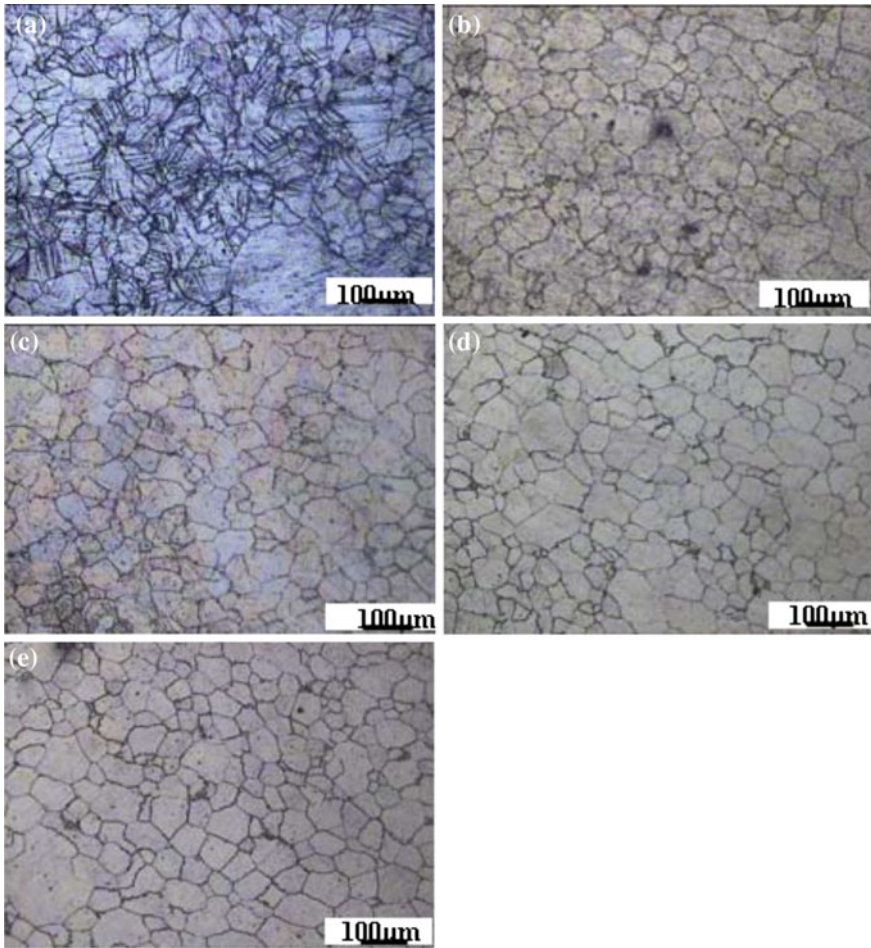


**Fig. 6.19** Optical micrographs of **a** non-EPT, **b** 126 Hz-EPT, **c** 204 Hz-EPT and **d** 265 Hz-EPT, **e** 309 Hz-EPT

simultaneously, and the twins quickly vanish. In comparison, for the static EPT specimens as shown in Fig. 6.15, the twins microstructure decrease gradually when the frequency increases from non-EPT to 209 and 253 Hz, and disappear after 294 Hz-EPT.

### 6.2.3 Dislocation Identity

The dislocation evolution under various frequencies of EPT can be observed from the TEM images. TEM bright field images of the as-tempered specimens under

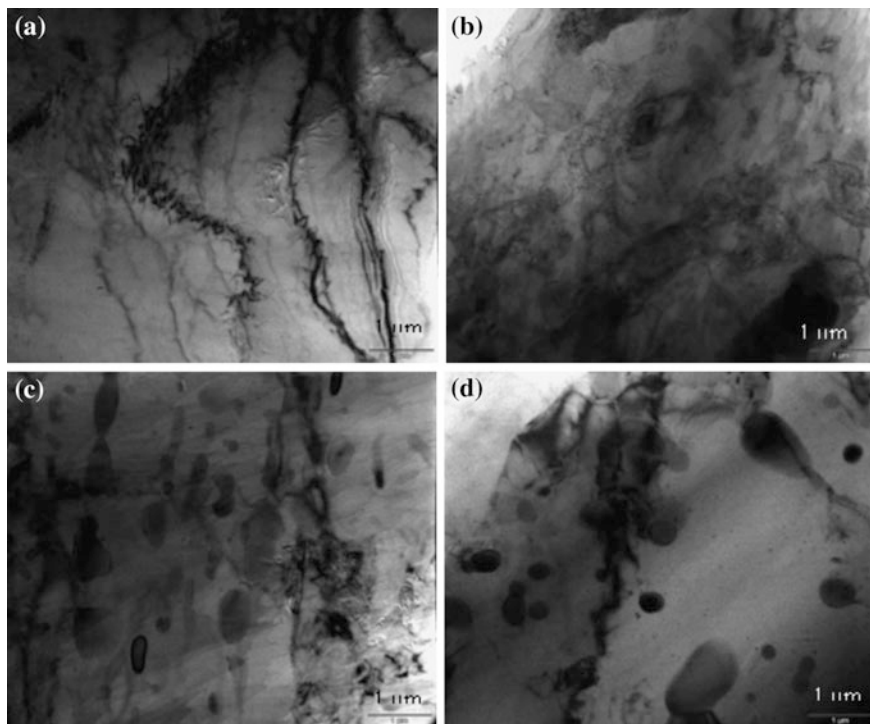


**Fig. 6.20** TEM bright field images of as-tempered specimens **a** non-EPT, **b** 120 Hz frequency of EPT, **c** 183 Hz frequency of EPT and **d** 252 Hz frequency of EPT

various frequencies of static EPT are shown in Fig. 6.20. In Fig. 6.20a, for the non-EPT specimen, there are some dislocation arrays and nodes, introduced from the previously thermal and thermo-mechanical treatments.

Due to the electron wind force factor, the defects in the specimen, such as dislocations and atomic vacancies, are pushed towards the sub-grain boundaries by electropulsing. After 120 Hz-EPT, the dislocation arrays and nodes decrease, as shown in the Fig. 6.20b. When the frequency of EPT increases to 183 Hz, the amount of dislocations is significantly reduced, as shown in Fig. 6.20c. It is suggested that under electropulsing, electron wind is formed and pushes the defects in the specimen, such as dislocations and atomic vacancies, towards the grain boundaries, where accumulation and annihilation of the dislocations occur at the same time (Zhu 2009). With increasing frequency of electropulsing, both the accumulation and the annihilation of the dislocations are enhanced, maintaining an adequate balance at the grain boundaries. Thus, the dislocation density decreases. After 252 Hz-EPT, dislocations can rarely be observed, as shown in Fig. 6.20d. The dislocation dynamics for the cold-rolled specimens under various frequencies of static EPT are shown in Fig. 6.14b, and the specimens under various frequencies of dynamic EPT are shown in Fig. 6.17b, confirming the aforementioned theory.

### 6.2.4 Driving Forces for Phase Transformations

The driving force for phase decomposition consists of various factors, including chemical Gibbs free energy, surface energy, strain energy, crystal orientation Gibbs free energy and EPT induced Gibbs free energy. The free energy equation for the phase transformation is as follows (Zhu et al. 2009b):

$$\Delta G = \Delta G_{\text{chem}} + \Delta G_{\text{surface}} + \Delta G_{\text{strain}} + \Delta G_{\text{orient}} + \Delta G_{\text{EPT}} \quad (6.1)$$

The driving force of the as-tempered specimens under static EPT is discussed in the following section. In conventional thermodynamics, the chemical Gibbs free energy ( $\Delta G_{\text{chem}}$ ) is considered to be the dominant factor in determining phase transformation. The surface energy ( $\Delta G_{\text{surface}}$ ) and preferred crystal orientation induced Gibbs free energy ( $\Delta G_{\text{orient}}$ ) are the main parts affecting phase transformation in the nanophase of alloy films. The strain energy ( $\Delta G_{\text{strain}}$ ) includes the internal strain energies, such as thermal stress during solidification of the melt, and external strain energies caused by tensile, creep, fatigue effect, etc. For the AZ91 specimens used in this study, the major factors influencing phase transformation are  $\Delta G_{\text{chem}}$  and  $\Delta G_{\text{EPT}}$ , because no nanofilm and external strain exist in the experiments. The EPT accelerates the phase transformation in two stages:

- (i) when  $\Delta G < 0$ , with addition of the EPT induced Gibbs free energy, the total Gibbs free energy of the specimen increases and is higher than that of the stable state. EPT accelerates the decomposition of the supersaturated  $\alpha$  phase and further precipitation of  $\beta$  phase is generated, till the final stable state is reached, where  $\Delta G = 0$ ;
- (ii) when  $\Delta G = 0$ , further EPT would continue to increase the Gibbs free energy of the alloy, where  $\Delta G > 0$ . As a result, the stable phases reverse-decompose and precipitation of  $\beta$  phases decreases.

For the quenching process, both  $\Delta G_{\text{chem}}$  and  $\Delta G_{\text{EPT}}$  are negative:

$$|\Delta G_{\text{quen}}| = -|\Delta G_{\text{chem}}| - |\Delta G_{\text{EPT}}| \quad (6.2)$$

The chemical Gibbs free energy and the EPT induced Gibbs free energy together accelerate the phase transformation from the supersaturated state of the non-EPT specimen to the saturated state of the 183 Hz-EPT specimen. For the up-quenching process, the positive increment of  $\Delta G_{\text{EPT}}$  induced by EPT is the only driving force for the phase transformation, and the specimen becomes unstable for reverse-transforms back to the initial state. For the cold-rolled specimens under static EPT, the decomposition of the  $\beta$  phase occurred first when  $\Delta G > 0$ , subsequently followed by the precipitation of the  $\beta$  phase as  $\Delta G < 0$ . For the specimens under dynamic EPT, only the decomposition of  $\beta$  phase occurred, reaching a stable state.



### 6.2.5 Electropulsing Kinetics

In EPT, the transient stress is caused by the electron wind, which is formed by the knock-on collision of high-rate electrons with the atomic nuclei. The transfer of energy from the electrons to the atoms is also much more effective than in the traditional thermal and thermo-mechanical processes. As shown in Figs. 6.13, 6.15, and 6.19, the sliding behaviour of the dislocations and the phase transformation are significantly affected by the EPT, and electron migration induced by the electric current can play an important role in the process. The effect of multiple electropulses through the specimens can be described by the atomic diffusion flux,  $J$ , in the Nernst–Einstein equation (Jiang and Dai 2009; Zhu 2009):

$$J = \frac{N_i \cdot D_i}{KT} \left( KT \cdot \frac{\partial \ln X_i}{\partial x} - \Omega \cdot \frac{\partial \sigma}{\partial x} + Z^* \cdot e \cdot \rho \cdot j \right) \quad (6.3)$$

where  $N_i$  stands for the density of the  $i$ th atom species,  $D_i$  is the pertinent diffusion coefficient,  $Z^*$  is the effective valence,  $e$  is the charge on an electron,  $\rho$  is the resistivity,  $j$  is the current density,  $X_i$  is the concentration of the  $i$ th solute,  $\Omega$  is the atom volume,  $\frac{\partial \sigma}{\partial x}$  is the stress gradient,  $K$  is the Boltzmann constant and  $T$  is the absolute temperature. The chemical gradient and composition gradient can be neglected under EPT because these effects are much weaker than that of electropulsing. The average atomic flux per second under EPT is given by (Jiang and Dai 2009):

$$J = J_t + J_a = \frac{2\pi D_1}{\Omega \ln\left(\frac{R'}{r_0}\right)} \cdot \left( l + \frac{\delta_c}{c_0} \right) + \frac{2N \cdot D_1 \cdot Z^* \cdot e \cdot \rho \cdot f \cdot j_m \cdot \tau_p}{\pi KT} \quad (6.4)$$

$$J_t = \frac{2\pi D_1}{\Omega \ln\left(\frac{R'}{r_0}\right)} \cdot \left( l + \frac{\delta_c}{c_0} \right) \quad \text{and} \quad J_a = \frac{2N \cdot D_1 \cdot Z^* \cdot e \cdot \rho \cdot f \cdot j_m \cdot \tau_p}{\pi KT} \quad (6.5)$$

The atomic flux in EPT consists of mainly two parts: the flux of the diffusion atoms caused by the thermal effect  $J_t$ , and the flux of the diffusion atoms caused by the athermal effect  $J_a$ .  $D_1$  is the lattice diffusion coefficient,  $c_0$  is the average concentration of vacancies,  $\delta_c$  is the supersaturation concentration of vacancies,  $r_0$ ,  $R'$  are the distances far from dislocation where the vacancy concentrations are  $c_0$  and  $c_0 + \delta_c$ , respectively,  $j_m$  is the peak current density,  $f$  is the frequency and  $\tau_p$  is the duration of each electropulse of EPT. Judging from Eq. (6.4), in the electropulsing process where  $j_m$ ,  $f$ , and  $\tau_p$  increase, the athermal effect  $J_a$  increases linearly. As these three parameters increase, the incremental athermal effect provides sufficient energy to accelerate the diffusional phase transformation and dislocation movements. Meanwhile, during the EPT, the temperature also increases because of the Joule heating effect, thus the thermal effect in EPT would also increase.

### 6.3 Machinability Enhancement by Electropulsing Treatment

Specimens under various EPT parameters were prepared and cut with a low-speed saw into rectangle pieces of 12 mm length, and prepared for diamond turning with different parameters. A low-speed saw was used in order to prevent the high temperature induced by high-speed cutting, which would cause microstructural changes and phase transformation in the specimen, and thus distort analysis of SPDT effect. The rectangular pieces were then affixed onto columnar plates. To make certain that each specimen had the same spindle speed during the cutting process, all the pieces were fixed on the plates with the same radius. These specimens were then machined by a single point diamond turning machine (Optoform<sup>®</sup> 30).

Face turning experiments were conducted on all the three groups of electropulsed specimens, including the as-tempered specimens with static EPT, the cold-rolled specimens with static EPT and the rolling specimens with dynamic EPT. The machinability changes of the specimens induced by EPT in SPDT were studied by observing the mean cutting force and surface roughness. For the as-tempered specimens with static EPT, three groups of face turning were studied: the effect of EPT on cutting force and surface roughness in Group-A, the effect of machining parameters on cutting force and surface roughness with EPT in Group-B, and the effect of cutting speed on the microstructure evolution of machined surface in Group-C. The proposed design of the experiments is to reveal the relationship between machining, material and EPT. A schematic illustration of the diamond turning process is shown in Fig. 6.21.

In Group-A, the AZ91 specimens, after different types of EPT, including as-tempered specimens with static EPT, cold-rolled specimens with static EPT and rolling specimens with dynamic EPT, were cut with a slow speed saw into rectangular shapes (plate specimen) with length of 12 mm, width of 4 mm and height

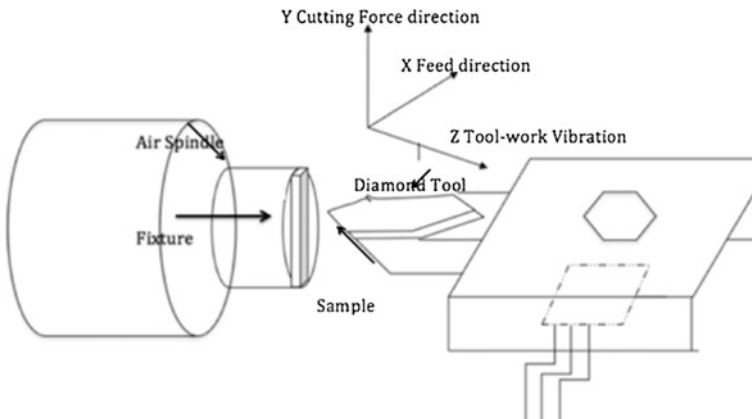
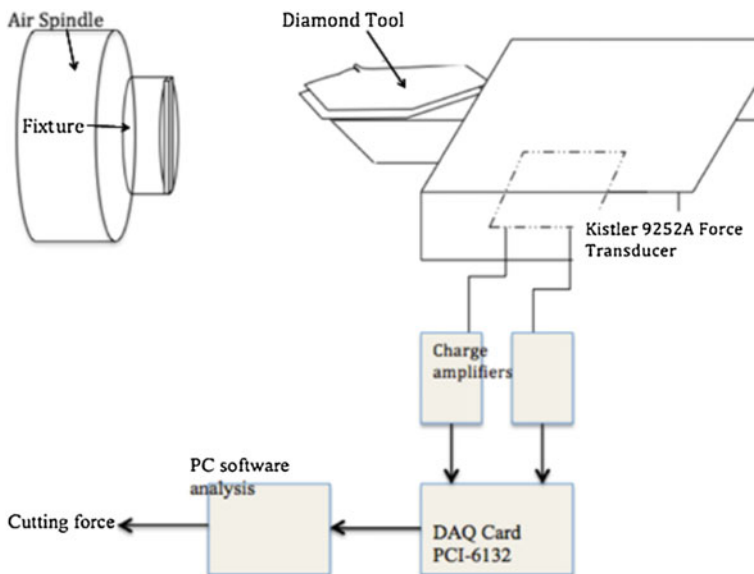


Fig. 6.21 Schematic illustration of single point diamond turning machine

**Table 6.4** Cutting conditions of Group-A for specimens with different types of EPT

EPT specimens	As-tempered with static EPT	Cold-rolled with static EPT	Rolling with dynamic EPT
Spindle speed (rpm)	8000	8000	8000
Feed rate (mm/min)	20	20	20
Depth of cut ( $\mu\text{m}$ )	20	20	20

of 1.9 mm. These plate specimens were then glued to the surface of an aluminium alloy cylinder with a radius of 12.7 mm, which would be chucked on the spindle. The cutting parameters of Group-A are listed in the Table 6.4. The tool nose radius was 2.503 mm and the rake angle was  $15^\circ$ . A force transducer, Kistler 9252A, was mounted with a pre-loaded force under the tool shank. A 14-bit multifunctional data acquisition (DAQ) card PCI-6132 (National Instrument) was configured on a PC workstation to record cutting force data (Fig. 6.22). The cutting forces during the cutting process for the specimens with various frequencies of EPT in the same group were compared, and the surface roughness changes after the cutting were discussed. The microstructures of the as-tempered specimens after turning were obtained by using SEM, and the surface roughness was measured by both the Contact Taylor Surf PGI 1230 Stylus measurement system and the Noncontact WYKO NT8000 interferometric measurement system. The chips produced in each cutting experiment were collected and images of their free surfaces were taken using JSM-6490 JEOL scanning electron microscopy.

**Fig. 6.22** Schematic illustration of cutting force measurement system

**Table 6.5** Cutting conditions of Group-B for as-tempered specimens with static EPT

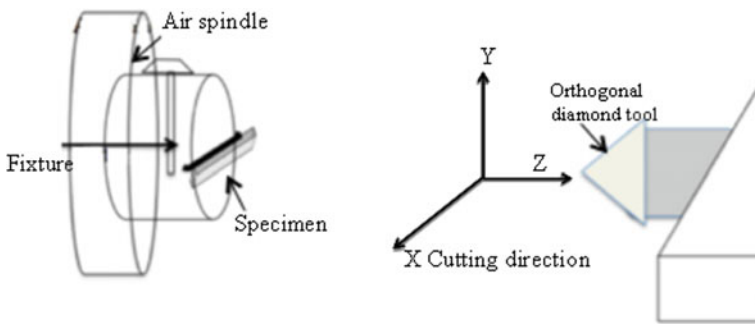
Depth of cut ( $\mu\text{m}$ )	5, 10, 20, 40
Spindle speed (rpm)	8000
Feed (mm/min)	20
Passes	3, 5, 10, 20
EPT specimen	252 Hz

**Table 6.6** Cutting conditions of Group-C for as-tempered specimens with static EPT

Cutting length (mm)	1, 3, 5
Cutting speed (mm/s)	837, 2512, 4187

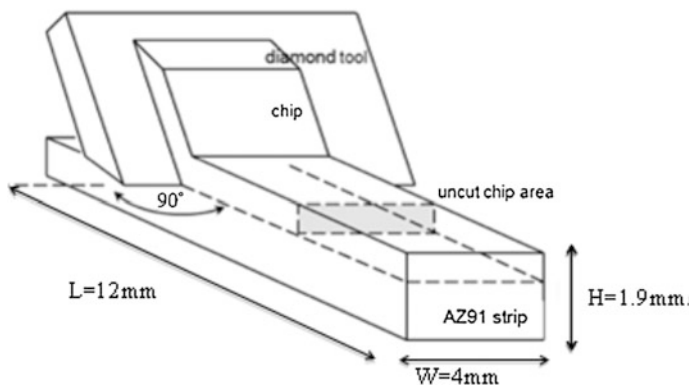
In Group-B, a fixed electropulsing parameter was selected for the as-tempered specimens to treat the work material before cutting. The depth of cut changed from 5 to 40  $\mu\text{m}$ , while keeping other cutting parameters constant. The detailed cutting conditions are listed in Table 6.5. In Group-C, the effect of cutting speed on the cutting force and microstructural changes of the specimen, was investigated on the as-tempered specimens. As the distance from centre was changed from 1 mm to 5 mm, the cutting speed changed from 837 to 4187 mm/s. Details of cutting conditions are listed in Table 6.6. The cutting parameters of the three experiments are listed in Tables 6.4, 6.5 and 6.6.

For the as-tempered specimens with static EPT, four specimens pre-treated with different frequencies of EPT were cut with a slow speed saw into rectangular shapes with length of 12 mm, width of 4 mm and thickness of 1.9 mm. The AZ91 specimens were mounted on the customised fixture as shown in Fig. 6.23. The diamond tool insert was mounted on a customised tool holder with the normal of the tool rake face parallel to the cutting direction. The parameters of straight cutting are listed in Table 6.7. The side face of specimen plates was polished to remove the oxidation layer and to ensure a straight cutting condition with a smaller thickness of about 1 mm. Its geometry is shown in Fig. 6.24. The chips were collected to examine the morphology of the side face and the tool-contact face by SEM.

**Fig. 6.23** Schematic illustration of straight cutting process

**Table 6.7** Cutting conditions of straight cutting process

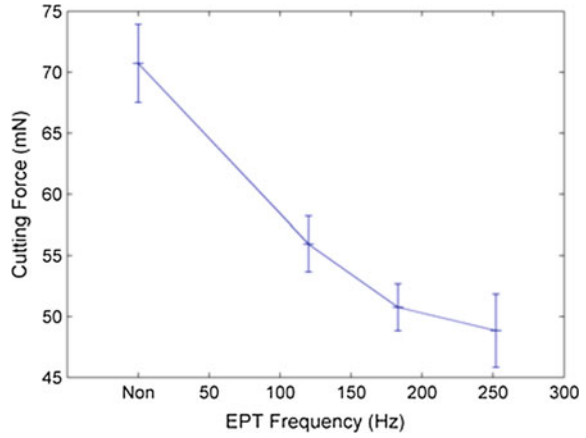
As-tempered specimens with different frequencies of static EPT	Non-EPT, 120 Hz, 183 Hz, 252 Hz
Cutting speed (mm/min)	500
Spindle speed (rpm)	0
Depth of cut ( $\mu\text{m}$ )	10
Tool nose radius (mm)	2.503

**Fig. 6.24** Schematic illustration of chip formation in straight cutting process

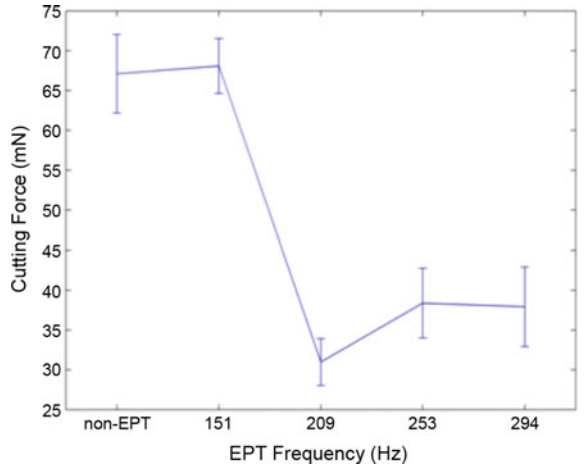
By comparing the measured values of the cutting force, the effect of EPT on cutting force can be discussed. For the as-tempered specimens with static EPT, it can be observed that when EPT frequencies increase, the cutting force under same cutting parameters decreases significantly, as shown in Fig. 6.25. With the non-EPT specimen, the mean cutting force is 70.72 mN, and when the frequency of EPT increases from 120 Hz to 183 and 252 Hz, the mean cutting force decreases from 55.92 to 50.75 mN and finally 48.84 mN, respectively. For the cold-rolled specimens with static EPT and the rolling specimens with dynamic EPT, it can also be observed that with increasing frequency of electropulsing, the cutting force decreases significantly, as shown in Figs. 6.26 and 6.27, respectively.

After the turning process, specimens with the same depth of cut, but various frequencies of EPT, were measured for surface roughness changes, using non-contact and contact measurement equipment. First, to get the surface profile data, the noncontact WYKO NT8000 was used for the reason that it would not damage the specimen surface while acquiring the profile image with sub-nanometer vertical resolution. In order to get an unbiased characterisation of the whole surface of the specimens, Contact Form Talysurf PGI1240 equipment was used to measure the surface roughness. For each specimen, seven lines with the same length of 10 mm were set as the measurement parameters to determine the surface roughness values.

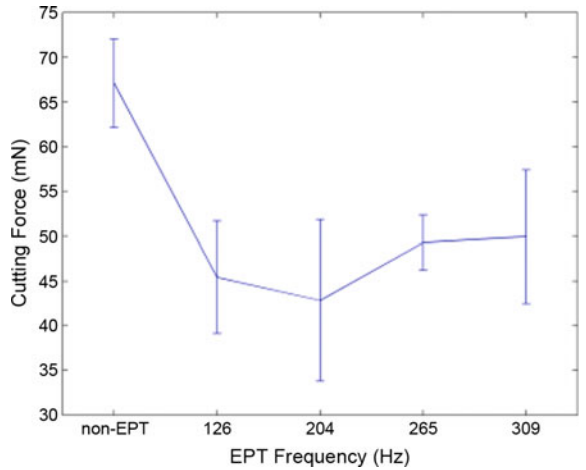
**Fig. 6.25** Mean cutting force of the as-tempered specimens under various frequencies of static EPT, with the depth of cut of 20  $\mu\text{m}$



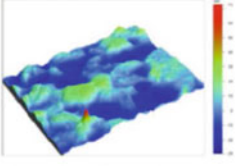
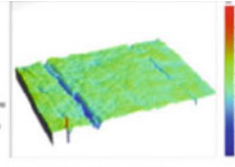
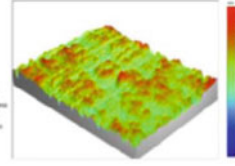
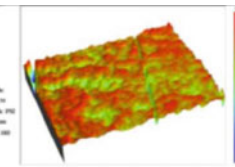
**Fig. 6.26** Mean cutting force of the cold-rolled specimens under various frequencies of static EPT (depth of cut of 20  $\mu\text{m}$ )



**Fig. 6.27** Mean cutting force of the rolling specimens under various frequencies of dynamic EPT (depth of cut 20  $\mu\text{m}$ )



**Table 6.8** Surface profiles of as-tempered specimens with various frequencies of static EPT

Non-EPT	 <p>Surface State: Ra: 9.78 nm Rq: 11.84 nm Rz: 102.87 nm</p> <p>Measurement Info: Magnification: 20.0x Measurement Mode: PWD Sampling: 400.00 um Sampling Rate: 200.00 um</p> <p><b>Ra=9.78nm Rq=11.84nm</b></p>
120 Hz	 <p>Surface State: Ra: 5.31 nm Rq: 8.36 nm Rz: 100.28 nm</p> <p>Measurement Info: Magnification: 20.0x Measurement Mode: PWD Sampling: 400.00 um Sampling Rate: 200.00 um</p> <p><b>Ra=5.31nm Rq=8.36nm</b></p>
183 Hz	 <p>Surface State: Ra: 5.48 nm Rq: 7.42 nm Rz: 70.51 nm</p> <p>Measurement Info: Magnification: 20.0x Measurement Mode: PWD Sampling: 400.00 um Sampling Rate: 200.00 um</p> <p><b>Ra=5.48 nm, Rq=7.42 nm</b></p>
252 Hz	 <p>Surface State: Ra: 5.17 nm Rq: 7.02 nm Rz: 60.47 nm</p> <p>Measurement Info: Magnification: 20.0x Measurement Mode: PWD Sampling: 400.00 um Sampling Rate: 200.00 um</p> <p><b>Ra=5.17nm, Rq=7.02nm</b></p>

For the as-tempered specimens, the surface profiles of various frequencies with static EPT under the same cutting conditions are listed in Table 6.8. It can be seen that the specimens with higher frequencies of static EPT show better surface finish, compared with the non-EPT specimen. The arithmetic roughness of the non-EPT specimen is 9.78 nm, and as the frequency of EPT increases from 120 to 183 Hz and 252 Hz, the arithmetic roughness changes from 5.31, 5.48 and 5.17 nm, respectively. The mean roughness values measured by the contact system are shown in Fig. 6.28.

The correlation between the measured mean cutting force and the surface roughness for different pre-machining electropulsing treatments is plotted in Fig. 6.29. With the non-EPT specimen, the mean cutting force in the turning process is larger than those electropulsing treated specimens, and the surface roughness after turning also shows the same trends. For the electropulsed specimens, after the 120, 183 and 252 Hz frequency of EPT, it is noticed that as the frequency increases, the mean cutting force and the surface roughness decrease. To sum up the normalised trend as shown in Fig. 6.29, the effect of EPT results in a

**Fig. 6.28** Ra and Rq changes of as-tempered specimens under various frequencies of static EPT, with the depth of cut of 20  $\mu\text{m}$

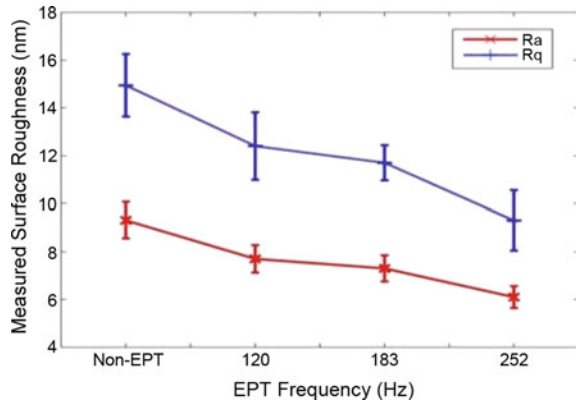
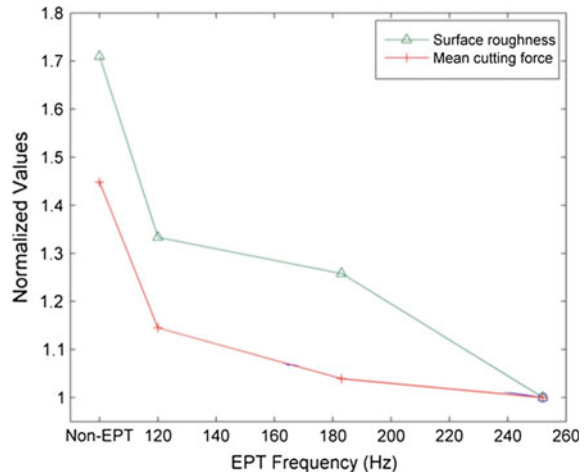


**Fig. 6.29** Correlation between mean cutting force and surface roughness of as-tempered specimens under various static EPT frequencies



decrease of the mean cutting force as well as the surface roughness. For the static EPT, and the dynamic EPT, the surface roughness by SPDT improved when the EPT frequency increased, as shown in Figs. 6.30 and 6.31.

In conclusion, with increasing frequency of electropulsing, the cutting force decreased significantly and the surface roughness improved. It was assumed that under electropulsing, large amounts of the deformation twins structure decreased, as the recrystallization was accelerated under electropulsing. The relatively homogeneous microstructure of the fine equiaxed grain structure, and the decreasing amounts of dislocation resulted in the decreasing cutting force and improving surface roughness for SPDT processing. The machinability of AZ91 alloy in SPDT was improved under EPT.

The as-tempered strip specimens without EPT (labelled as “non-EPT”) and with the EPT treatment at 252 Hz (labelled as “252 Hz-EPT”) were observed by SEM after diamond turning (Fig. 6.32). The strips were divided into three parts by



**Fig. 6.30** Surface roughness changes of cold-rolled specimens under various frequencies of static EPT with the depth of cut of 20  $\mu\text{m}$

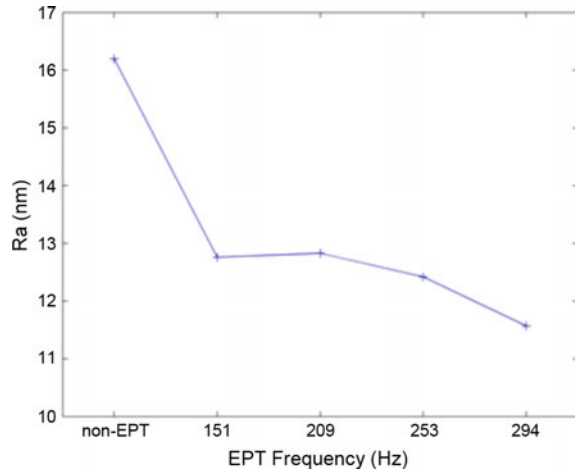
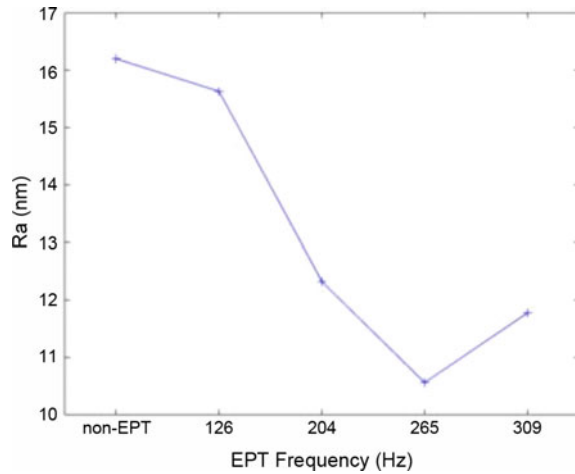


**Fig. 6.31** Surface roughness changes of rolling specimens under various frequencies of dynamic EPT with the depth of cut of 20  $\mu\text{m}$



different distances from the middle of 1, 3 and 5 mm. The applied cutting speed in the diamond turning increased with the distance from the middle of the strips. Thus, the effective cutting speeds for the three strip specimens were about 837, 2512 and 4187 mm/s, respectively. The captured SEM micrographs in the Fig. 6.32 show the shapes and forms of the  $\alpha$  phase under the non-EPT and the 252 Hz-EPT conditions.

As the cutting speed increases, the form of the  $\alpha$  phase (high-contrast strips) changes from a ball shaped mass into dispersed strips, and as the cutting speed continues to increase from  $v_2$  to  $v_3$ , the strips become more dispersed, changing from long large ones into short small ones. The direction of these strips is the same as the cutting direction; therefore, the elongated strips of the  $\alpha$  phase can be used to study the effect of microcutting on the microstructure of a machined surface.

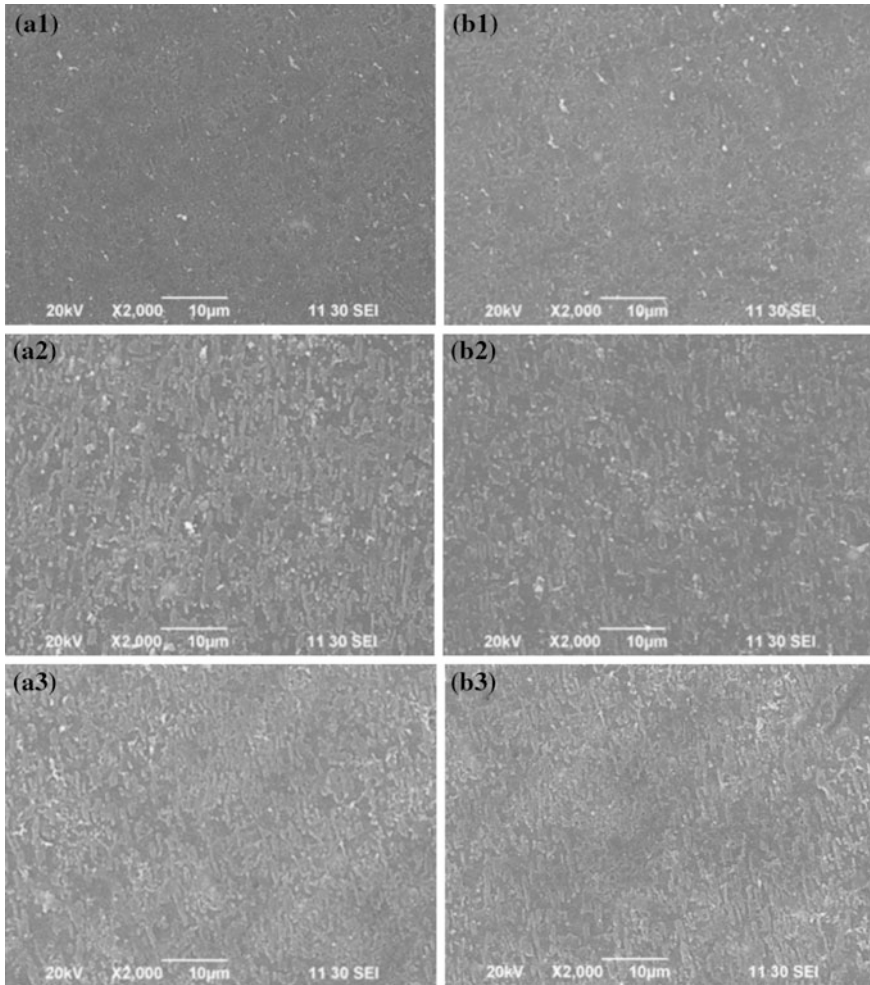


**Fig. 6.32** SEM micrographs of the as-tempered specimen under 5  $\mu\text{m}$  depth of cut with **a** non-EPT and **b** 252 Hz-EPT in different cutting speeds (1)  $v_1 = 837$  mm/s, (2)  $v_2 = 2512$  mm/s, (3)  $v_3 = 4187$  mm/s

Apart from the microstructural changes induced by the cutting speed, the experimental results indicate that a similar microstructural change occurs with different depths of cut on the workpiece material, with the EPT treatment at 252 Hz, before machining. When a small depth of cut was used (5  $\mu\text{m}$  as in Fig. 6.33a), the rubbing effect induced by the elastic deformation of the deformed layer is pronounced, which increases the tool-work friction and heat generation. Therefore, as a complex result of the heating effect and imposed strain/stress, the elongation of the  $\alpha$  phase along the cutting direction in Fig. 6.33a is more significant than that in Fig. 6.33b, where a larger depth of cut of 10  $\mu\text{m}$  is employed. At a depth of cut of

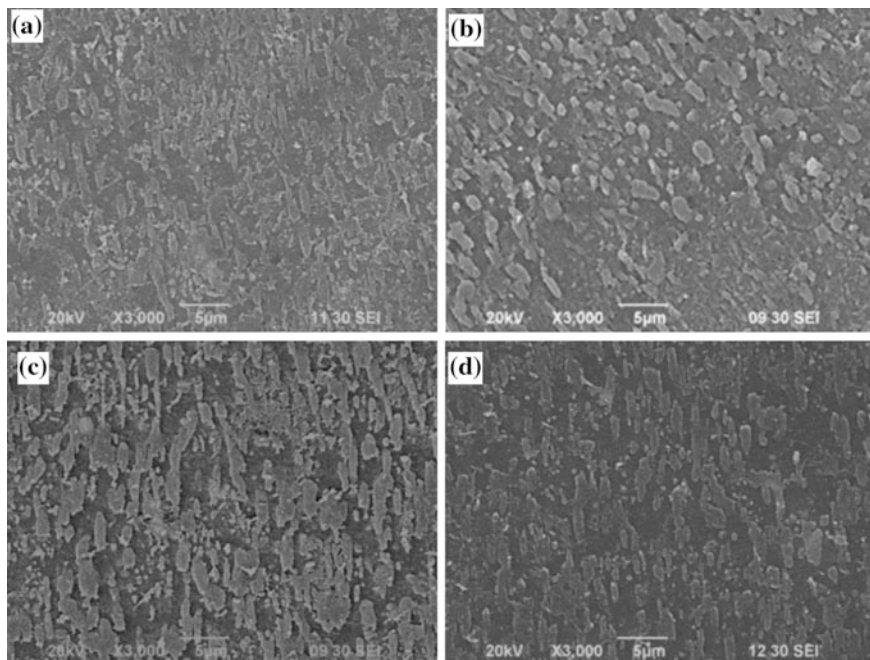


**Fig. 6.33** SEM micrographs of the 252 Hz EPT with the depth of cut **a** 5  $\mu\text{m}$ , **b** 10  $\mu\text{m}$ , **c** 20  $\mu\text{m}$ , **d** 40  $\mu\text{m}$

10  $\mu\text{m}$ , as in Fig. 6.33b, the  $\alpha$  phase starts to change from spherical to rod shape with one dimension elongated along the cutting direction. Most of the  $\alpha$  phase spheres are transformed into rod shapes, as shown in Fig. 6.33c, d, as the depth of cut increases to 15 and 20  $\mu\text{m}$ , respectively. This transformation is attributed to the imposed strain/stress field and heat generation by the friction force and plastic work induced by the micro-cutting process.

The chips during the face turning process were collected by using a vacuum pump with a philter paper on top of the inlet. The micrographs of the free surface of chips were recorded by SEM, and are shown in Fig. 6.34. It is observed that the density of the lamella layers in the serrated chips increases with increasing of EPT frequency.

Serrated chips with catastrophic shear bands are observed in the SEM micrograph of the side face of the chips produced in the straight cutting experiment, as shown in Fig. 6.35. The notation is adopted from the model proposed by Cotterell and Byrne (2008), where  $p_c$  is the distance between adjacent shear bands, and the catastrophic shear strain is expressed by  $\varepsilon_c = p_{sb}/\delta_{sb}$ , i.e. the ratio of shear band projection  $p_{sb}$  to shear band thickness  $\delta_{sb}$  as shown in Fig. 6.36.

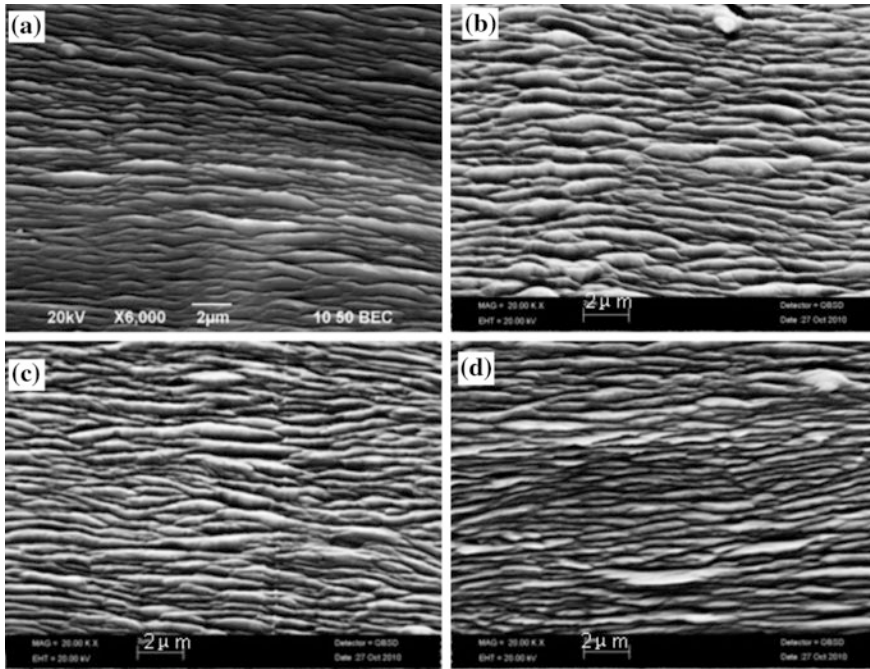


**Fig. 6.34** SEM micrographs of free surface of chips in face turning experiment under **a** non-EPT, **b** 120 Hz frequency of EPT, **c** 183 Hz frequency of EPT and **d** 252 Hz frequency of EPT

As shown in Fig. 6.37, the above stick-slip procedure takes place in the secondary deformation zone. The frictional force can further be clearly examined in the micrographs of tool-contact surface of chips in Fig. 6.38b, c. From a physical point of view, the static friction coefficient between the contact surfaces is larger than their kinetic friction coefficients. Therefore, the elastic strain builds up the larger static friction force in the location indicated by arrows in Fig. 6.38b. Eventually the elastic strain induced force overcomes the static friction or catastrophic shear bands occur to reduce the stress capacity of the chip segment in contact with the tool rake face. Both phenomena lead to an abrupt load drop on the cutting tool where the “slip” occurs, as shown in the area between the arrows in Fig. 6.38b. It can also be evidenced that the distance between adjacent static friction marks (indicated by the arrows) is about 13  $\mu\text{m}$ , which is consistent with the measured distance (as shown by  $p_c$  in Fig. 6.35d) between two neighbouring shear bands in Fig. 6.35b.

Face turning and straight cutting experiments have been conducted to study the machinability and microstructural changes with the EPT of AZ91. The work materials used in the experiments were treated with various EPT parameters. The effect of pre-machining EPT treatment on the micro-cutting process is identified by the measurement and study of surface roughness, cutting force, chip morphology and microstructural changes. The major findings in this chapter are summarised as below:

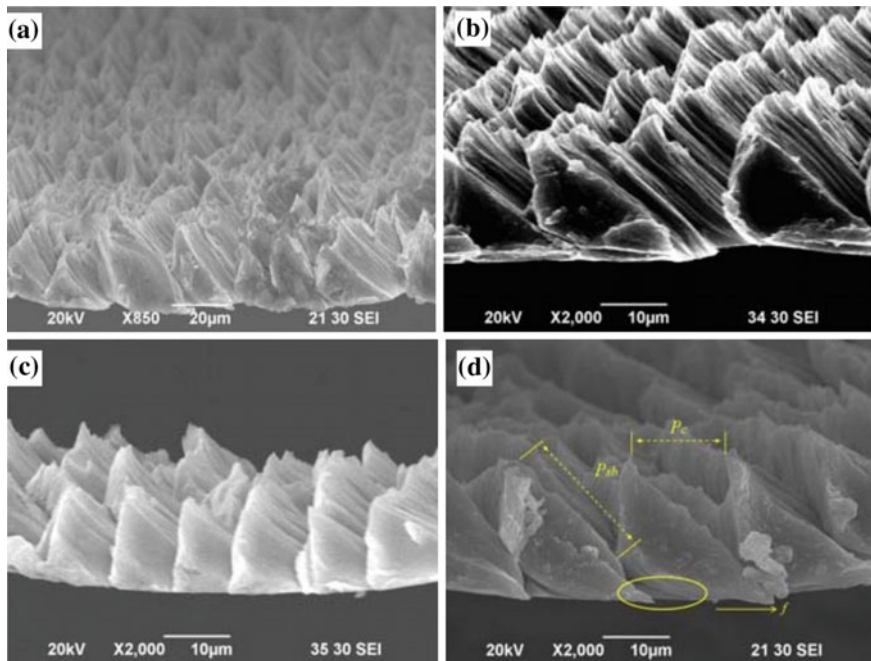
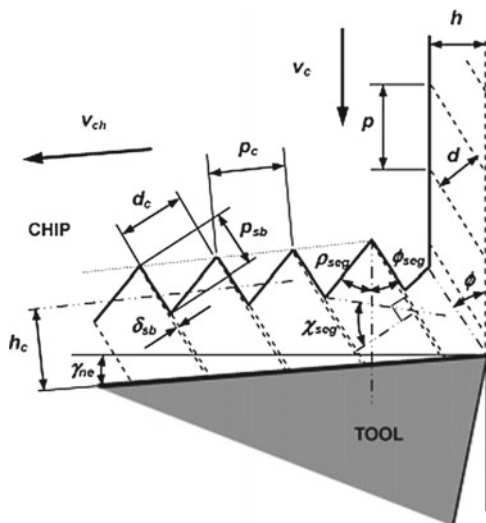


**Fig. 6.35** SEM micrographs of side face of chips in the straight cutting experiments under **a** non-EPT, **b** 120 Hz frequency of EPT, **c** 183 Hz frequency of EPT and **d** 252 Hz frequency of EPT

**Fig. 6.36** Segmented chip geometry [After Cotterell and Byrne (2008)]



$p_c$ : distance between adjacent shear bands;  $p_{sb}$ : shear band projection  
 $\delta_{sb}$ : shear band thickness;  $\epsilon_c = p_{sb} / \delta_{sb}$ : catastrophic shear strain

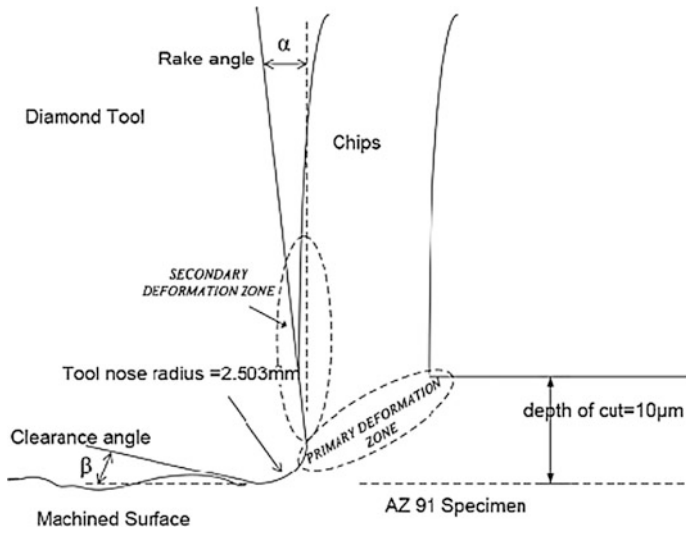


Fig. 6.37 Side view of chip morphology and principle of straight cutting

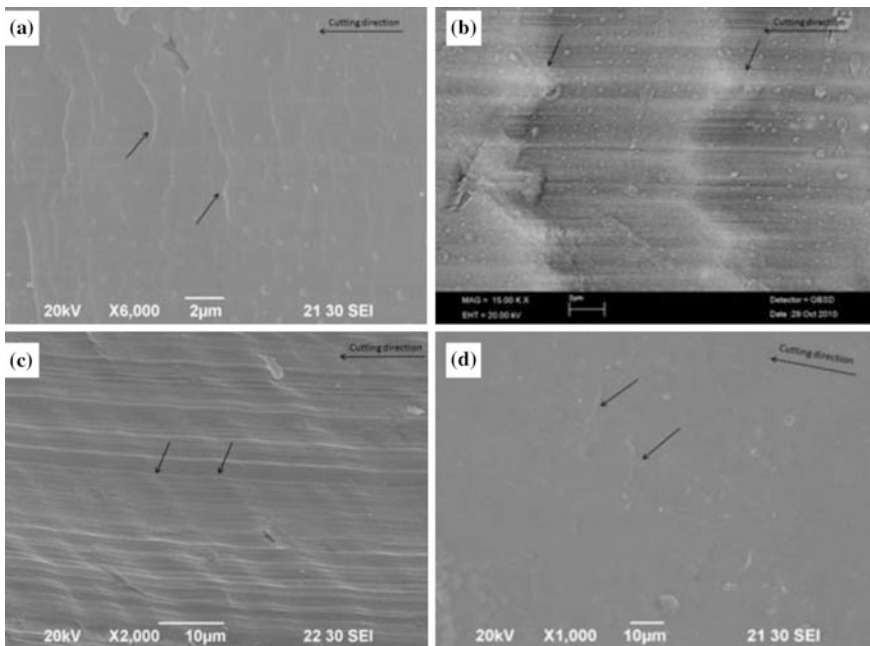


Fig. 6.38 SEM micrographs of tool-contact face of chips in straight cutting experiments under a non-EPT, b 120 Hz frequency of EPT, c 183 Hz frequency of EPT and d 252 Hz frequency of EPT

- (i) with EPT treatment, the cutting force can be significantly reduced, and the surface roughness can be improved. Consistent results can also be correlated with the EPT induced microstructural change, as described in the earlier chapters;
- (ii) on the other hand, segmented or serrated chip morphology is identified as one of the characteristics in the microcutting of as-tempered AZ91 alloy with static EPT. Differing in the serrated chips produced in the microcutting of most nonferrous materials, such as Al and Cu alloys, the shear band projection length is extremely high compared with the shear band thickness. This phenomenon can be attributed to the large elongation property of EPT treated material. In this regard, a relatively small volume of material deformation in the primary shear zone can accommodate the accumulated elastic stress in the chips; and
- (iii) the effect of super-plasticity in the treated specimen results in a seizing effect on the tool-chip interface, which results in a typical stick-slip phenomenon during chip formation.

## References

- Campbell, J., & Conrad, H. (1994). Influence of electric current on the quench aging of a low carbon steel. *Scripta Metallurgica et Materialia*, 31, 69–74.
- Cao, W. D., Lu, X. P., Sprecher, A. F., & Conrad, H. (1990). Increased hardenability of steel by an external electric field. *Materials Letters*, 9, 193–197.
- Conrad, H. (2000). Effects of electric current on solid state phase transformations in metals. *Materials Science and Engineering A*, 287, 227–273.
- Conrad, H., Cao, W. D., Lu, S. P., & Sprecher, A. F. (1989a). Effect of electric field on super-plasticity of 7475 Al. *Scripta Metallurgica*, 23, 821–824.
- Conrad, H., Cao, W. D., Lu, S. P., & Sprecher, A. F. (1991). Effect of electric field on cavitation in superplastic aluminum alloy 7475. *Materials Science and Engineering A*, 138, 247–258.
- Conrad, H., Guo, Z., & Sprecher, A. F. (1989b). Effect of an electric field on recovery and recrystallization of Al and Cu. *Scripta Metallurgica*, 23, 697–702.
- Conrad, H., Karam, N., & Mannan, S. (1983). Effect of electric current pulses in the recrystallization of copper. *Scripta Metallurgica*, 17(3), 411.
- Conrad, H., Karam, N., & Mannan, S. (1984). Effect of prior cold work on the influence of electric current pulses on the recrystallization of copper. *Scripta Metallurgica*, 18, 275–280.
- Cotterell, M., & Byrne, G. (2008). Dynamics of chip formation during straight cutting of titanium alloy Ti-6Al-4 V. *CIRP Annals-Manufacturing Technology*, 57, 93–96.
- Jiang, M. Q., & Dai, L. H. (2009). Formation mechanism of lamellar chips during machining of bulk metallic glass. *Acta Materialia*, 57, 2730–2738.
- Lloyd, J. R. (1999) Electromigration in integrated circuit conductors. *Journal of Physics D: Applied Physics* 32(17), R109–R118
- Li, S., & Conrad, H. (1998). Electric field strengthening during superplastic creep of Zn–5wt% Al: a negative electroplastic effect. *Scripta Materialia*, 39, 847–851.
- Livesey, S. J., Duan, X., Priestner, R., & Collins, J. (2001). An electroplastic effect in 31/4% silicon steel. *Scripta Materialia*, 44, 803–809.
- Mishra, R.S., Mukherjee, A. K. (2000). Electric pulse assisted rapid consolidation of ultrafine grained alumina matrix composites. *Materials Science and Engineering: A* 287(2), 178–182

- Mizubayashi, H., Kameyama, N., Hao, T. & Tanimoto, H. (2001), Crystallization under electropulsing suggesting a resonant collective motion of many atoms and modification of thermodynamic parameters in amorphous alloys, *Phys. Rev. B*, 64, 054201.
- Okazaki, K., Kagawa, M. & Aono, Y. (1967). An analysis of thermally activated flow in an Fe-0.056 at.-% Ti alloy using stress relaxation, *Z. Metallkde*, 67, 47–56.
- Qin, R., Su, S. X., Guo, J. D., He, G. H., & Zhou, B. L. (1998). Suspension effect of nanocrystalline grain growth under electropulsing. *Nanostructured Materials*, 10, 71–76.
- Qin, R., & Su, S. (2002). Thermodynamics of crack healing under electropulsing. *Journal of materials research*, 17(08), 2048–2052.
- Tang, G., Zheng, M., Zhu, Y., Zhang, J., Fang W. & Li, Q. (1998). *Iron and Steel*, 33(9), 35–37 (in Chinese).
- Tang, G., & Zhang, J. (2003). The engineering application of the electroplastic effect in the cold-drawing of stainless steel wire. *Journal of Materials Processing Technology*, 137, 96–99.
- Tang, G., Zhang, J., Zheng, M., Zhang, J., Fang, W., & Li, Q. (2000). Experimental study of electroplastic effect on stainless steel wire 304L. *Materials Science and Engineering A*, 281, 263–267.
- Teng, G., Chao, Y., Dong, L., Geng, Y., & Lai, Z. (1996). Features of nanocrystallization of metallic glass fe 78b 13si 9 induced by high-current-density electropulsing. *Japanese journal of applied physics*, 35(10R), 5320–5325.
- To, S., Zhu, Y. H., Lee, W. B., Liu, X. M., Jiang, Y. B., & Tang, G. Y. (2009). Effect of current density on electropulsing induced phase transformations in a Zn-Al based alloy. *Applied Physics A*, 96(4), 939–944.
- Troitskii, O. A., & Likhtman, V. I. (1963, January). The anisotropy of the action of electron- and  $\gamma$ -radiation on the deformation process of brittle zinc single crystals. In *Dokl. Akad. Nauk SSR* (Vol. 148). , USSR: Inst. of Physics and Chemistry, Academy of Sciences
- Troitskii, O.A., & Savenko, V.S. (1986). Multi-stage electroplastic drawing of copper wire. *Russian Metallurgy*, 5, 96–98
- Xiao, S. H., Guo, J. D., & Li, S. X. (2002). The effect of electropulsing on dislocation structures in [233] coplanar double-slip-oriented fatigued copper single crystals. *Philosophical Magazine Letters*, 82, 617–622.
- Yang, D., & Conrad, H. (2001). Exploratory study into the effects of an electric field and of high current density electropulsing on the plastic deformation of TiAl. *Intermetallics*, 9, 943–947.
- Yao, K. F., Wang, J., Zheng, M., Yu, P., & Zhang, H. (2001a). A research on electroplastic effects in wire-drawing process of an austenitic stainless steel. *Scripta Materialia*, 45(5), 533–539.
- Yao, K., Yu, P., & Wang, J. (2001b). Effects of high-density current pulses on work hardening behaviors of austenite stainless steel in wire-drawing deformation. *Acta Metallurgica Sinica (English Letters)*, 14(5), 341–346.
- Zhou, Y., Guo, J., Gao, M., & He, G. (2004). Crack healing in a steel by using electropulsing technique. *Material Letters*, 58, 1732–1736.
- Zhou, Y., Qiao, D., He, G., & Guo, J. (2003). Improvement of mechanical properties in a saw blade by electropulsing treatment. *Material Letters*, 57, 1566–1570.
- Zhu, Y. H., To, S., Lee, W. B., Liu, X. M., Jiang, Y. B., & Tang, G. Y. (2009a). Effects of dynamic electropulsing on microstructure and elongation of a Zn-Al alloy. *Materials Science and Engineering A*, 501(1–2), 125–132.
- Zhu, Y. H., To, S., Lee, W. B., Liu, X. M., Jiang, Y. B., & Tang, G. Y. (2009b). Electropulsing induced phase transformation in a Zn-Al based alloy. *Journal of Material Research*, 24(8), 2661–2669.



# Chapter 7

## Microplasticity Analysis for Materials Characterisation

**Abstract** During the last few decades, much research work has been done to develop accurate tool force models for studying the characteristics of the cutting process in ultraprecision machining based on the concept of shear angles in the chip formation, the fluctuation of which leads to fluctuation of the deformed chip thickness and hence the cutting forces. A microplasticity model is developed in this chapter to analyse the variation of the shear angle and hence the cutting force in ultraprecision diamond turning. The model took into account the effect of material anisotropy due to the changing crystallographic orientation of the workpiece being cut and a spectrum analysis technique is deployed to reveal the features of the cutting force patterns. A series of cutting experiments was conducted on a single crystal with different crystallographic cutting plane normals. The complexity of the shear angle formation is further revealed by a microstructural analysis of the chip cross-sections showing plasticity by means of scanning electron micrographs.

### 7.1 Shear Angle and Micro-Cutting Force Prediction

#### 7.1.1 *Microplasticity Model for Shear Angle Prediction*

A shear angle relationship generally has the form of

$$f(\phi, \alpha, \beta, \lambda) = 0, \tag{7.1}$$

where  $\phi$ ,  $\alpha$  and  $\beta$  are the shear angle, rake angle and friction angle respectively,  $\lambda$  is a material factor which is not considered in the continuum solution of conventional machining. In the analysis, the following assumptions are made: (1) plane strain orthogonal cutting is used, (2) the rake angle is zero and the tool is sharp, (3) the tool is perfectly lubricated and there is no shear on the rake face and (4) the workpiece is a good conductor of heat and cutting is performed under isothermal conditions.

In the microplasticity model, the basic cutting mechanism that occurs in ultraprecision diamond turning of a polycrystalline aggregate is considered to be similar

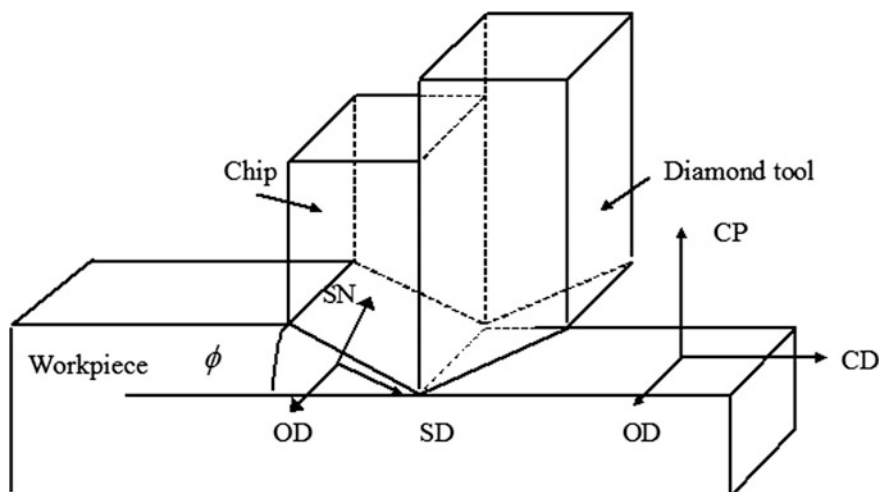
to that in the machining of a single crystal. During machining, the tool tip acts as a strong source of dislocations. Fine cracks are produced near the vicinity of the tool tip and trigger the primary shearing process. As the tool advances, the material ahead of the tool is compressed in the cutting direction and a shear band joining the top of the tool and the surface of the work material develops. The effect of ploughing and sliding due to tool edge radius is ignored. The deformation is considered to be accomplished by the crystallographic slip only. Equal hardening of the slip systems is assumed. A large plastic deformation in the shear zone is treated as a succession of incremental plastic incompressible strains and the workpiece material is assumed to be rigidly plastic and incompressible.

Referring to the workpiece coordinate system (CD-CP-OD) as shown in Fig. 7.1, the symmetric strain tensor in the shear band,  $\varepsilon_w$ , is given by:

$$\varepsilon_w = d\tau/2 \begin{bmatrix} \sin 2\phi & 0 & \cos 2\phi \\ 0 & 0 & 0 \\ \cos 2\phi & 0 & -\sin 2\phi \end{bmatrix}, \quad (7.2)$$

where  $d\tau$  is the shear strain in the shear band.

The crystallographic orientation of the crystal is represented by the Miller indices such that  $(hkl)$  is parallel to the cutting direction and  $[uvw]$  is parallel to the



$\phi$  = shear angle

Workpiece coordinate system:

CD = Cutting direction

CP = Cutting plane normal

OD = Observation direction

Shear band coordinate system:

SD = Shear direction

SN = Shear plane normal

OD = Observation direction

Fig. 7.1 The co-ordinate system for the cutting geometry

normal to the cutting plane. The imposed strain tensor,  $\varepsilon_w$ , is transformed from the workpiece coordinate system (CD-CP-OD) to the crystallographic axis of the crystal where the crystallographic slip system is based, i.e.

$$\varepsilon_c = \mathbf{P}\varepsilon_w\mathbf{P}^T, \quad (7.3)$$

where  $\varepsilon_c$  is the strain tensor referred to the cube axes of the crystal,  $\mathbf{P}$  is the transformation matrix and  $\mathbf{P}^T$  is its transpose.

$$\mathbf{P} = \begin{bmatrix} r_1 & u_1 & n_1 \\ r_2 & u_2 & n_2 \\ r_3 & u_3 & n_3 \end{bmatrix}, \quad (7.4)$$

where

$$r_1 = \frac{u}{\sqrt{u^2 + v^2 + w^2}}, \quad r_2 = \frac{v}{\sqrt{u^2 + v^2 + w^2}}, \quad r_3 = \frac{w}{\sqrt{u^2 + v^2 + w^2}} \quad (7.5)$$

$$n_1 = \frac{h}{\sqrt{h^2 + k^2 + l^2}}, \quad n_2 = \frac{k}{\sqrt{h^2 + k^2 + l^2}}, \quad n_3 = \frac{l}{\sqrt{h^2 + k^2 + l^2}} \quad (7.6)$$

$$u_1 = n_2r_3 - n_3r_2, \quad u_2 = n_3r_1 - n_1r_3, \quad u_3 = n_1r_2 - n_2r_1. \quad (7.7)$$

The increment of plastic work done during deformation  $dW$  is given by:

$$dW = \sigma d\varepsilon_w, \quad (7.8)$$

where  $\sigma$  is the equivalent stress or the plastic work per unit volume and strain, and  $d\varepsilon_w$  is the macroscopic effective strain.  $\phi$  coincides with the direction of the maximum shear stress and makes an angle of  $45^\circ$  with the cutting direction. If the shear angle deviates from  $45^\circ$  by an angle  $\psi$ , the shear strain in the shear band will be increased by a factor of  $1/\cos 2\psi$  in order to produce the same amount of macroscopic deformation. The shear band will occur at an angle  $\phi$  such that the plastic work done in deforming the metal will be the minimum. It should be noted that the shear band is macroscopic in nature and the shear band may not be parallel to a particular crystallographic slip plane of the crystal. However, the shear in the band has to be accomplished by a homogeneously distributed slip, i.e. all alternative slip systems co-operate in the shear band development. Hence the Taylor model of polycrystalline plasticity can be applied for the analysis of the shear band formation. The virtual work equation for deforming a single crystal can be written as:

$$\sigma d\varepsilon_w = \tau_c d\Gamma, \quad (7.9)$$

where  $d\Gamma$  is the total dislocation shear strain accumulated in the crystal and  $\tau_c$  is the critical resolved shear stress on the active slip systems.

The effective strain  $d\varepsilon_w$  is related to the total dislocation shear strain by the Taylor factor  $M$ , i.e.

$$M = \frac{d\Gamma}{d\varepsilon_w} \quad (7.10)$$

and

$$\sigma = M\tau_c. \quad (7.11)$$

The Taylor factor  $M$  is a dimensionless number that is sensitive to the crystallographic orientation of the material being cut. It is often used as an index of plastic anisotropy—the extent to which the strength  $\sigma$  of a crystal varies with crystallographic orientation for a given critical shear stress  $\tau_c$ . A large value of  $M$  indicates a large shear strength of the crystal being cut and hence the cutting force. Any variation in shear strength will cause a fluctuation in cutting force.  $M$  is calculated according to the maximum work principle of Bishop and Hill (1951) which states that the state of actual stress  $\sigma_{ij}$  required to cause a given increment of strain  $d\varepsilon_{ij}$  is the one that maximises the work done during deformation  $dW$ . Referring the stress and the strain to the cubic axes, the plastic work done,  $dW$ , during deformation is given by:

$$dW = -Bd\varepsilon_{11(c)} + Ad\varepsilon_{22(c)} + 2Fd\varepsilon_{23(c)} + 2Gd\varepsilon_{13(c)} + 2Hd\varepsilon_{12(c)}, \quad (7.12)$$

where  $A = (\sigma_{22(c)} - \sigma_{33(c)})/\sqrt{6}\tau_c$ ,  $B = (\sigma_{33(c)} - \sigma_{11(c)})/\sqrt{6}\tau_c$ ,  $F = \sigma_{23(c)}/\sqrt{6}\tau_c$ ,  $G = \sigma_{13(c)}/\sqrt{6}\tau_c$ ,  $H = \sigma_{12(c)}/\sqrt{6}\tau_c$ .

The work done is calculated for all 56 possible stress states and the one whose work done value is the highest becomes the yield stress state (Reid 1973). The Taylor factor  $M$  can be determined by substituting the calculated value of maximum work done  $dW$  into the following equation:

$$M = \frac{dW}{(\tau_c d\varepsilon_{ij(c)})}. \quad (7.13)$$

Since the resolved shear stress on the inclined plane varies as  $1/\cos 2\psi$  from the  $45^\circ$  plane, an effective Taylor factor  $M'$  is defined as  $M/\cos 2\psi$ . In the early simple model developed by Lee (1990), the shear angle was taken to be one at which the effective Taylor factor was at a minimum. However, the variation of the effective Taylor factor  $M'$  with shear angle is often associated with a plateau and a range of shear angles is then possible based on the principle of minimum work alone. The drawback of this uncertainty can be removed if the load instability criterion is imposed. A shear band will form as:

$$\frac{1}{\sigma} \frac{d\sigma}{d\varepsilon_w} = \frac{1}{M} \frac{dM}{d\varepsilon_w} + \frac{M}{\tau_c} \frac{d\tau_c}{d\Gamma} \leq 0. \quad (7.14)$$

$(1/M)(dM/d\varepsilon_w)$  depends on the rate of change of the crystallographic orientation of the material with strain, and is called the texture softening factor  $S$  if it is negative, or the texture hardening factor if it is positive. The second term  $(M/\tau_c)(d\tau_c/d\Gamma)$  represents the slip plane hardening contribution which is usually positive. Hence, a shear band will develop when  $(1/M)(dM/d\varepsilon_w)$  is the most negative. The above analysis can be extended to a polycrystalline material. When more than one grain is considered,  $M$  will be averaged over all grain orientations being considered.

## 7.1.2 Texture Softening Factor

### 7.1.2.1 Selection of Active Set of Slip Systems

The shear strain in the band has to be accomplished by the slip systems co-operating in the development of the shear band. For a crystal to undergo an arbitrary plastic strain or deformation by slip, five independent slip systems (represented in terms of the slip direction  $\mathbf{b}$  and a slip plane normal  $\mathbf{n}$ ) are needed. In face-centred cubic (FCC) crystals, the (111) [110] family of slip systems is dominant. The labels of the slip systems for the (111) [110] family of slip systems are tabulated in Table 6.1. Taking the system  $a_1$  as an example, the slip plane normal and the slip direction are  $\mathbf{n} = 1/\sqrt{3}, 1/\sqrt{3}, 1/\sqrt{3}$  and  $\mathbf{b} = 0, 1/\sqrt{2}, -1/\sqrt{2}$  respectively. Reid (1973) has summarised the possible slip systems for the stress states of the (111) [110] family.

For fcc crystal structures, there are many ways of choosing an active set of five independent systems from the total number of possible slip systems. Taylor (Reid 1973) postulated that the preferred set of slip systems will be that for which the sum of the shears on each system is a minimum. As a slip system is operating, it is assumed that the shear stress acting on the system is equal to the critical resolved shear stress  $\tau_c$  for slip. In order to simplify the calculation, the critical resolved shear stress  $\tau_c$  is put to be  $1/\sqrt{6}$  arbitrary units. Suppose that a small increment of strain represented by  $[\varepsilon]$  is imposed on a crystal, this is related to the shears  $[\gamma]$  that would be required for a given set of five independent slip systems to accomplish the strain as follows:

$$[\varepsilon] = [E][\gamma], \quad (7.15)$$

where  $[E]$  are the direction cosines of the five slip systems. Equation (7.14) can be written in full as:

$$\begin{pmatrix} \epsilon_{22(c)} \\ \epsilon_{33(c)} \\ 2\epsilon_{23(c)} \\ 2\epsilon_{13(c)} \\ 2\epsilon_{12(c)} \end{pmatrix} = \begin{pmatrix} (n_2^1 b_2^1) & (n_2^2 b_2^2) & (n_2^3 b_2^3) & (n_2^4 b_2^4) & (n_2^5 b_2^5) \\ (n_3^1 b_3^1) & (n_3^2 b_3^2) & (n_3^3 b_3^3) & (n_3^4 b_3^4) & (n_3^5 b_3^5) \\ (n_3^1 b_3^1 + n_3^1 b_2^1) & (n_3^2 b_3^2 + n_3^2 b_2^2) & (n_3^3 b_3^3 + n_3^3 b_2^3) & (n_3^4 b_3^4 + n_3^4 b_2^4) & (n_3^5 b_3^5 + n_3^5 b_2^5) \\ (n_1^1 b_1^1 + n_1^1 b_2^1) & (n_1^2 b_1^2 + n_1^2 b_2^2) & (n_1^3 b_1^3 + n_1^3 b_2^3) & (n_1^4 b_1^4 + n_1^4 b_2^4) & (n_1^5 b_1^5 + n_1^5 b_2^5) \\ (n_1^1 b_2^1 + n_1^1 b_1^1) & (n_1^2 b_2^2 + n_1^2 b_1^2) & (n_1^3 b_2^3 + n_1^3 b_1^3) & (n_1^4 b_2^4 + n_1^4 b_1^4) & (n_1^5 b_2^5 + n_1^5 b_1^5) \end{pmatrix} \begin{pmatrix} \gamma_1 \\ \gamma_2 \\ \gamma_3 \\ \gamma_4 \\ \gamma_5 \end{pmatrix} \quad (7.16)$$

In the notation used, the superscript indicates the referred slip system and is not a power. In order to have the five slip systems to be independent, the inverse of  $[E]$  or  $[E^{-1}]$  must exist, and this requires the determinant of  $[E]$  or  $|E|$  to be non-zero. Equation (7.16) can be uniquely solved for the shears as:

$$[\gamma] = [E^{-1}][\epsilon] \quad (7.17)$$

According to the Taylor criterion (Reid 1973), the work done  $\delta w$  in activating the preferred set of slip systems is less than that of all other sets of systems that could geometrically accomplish the strain, i.e.

$$\delta w = \tau_c \sum \delta \gamma, \quad (7.18)$$

where the summation sign denotes the sum of the incremental shears, on each of the five independent systems of a set. In other words, the sum of the total shears  $\sum \gamma$  as determined by Eq. (7.17) should be the minimum. The Taylor criterion provides one possible way to predict the set of slip systems which will actually operate while the strain is being imposed (Table 7.1).

Bishop and Hill have proposed another principle for the prediction of active slip system, stating that in the deformation of a single crystal, the actual stress corresponding to a given strain is not less than any other stress that satisfies the yielding conditions (Reid 1973). In other words, the state of stress giving the maximum value of  $dW$  in Eq. (7.12) will actually motivate the strain. Bishop and Hill's Principle of Maximum Work criterion has been reported to give the same results as the Taylor criterion in the prediction of the active set of slip systems (Reid 1973). When considering (111) [110] slip, the Bishop and Hill criterion has the advantage that the maximum of only 56 stress states is sought, whereas the minimum of 384 stress states is required in the Taylor criterion.

**Table 7.1** Labels for the slip systems

Slip plane, $\mathbf{n}$	111			$\bar{1}\bar{1}\bar{1}$			$\bar{1}\bar{1}1$			111		
Slip direction, $\mathbf{b}$	01 $\bar{1}$	$\bar{1}01$	$\bar{1}\bar{1}0$	0 $\bar{1}\bar{1}$	101	$\bar{1}10$	01 $\bar{1}$	101	$\bar{1}\bar{1}0$	0 $\bar{1}\bar{1}$	$\bar{1}01$	110
Slip system	$a_1$	$a_2$	$a_3$	$b_1$	$b_2$	$b_3$	$c_1$	$c_2$	$c_3$	$d_1$	$d_2$	$d_3$

However, ambiguities still exist in the selection of active slip systems based on the Bishop and Hill criterion since the selected stress states give either five out of six or five out of eight possible combinations of slip systems for accomplishing a given strain. The ambiguity in identifying the set of five slip systems is resolved in the present study by selecting the set of active slip systems which minimises the second-order plastic work as proposed in (Lee and Chan 1990). In this method, an infinitesimal strain is applied to each possible set of the slip systems, leading to a small crystal rotation. For a given imposed strain state, the second-order plastic work  $dW'$  for each possible combination of slip system can be determined from:

$$dW = \sigma_{ij} d\epsilon_{ij}, \quad (7.19)$$

where  $\sigma_{ij}$  and  $d\epsilon_{ij}$  are the new stress and strain components, respectively, due to the rotation and the strain hardening of the crystal. The set of active slip systems which corresponds to the minimum second-order plastic work will then be selected.

### 7.1.2.2 Determination of Texture Softening Factor

The texture softening factor  $S$  is computed numerically by determining the rate of lattice rotation ( $d\Omega/d\epsilon_w$ ) and the associated change in the Taylor factor ( $dM/d\Omega$ ) as follows:

$$S = \frac{1}{M} \frac{d\Omega}{d\epsilon_w} \frac{dM}{d\Omega}. \quad (7.20)$$

Suppose an infinitesimal strain  $[\epsilon']$  is applied to the active set of slip systems determined. The strain components of  $[\epsilon']$  are related to the active set of five independent slip systems by

$$[\epsilon] = [E][\gamma] \quad (7.21)$$

$$\begin{pmatrix} \epsilon_{22} \\ \epsilon_{33} \\ 2\epsilon_{23} \\ 2\epsilon_{13} \\ 2\epsilon_{12} \end{pmatrix} = [E] \begin{pmatrix} \gamma^1 \\ \gamma^2 \\ \gamma^3 \\ \gamma^4 \\ \gamma^5 \end{pmatrix}, \quad (7.22)$$

where  $[E]$  is a square matrix that denotes the direction cosines of the selected active slip systems with respect to the cube axes of the crystal. The value of the shears on each slip system can be obtained by rewriting Eq. (6.21) as:

$$[\gamma] = [E^{-1}][\varepsilon] \quad (7.23)$$

The shear  $[\gamma]$  will cause lattice rotation and the lattice rotation tensor  $\mathbf{W}$  is given by:

$$\begin{aligned} \mathbf{W} &= \begin{pmatrix} \omega_{11} & \omega_{12} & \omega_{13} \\ \omega_{21} & \omega_{22} & \omega_{23} \\ \omega_{31} & \omega_{32} & \omega_{33} \end{pmatrix} \\ &= \frac{1}{2} \sum_{s=1}^5 \begin{pmatrix} 0 & (b_1^s n_2^s - b_2^s n_1^s) \gamma^s & (b_1^s n_3^s - b_3^s n_1^s) \gamma^s \\ (b_2^s n_1^s - b_1^s n_2^s) \gamma^s & 0 & (b_2^s n_3^s - b_3^s n_2^s) \gamma^s \\ (b_3^s n_1^s - b_1^s n_3^s) \gamma^s & (b_3^s n_2^s - b_2^s n_3^s) \gamma^s & 0 \end{pmatrix} \end{aligned} \quad (7.24)$$

Assume the initial orientation of the lattice to be  $\mathbf{P}$  as given in Eq. (7.4) and the shears will cause the crystal to rotate to a new orientation  $\mathbf{P}'$  given by:

$$\mathbf{P}' = (\mathbf{I} - \mathbf{W})\mathbf{P}, \quad (7.25)$$

where  $\mathbf{I}$  is the unit matrix.

The net rotation  $d\Omega$  can be determined by:

$$d\Omega = \sqrt{\omega_{12}^2 + \omega_{13}^2 + \omega_{23}^2}. \quad (7.26)$$

Referring the stress and the strain to the cubic axes, the plastic work done,  $dW$ , during this deformation is given by:

$$dW = -Bd\varepsilon_{11(c)} + Ad\varepsilon_{22(c)} + 2Fd\varepsilon_{23(c)} + 2Gd\varepsilon_{13(c)} + 2Hd\varepsilon_{12(c)}. \quad (7.27)$$

The corresponding change in Taylor factor  $dM$  can be determined by substituting the calculated value of maximum work done  $dW$  into the following equation:

$$dM = \frac{dW}{(\tau_c d\varepsilon_{ij(c)})} \quad (7.28)$$

Hence, the Texture Softening Factor  $S$  can be determined by Eqs. (7.13), (7.20), (7.26) and (7.28).

### 7.1.3 Criterion for Shear Angle Prediction

Figure 7.2 shows a flow chart for the selection criterion for the most probable shear angle. The criterion is based on the combination of the effective Taylor factor  $M'$ ,



the number of slip systems and the texture softening factor in sequence until a unique solution is obtained.

In order to predict the most likely shear angles, the minimum  $M'$  is calculated first. Should a range of shear angles all possess the same minimum  $M'$ , then the one with both minimum  $M'$  and the smallest number of slip systems will be selected. If

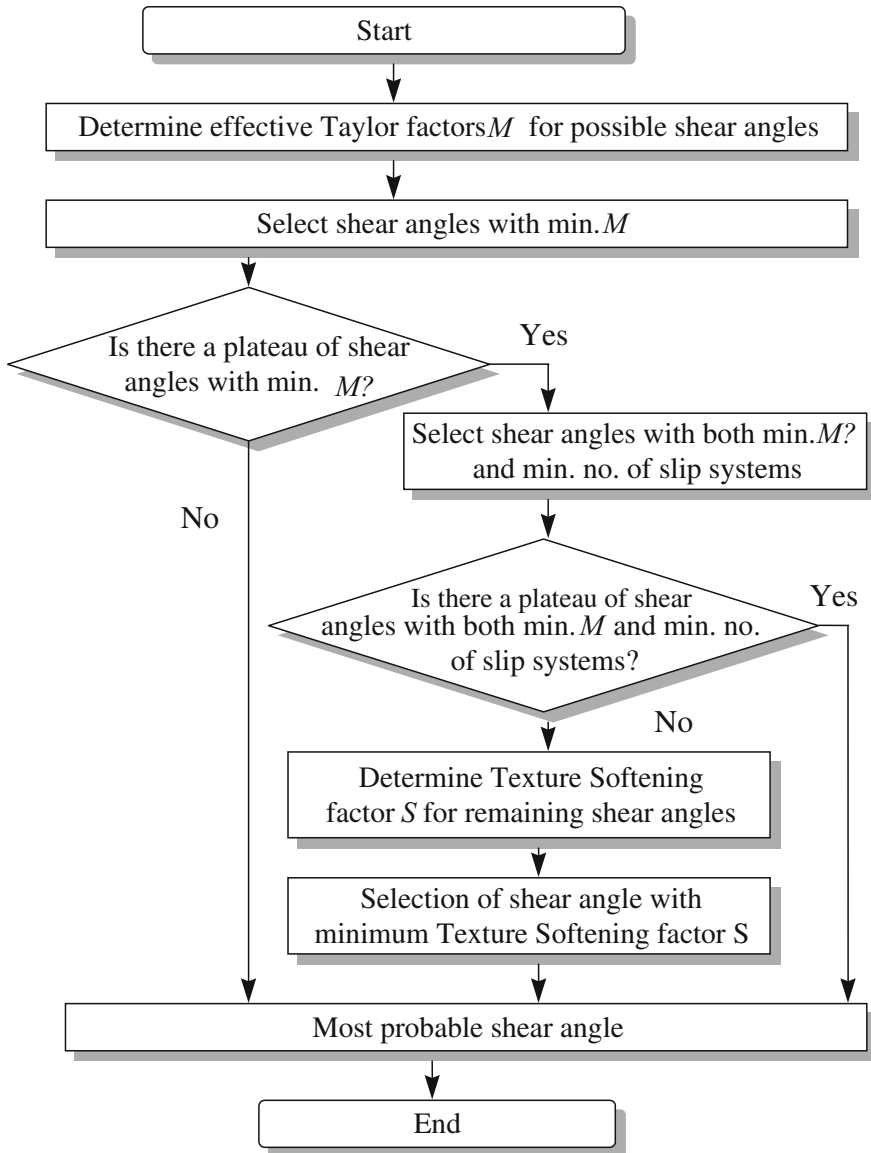


Fig. 7.2 Flow chart for the selection of the most probable shear angle

there is still no unique shear angle, the one with the minimum  $M'$ , the smallest number of slip systems and with the smallest Taylor Softening Factor  $S$  will be the most likely shear angle. The input to the program is the crystallographic orientation, its volume fraction (one for single crystal), deformation tensor and the output is the selected shear angle.

### 7.1.4 Prediction of Micro-Cutting Forces Variation

Figure 7.3 shows the various force components and their relationships in orthogonal cutting.  $F_c$  and  $F_t$  are the cutting and thrust forces that are parallel and perpendicular to the motion of the tool, respectively.  $F_s$  is the shear force component parallel to the shear plane while  $F_R$  is the resulting cutting force. From Fig. 6.3, the relationships of the cutting forces can be derived as follows:

$$F_s = F_R \cos(\phi + \beta - \alpha) \quad (7.29)$$

$$F_s = \tau_s A_s = \frac{\tau_s A_c}{\sin \phi}, \quad (7.30)$$

where  $A_s$  is the area of shear plane,  $A_c$  is the area of the undeformed chip section,  $\phi$  is the shear angle,  $\alpha$  is the rake angle of the diamond tool,  $\tau_s$  is the shear stress of the single crystal. From Eqs. (7.29) and (7.30),

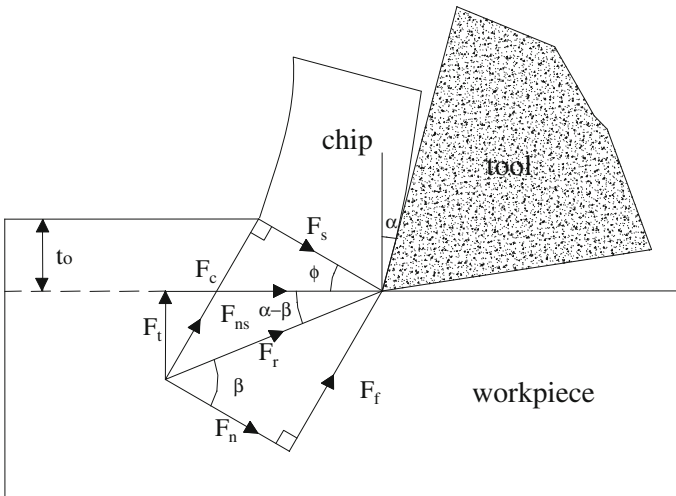


Fig. 7.3 Cutting force diagrams

$$F_R = \frac{\tau_s A_c}{\sin \phi \cos(\phi + \beta - \alpha)} \cdot 1 \quad (7.31)$$

Referring to the cutting geometry shown in Fig. 7.3,

$$F_c = F_R \cos(\beta - \alpha) \quad (7.32)$$

$$F_t = F_R \sin(\beta - \alpha) \quad (7.33)$$

In the above equations,  $\phi$  varies with the changing cutting direction, and  $\beta$  is found to be small and varies for different crystallographic orientations. The friction angle can be approximated as fairly constant for a given tool and the workpiece configuration and for a given cutting velocity. From Eqs. (7.31) to (7.33) and the shear angle calculated from the microplasticity model, the corresponding cutting force,  $F_c$ , and the thrust force,  $F_t$ , can be derived as below:

$$F_c = \frac{\tau_s A_c \cdot \cos(\beta - \alpha)}{\sin \phi \cdot \cos(\phi + \beta - \alpha)} \quad (7.34)$$

$$F_t = \frac{\tau_s A_c \cdot \sin(\beta - \alpha)}{\sin \phi \cdot \cos(\phi + \beta - \alpha)}, \quad (7.35)$$

where  $\phi$  is the shear angle that is determined by the microplasticity model. The friction angle  $\beta$  between the tool and the chip material is determined from the coefficient of tool face friction  $\mu$  as:

$$\beta = \tan^{-1}(\mu). \quad (7.36)$$

When the rake angle is zero, Eqs. (7.34) and (7.35) are reduced to the following:

$$F_c = \frac{\tau A_c \cdot \cos \beta}{\sin \phi \cdot \cos(\phi + \beta)} \quad (7.37)$$

$$F_t = \frac{\tau A \cdot \sin \beta}{\sin \phi \cdot \cos(\phi + \beta)} \quad (7.38)$$

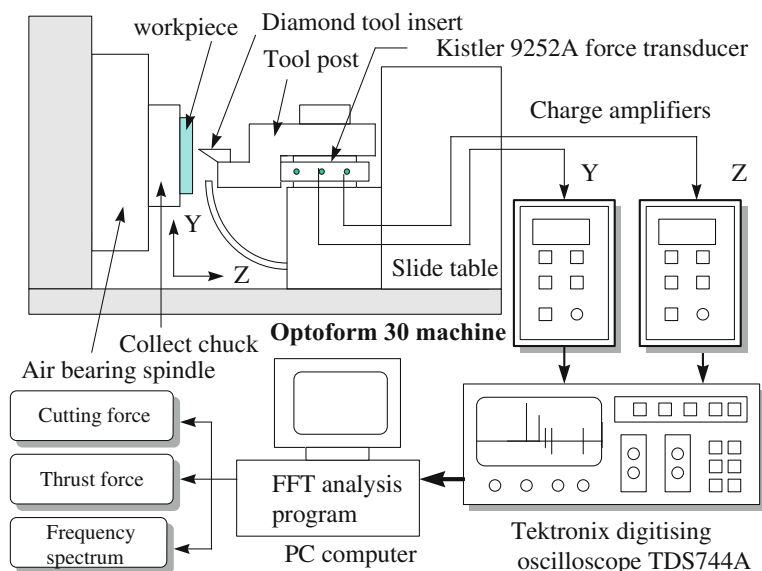
For the purpose of calculation of the fluctuation in cutting forces due to change of shear angle and friction angle, the absolute value of  $\tau_s$  and  $A_c$  need not be known. From the above equation, the cyclic variation of the cutting forces in one revolution of cut of the workpiece can be determined, provided that the friction angle  $\beta$  is known. Unlike  $\phi$ ,  $\beta$  cannot be determined experimentally during cutting nor can it be predicted from our current knowledge of friction modelling, so various values of  $\beta$  have to be assigned to represent different friction conditions between the diamond tool and workpiece. The  $\beta$  value can be found if an additional equation is available. Such an extra “equation” in this case is the power spectrum density which is related

**Table 7.2** Specifications of the work materials

Specimen no.	Specifications of work materials
1	Aluminium single crystal with (001) as the cutting plane
2	Aluminium single crystal with (110) as the cutting plane
3	Aluminium single crystal with (111) as the cutting plane

**Table 7.3** Cutting conditions for the cutting tests

Spindle speed	3000 rpm
Feed rate	20 mm min <sup>-1</sup>
Depth of cut	15 μm
Tool radius	0.774 mm

**Fig. 7.4** A schematic diagram of the signal flow in cutting force measurement

to the autocorrelation function by means of Fourier transforms. A power spectrum analysis of the theoretical cutting force variation can be made with different assigned  $\beta$  values, and can be compared with the experimental power spectrum of the force signals determined from cutting experiments. The cutting force model will be valid if the dominant frequency of the experimental force signals can be reproduced in the predicted power spectrum. The cutting force is known to be very sensitive to the frictional condition between the tool and the workpiece. Under such a scheme, the most likely value of the friction angle  $\beta$  can be found and determined when the characteristics of the theoretical and experimental power spectrum match with each other.

## 7.2 Variation in Shear Angle and Cutting Force

The cutting force model was verified through a series of cutting experiments. Tables 6.3 and 7.2 tabulate the specifications of the workpiece and the cutting conditions being used respectively. The diameter of the workpiece was 12.7 mm. A single crystal diamond tool with rake angle of  $0^\circ$ , front clearance angle of  $10^\circ$  and tool nose radius of 0.774 mm was used. The initial crystallographic orientation of the specimens was checked by a standard reflection technique on an X-ray diffractometer. In order to remove the work-deformed layer generated during the pre-machining process, the surfaces of the specimens were electropolished prior to the cutting tests (Table 7.3).

All face cutting tests were performed on a two-axis CNC ultraprecision lathe (Optoform 30 from Taylor Hobson Pneumo Co.) The cutting and thrust forces were captured approximately with the tool at the midway point between the periphery and the centre of the workpiece. Since the captured time (0.2 s) is relatively small compared with the overall cutting cycle (19 s), it is assumed that the mean cutting forces are quasi-static in the measuring range. Figure 7.4 shows a schematic diagram of the signal flow in the micro-cutting force experiments. The cutting and

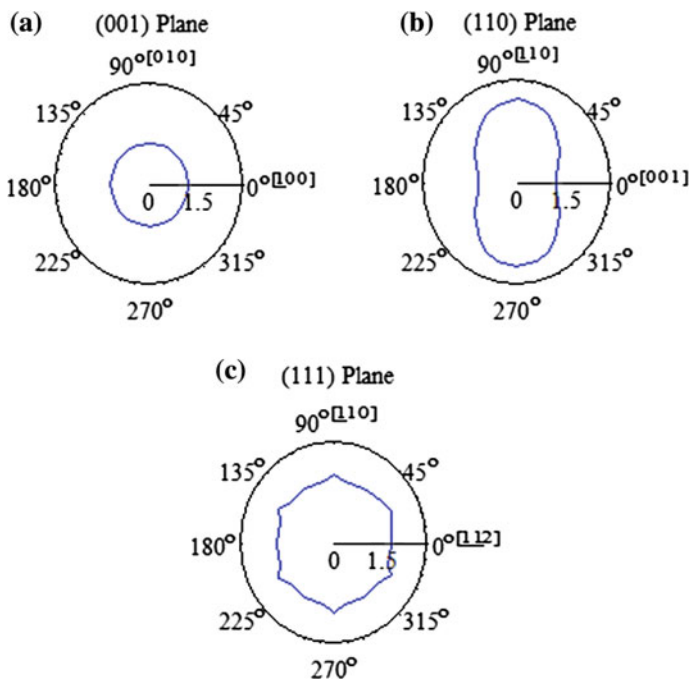


**Fig. 7.5** Predicted variation of Taylor factor ( $M$ ) with crystal orientations in cutting aluminium single crystals on **a** (001) plane, **b** (110) plane and **c** (111) plane

thrust forces were measured by a Kistler 9252A piezoelectric force transducer mounted directly under the tool post. The force signal captured from the transducer was first pre-amplified by a charge amplifier and the analogue voltage output was recorded and digitised by a digitising oscilloscope (Tektronix TDS744A). Then, the digitised signal was passed to a personal computer for analysing. The variation of the micro-cutting force was analysed by a power spectrum analysis technique.

### 7.2.1 Shear Angle Predictions and Experimental Methods

Figures 7.5, 7.6, 7.7 show the predicted Taylor factor, texture softening factor and shear angle variation in diamond turning of aluminium single crystals. There is little variation in the Taylor factor along different crystallographic directions on the (001) plane. A cyclic pattern is found for the (011) cutting plane, on which the Taylor factor is the highest at  $90^\circ$  and  $270^\circ$  from the  $[110]$  direction. On the (111) plane, there is a sixfold cyclic fluctuation during one revolution of the workpiece. The corresponding changes in the texture softening factor are shown in Fig. 7.6 for the three orientations. Where the Taylor factor indicates the resistance of the crystal to shear, the texture softening factor, as defined by  $\left(\frac{1}{M} \frac{dM}{dc}\right)$ , is associated with the softening brought about by the rotation of the lattice. Each of the

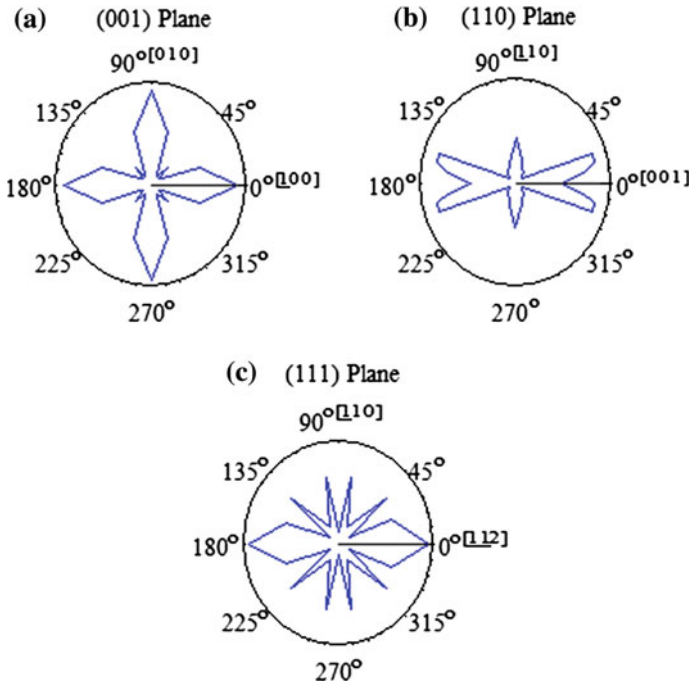


**Fig. 7.6** Predicted variation of texture softening factor with crystal orientations in cutting aluminium single crystals on **a** (001) plane, **b** (110) plane and **c** (111) plane

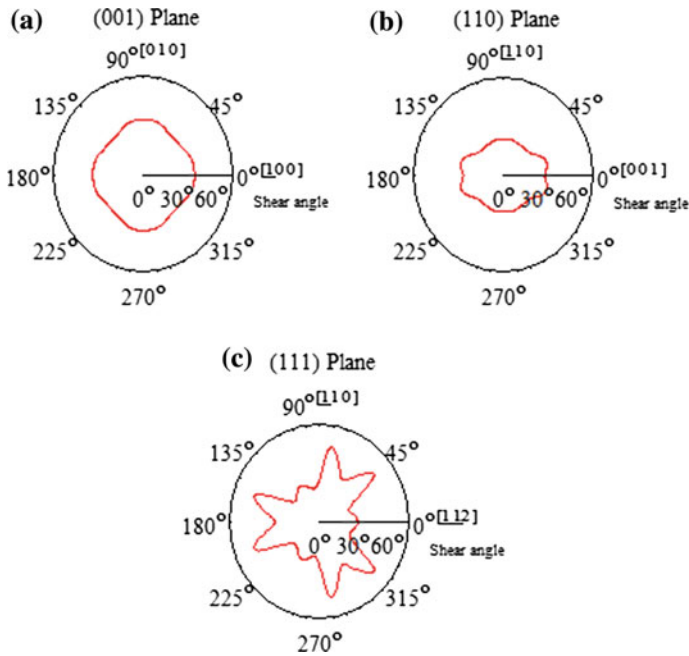


**Fig. 7.7** Predicted variation of shear angle with crystal orientations in cutting aluminium single crystals on **a** (001) plane, **b** (110) plane and **c** (111) plane

cutting planes under study shows a distinctive pattern in the variation of shear angle as shown in Fig. 7.7. The variation of the shear angle is the smallest on the (001) plane.

Cutting was performed on the (001), (110) and (111) planes. Figures 7.8, 7.9 and 7.10 show the predicted variation of the cutting forces under different friction conditions. The corresponding predicted variation of the thrust force is shown in Figs. 7.11, 7.12 and 7.13. There exists a fundamental cyclic frequency of the variation of the cutting force for each workpiece revolution. As observed from Figs. 7.8a, 7.9a, 7.10a, 7.11a, 7.12a and 7.13(a), the fundamental cyclic frequency of the variation of the cutting forces is found to be four for the (001) crystal under different friction conditions. For the (110) crystal, the fundamental cyclic frequency of the variation of the cutting force is found to be two under different friction conditions, as shown in Figs. 7.8b, 7.9b, 7.10b, 7.11b, 7.12b and 7.13b (Fig. 7.5).

From Figs. 7.8c, 7.9c, 7.10c, 7.11c, 7.12c and 7.13c, it is found that the (111) crystal appears to possess two fundamental cyclic frequencies of the cutting force variation which are six for low friction condition (i.e.,  $\mu = 0.12$ ) and three for the median (i.e.,  $\mu = 0.26$ ) and high friction conditions (i.e.,  $\mu = 0.33$ ). The cyclic cutting forces are found to be made up of two patterns hereto referred to as the

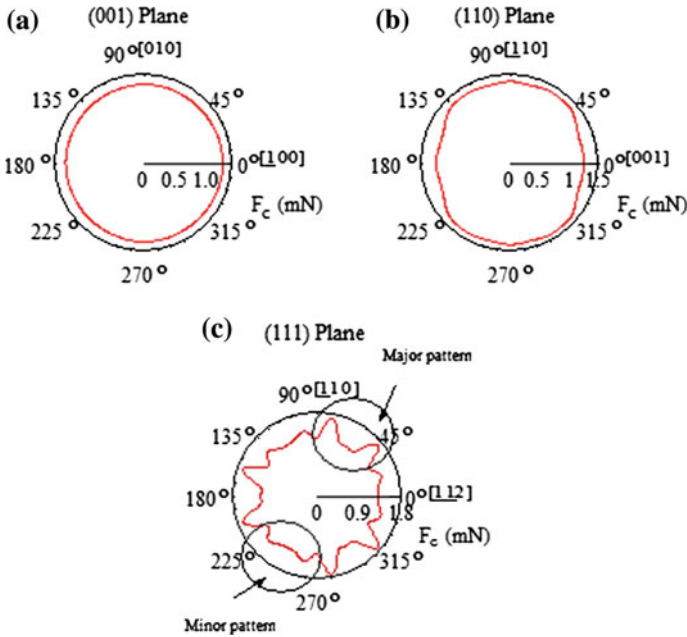


**Fig. 7.8** Predicted variation of cutting force with crystal orientations in cutting aluminium single crystals on **a** (001) plane, **b** (110) plane and **c** (111) plane with coefficient of friction of 0.12

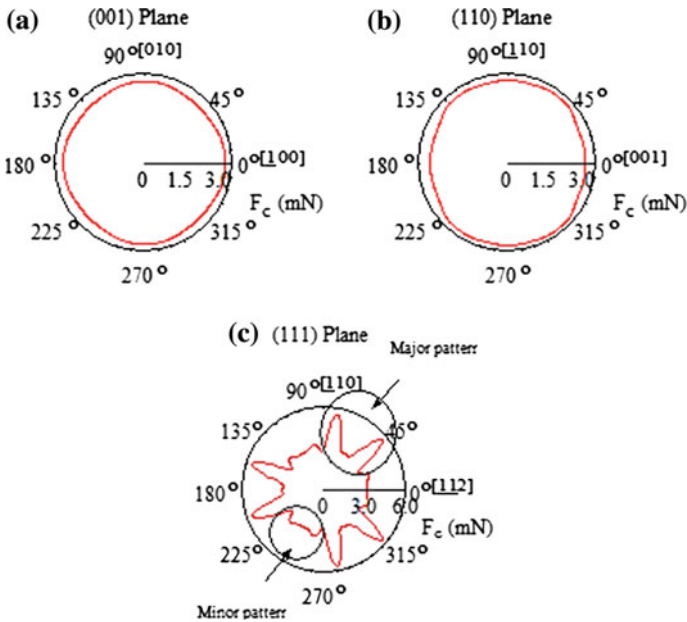


**Fig. 7.9** Predicted variation of cutting force with crystal orientations in cutting aluminium single crystals on **a** (001) plane, **b** (110) plane and **c** (111) plane with coefficient of friction of 0.26



major pattern with higher amplitude and a minor pattern with lower amplitude. As friction increases, the magnitude of the major pattern is found to increase accordingly, while that for the minor pattern appears to be unchanged. This explains the change of the sixfold to threefold variation of the cutting forces with increasing friction. To verify these findings, spectrum analysis is employed to extract the features of the cutting force patterns.

The diamond face turning was done at a speed of 8000 revolutions per minute and direct capture of the shear angle was impossible. The experimental cutting data taken from Lee and Zhou (1993) was used for comparison. Specimens with a selected crystallographic orientation were cut from a copper single crystal in the form of plates by a wire cutting machine. The orientation of the samples was chosen to enable cutting to be done on the (230) plane along different cutting directions. Prior to cutting, each specimen was electropolished. A single crystal diamond tool with a rake angle of  $0^\circ$  and a clearance angle of  $5^\circ$  was used. Cutting was performed on an NC milling machine. The tool was held stationary and cutting was performed by traversing the work table at a constant speed of  $200 \text{ mm min}^{-1}$ . The specimen was clamped on a spring-actuated quick-stop device and the cutting was stopped midway. The acceleration of a quick-stop device mounted on the worktable used was  $2.9 \text{ m s}^{-2}$ . The microstructure of the pre-polished longitudinal section of the sample was examined by a scanning electron microscope. The measured shear

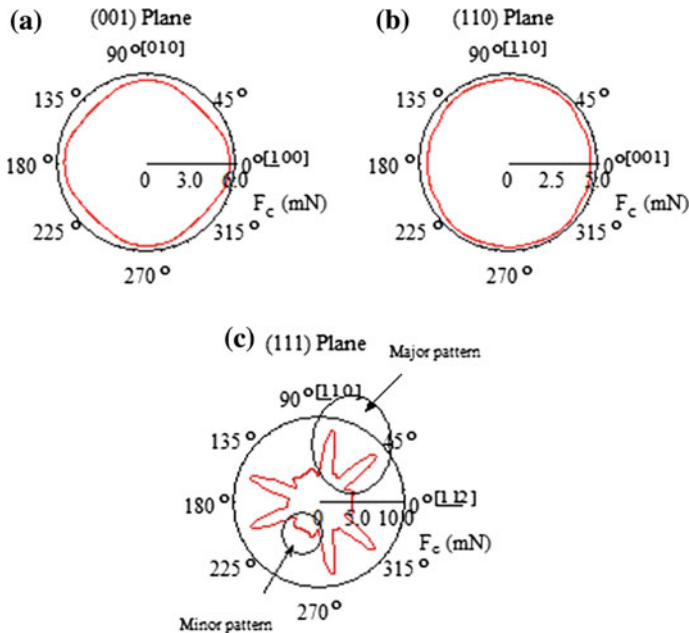


**Fig. 7.10** Predicted variation of cutting force with crystal orientations in cutting aluminium single crystals on **a** (001) plane with measured coefficient of friction of 0.38, **b** (110) plane with measured coefficient of friction of 0.35 and **c** (111) plane with measured coefficient of friction of 0.33

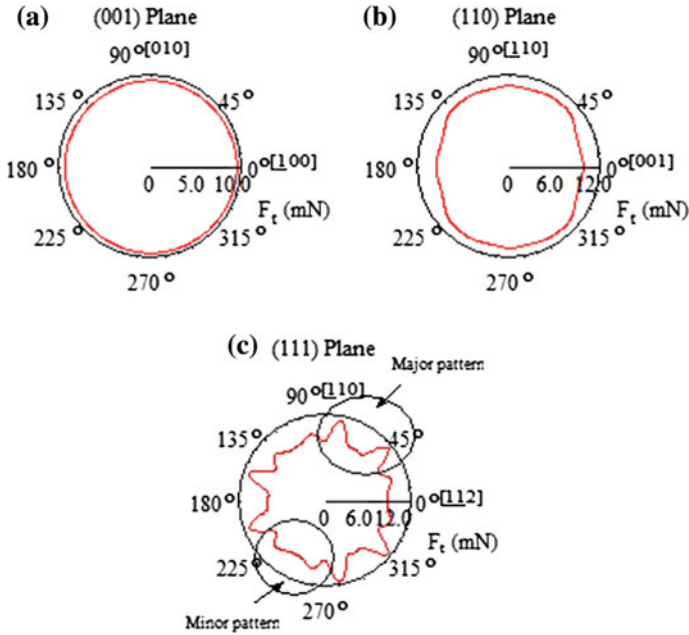


**Fig. 7.11** Predicted variation of thrust force with crystal orientations in cutting aluminium single crystals on **a** (001) plane, **b** (110) plane and **c** (111) plane with coefficient of friction of 0.12

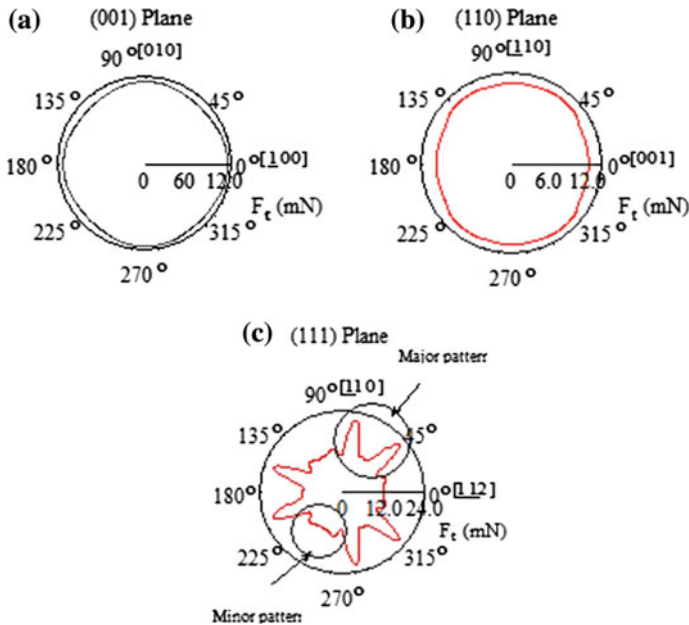


**Fig. 7.12** Predicted variation of thrust force with crystal orientations in cutting aluminium single crystals on **a** (001) plane, **b** (110) plane and **c** (111) plane with coefficient of friction of 0.26

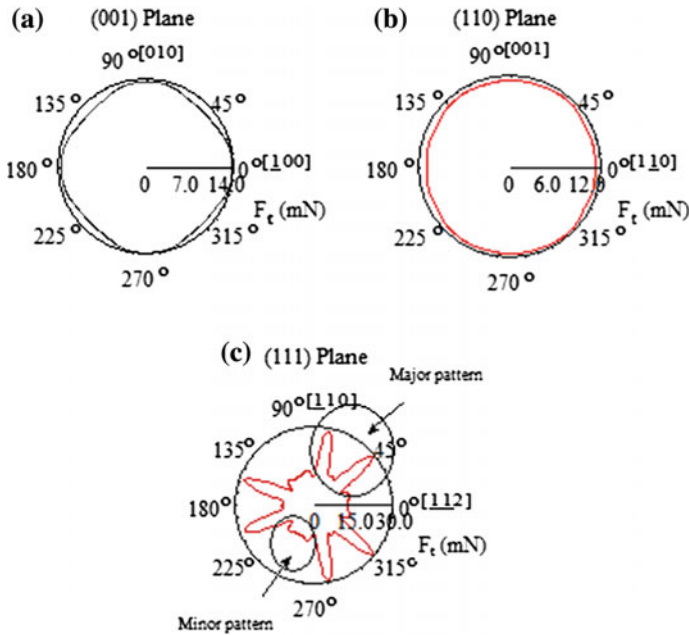
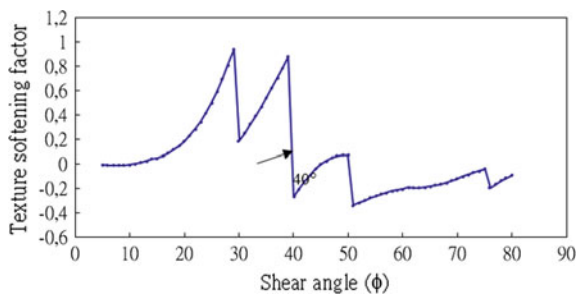


**Fig. 7.13** Predicted variation of thrust force with crystal orientations in cutting aluminium single crystals on **a** (001) plane with measured coefficient of friction of 0.379, **b** (110) plane with measured coefficient of friction of 0.353 and **c** (111) plane with measured coefficient of friction of 0.329

**Table 7.4** The measured and predicted shear angle for the different cutting direction on (230) plane

	Cutting plane	Cutting direction	Measured shear angle	Predicted shear angle
(i)	(230)	[001]	38	40
(ii)	(230)	$[\bar{3}24]$	33	37

**Fig. 7.14** Variation of texture softening factor with potential shear angle in the (230) crystal along [001] cutting direction



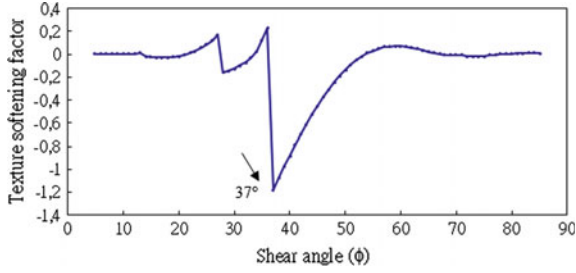


**Fig. 7.15** Variation of texture softening factor with potential shear angle in the (230) crystal along  $[\bar{3}24]$  cutting direction

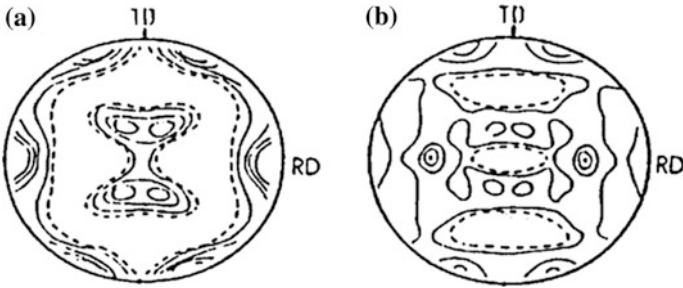
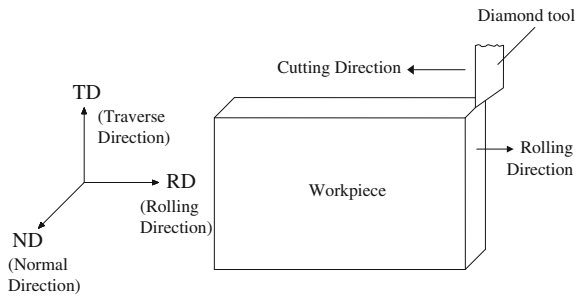


**Fig. 7.16** (111) pole figure of brass plates **a** cold-rolled and **b** annealed

**Table 7.5** Components of brass material

Code no.	Material and condition	Orientation and components
(i)	Brass (Cu-20%Zn) cold-rolled (95% reduction)	$\{011\} \langle 211 \rangle$ (79.2%) + $\{011\} \langle 100 \rangle$ (20.8%)
(ii)	Brass (Cu-20%Zn) annealed (322°, 0.5 min)	$\{236\} \langle 385 \rangle$ (84.5%) + $\{011\} \langle 100 \rangle$ (8.7%) + $\{011\} \langle 211 \rangle$ (6.8%)

**Fig. 7.17** The cutting direction of the brass plate



angles for the two different cutting directions are tabulated in Table 7.4. From the microplasticity model, the variation of the texture softening factor for the (230) copper single crystal is shown in Figs. 7.14 and 7.15.

A comparison between the predicted result and the experimental angle is listed in Table 7.4. There is a good correlation between the predicted value and the one from direct measurement.

A comparison of the experimental shear angle with the predicted one was also made in machining alloy brass. To simplify the calculation, only the ideal orientations with their volume fractions quoted from published experimental orientation distribution functions for the two brass plates were used, without considering their scatter. The {111} pole figure of the two materials is shown in Fig. 7.16a, b and their main components are listed in Table 7.5. Cutting was performed on the

**Fig. 7.18** Variation of **a** Taylor factor at different shear angles for **b** texture softening factor for cold-rolled

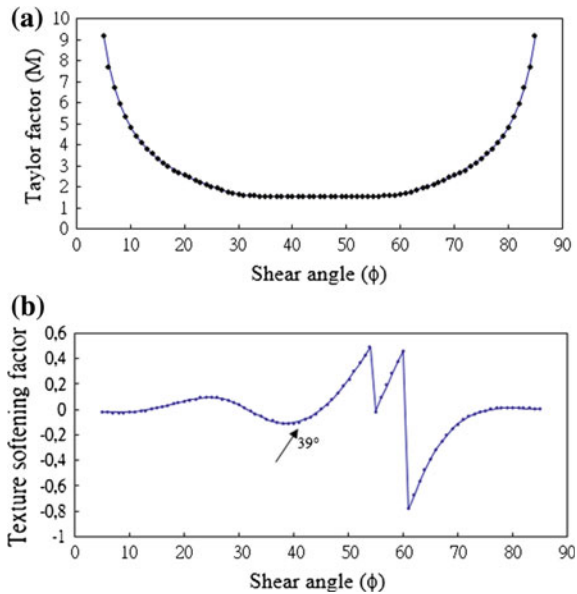
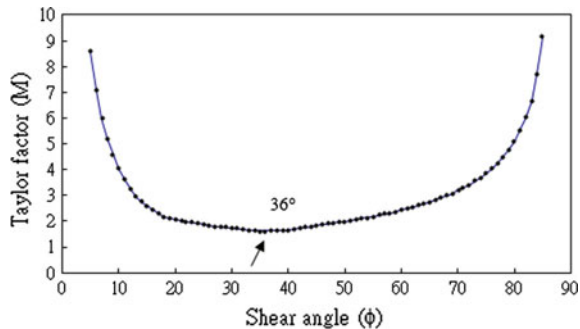


**Fig. 7.19** Variation of Taylor factor at different shear angles for annealed plate



transverse plane and the cutting direction was parallel to the rolling direction of the plate (Fig. 7.17). The plates were of fine-grained brass and the depth of cut was large enough to machine a representative volume of the bulk material.

In the cold-rolled plate, the Taylor factor is a minimum  $36^{\circ}$ – $54^{\circ}$  (Fig. 7.18a), and no minimum number of slip systems exists. The change in the texture softening factor with shear angle is shown in Fig. 7.18b and according to the flow chart shown in Fig. 7.2, the predicted shear angle is  $39^{\circ}$ . In the annealed plate, a unique minimum of the Taylor factor is found (Fig. 7.19) at  $36^{\circ}$ .

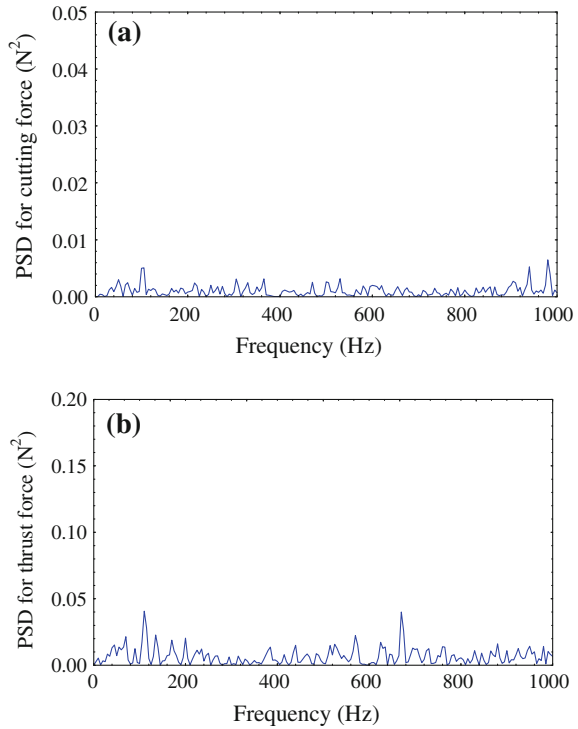
## 7.2.2 Power Spectrum Analysis of Cutting Force

The power spectrum of the cutting force is analysed under various friction conditions. The coefficients of friction  $\tan \beta$  used in simulation are the ones determined by the nanoindentation test [i.e., 0.38 on (001) plane, 0.35 on (011) plane and 0.33 on (111)]

**Table 7.6** Conditions in the spectrum analysis of the cutting forces

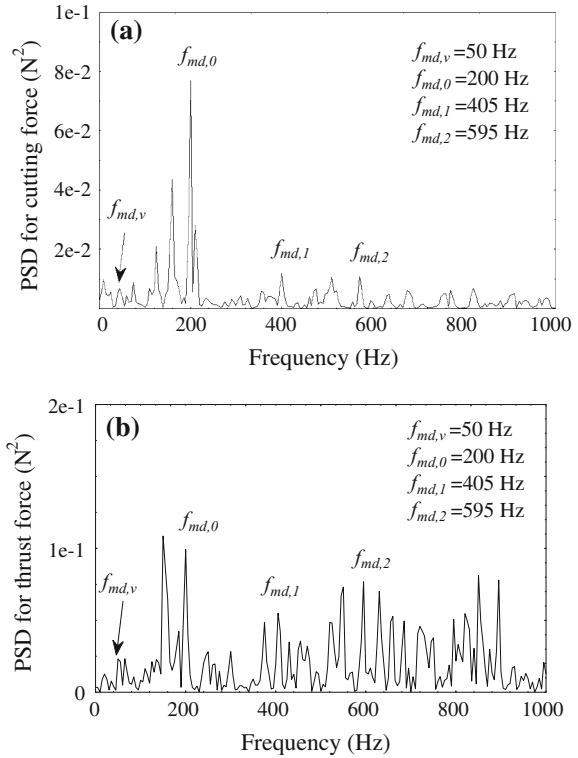
Condition no.	Description
M001	Measured spectral plots in diamond face turning of (001) aluminium single crystal with a coefficient of friction of 0.38
PL001	Predicted spectral plots in diamond face turning of (001) aluminium single crystal with a coefficient of friction of 0.12
PM001	Predicted spectral plots in diamond face turning of (001) aluminium single crystal with a coefficient of friction of 0.26
PH001	Predicted spectral plots in diamond face turning of (001) aluminium single crystal with a coefficient of friction of 0.38
M011	Measured spectral plots in diamond face turning of (011) aluminium single crystal with a coefficient of friction of 0.35
PL011	Predicted spectral plots in diamond face turning of (011) aluminium single crystal with a coefficient of friction of 0.12
PM011	Predicted spectral plots in diamond face turning of (011) aluminium single crystal with a coefficient of friction of 0.26
PH011	Predicted spectral plots in diamond face turning of (011) aluminium single crystal with a coefficient of friction of 0.35
M111	Measured spectral plots in diamond face turning of (111) aluminium single crystal with a coefficient of friction of 0.33
PL111	Predicted spectral plots in diamond face turning of (111) aluminium single crystal with a coefficient of friction of 0.12
PM111	Predicted spectral plots in diamond face turning of (111) aluminium single crystal with a coefficient of friction of 0.26
PH111	Predicted spectral plots in diamond face turning of (111) aluminium single crystal with a coefficient of friction of 0.33

**Fig. 7.20** Power spectral plots for **a** the cutting and **b** the thrust forces in air cutting



plane. Other values represented in the literature are also used in the simulation (e.g., 0.12 and 0.26 from the work by Yuan et al. 1996). Table 7.6 shows the conditions used in the power spectrum analysis of the cutting forces. The background spectral plots for the cutting and thrust forces were first obtained during air cutting. The results are depicted in Fig. 7.20. It is noticed that the background spectrum is composed of random frequency components with a low power spectral density (PSD). These can be attributed to the spray of coolant and fine vibration of the machine. Figure 7.21 shows the measured and Figs. 7.22, 7.23 and 7.24 show the predicted spectral plots for the variation of cutting forces in diamond turning of the (001) crystal plane. Remarkable frequency components ( $f_{p,v}$ ,  $f_{pd,0}$ ,  $f_{pd,1}$  and  $f_{pd,2}$ ) are observed in the predicted spectral plots (Figs. 7.22, 7.23, 7.24) for the (001) crystal and they are also reflected in the measured spectral plots (i.e.,  $f_{m,v}$ ,  $f_{md,0}$ ,  $f_{md,1}$  and  $f_{md,2}$ ) shown in Fig. 7.21. The first frequencies,  $f_{p,v}$  and  $f_{m,v}$ , are found to be close to the fundamental rotational frequency of the spindle (i.e., at 50 Hz). Comparing Figs. 7.21, 7.23 and 7.24, we can see that both the predicted and the measured spectra exhibit a dominant frequency component (i.e.,  $f_{pd,0}$  for the predicted spectra and  $f_{md,0}$  for the measured spectra) which can be correlated to the fundamental rotational frequency of the spindle (i.e.,  $f_{p,v}$  and  $f_{m,v}$  for

**Fig. 7.21** Measured power spectral plots for the **a** cutting and **b** thrust forces for face turning of aluminium single crystal on (001) plane



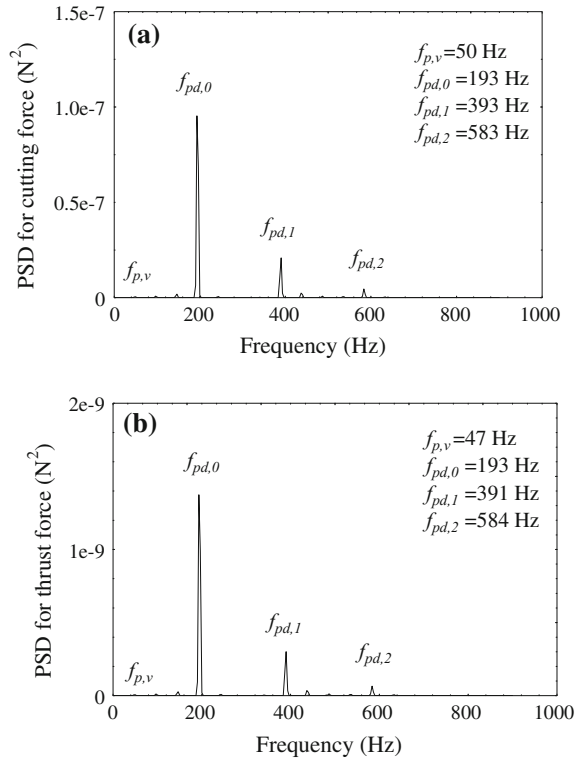
the predicted and measured spectra, respectively) by the periodicity ( $n$ ) of the fluctuation of the cutting forces. The relationship can be deduced as:

$$n = \frac{\text{dominant frequency component}}{\text{fundamental rotational frequency of spindle}}. \quad (7.39)$$

As shown in Table 7.7, the measured periodicity of the cutting force variation is found to be four, which agrees well with the predicted one under various friction conditions. This conforms to the simulation results for the (001) crystal. The measured frequency components  $f_{md,1}$  and  $f_{md,2}$  appear almost exactly at the first and second harmonics of the measured dominant frequency component  $f_{md,0}$ . Similar components (i.e.,  $f_{pd,1}$  and  $f_{pd,2}$ ) are also found in the predicted spectra, as shown in Figs. 7.22, 7.23 and 7.24. It is interesting to note that the PSD of these harmonic components is affected by the coefficient of friction. The PSD of the harmonic components is found to decrease significantly as the coefficient of friction increases. The measured spectrum closely resembles that predicted under low friction conditions ( $\mu = 0.12$ ). This can be explained by the fact that the actual coefficient of friction could be smaller than that for the value determined from nanoindentation tests since the cutting test was conducted under lubrication



**Fig. 7.22** Predicted power spectral plots for the **a** cutting and **b** thrust forces for face turning of aluminium single crystal on (001) plane and a coefficient of friction of 0.120

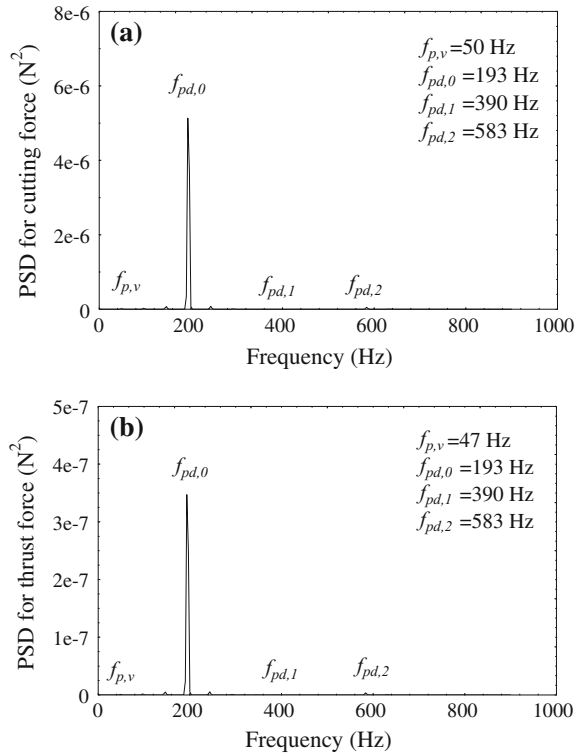


condition rather than under dry cutting condition as measured by the nanoindentation method.

Figures 7.25, 7.26, 7.27 and 7.28 show the measured and predicted spectral plots for the variation of cutting forces in the diamond turning of the (110) crystal plane. Similar to the (001) crystal, remarkable frequency components ( $f_{p,v}$ ,  $f_{pd,0}$ ,  $f_{pd,1}$  and  $f_{pd,3}$ ) are observed in the predicted spectral plots (Figs. 6.26, 6.27, 6.28) for the (110) crystal and they are also reflected in the measured spectral plots (i.e.,  $f_{m,v}$ ,  $f_{md,0}$ ,  $f_{md,1}$  and  $f_{md,3}$ ) as shown in Fig. 7.25. Both the predicted and the measured spectra exhibit dominant frequency components (i.e.,  $f_{pd,0}$  for the predicted spectra and  $f_{md,0}$  for the measured spectra) which are closely related to the periodicity of variation.

From Table 7.8, the measured fundamental cyclic frequency of the cutting force variation on (011) plane is found to be two, which agrees with the predicted ones under various friction conditions. This also agrees well with the simulation results for the (110) crystal. The measured frequency components  $f_{md,1}$  and  $f_{md,3}$  appear almost exactly at the first and third harmonics of the measured dominant frequency component  $f_{md,0}$ . Similar components (i.e.,  $f_{pd,1}$  and  $f_{pd,3}$ ) are also found in the predicted spectra as shown in Figs. 7.26, 7.27 and 7.28. Similar to the (001) crystal, the PSD of these harmonic components decrease with increasing coefficient of

**Fig. 7.23** Predicted power spectral plots for the **a** cutting and **b** thrust forces for face turning of aluminium single crystal with (001) plane and coefficient of friction of 0.260



friction, and the measured spectra match the spectra predicted under low friction conditions ( $\mu = 0.12$ ).

In comparing Figs. 7.29, 7.30, 7.31 and 7.32, distinctive patterns of frequency distributions are observed for both the measured and predicted spectra of the (111) crystal plane. The spectral plots exhibit two dominant frequency components, i.e.  $f_{ma,0}$  and  $f_{mb,0}$  for the measured spectral plots, and  $f_{pa,0}$  and  $f_{pb,0}$  for the predicted spectral plots. The captioned components appear at almost the exact periodicity of three and six as determined for the (111) crystal. The measured frequency components  $f_{ma,1}$  and  $f_{ma,2}$  appear at almost exactly at the first and second harmonics of the measured first dominant frequency component  $f_{ma,0}$  while that for the measured second dominant frequency component  $f_{mb,0}$  appears at  $f_{mb,1}$  and  $f_{mb,2}$ , respectively. Similar components (i.e.  $f_{pa,1}$ ,  $f_{pa,2}$ ,  $f_{pb,1}$  and  $f_{pb,2}$ ) are also found in the predicted spectra as shown in Figs. 7.30, 7.31 and 7.32. Similar to (001) and (110) crystals, the measured spectra are predicted under low friction conditions ( $\mu = 0.12$ ).

From Table 7.9, the predicted dominant frequency components are found to agree well with the measured results. The contribution of the two dominant frequency components is sensitive to the friction conditions. Under low friction conditions (Fig. 7.30), the contribution of the second dominant frequency component ( $f_{pb,0}$ ) appears to be greater than that for the first dominant frequency

**Fig. 7.24** Predicted power spectral plots for the **a** cutting and **b** thrust forces for face turning of aluminium single crystal with (001) plane and coefficient of friction of 0.379

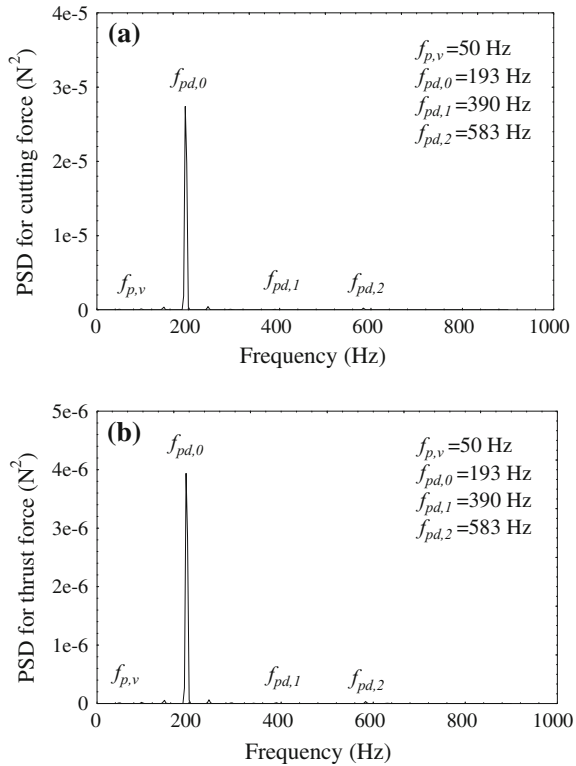
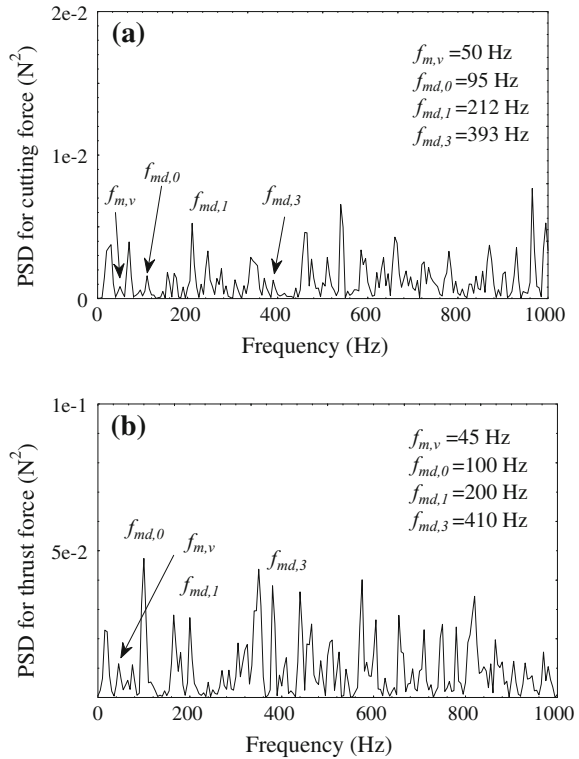


**Table 7.7** A comparison between the predicted and measured dominant frequency components for the variation of the cutting forces for diamond turning of (001) aluminium single crystal

Condition no.	Dominant frequency component (Hz)		Periodicity of cutting forces fluctuation (cycles per workpiece revolution)	
	Cutting force	Thrust force	Cutting force	Thrust force
M001	200	200	4.00	4.00
PL001	193	193	3.86	3.86
PM001	193	193	3.86	3.86
PH001	193	193	3.86	3.86

component ( $f_{pa,0}$ ). As the coefficient of friction increases, the situation reverses and the contribution of the first dominant frequency component (Figs. 7.31, 7.32) becomes higher than that under low friction conditions. The cyclic cutting forces are made up of the major pattern with higher amplitude and a minor pattern with lower amplitude. The presence of six peaks per cycle of workpiece revolution is well predicted except that there is a change in the amplitude of the peak at major

**Fig. 7.25** Measured power spectral plots for the **a** cutting and **b** thrust forces for face turning of aluminium single crystal on (110) plane

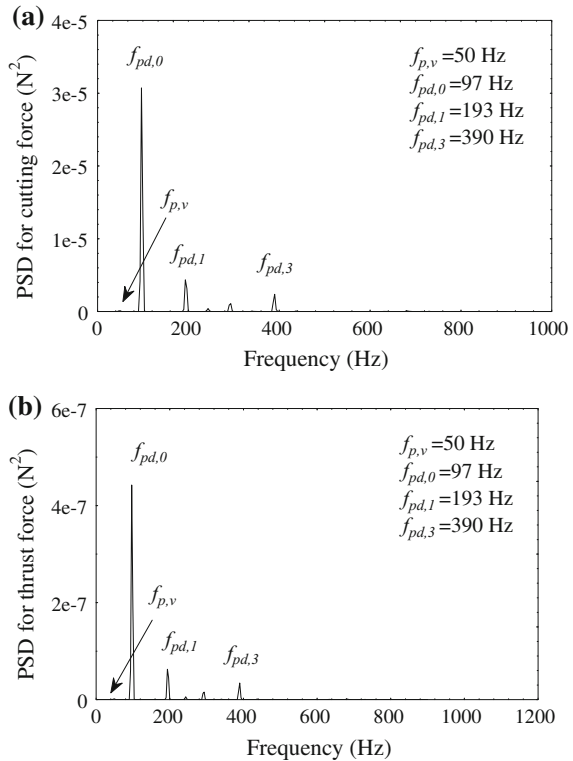


and minor patterns under different friction conditions. The experimental results confirm that the (111) single crystal possesses two patterns of cyclic variation, a periodicity of three for the domination of the major pattern under medium and high friction conditions, a periodicity of six for the domination of both the major and the minor patterns of the cutting force variation under low friction conditions.

For the three crystals being investigated, it is also found that the predicted power spectral densities (PSD) increase as the coefficient of friction increases. The remarkable increase in PSD of the frequency components with coefficient of friction illustrates that the influence of the crystallographic orientation of single crystal materials could be pronounced as the friction between the tool and the cutting surface increases. These findings imply the importance of the effect of friction on the periodic fluctuation of micro-cutting forces in diamond turning of single crystal materials. In an earlier power spectrum study by Lee and Cheung (2001), the effect of friction was ignored and the details of the cyclic variation in cutting force were not fully reproduced.

The small discrepancy observed in the power spectral densities (PSD) between the predicted and the measured spectra are likely due to the following reasons:

**Fig. 7.26** Predicted power spectral plots for the **a** cutting and **b** thrust forces for face turning of aluminium single crystal with (110) plane and coefficient of friction of 0.120



- the coolant spray which will introduce disturbances to the cutting force signals and hence the frequency spectrum at the high-frequency range;
- the progress of tool wear during machining.

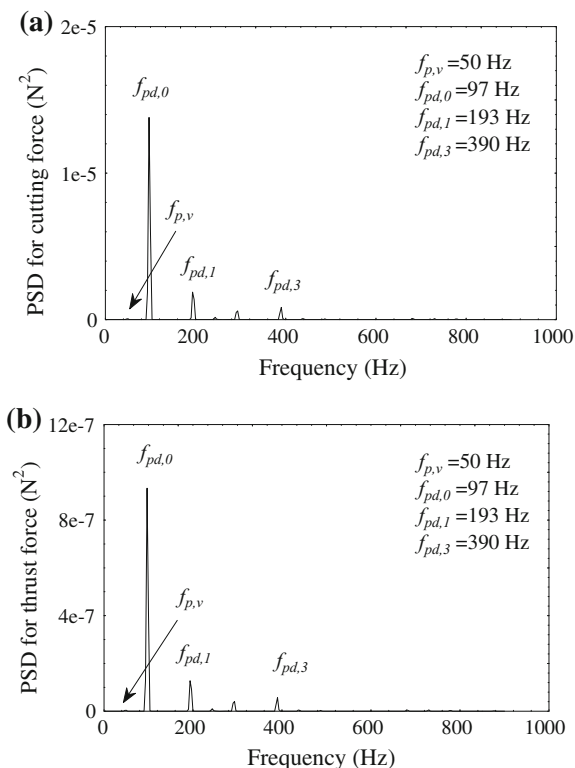
Overall, the microplasticity model is capable of explaining the variation of micro-cutting forces in diamond turning crystalline materials. The main features of the cutting force patterns are well predicted and confirmed by the cutting tests. There is good agreement between the experimental findings and the predicted results.

### 7.3 Microstructural Characterisation of Deformation Banding

#### 7.3.1 Typical Cutting-Induced Shear Band

An analysis of the deformation features was made on the two scanning electron micrographs in the experimental work by Zhou and Lee (1993). Figure 7.33 shows

**Fig. 7.27** Predicted power spectral plots for the **a** cutting and **b** thrust forces for face turning of aluminium single crystal on (110) plane and a coefficient of friction of 0.260



the geometry of the chip formation in metal cutting. The shear zone can be a sharp boundary or a diffuse region depending on the orientation of the crystal being cut. The shear angle determines the direction of chip flow in metal cutting and is known to be highly dependent on the crystal orientation of the workpiece being cut (Lee 1990). Figure 7.34 shows the typical shear zone formation of a copper single crystal when cutting was done along the [001] direction on the (230) plane. The shear band is found to be distributed homogeneously in the deformed layer. The deformation in the chip is similar to that found in the pre-cut layer and the shear band makes an angle of  $38^\circ$  with the cutting direction. This finding is of significance as in the macroscopic continuum analysis of shear planes in metal cutting, the shear plane is assumed to be in the direction of maximum shear stress and a shear angle greater than  $45^\circ$  is not allowed (Shaw 1984). A shear band arises when the normal slip process is prohibited due to the constraints of the cutting geometry and the orientation of the slip system to the cutting direction.

Based on the microplasticity model of shear band formation, the shear angle for the copper single crystal shown in Fig. 7.35 is expected to be around  $40^\circ$  from the cutting direction. This was confirmed by experimental results. The composed slip activities of the following slip systems were calculated and are shown in Table 7.10.

**Fig. 7.28** Predicted power spectral plots for the **a** cutting and **b** thrust forces for face turning of aluminium single crystal on (110) plane and a coefficient of friction of 0.353

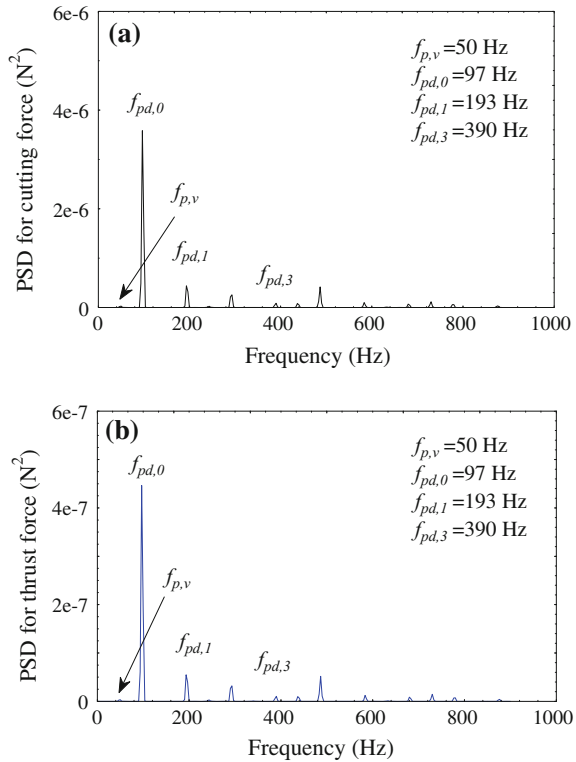


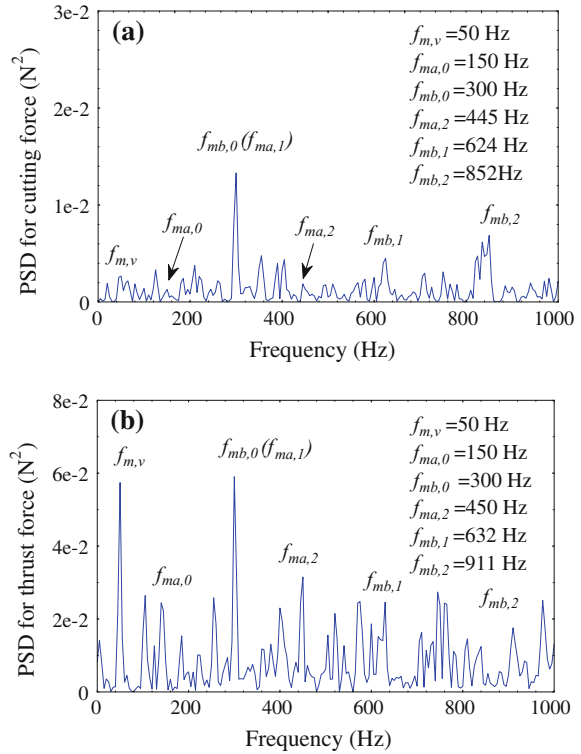
**Table 7.8** A comparison between the predicted and measured dominant frequency components for the variation of the cutting forces for diamond turning of (110) aluminium single crystal

Condition no.	Dominant frequency component (Hz)		Periodicity of cutting forces fluctuation (cycles per workpiece revolution)	
	Cutting force	Thrust force	Cutting force	Thrust force
M110	95	100	1.90	2.00
PL110	97	97	1.94	1.94
PM110	97	97	1.94	1.94
PH110	97	97	1.94	1.94

### 7.3.2 Orthogonal Cutting-Induced Kink Band

Figure 7.35 shows the shear zone formation of a copper single crystal when cutting was done along [324] and on a (230) plane. The features of the thus-formed shear bands under the chip are different from those commonly found in polycrystals.

**Fig. 7.29** Measured power spectral plots for the **a** cutting and **b** thrust forces for face turning of aluminium single crystal on (111) plane



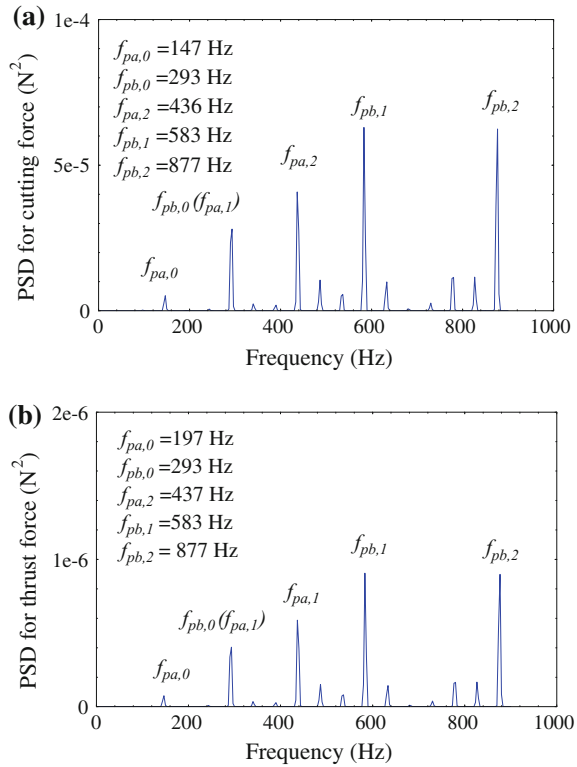
Contrary to general belief, in a wide shear zone, the boundary between the pre-cut large and the chip is sharply defined. In this crystal, the cutting direction is parallel to the slip direction and is orientated unfavourably for chip formation. A complex picture of the deformation band is observed in the vicinity of the shear zone, as shown in Fig. 7.36. Three sets of deformation bands are identified and listed in Table 7.11.

The strain field experienced within the deformation layer directly below the freshly cut surface is expected to be plane strain compression, with compression along the cutting direction. The bands induced by plane strain (Type I bands) make an angle of  $135^\circ$  with the cutting direction. From a plane strain compression analysis of the shear band angle, we can conclude that such a band is expected to occur at  $127^\circ$  and is thus close to the observed experimental one found in the cutting of the copper single crystal shown in Fig. 7.35.

Type II bands could only be found in the pre-cut layer, and are transformed to type III bands once they are deformed to become a part of the chip. Judging from the macroscopic features, the band is the result of simple shear induced by the cutting action as the slip plane is close to the cutting direction.



**Fig. 7.30** Predicted power spectral plots for the **a** cutting and **b** thrust forces for face turning of aluminium single crystal on (111) plane and a coefficient of friction of 0.120



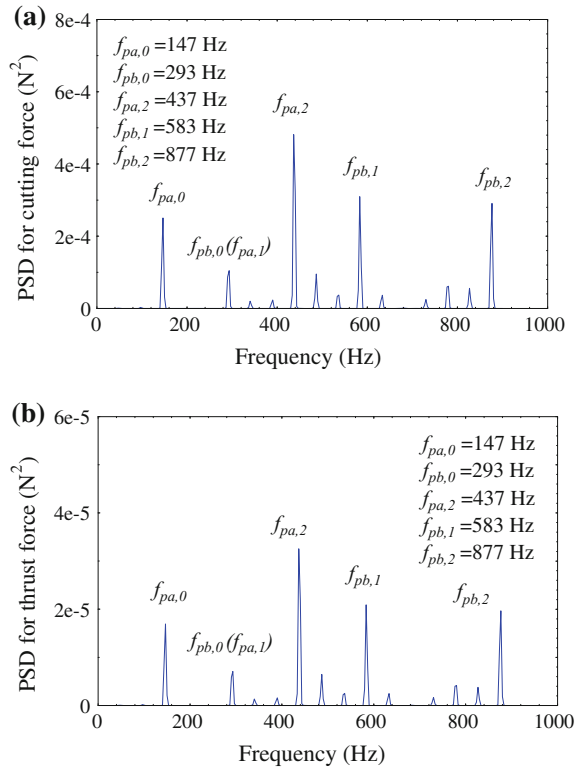
A Type III band is found in the shear zone and resembles a kink band found in an hcp single crystal. The microscopic slip activities inside the kink were not close to the direction of the macroscopic shear. Also, two different kinds of boundary could be seen. The boundary between the Type III band and the chip was very well-defined and sharp while that between the pre-cut layer and the band was very diffuse.

The evolution of a kink instead of a conventional Type I deformation band is expected to be the result of a competition event between the imposed macroscopic plane strain compression, due to the cutting mechanism, and the additional constraint imposed on the microscopic slip activities due to the geometry of the cutting tool and the workpiece.

### 7.3.3 Cutting Induced Kinking Within the Sliding Region

The strain field around the shear zone is plane strain compression. Thus, it is trivial to expect that a conventional shear band will be formed if the shear direction of Type I deformation band makes an angle of  $45^\circ$  rather than  $135^\circ$  with the cutting

**Fig. 7.31** Predicted power spectral plots for the **a** cutting and **b** thrust forces for face turning of aluminium single crystal on (111) plane and a coefficient of friction of 0.260



direction. However, if the strain field does not trigger any microscopic slip systems, a very different form of deformation band will result. As far as the geometry of the cutting tool and the workpiece is concerned, the macroscopic shear direction within the Type III deformation band cannot be more than  $90^\circ$  from the cutting direction. Thus, the interaction between the macroscopic shear and the microscopic slip of the deformation band will significantly affect the features of the Type III band. The following three features are discussed: kinking, lattice rotation and strain localisation.

The most classical and well-known kinking occurs in the compression of hcp single crystal when the compression axis is close to the  $c$  axis, which is the glide direction of the crystal. Because of the non-existence of any slip systems other than the slip along the  $c$  axis, a kink is formed. This is to be compared with the formation of the Type III deformation band reported in the present work. The shear direction within the pre-cut layer is also very close to the compression axis which, in this case, is the cutting direction. Judged from this point of view, the criteria for the formation of Type III deformation band and classical kinking in hcp are very

**Fig. 7.32** Predicted power spectral plots for the **a** cutting and **b** thrust forces for face turning of aluminium single crystal on (111) plane and a coefficient of friction of 0.329

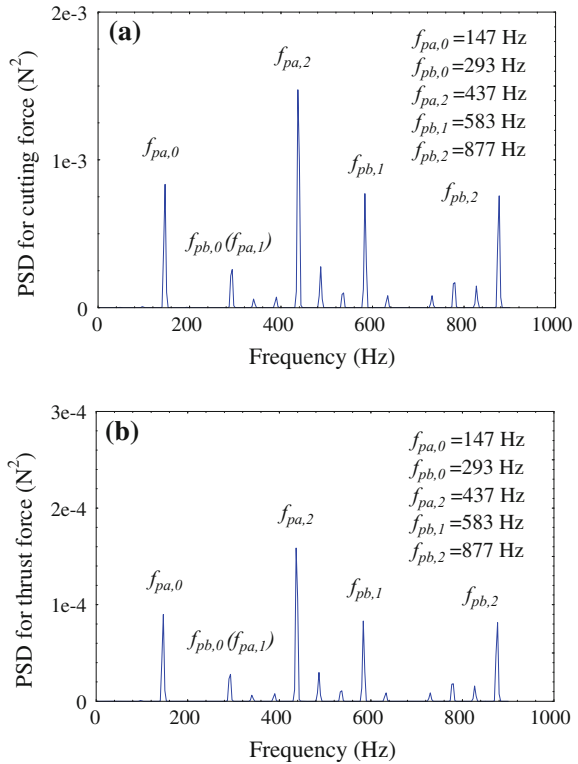


**Table 7.9** A comparison between the predicted and measured dominant frequency components for the variation of the cutting forces for diamond turning of (111) aluminium single crystal

Condition no.	Dominant frequency component (Hz)		Periodicity of cutting forces fluctuation (cycles per workpiece revolution)	
	Cutting force	Thrust force	Cutting force	Thrust force
M111 <sup>a</sup>	150	150	3.00	3.00
M111 <sup>b</sup>	300	300	6.00	6.00
PL111 <sup>a</sup>	147	147	2.94	2.94
PL111 <sup>b</sup>	293	293	5.86	5.86
PM111 <sup>a</sup>	147	147	2.94	2.94
PM111 <sup>b</sup>	293	293	5.86	5.86
PH111 <sup>a</sup>	147	147	2.94	2.94
PH111 <sup>b</sup>	293	293	5.86	5.86

<sup>a</sup> For first dominant frequency component (i.e.,  $f_{ma,0}, f_{pa,0}$ )

<sup>b</sup> For second dominant frequency component at (i.e.,  $f_{mb,0}, f_{pb,0}$ )

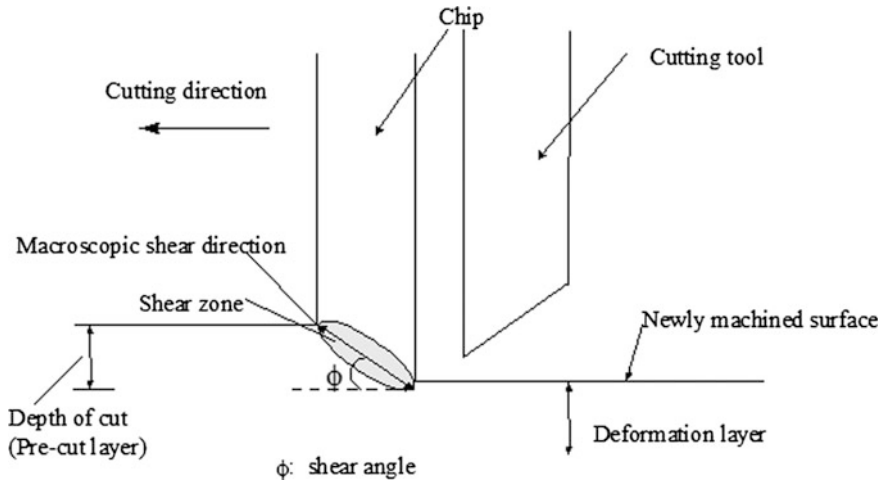


Fig. 7.33 The geometry of chip formation

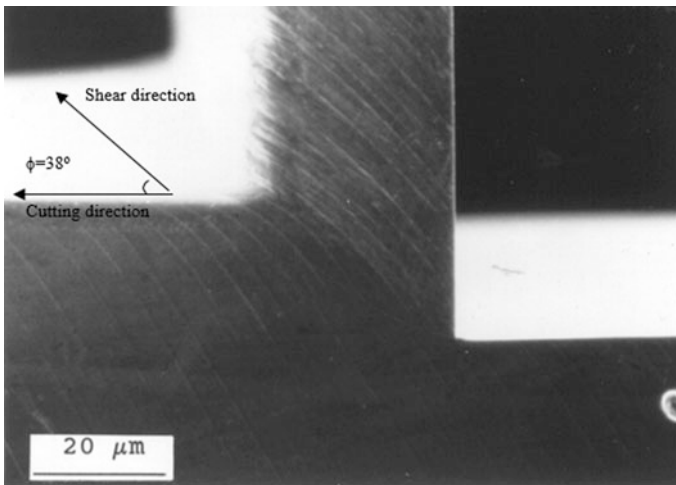
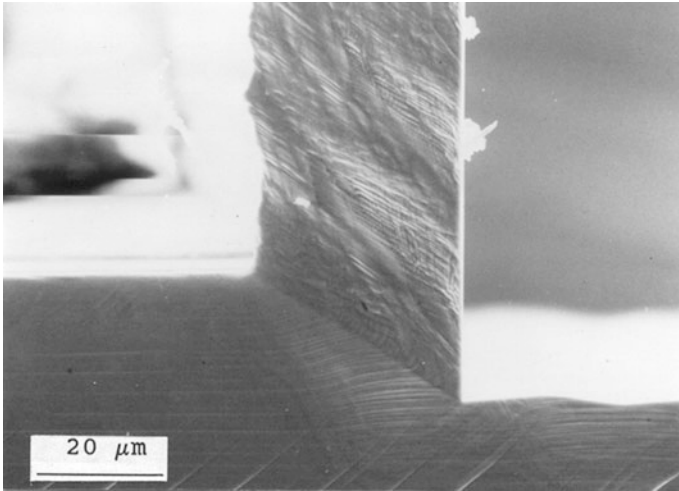
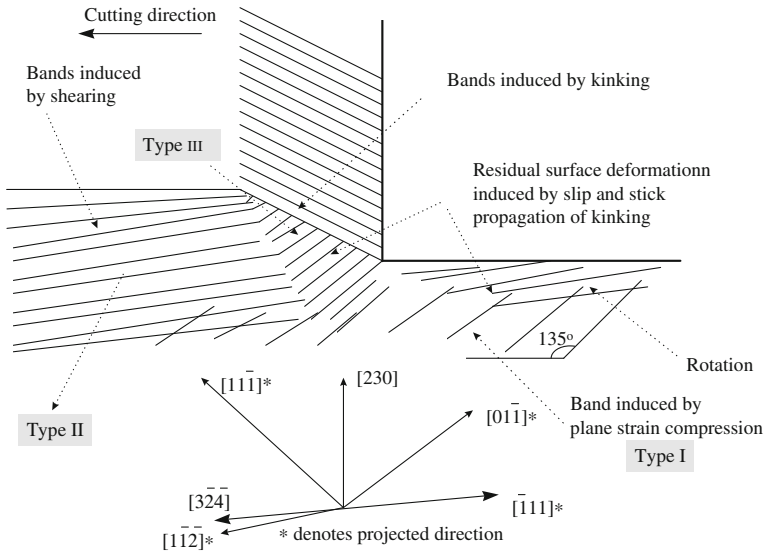


Fig. 7.34 SEM micrograph of shear zone formation of a copper single crystal when cutting was done along [001] direction on (230) plane

similar. Kinking was reported in microforming a zinc single crystal when the basal plane is parallel perpendicular or  $45^\circ$  to the cutting direction. It was the first time that similar kinking phenomenon was found in the machining of copper alloy which is of fcc structure.



**Fig. 7.35** SEM micrograph of shear zone formation of a copper single crystal when cutting was done along  $[3\bar{2}4]$  direction on  $(230)$  plane



**Fig. 7.36** A schematic diagram of the deformation band shown in Fig. 7.35

**Table 7.10** The calculation of slip system

Slip system	Shear ratio (%)
a1 (1 1 1)[0 1 $\bar{1}$ ]	21
b1 (1 1 $\bar{1}$ )[0 1 1]	46.5
-b2 (1 1 $\bar{1}$ )[ $\bar{1}$ 0 $\bar{1}$ ]	31.5

**Table 7.11** Deformation bands in metal cutting

Deformation band	Location
Type I	Within the deformation layer directly below the freshly cut surface
Type II	Within the pre-cut layer
Type III	Within the shear zone

Since the direction of microscopic slip is different to that of macroscopic shear, lattice rotation would have occurred. Despite the fact that the direction of the macroscopic shear is at a right angle of the microscopic, the compatibility problem could still be accommodated by suitable lattice rotation. The extent of lattice rotation depends on both the shear strain and the difference in angle between the microscopic and macroscopic processes. The extent of lattice rotation increases with shear strain and the difference in the shear direction.

Because of the differences in the extent of deformation within and outside the shear zone, two different kinds of interface could form. The diffuse boundary is actually a trace of a Type III deformation band being developed within a relatively undeformed layer while the sharp boundary is parallel to the shear direction within the chip.

## References

- Bishop, J. F. W., & Hill, R. (1951). A theory of plastic distortion of a polycrystalline aggregate under combined stresses. *Philosophic Magazine*, 42, 1298.
- Lee, W. B. (1990). Prediction of microcutting force variation in ultraprecision machining. *Precision Engineering*, 12(1), 25.
- Lee, W. B., & Chan, K. C. (1990). Symmetry requirement in shear band formation. *Scripta Metallurgica and Materialia*, 25, 997.
- Lee, W. B., & Cheung, C. F. (2001). A dynamic surface topography model for the prediction of nano-surface generation in ultra-precision machining. *International Journal of Mechanical Sciences*, 43, 961–991.
- Lee, W. B., & Zhou, M. (1993). A theoretical analysis of the effect of crystallographic orientation on chip formation in micro-machining. *International Journal of Machine Tools and Manufacture*, 33(3), 439.
- Reid, C. N. (1973). *Deformation geometry for material scientists*. Oxford: Pergamon Press.

- Shaw, M. C. (1984). Shear strain in cutting. In J. R. Crookall & M. C. Shaw (Eds.), *Metal cutting principles* (p. 168). Oxford: Clarendon Press.
- Yuan, Z. J., Zhou, M., & Dong, S. (1996). Effect of diamond tool sharpness on minimum cutting thickness and cutting surface integrity in ultraprecision machining. *Journal of Materials Processing Technology*, 62, 327.
- Zhou, M., & Lee, W.B. (1993). *International Journal of Machine Tools Manufacturing*, 33(3), 439.

**Part III**  
**Theory and Mechanism of Ultra-Precision**  
**Diamond Turning**



# Chapter 8

## Shear Bands in Ultra-Precision Diamond Turning

**Abstract** Shear bands are common phenomena reported in various metal-working processes, such as forming, forging, hot rolling, cold rolling and high-speed cutting. In the micro-cutting process, there is strong experimental evidence that the fluctuation in cutting force is related to the variation of chip thickness and is related to the shear plane angle of the metals being cut. This chapter investigates the mechanism of elastic strain-induced shear bands and regularly space shear bands with a generalised model for shear angle prediction.

### 8.1 Shear Band Theory for Deformation Processes in Machining

The earliest attempts to establish this relationship were described by Black (1971) and Saito (1978). The formation of shear bands and the shear direction are among the key factors affecting the surface finish in ultra-precision machining technology. Lee and co-authors (Lee 2005; Lee et al. 2003) proposed a mesoplasticity model to study the relationship between cutting force and shear direction in the orthogonal metal cutting process in single point diamond turning.

Two major areas have been extensively investigated by researchers: (1) the modelling of the cutting process and the formation of shear bands and (2) the development of material constitutive equations to improve the simulation results of chip morphology.

Fang (2003a, b) developed a new slip-line model for machining with a round-edge tool. He proposed a hodograph on which he derived a set of analytical equations to predict the thickness of and the shear strain rate in the primary shear zone (PSZ). However, his new slip-line model was designed for orthogonal cutting with continuous chip formation only and was based on the assumption that a rigid plastic material was under plane strain compression. Thus, the material used in his model could not bounce back when the imposed strain was removed. Moreover, the effect of elastic strain stored in the material in the course of cutting was neglected.

Burns and Davies (2002) postulated a localised plastic deformation zone right on top of the tool tip in the PSZ, and proposed that the shear band in high-speed machining was induced by the localised compressive stress which caused a gradient in the shear stress, i.e. the shear band was initiated in the region around the tool tip and was then propagated outward to the free edge of the chip.

To take account of the effect of the formation of shear bands, a number of material constitutive models have been proposed to establish the necessary criteria for shear band propagation and to model the phenomenon of stress collapse inside shear bands. In the earlier work, Recht (1964) studied the dynamic plastic behaviour of materials which was then named catastrophic thermoplastic shear. Recht proposed a model to further explain the adiabatic shear theory of saw-tooth chip formation (Recht 1985). In the model, an assumption was made that for some reason thermoplastic instability occurred which extended from the tool tip upward towards the free surface. However, this model could not predict why shear bands could be initiated at the free edge. Recently Medyanik et al. (2007) proposed a new ductile failure criterion which assumed that dynamic recrystallisation took place during shear band propagation. Rhim and Oh attempted to prove that the recrystallisation conditions could be satisfied using FEM simulation (Rhim and Oh 2006). However, these models did not cope with the more fundamental problem of what preceded and later induced shear band propagation.

In a more general case, the phenomenon of adiabatic shear banding was studied in a direct compressive Hopkinson pressure bar system (DCHP) and succeeded by a FEM simulation (Teng et al. 2007). In the FEM simulations, the Johnson–Cook model was selected for the constitutive equations with different mesh sizes and it was concluded in their simulation results that sufficiently small meshes must be used in the FEM models so that the resolution of the FEM simulation could be high enough to capture the same phenomena as in the experiments. However, a complicated constitutive model is not a necessary condition, since the mechanism of adiabatic shear banding is believed to be driven by mechanics rather than materials (Teng et al. 2007).

High strain rate, such as encountered in high-speed machining and impact and torsion experiments, favours the formation of shear bands (Guduru et al. 2001). Most of the solid material in the vicinity of shear bands experiences relatively little plastic deformation whereas the bands themselves experience very large plastic strains ( $10$ – $10^2$ ) and propagate at very high rates of  $10^5$ – $10^7$   $\text{s}^{-1}$ . At such high strain rates, the rate of local heat generation is much larger than the rate of heat conduction to the surrounding material. To form an adiabatic shear band, the initiation process demands a high strain rate to cause strain inhomogeneity which is later aggravated by adiabatic softening. Since shear bands can be observed in cold-rolled copper and brass under a much lower imposed strain rate, it is always an intriguing question to ask why the low imposed strain rate can trigger a higher strain rate inside the shear bands.

Recent research on the formation of shear bands reveals that (1) work softening must occur. Most of the constitutive models, though diversified widely in their formulations and assumptions, unanimously predict that localised shearing within

shear bands will induce softening; (2) the effect of elastic strain building up in work materials in the course of machining on shear band formations has been neglected; (3) so far, no model or experiment has indicated that shear bands are initiated at the free edge of the serrated chips.

According to the experimental observations, conventional and precision machining of metals can produce three basic types of chip: discontinuous, continuous and continuous chips with built-up edge (Merchant 1945a). However, experimental results reveal that in ultra-precision machining of non-ferrous materials, serrated chips with regularly spaced shear bands (RSSB) are the most common chip type in single point diamond turning. The shear bands are initiated at the free edge of the chip and propagate through the tool tip almost along a planar path (Wang et al. 2010). Different types of deformation bands and their formation were studied by Lee et al. (1999) on single crystal materials. However, their shear bands were not very thick or well defined. Duan and Wang have observed thick shear bands of up to 3  $\mu\text{m}$  wide in high-speed orthogonal cutting of high strength low alloy (HSLA) steel (Duan and Wang 2005). However, they did not mention the necessary conditions favouring the production of such thick RSSB. Inspired by their work, heavily cold-rolled brass with high yield strength is used in this study. Ferrous materials are avoided because they cannot be machined by diamond tools without inducing excessive tool wear.

Merchant's model holds well for continuous (uniform) chip formation, as applied in the machining of amorphous material (Jiang and Dai 2009) which can be regarded as homogeneous with isotropic properties, but discrepancies have been identified between the theory and experimental data since most engineering materials are crystalline in nature. Much effort has been therefore exerted to modify Merchant's model to comply with the different experimental results, such as the results produced by Lee and Shaffer (1951), Stabler (1951), Molinari and Moufki (2008), etc. However, their modification did not consider the presence and effect of material anisotropy and the occurrence of RSSB. In addition, their corrections hold better for cutting tools with a zero rake angle, but fail for those with a negative rake angle. Thus, they cannot be applied in ultra-precision machining since a large error exists in the prediction of shear angle by their modified models. Therefore, it is of importance to study RSSB and develop a physical explanation for cutting force and shear angle prediction.

## 8.2 Regularly Spaced Shear Bands and Morphology of Serrated Chips

Serrated chips with regularly spaced shear bands (RSSB) are commonly observed in the microcutting of non-ferrous materials with diamond tools. This chapter investigates chip morphology with RSSB produced in the orthogonal microcutting of cold-rolled brass. Critical discussion is given on why Merchant's model and its

modified versions fail whenever RSSB is evolved. A generalised model is proposed in this chapter based on the theory of elastic strain-induced shear bands, where Merchant's model and its derivatives are construed as special cases.

Systematic experimental work is conducted for discussion on RSSB. The material used in this experiment was an  $\alpha$ -brass sheet of a thickness of 10 mm. The brass sheet was cold rolled to a reduction ratio of 90%. The work material was then wire cut into a rectangular shape 0.9 mm thick, 4 mm wide and 12 mm long along the rolling direction. The side surfaces of the wire-cut sample were diamond turned to ensure a pair of parallel side surfaces, with a distance of 600  $\mu\text{m}$  on average in between them. The side surfaces were further ground with silicon carbide grinding paper of grit size 600 and polished with 6 and 1  $\mu\text{m}$  diamond polishing compounds to remove the work-deformed layer generated by the previous machining process. The prepared sample was mounted onto a specially designed fixture. During the orthogonal cutting experiment, as shown in the schematic of Fig. 8.1, the diamond tool moved along the rolling direction with a constant cutting speed of 100 mm/min and a depth of cut of 15  $\mu\text{m}$ . Two monocrystal diamond tools with a zero rake angle and  $-25^\circ$  rake angle, respectively, were used in the two sets of orthogonal cutting experiments. The clearance angle of the diamond tool was  $7^\circ$  with a tool nose radius of 1.288 mm. Since the diamond tool underwent a horizontal movement and stopped at the centre of the workpiece, the produced chip was not detached from the workpiece. The chip morphology and spatial location and geometry of the chip were retained for further calculation. During orthogonal cutting, the cutting force ( $F_c$ ) and thrust force ( $F_t$ ) were measured by a Kistler 9252A piezoelectric force transducer mounted under the tool holder and recorded by a Tektronix TDS 744A digitising oscilloscope. The dimensionless value of  $F_c/F_t$  was utilised in the present work. After orthogonal cutting, the workpiece was transferred to a scanning electron microscope. The images of chip formation were taken along the normal direction of the side surface. To guarantee a reliable measurement of the shear angle based on SEM images, the perpendicularity error was restricted within  $5^\circ$ , in general.

Serrated chips with RSSB could be observed for different depths of cut, for a cutting tool with a zero rake angle, as shown in Fig. 8.2a1–a3. As for the cutting tool with a  $-25^\circ$  rake angle (Fig. 8.2b1–b3), irregularly spaced coarse shear bands were identified in the primary deformation zone (PDZ). Besides the thick shear bands, a set of finer shear bands was found in the divergent directions. According to the previous theory of Wang et al. (2010c), this phenomenon results from the complex elastic strain distribution in the large volume inside PDZ. However, chip formation depends on the generation of the RSSB.

The measured cutting force ratios  $F_c/F_t$  in all sets of experiments are listed in Table 8.1. Based on the cutting force ratio, the shear angle can be calculated by Merchant's model in Eq. (8.1) and is denoted by " $\phi_{\text{MExp}}$ ". Lee and Shaffer's model [LS model, Eq. (8.2)] and Stabler model [S model, Eq. (8.3)] are also employed to predict the shear angles based on the measured cutting force ratios.  $\phi$ ,  $\alpha$  and  $\beta$  are

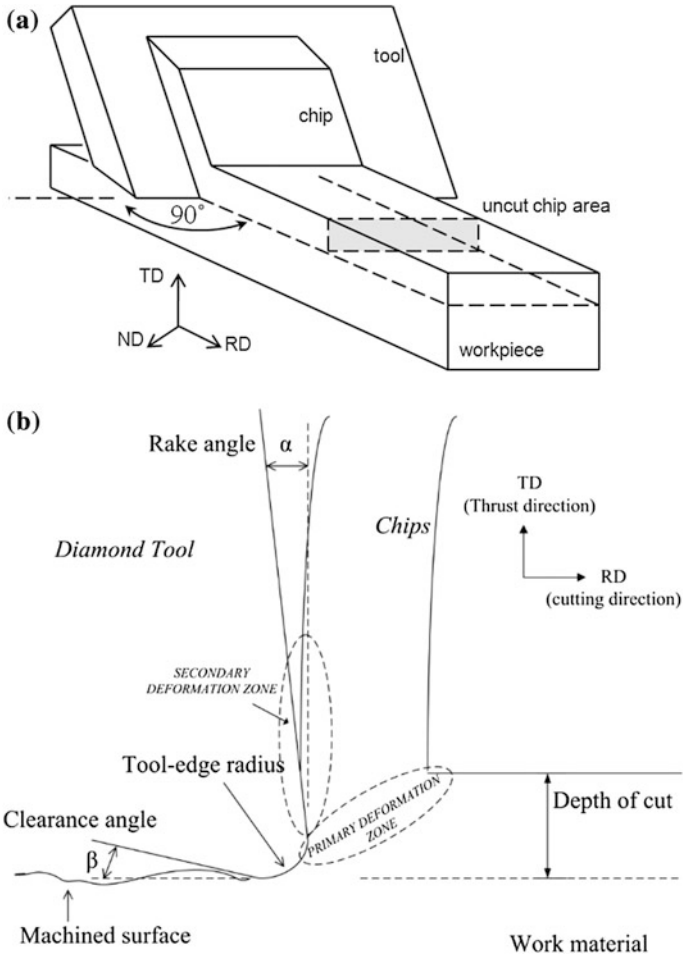


**Fig. 8.1** Schematic of **a** orthogonal cutting and **b** the geometry of chip formation

the shear angle, tool rake angle and friction angle, respectively. This notation applies throughout the context.

$$\phi_M = \frac{\pi}{4} + \frac{\alpha - \beta}{2}, \quad \text{where } \beta = \arctan \frac{F_t + F_c \tan \alpha}{F_c - F_t \tan \alpha} \quad (8.1)$$

$$\phi_{LS} = \frac{\pi}{4} + \alpha - \beta \quad (8.2)$$

$$\phi_S = \frac{\pi}{4} + \frac{\alpha}{2} - \beta \quad (8.3)$$

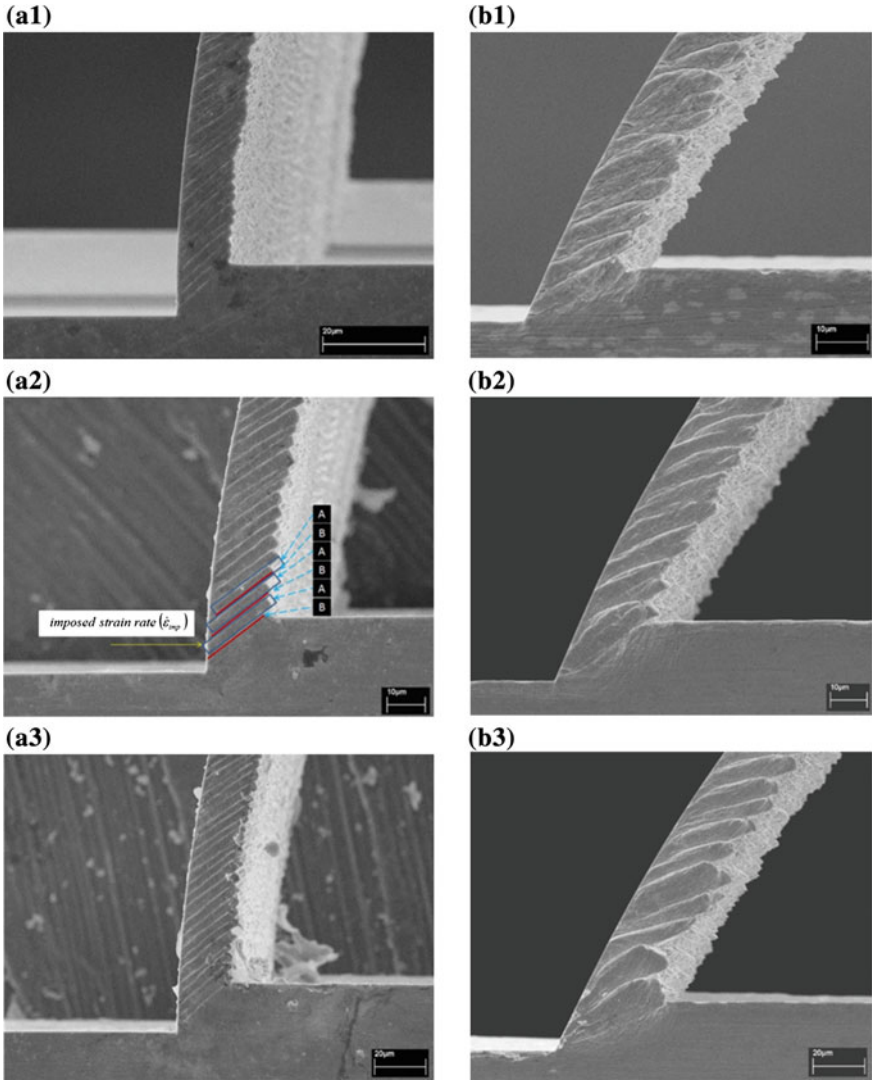


**Fig. 8.2** SEM micrographs of serrated chips in orthogonal cutting with a cutting tool of **a**  $0^\circ$  rake angle and **b**  $-25^\circ$  rake angle, at a depth of cut of *l* 10  $\mu\text{m}$ , 2 15  $\mu\text{m}$  and 3 20  $\mu\text{m}$

On the other hand, finite element modelling of continuous chip formation is adopted following the same procedure as described in Wang et al. (2010b). A 2D orthogonal cutting model is established in MSC.Marc. The calculated cutting force ratio  $F_c/F_t$  and predicted shear angles by different models are listed in Table 8.2. For comparison with the observed reference shear angles in the SEM micrographs, the predicted and measured shear angles are plotted in Fig. 8.3a, b for cutting tools with zero and  $-25^\circ$  rake angles, respectively. The reference shear angle is defined

**Table 8.1** Experimental results and predicted shear angles by cutting/thrust force (M/LS/S)

Depth of cut ( $\mu\text{m}$ )	Rake angle = $0^\circ$	Shear angle ( $\phi$ )			Rake angle = $-25^\circ$	Shear angle ( $\phi$ )		
	$F_c/F_t$	M	LS	S	$F_c/F_t$	M	SL	S
10	6.39	43.05	41.11	38.61	2.73	34.95	24.90	37.40
15	6.62	43.20	41.41	38.91	3.02	35.83	26.66	39.16
20	7.51	43.71	42.41	39.91	2.88	35.43	25.86	38.36

**Table 8.2** FEM simulated results (uniform chip formation)

Depth of cut ( $\mu\text{m}$ )	Rake angle = $0^\circ$	Shear angle ( $\phi$ )			Rake angle = $-25^\circ$	Shear angle ( $\phi$ )		
	$F_c/F_t$	M	LS	S	$F_c/F_t$	M	SL	S
10	5.4130	42.27	39.53	37.03	1.8274	30.66	16.31	28.81
15	7.5063	43.71	42.41	39.91	1.8999	31.12	17.24	29.74
20	8.7197	44.23	43.46	40.96	1.9409	31.37	17.74	30.24

as the angle between the cutting direction and the shear direction of RSSB, as indicated in Fig. 8.2a2. The prediction errors of the shear angles by Merchant's model are further evaluated. For the zero rake angle tools at different depths of cut, the prediction errors are within 4%; however, large errors of over 100% can be found where Merchant's model fails (Table 8.3). The other modified (LS and S) model shows overcorrection in Fig. 8.3, as the physical basis of the correction is debatable.

Merchant's model actually determines an angle for the shear plane. As RSSB is commonly observed in ultra-precision microcutting, the "shear band" angle needs to be determined. The difference between the measured shear angle on the SEM images ( $\phi_{\text{SEM}}$ ) and the shear angle predicted by Merchant's model based on the experimental data ( $\phi_{\text{MExp}}$ ) for a cutting tool with a  $-25^\circ$  rake angle is shown in Table 8.4. The source of such large prediction error is plotted in Fig. 8.14a, where a single block of a deformed chip with RSSB is shown. The total thickness of the block is  $l_A + l_B$ , and the RSSB has a thickness of  $l_B$ . The thicknesses and the lengths of shear bands  $l_{\text{SB}}$  can be measured directly from the SEM micrographs. The prediction error of Merchant's model ( $\Delta\phi$ ) can be estimated by the triangular relationship in Eq. (8.4).

$$\Delta\phi = \arctan\left(\frac{l_A + l_B}{l_{\text{SB}}}\right) \quad (8.4)$$

However, the calculation errors on the shear angles by the RSSB models do not exceed 6%, as shown in the last column of Table 8.4. In Merchant's equation, the cutting force is calculated by integration over the thickness of the whole block (as indicated in Fig. 8.2a2) in Eq. (8.5), where the integration area is denoted by  $A_{\text{AB}}$ , and the width of the chip (the thickness of the workpiece sample) is denoted by  $w$ .

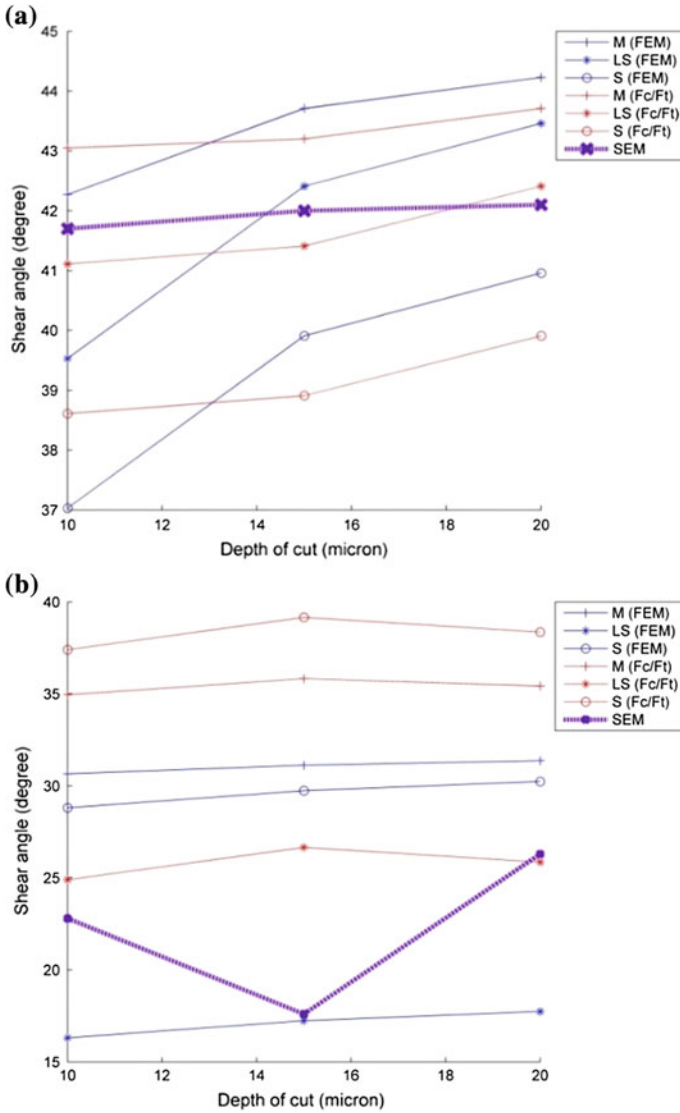


**Fig. 8.3** Prediction of shear angles in orthogonal cutting with a cutting tool of **a** 0° rake angle and **b** -25° rake angle. In the calculation, cutting force data are acquired in straight cutting experiments and finite element simulations. The reference shear angle is measured on SEM micrographs



**Table 8.3** Measured shear angle from SEM images

Depth of cut ( $\mu\text{m}$ )	Measured shear angle, $\phi_{\text{SEM}}$ ( $^\circ$ ) (rake angle = $0^\circ$ )	Variation from predicted shear angle by Merchant's model, $(\phi_{\text{M}} - \phi_{\text{SEM}})/\phi_{\text{SEM}}$ (rake angle = $0^\circ$ )	Measured shear angle, $\phi_{\text{SEM}}$ ( $^\circ$ ) (rake angle = $-25^\circ$ )	Variation from predicted shear angle by Merchant's model, $(\phi_{\text{M}} - \phi_{\text{SEM}})/\phi_{\text{SEM}}$ (rake angle = $-25^\circ$ )
10	41.7	1.35 (+3.24%)	22.8	12.15 (+53.30%)
15	42.0	1.2 (+2.86%)	17.6	18.23 (+103.6%)
20	42.1	1.61 (+3.82%)	26.3	9.13 (+34.71%)

**Table 8.4** Difference between shear plane angle (predicted by Merchant's model) and shear band angle (observed from SEM images)

Depth of cut ( $\mu\text{m}$ )	Measured shear angle, $\phi_{\text{SEM}}$ ( $^\circ$ ) (rake angle = $-25^\circ$ )	$\Delta\phi$ (rake angle = $-25^\circ$ )	Calculation error with $(\phi_{\text{RSSB}} - \phi_{\text{SEM}})/\phi_{\text{SEM}}$ (rake angle = $-25^\circ$ ) (%)
10	22.8	12.8043	5.39
15	17.6	19.2900	5.81
20	26.3	9.6480	5.67

$$F_{\text{M}} = \int_{A_{\text{AB}}} \sigma \, dA_{\text{AB}} \quad (A_{\text{AB}} = (l_{\text{A}} + l_{\text{B}}) \cdot w) \quad (8.5)$$

On the other hand, the shear band model integrates the stress in a much smaller area. Since  $l_{\text{B}} \cdot w \ll (l_{\text{A}} + l_{\text{B}}) \cdot w$  and the shear band model integrates only the stress induced by the elastic strain in the large area  $l_{\text{A}} \cdot w$ , thus the resulting cutting force is much smaller than that predicted by Merchant's model. In turn, using the proposed theory of RSSB, a smaller shear angle is predicted which is close to the experimental results ( $\phi_{\text{SEM}}$  in Table 8.4).

## 8.3 Finite Element Method Modelling for Elastic Strain-Induced Shear Bands

### 8.3.1 Characterisation of Elastic Strain-Induced Shear Bands

Machining of copper-based alloys tends to produce irregularly spaced chip serrations. However, turning cold-rolled material can sometimes produce regularly spaced chip serrations. Regularly spaced chip serrations are indeed layers of shear bands that grow and agglomerate to become chip serrations. The morphology of parallel adiabatic shear bands in the serrated chips (Fig. 8.2a2) can be observed directly on the polished surface with a scanning electron microscope.

Taking account of the cyclic behaviour in chip formation (Fig. 8.2a2), a zero-feed face cutting experiment was conducted to explore the cyclic feature on the machined surface of aluminium alloy. Aluminium alloy 6061 (alloyed with magnesium and silicon) is easy to machine and can be precipitation-hardened. It is a common work material which can be used to produce reflectors and high precision components in ultra-precision machining. A rod Al6061-T6 workpiece with a diameter of 12.7 mm was mounted with a vacuum chuck on the air spindle of an Optoform 30 (Rank Pheumo) single point diamond turning machine. The face cutting was performed with a spindle speed of 2000 rpm and a depth of cut of 10  $\mu\text{m}$ . A single point diamond cutting tool (tool nose radius 1.48 mm) was employed in the experiment. In order to eliminate the influence induced by the variation of the surface cutting speed, the feed rate was set to 0 mm/min. The cutter moves towards the workpiece with the depth of cut increasing from zero to its maximum (set at 10  $\mu\text{m}$ ). The cutting location was chosen at a radius of 5 mm away from the centre of the workpiece. Thus, the surface speed was approximately 62.8 m/min at the cutting location.

Figure 8.4a shows a photograph of the tool mark segment which was taken using an optical microscope. A series of notch-like marks lining up tangentially to the cutting direction can be observed inside the groove of the cutting marks. To calculate the frequency, or the cycle of the generation of such marks, the distance between two notch-like marks is measured with the help of the non-contact optical profiler Wyko NT8000. The average distance  $s$  is calculated to be around 73.7  $\mu\text{m}$  based on the original 2D profile data in Fig. 8.4b. The frequency ( $f_{\text{calc}}$ ) of the generation of the notch-like tool marks can be calculated by Eq. (8.6).

$$f_{\text{calc}} = \frac{\text{Cutting speed}}{\text{Avg. notch dist. (s)}} = \frac{2\pi \times 5 \text{ mm} \times (2000 \text{ rpm}/60 \text{ s})}{0.0737 \text{ mm}} \approx 14.2 \text{ kHz} \quad (8.6)$$

## 8.3.2 Finite Element Method Modelling

### 8.3.2.1 Setup of Finite Element Model

With regard to the micro-cutting conditions in the experiment, the quasi-static finite element model is built on the assumption that the imposed strain rate is constant and the induced strain is assumed to pass through the workpiece at a finite rate. The subsequent localised plastic deformation in the form of shear bands is due to work softening. Since the depth of cut is a thousand times larger than the round-edge radius of the diamond tool employed in the experiment on a single point diamond turning machine, the round-edge effect is ignored in the study. The stiffness of the diamond tool is much higher than that of the work materials; the cutting tool is assumed to be rigid in the models.

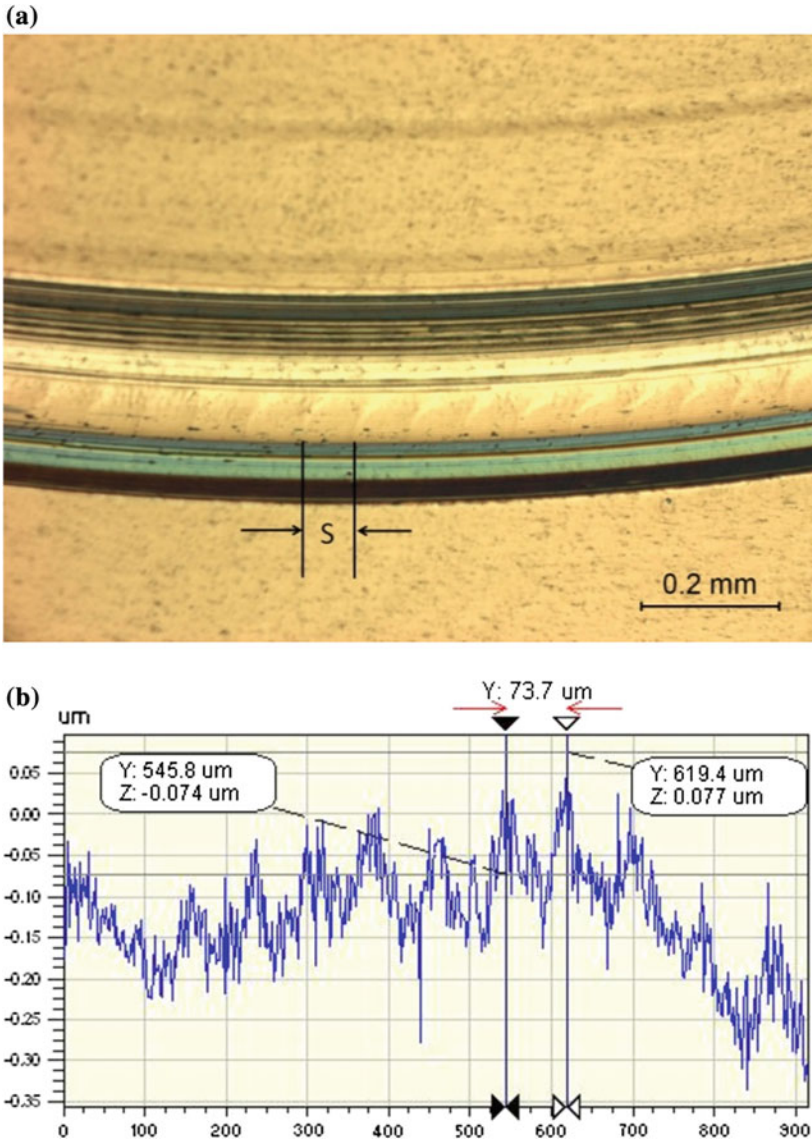


**Fig. 8.4** a Notch-like marks lining up tangentially to the cutting direction in the zero-feed cutting on Al6061-T6 workpiece and b measurement of distance (s) in 2D profile

The objective of the FEM modelling is to investigate the inducing factor (elastic strain concentration) established before the formation of the shear bands, i.e. the factor leading to the onset of the highly localised material softening effects. The catastrophic plastic deformation during the propagation of shear bands is expected to produce a tremendous heating effect and sharp temperature rise making most of

the assumed parameters like elastic modulus and yield point no longer constant. Therefore, the FEM model is only applicable up to the very moment immediately before the initiation of shear bands.

The heavily cold-rolled brass used in the experiments, as discussed in this chapter, is stable in terms of texture development, subject to the applied cutting condition. The crystal texture revealed under X-ray pole figure confirmed that they do not change upon further deformation. The heavily cold-rolled brass is mainly deformed elastically over the stressed volume before failing by adiabatic shear bands (ASBs) concentrated over a very small volume in the form of intensive plastic deformation. The geometric parameters of the model are derived from information collected from SEM (Fig. 8.2a2). Furthermore, the effect of tool-chip friction is ignored because no obvious heating effect has been observed on the cutter side of the chip as compared with that on the free side.

The constitutive equation required by the FEM model is developed to simulate the strain–stress relationship leading to the formation of shear bands. The constitutive model (TANH) developed by Calamaz et al. (2011) is adopted to describe the strain softening effect. The TANH model (Eq. 8.7) is based on the Johnson–Cook (JC) model (Johnson and Cook 1985) (Eq. 8.8) and the hypothesis of dynamic recovery and recrystallisation mechanism in adiabatic shear bands. The TANH model can capture the strain softening phenomenon, i.e. the flow stress decreases when the strain reaches a particular value. With the local temperature increasing, the flow stress will decrease more steeply in the TANH model than in the JC model, due to the different softening mechanisms behind the mathematical equations.

$$\sigma = \left( A + B\varepsilon^n \left( \frac{1}{\exp(\varepsilon^a)} \right) \right) \left( 1 + c \ln \frac{\dot{\varepsilon}}{\dot{\varepsilon}_0} \right) \left( 1 - \left( \frac{T - T_r}{T_m - T_r} \right)^m \right) \left( D + (1 - D) \tanh \left( \frac{1}{(\varepsilon + S)^\varepsilon} \right) \right)$$

with  $D = 1 - \left( \frac{T}{T_m} \right)^d$  and  $S = \left( \frac{T}{T_m} \right)^b$

(8.7)

$$\sigma = (A + B\varepsilon^n) \left( 1 + C \ln \frac{\dot{\varepsilon}}{\dot{\varepsilon}_0} \right) \left( 1 - \left( \frac{T - T_r}{T_m - T_r} \right)^m \right),$$
(8.8)

where  $A$ ,  $B$ ,  $C$ ,  $n$  and  $m$  are the constants of the Johnson–Cook model,  $a$ ,  $b$ ,  $c$ ,  $d$  are material constants obtained by the experiments in the TANH model,  $\sigma$  is the equivalent flow stress,  $\varepsilon$  the equivalent plastic strain,  $\dot{\varepsilon}$  and  $\dot{\varepsilon}_0$  are the equivalent and reference equivalent plastic strain, and  $T$ ,  $T_r$  and  $T_m$  are the workpiece temperature, room and melting temperature, respectively.

The constants of Johnson–Cook and TANH law of brass and Al 6061 are given by Johnson et al. (1983) and Rule (1997), respectively. The thermal conductivity of brass is 121 W/m K and the specific heat is 386.7 J/kg °C (Table 8.5).

Cold-rolled brass is heavily textured and can be described by the ideal orientation  $\{110\}$   $\langle 112 \rangle$ , with orientation spread linking  $\{011\}$   $\langle 211 \rangle$  with  $\{011\}$   $\langle 100 \rangle$  (Lee and Duggan 1988). In order to consider the texture effect on the simulation

**Table 8.5** The constants of Johnson–Cook law of brass

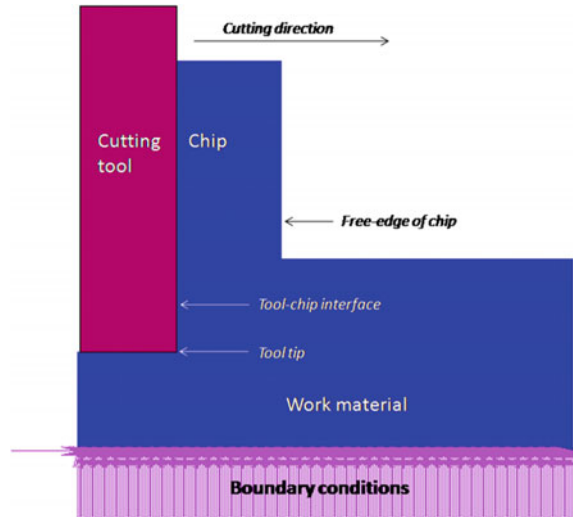
Material	A (MPa)	B (MPa)	$n$	C	M	$T_m$ (K)
Brass	62	186	0.34	0.007	0.5	1189
Al6061	293	121.26	0.23	0.002	1.34	855

results, the values of elastic modulus and hardness are measured by nano-indentation tests on 90% cold-rolled  $\alpha$ -brass. The average elastic modulus of 66.67 GPa and hardness of 2.49 GPa are obtained based on the loading–unloading curves. The adoption of estimated parameters utilised in the FEM model is based on the methodology employed by Simoneau et al. (2006).

The JC model (Johnson and Cook 1983) has been proposed for a wide range of materials subjected to large strains, high strain rate and high temperatures, which are also the appropriate machining conditions. Thus, the JC model is widely adopted in finite element modelling of machining and micro-cutting processes (Davim and Maranhao 2009; Calamaz et al. 2011; Zong et al. 2007; Budak and Ozlu 2008). It is commonly understood that the depth of cut in single point diamond turning is usually less than the average grain size of a polycrystalline aggregate (Sze et al. 2006), thus the isotropic constitutive model is invalid. However, in the straight cutting experiments in this section, the brass work material has been cold rolled with a thickness reduction of more than 90%. After the cold-rolling process, the grains are elongated along the rolling direction (RD) and compressed down to less than 5  $\mu\text{m}$  on average along the normal direction (ND). In the succeeding straight cutting experiment, the diamond tool moves along RD and removes the material on the RD-ND plane with a depth of cut of 15  $\mu\text{m}$ . Thus, the straight cutting is actually performed on a large set of aggregated grains along ND. In such a heavily textured work material, the orientation of the grains and the grain size measured along ND tends to be similar. Thus, the finite element takes on the assumption of uniform work material. Furthermore, as measured in Table 8.3, the shear angles are very close to  $45^\circ$  for straight cutting with zero rake angle tools. Therefore, anisotropic crystal plasticity is not a dominant factor in this straight cutting experiment. In other words, the orthogonal microcutting is along the rolling direction (RD) with a plane strain assumption, and the semi-quantitative research is focused on the stress states and the elastic strain-dominated PDZ leading to the onset of the highly localised material softening effects. With the assumptions of plane strain and elasticity-dominated PDZ, an isotropic JC constitutive equation is adopted, without taking crystal plasticity into consideration.

Based on the above-mentioned assumptions, a simplified finite element model (Fig. 8.5) is employed for the analysis of the micro-cutting process with predefined chip morphology according to the chip geometry imaged by SEM (Fig. 8.2a2). In the finite element model, a rigid cutting tool is moving along the cutting direction, and the displacement boundary conditions are applied to the bottom of the work-piece to disable any displacement on the bottom nodes during simulation. The rigid-deformable contact condition is included in the model to define the contact

**Fig. 8.5** FE model for micro-cutting process with predefined chip morphology



boundary condition at the tool-chip and the tool-workpiece interfaces. This finite element model holds for the problem of plane strain orthogonal cutting. Plane strain is assumed in the FE model, which is valid for orthogonal cutting or straight cutting. In orthogonal cutting, the following conditions are satisfied: (1) the tool is perfectly sharp and there is no contact along the clearance face; (2) the shear surface is a plane extending upward from the cutting edge; (3) the cutting edge is a straight-line extending perpendicular to the direction of motion and generates a plane surface as the work moves past it; (4) the chip does not flow to either side (plane strain); (5) the depth of cut is constant; (6) the width of the tool is greater than that of the workpiece; (7) the work moves relative to the tool with uniform velocity; (8) a continuous chip is produced with no build-up edge and (9) the shear and normal stresses along the shear plane and tool are uniform (strength of materials approach). Such an ideal two-dimensional cutting operation is referred to as orthogonal cutting that completely suppresses the concept of inhomogeneous strain by assuming that the material behaves in a completely homogeneous fashion (Shaw 2005). The heat generation in the PSZ is related to the initiation and formation of adiabatic shear bands. Trent and Wright (2000) stated that 99% of the work done is contributed to heat the chip, the tool and the work material because of the very large amount of plastic strain (in PSZ). In the finite element model described in this chapter, the heat generation due to plastic work is defined in MSC.Mentat through the PLASTIC HEAT GENERATION option as the heat transfer boundary condition applying to all the elements. Room temperature is set in the initial condition, as required by the Johnson–Cook model ( $T_{\text{room}} < T < T_{\text{melt}}$ ).

### 8.3.2.2 Simulation Results and Analysis

The output of the simulation results includes the elastic and plastic strain/stress, the cutting force on the rigid cutting tool, the plastic strain work, etc. The simulated evolution of the equivalent elastic strain is shown in Fig. 8.6. The scalar quantity equivalent strain is often used to describe the state of strain in solids. The equivalent strain ( $\epsilon_{eq}$ ) is calculated with the deviatoric strain tensor ( $\epsilon^{dev}$ ):

$$\epsilon_{eq} = \sqrt{\frac{2}{3} \epsilon^{dev} : \epsilon^{dev}} = \sqrt{\frac{2}{3} e_{ij}^{dev} e_{ij}^{dev}} \tag{8.9}$$

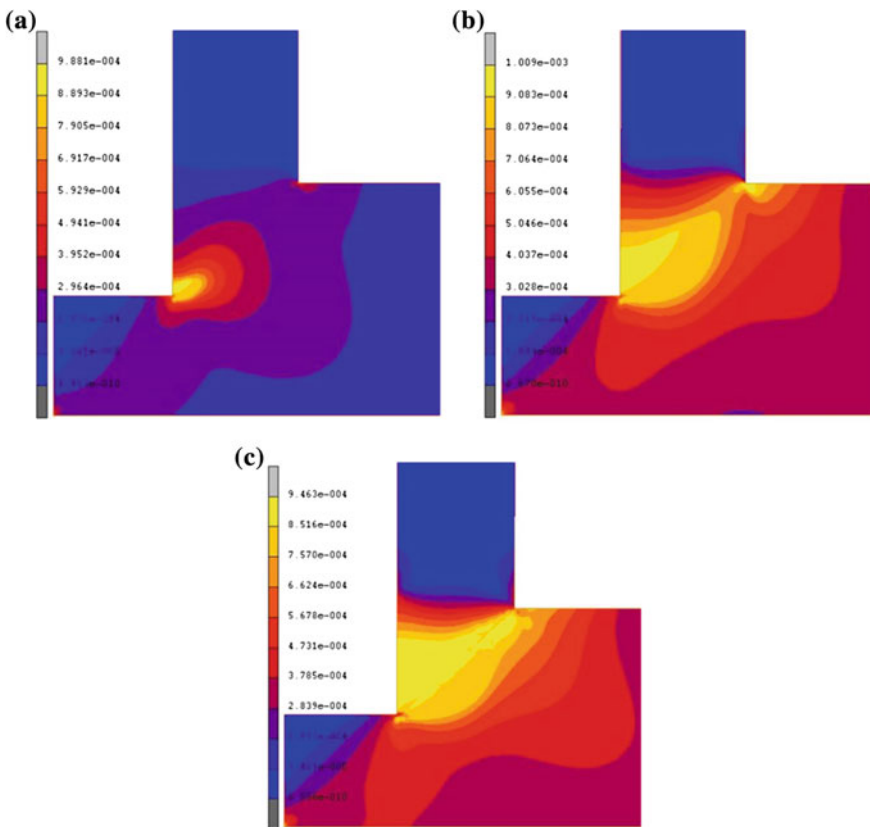


**Fig. 8.6** Evolution of equivalent elastic strain: **a** the onset of elastic strain concentration at the free edge of a chip; **b** the evolution of elastic strain with the advancing of the cutting tool; **c** formation of shear band

where

$$\boldsymbol{\varepsilon}^{\text{dev}} = \boldsymbol{\varepsilon} - \frac{1}{3} \text{tr}(\boldsymbol{\varepsilon}) \mathbf{1} = \varepsilon_{ij} - \frac{\varepsilon_{kk}}{3} \delta_{ij} \quad (8.10)$$

The equivalent strain is the work conjugate to the equivalent stress defined as:

$$\sigma_{\text{eq}} = \sqrt{\frac{3}{2} \boldsymbol{\sigma}^{\text{dev}} : \boldsymbol{\sigma}^{\text{dev}}} \quad (8.11)$$

In general, the elastic strain is concentrated at the tool tip region first, then at the free edge of the chip (Fig. 8.6a). Figures 8.6b, c show the increasing and releasing of the concentration of the elastic strain, respectively. The equivalent plastic strain is shown in Fig. 8.7, from which it can be inferred that the concentration of the elastic strain on the free-edge side induces plastic deformation in a relatively small region, and then the plastic deformation propagates from the free edge towards the tool tip.

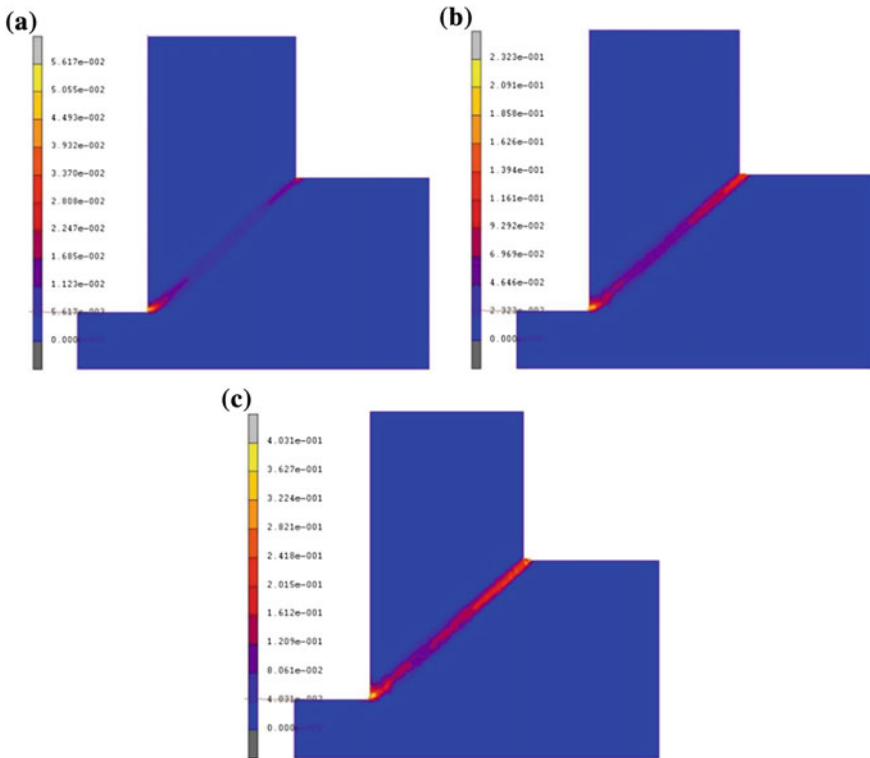


**Fig. 8.7** Evolution of equivalent plastic strain: **a** the onset of plastic strain concentration at the free edge of a chip; **b** propagation from the free edge; **c** formation of shear band



The Initiation of Shear Bands

The equivalent of the Cauchy stress distribution in the PSZ is shown in Fig. 8.8. The inhomogeneous elastic strain concentration occurs in the narrow zone shown between the two broken lines. At a constant strain rate, the elastic stress is first concentrated in the area denoted by B1 (tool tip).

The imposed elastic strain is transmitted at a finite rate in the PSZ. Thus, the elastic stress concentration occurs at location A1 (the corner of the free surface of the chip). When the local stress at A1 exceeds the material elastic limit, it undergoes plastic deformation to release the stress. In such cases, the elastic strain evolves into plastic strain which in turn triggers the release of energy in the form of heat. From the simulation result, it can be observed that the shear band is initially induced by the elastic stress concentration at A1 (Fig. 8.8) on the free edge of the chip.

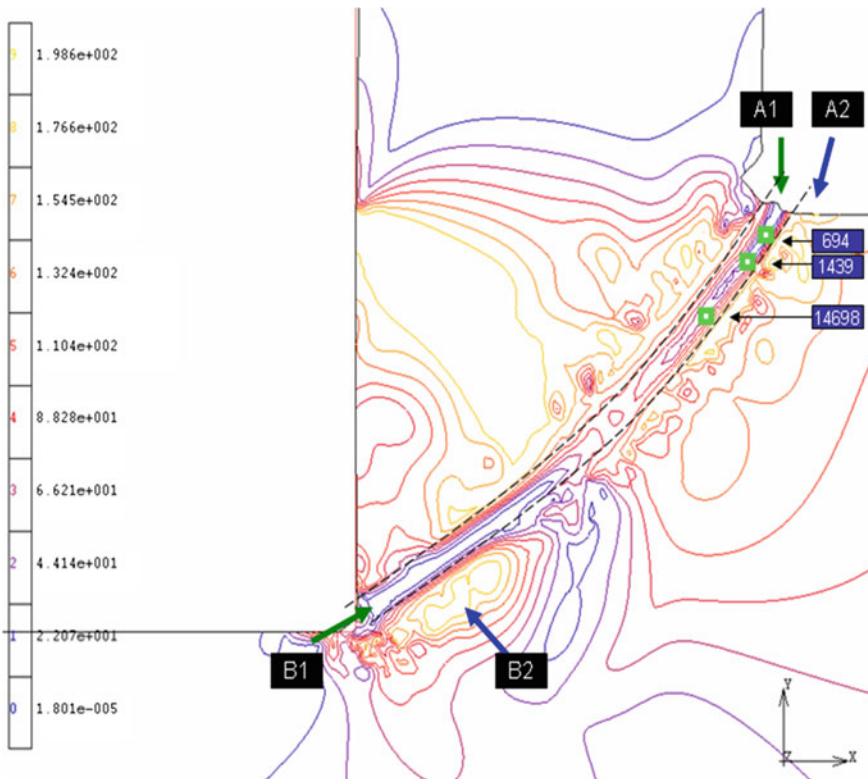
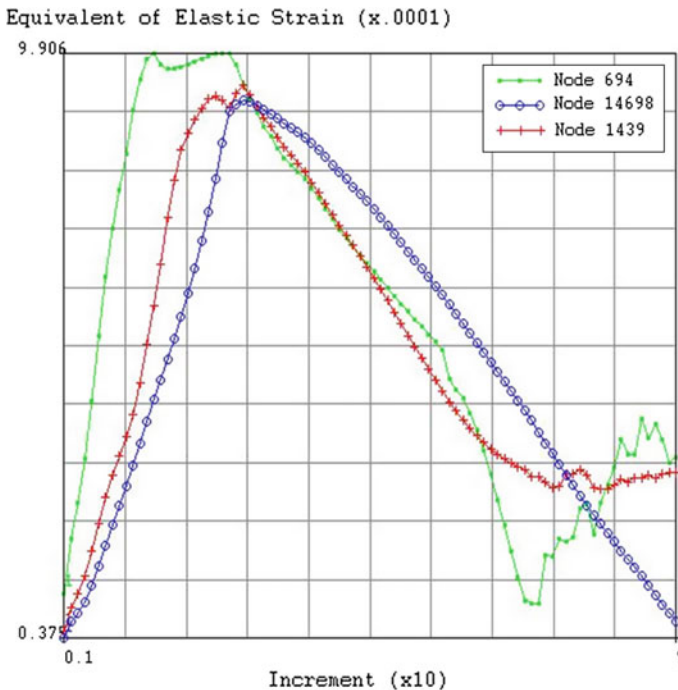


Fig. 8.8 Equivalent of Cauchy stress (in MPa) in primary deformation zone

### The Propagation of Shear Bands

Due to the work-softening behaviour of the work material, the localised plastic strain in the form of shear bands propagates from the free edge towards the tool tip location. This can be observed in Fig. 8.7a–c, accompanied by the stress release in Fig. 8.6a–c. The simulated output is analysed on the three designated nodes (numbered 694, 1439, and 14698) in the PDZ. Node 694 is closest to the free edge of the chip, and node 14698 is farthest from the free edge, leaving node 1439 in between. The equivalent elastic strain on the three nodes is shown in Fig. 8.9. The elastic strain is concentrated at these three nodes sequentially, namely the peak of the elastic strain on node 694 comes first; after this a sharp drop of elastic strain takes place due to the induced plastic strain, then the same procedure is repeated on nodes 1439 and 14698, one after another. Thus, Fig. 8.9 suggests that the shear band propagates from the free edge towards the tool tip step by step. Such a propagation process is accomplished through the repeated elastic–plastic deformation cycles during the formation of shear bands in a very short period of time.

Furthermore, with the advancement of the cutting tool, the elastic-stressed chip above the formed shear band will be pushed upward and forward to follow the exact shape shown in Fig. 8.2a2. Meanwhile, the elastic stress concentration that can be found in regions A2 and B2 (Fig. 8.8) facilitates the repeated production of serrated



**Fig. 8.9** Equivalent of elastic strain on the three selected nodes in the primary deformation zone

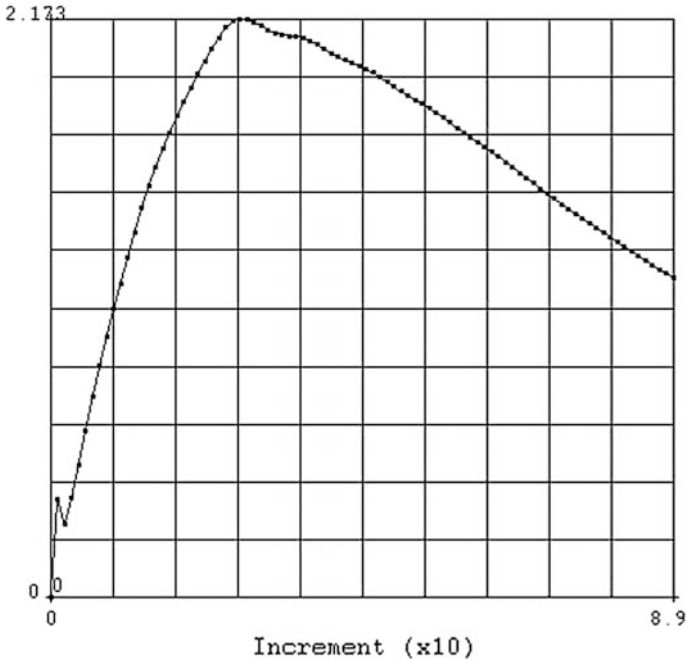


**Fig. 8.10** Simulated curve of cutting force (vertical axis, unit: N) on cutting tool with load drop

chips. The load drop on the cutting tool is due to the single coarse shear band formation during the cutting process as depicted in Fig. 8.10. Before the formation of the single shear band, the elastic energy accumulates. Thus, the cutting force is increased momentarily and immediately before a coarse shear band is formed. With the emergence of a single coarse shear band, the plastic deformation releases the stored elastic energy which leads to a load drop on the cutting tool.

#### 8.4 Analytical Model of Shear Band Formation and Influences

Elastic strain accumulates over a much larger volume inside the PSZ, while the shear bands occur in a small fraction of volume. The abrupt discharge of the elastic strain energy provides the triggering force for the formation of a relatively thin shear band. Given that machining is carried out at a constant displacement rate, the imposed stress is alleviated very quickly, whereas the plastic strain increases. Without the help of accumulated elastic strain, the development of the shear band is expected to be retarded by diminishing imposed stress. Thus, an elastic strain-induced shear band is important because it can explain why a slowly imposed

strain rate could trigger a higher strain rate inside the shear band under a constant cutting speed. An analytical model is proposed to study the different stages of the formation of ASBs and their influence on the cutting force and morphology of chips.

### 8.4.1 Onset of the Formation of Shear Bands

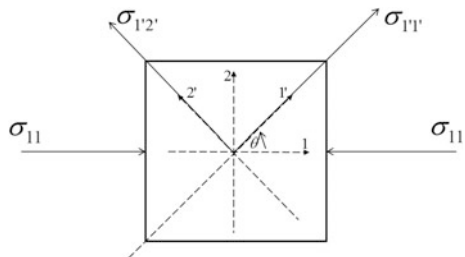
An infinitesimal element is selected in the PDZ to investigate the stress status during the formation of the shear bands (Fig. 8.11). For simplicity, only the dominant factors are considered. The friction force and other stresses remotely associated with the shear band are ignored. Before the formation of shear bands, simple compression along the cutting direction can be assumed in the coordinate system 1–2. The shear stress  $\sigma_{1'2'}$  can be calculated from Eq. (8.12), where  $\theta$  is the angle between the coordinates 1–2 and 1'–2'. The yield point of the work material along the shear plane is written as  $\tau_{\text{yield}}$ . Thus, if the shear stress  $\sigma_{1'2'}$  is smaller than  $\tau_{\text{yield}}$ , the material undergoes elastic deformation; if  $\sigma_{1'2'}$  goes beyond  $\tau_{\text{yield}}$ , the formation of adiabatic shear bands is induced.

$$\begin{cases} \sigma_{1'1'} = \frac{\sigma_{11}}{2}(1 + \cos 2\theta) \\ \sigma_{1'2'} = \frac{\sigma_{11}}{2}\sin 2\theta \end{cases} \quad (8.12)$$

From the aspect of elastic strain energy of the work material related to chip formation, the elastic strain energy in the PDZ  $E_{\text{wp}}^e$  can be obtained by Eqs. (8.13) and (8.14). Equation (8.13) is used to calculate the accumulated energy in the elastically deformed infinitesimal element, while Eq. (8.14) provides a generic expression in the three-dimensional space and is applicable to both linear and nonlinear elasticity. The two-dimensional analytical model can be derived as a special case of Eq. (8.14) accordingly.

$$dE_{\text{wp}}^e = \int \sigma_{ij} d\epsilon_{ij} \quad (8.13)$$

**Fig. 8.11** The stress in an infinitesimal element in the primary deformation zone before the onset of adiabatic shear bands



$$E_{wp}^e = \int (dE_{wp}^e) dV = \int \left( \int \sigma_{ij} d\epsilon_{ij} \right) dV \tag{8.14}$$

In the analytical model, the cutting tool is regarded as a deformable body with a much greater Young’s modulus and yield point than the work material. Therefore, due to the contact between the tool and work material during the micro-cutting process, if the system is confined to consisting of only the tool and the work material, the total energy of the system is conservative. Thus, the cutting tool also stores elastic energy. The amount of the energy  $E_{tool}^e$  satisfies Eq. (8.15), and it can also be denoted as  $E_{tool}^+$ , which is the increment of the elastic energy on the cutting tool.

$$E_{tool}^e = E_{wp}^e = E_{tool}^+ \tag{8.15}$$

Equation (8.14) holds for the total energy in the loading–unloading cycle of chip formation, with the assumption of conservation of energy. For a period from  $t_0$  to  $t_3$  as plotted in Fig. 8.12, the total energy  $E$  can be obtained by integration of the power within a chip formation cycle, i.e.  $\int_{t_0}^{t_3} P dt$ . Furthermore, regarding the small deformation in the elastic state of the tool tip, a beam bending model can be adopted to describe the energy accumulated in the cutting tool tip. Consider the beam is under a bending moment  $M$  and all the displacements on one end of the beam are constrained. A small element is selected with the edge rotation angle  $\theta$ . Thus the work done on the selected element can be expressed by Eqs. (8.16) and (8.17), where  $x$  is the length away from the fixed end, and  $E$  and  $I$  are Young’s modulus

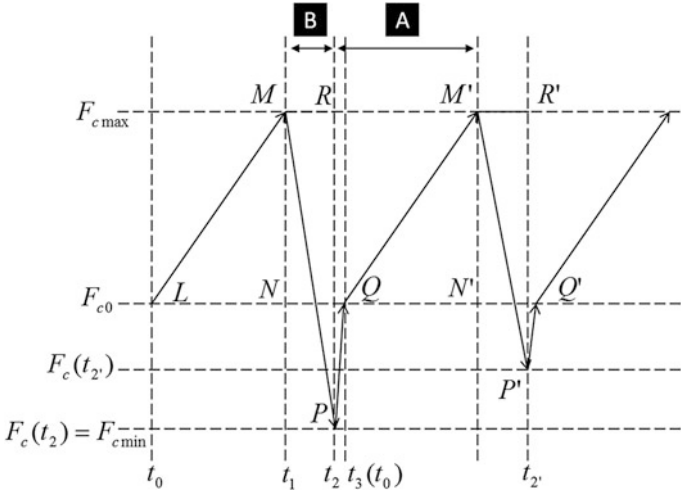


Fig. 8.12 The schematic diagram of cyclic fluctuation of cutting force against time

and the moment of inertia, respectively. Therefore, the energy increment on the tool tip can be obtained by the integration in Eq. (8.18).

$$dV_\varepsilon = dW = \frac{1}{2}Md\theta \quad (8.16)$$

$$d\theta = \frac{d^2w}{dx^2}dx = \frac{M}{EI}dx \quad (8.17)$$

$$E_{\text{tool}}^+ = V_\varepsilon = \frac{1}{2} \int Md\theta = \frac{1}{2} \int \frac{M^2}{EI} dx = \frac{M^2l}{2EI} \quad (8.18)$$

### 8.4.2 Formation of Shear Bands

During the formation of adiabatic shear bands, the heat-induced softening effect takes place in the PSZ. A theoretical calculation to estimate and explain the temperature rise in PSZ can be found below (Trent and Wright 2000):

$$\Delta T_p = \frac{k_p V_s}{\rho c V_n} (1 - \beta), \quad (8.19)$$

where  $\Delta T_p$  denotes the temperature rise in PSZ,  $V_s$  and  $V_n$  are the shear velocity and the velocity normal to the shear plane,  $\rho$  and  $c$  are the density and specific heat of work material, and  $\beta$  is the proportion of heat generated that conducts into the work material.  $V_s$  and  $V_n$  can be calculated from the simple hodograph for machining. In the straight cutting experiment in the present study, sharp and straight shear bands with regular spacing can be observed in Fig. 8.2a2. This observation implicitly justifies the condition  $V_n \ll V_s$ ; otherwise the clear shear bands are curved or cannot appear at all. Therefore, the value of the temperature rise  $\Delta T_p$  can be considerably high in the PSZ leading to material softening and the formation of shear bands, although a relatively lower temperature rise may be present in a larger volume of chip due to heat conduction and dissipation.

According to the simulation result of the FEM model, the load drop on the cutting tool can be found from Fig. 8.10. Since the cutting tool is elastically deformed, during the formation of ASBs, the load drop will lead to the release of the stored elastic energy ( $E_{\text{tool}}^-$ ). A real variable  $k_+$  is introduced to describe the energy transfer (Eq. 8.20). If  $k_+ = 1$ , the previously stored elastic energy is fully released. We define this situation as “full disengagement” on the tool-chip interface. If  $k_+ < 1$ , only a part of the stored elastic energy is released so we define such a situation as “partial disengagement”. However, the term “disengagement” does not necessarily imply that there is no contact between the tool tip and the work material in the tool-chip interface. Such “disengagement” can be interpreted as a state in

which the induced force on the tool tip is smaller than the reference force  $F_{c0}$ , as shown in Fig. 8.12. Thus, when “full disengagement” takes place, the cutting force of the tool tip will drop from the maximum  $F_{c\max}$  to its minimum  $F_{c\min}$  (segment  $\overrightarrow{MP}$ ). When “partial disengagement” takes place, the cutting force of the tool tip will drop from the maximum  $F_{c\max}$  to  $F_c(t_2)$ , whose value lies between  $F_{c\min}$  and  $F_{c0}$  (segment  $\overrightarrow{M/P'}$ ). No matter which type of disengagement plays the role of releasing the stored elastic energy on the tool tip, the succeeding cutting force (at the moment  $t_2$  or  $t_2'$ ) will be below the reference cutting force  $F_{c0}$ ,

$$k_+^- = \frac{E_{\text{tool}}^-}{E_{\text{tool}}^+} \in (0, 1] \quad (8.20)$$

Looked at from the point of view of the transformation of the elastic energy, the accumulation of elastic energy on the tool tip ( $E_{\text{tool}}^+$ ) is determined by the area of  $\Delta\text{LNM}$  ( $A_{\Delta}^+$ ), and the dissipation of elastic energy on the tool tip ( $E_{\text{tool}}^-$ ) is determined by the area of  $\Delta\text{MPR}$  ( $A_{\Delta}^-$ ). Although the curves LM and MP are not necessarily straight lines, for simplicity, we still adopt straight lines in the schematic diagram in Fig. 8.12 and a triangular sign  $\Delta$  in the expressions. According to the conservation law for the system energy, the equality of Eq. (8.21) must be satisfied in order to produce a case of full disengagement, with the condition of a constant cutting speed. Similarly, for the case of partial disengagement, the condition of Eq. (8.21) should be modified as  $(A_{\Delta}^+) > (A_{\Delta}^-)$ . Furthermore, based on the condition of Eq. (8.21) and  $(t_2 - t_1) < (t_1 - t_0)$ , it can be proven that  $F_c(t_2) < F_{c0}$ .

$$A_{\Delta}^+ = A_{\Delta}^- \quad (8.21)$$

### 8.4.3 An Analytical Model of Cyclic Fluctuation of Cutting Force

Based on the schematic diagram in Fig. 8.12, the complete cycle can be found as  $t_0 \rightarrow t_1 \rightarrow t_2 \rightarrow t_3$  ( $t_0$ ). In the stage  $t_0 \rightarrow t_1$ , the cutting force increases with the accumulation of elastic energy on the tool tip. In the stage  $t_1 \rightarrow t_2$ , the formation of ASBs leads to a decrease in cutting force and the full or partial disengagement on the tool-chip interface. In the stage  $t_2 \rightarrow t_3$  ( $t_0$ ), the tool-chip engagement is recovered, and the cutting force rises to the value of the reference cutting force to complete one cycle. Actually, the frequency of the cyclic fluctuation of the cutting force can be found in the experiment.

According to the above analysis, the cutting force can be expressed in the generic form in Eq. (8.22). The cutting force is a function of the cycle time ( $t_c$ ) and the cutting time ( $t$ ), and consists of two parts, i.e. the cutting force induced by perfectly plastic deformation ( $F_c^{\text{PP}}$ ) and the superposed force ( $F_c^{\text{SP}}$ ). The part  $F_c^{\text{PP}}$

is based on the reference cutting force  $F_{c0}$ , and part  $F_c^{\text{SP}}$  is adopted to introduce the cyclic fluctuation into the model.  $k_1$ ,  $k_2$  and  $a$  are constants obtained from experiments.  $\varsigma$  is the fraction of the cycle time over the maximum possible cycle time. The function  $f(t)$  is in the form of Eqs. (8.24) and (8.25) with a finite value. In Eq. (8.26),  $\eta_t$  is employed to evaluate the ratio of the duration of stages A and B in Fig. 8.12. A rough estimation of the value of  $\eta_t$  is also given in Eq. (8.26), based on the direct measurement of the length ratio of  $l_A$  and  $l_B$  in Fig. 8.2a2.

$$F_c(t_c, t) = F_c^{\text{PP}} + F_c^{\text{SP}} = k_1(a - \varsigma)F_{c0} + k_2 t_c \cdot f(t) \quad (8.22)$$

$$\varsigma = \frac{t_c}{t_{c \max}} \leq 1 \quad (8.23)$$

$$f(t) = \begin{cases} f^+(t), & t \in \left[0, \frac{\eta_t}{1 + \eta_t} t_c\right] \\ f^-(t), & t \in \left[\frac{\eta_t}{1 + \eta_t} t_c, t_c\right] \end{cases} \quad (8.24)$$

$$\dot{f}^+(t) < 0, \dot{f}^-(t) < 0 \quad (8.25)$$

$$\eta_t = \frac{t_1 - t_0}{(t_3 - t_2) + (t_2 - t_1)} = \frac{t_1 - t_0}{t_3 - t_1} = \frac{t_A}{t_B} \approx \frac{l_A}{l_B} \quad (8.26)$$

As the value of  $(1 - \varsigma)$  increases (i.e. the cycle time decreases), the frequency of fluctuation increases and the amplitude decreases. Therefore, the serrated chips with ASBs will evolve into uniform chips without cyclic fluctuation of the cutting force, as determined by Eq. (8.27).

$$\lim_{t_c \rightarrow 0} F_c(t_c, t) = k_1 F_{c0} \quad (8.27)$$

The proposed model covers uniform and serrated chip morphology, which can be found to possess a good correlation with the experimental data and model in Recht's work (Recht 1964). Recht's model includes the conditions of uniform deformation, and serrated chips with closely and widely spaced zones based on the observation in their experiments. The experimental results and the chip morphology in this chapter are in line with Recht's work. Furthermore, the model presented in this chapter comprehensively investigates the different phases of the formation of shear bands and their influence on cutting force, the status of tool-chip contact and the cyclic behaviour of the tool-tip displacement during the cutting process.

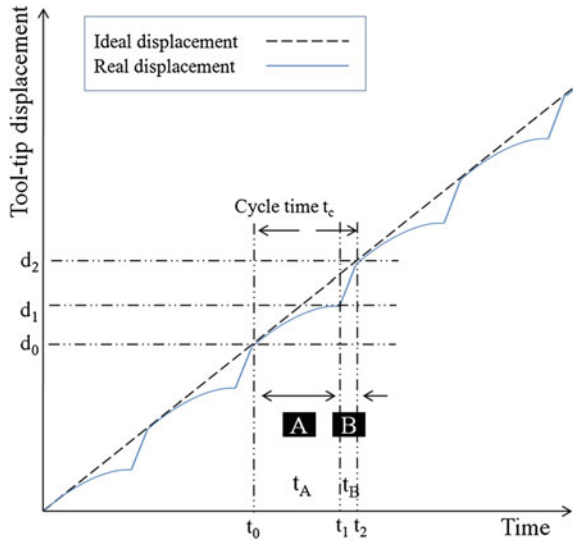


#### 8.4.4 *The Cyclic Fluctuation of the Displacement of the Tool Tip*

According to the image of the tool mark in the zero-feed face cutting experiment and the calculation of frequency, the cutting force during face cutting exhibits the characteristics of cyclic variation. The cyclic variation of cutting force is directly related to the formation of elastic strain-induced shear bands, which lead to the generation of serrated chips. For the sake of discussion, in this section, the cutting tool is not regarded as a rigid body though the elastic strains in the cutter tool induced by the cutting process will be much smaller than those in the workpiece. During the cutting process along the cutting direction, the cutting tool experiences two stages in one cycle (A–B) also as defined in Fig. 8.12: (1) in stage A, the work material engaging in contact with the cutting tool is elastically deformed, and the elastic strain energy in both the work material and tool tip increases until it reaches its maximum. Therefore, the cutting force increases with accumulation of elastic strain energy, as shown by the increasing segment of the curve simulated in Fig. 8.10; (2) in stage B, the abrupt load drop occurs at the turning from stage A to stage B, where the adiabatic shear band is formed suddenly. In the cutting tool, the accumulated elastic strain energy is released in a short period of time. The transition from stage A to B is also regarded as the cause of the notch-like tool marks identified.

A schematic diagram is given in Fig. 8.11 to explain the cyclical behaviour of the tool tip during the cutting process with the formation of ASBs and serrated chips. As the cutting process is designed to take place at a constant speed, the ideal displacement of the tool tip can be depicted as a broken straight line, as shown in Fig. 8.11. However, in actual practice and according to the above analysis, tool-tip displacement can be decelerated momentarily. This phenomenon is shown in the solid lines drawn in Fig. 8.13. The start time of one cycle is denoted as  $t_0$  and the end as  $t_2$ , while the transition point from stage A to B is denoted as  $t_1$ . The corresponding tool-tip displacements ( $d$ ) are denoted with the same subscript numbers. From  $t_0$  to  $t_1$ , due to the accumulation of elastic strain energy in stage A, the velocity of the tool tip is decreased nonlinearly to the minimum at time  $t_1$ . Regarding the aspect of displacement, the displacement value goes from  $d_0$  to  $d_1$  which deviates from the ideal case. The formation of ASBs at the beginning of stage B ( $t_1$ ) releases the stress on the tool tip; therefore, the tool tip accelerates to meet the ideal displacement (from  $d_1$  to  $d_2$ ) with a much faster velocity (the slope of the segment of solid line in stage B). During the formation of serrated chips, the stage A–B cycle repeats itself, and the true cutting speed fluctuates around the expected mean cutting speed of the ideal case. Moreover, the same fluctuation is valid for the cutting force. In stage A, due to the accumulation of the elastic strain energy on the tool tip, the cutting force, whose value can be recorded by a force sensor and an oscilloscope, increases. The onset of load drop is found at the moment when the transition from stage A to B takes place. In stage B, due to the release of the previously accumulated elastic strain energy, the cutting force is then

**Fig. 8.13** The cyclical behaviour of the tool tip during the cutting process with formation of adiabatic shear bands and serrated chips



decreased. Such a cycle is repeated with the entire micro-cutting process at a particular frequency and in line with the frequency of the generation of chip serrations.

The cyclic behaviour of tool-tip displacement contributes to the variation of induced strain rates during the micro-cutting process. As a constant cutting speed is applied to the workpiece, the imposed strain rate ( $\dot{\epsilon}_{imp}$ ) remains constant while the tool tip is advancing. With regard to the previous analysis and Fig. 8.13, the induced strain rates in sections A ( $\dot{\epsilon}_A$ ) and B ( $\dot{\epsilon}_B$ ) follow the relationship in Eq. (8.28). The imposed strain rate is not always equal to the induced strain rate in chip formation (all terms are equal). The equality holds as long as Eq. (8.23) is satisfied, i.e. in the case of uniform chip formation.

$$\dot{\epsilon}_A \leq \dot{\epsilon}_{imp} \leq \dot{\epsilon}_B \tag{8.28}$$

In section A, the accumulation of elastic strain energy decreases the induced strain rate, whilst in section B, the release of elastic energy stored on the tool tip and the effect of material softening boosts the induced strain rate, to make the induced strain rate exceed the imposed one. In such manner, the induced strain rate in chip formation also possesses cyclic characteristics.

To sum up, the initiation and the inducing factor of adiabatic shear bands within regularly spaced chip serration are analysed. The influence of shear bands on the cutting force and on the formation of serrated chips in the micro-cutting process is also considered. An FEM and analytical model have been developed to interpret the physics behind the experimental results, and an analytical function of cutting force

is proposed. The analysis in this chapter covers a variety of aspects during the micro-cutting process, including stress/strain status, force, energy and geometry. Both the experiment and the modelling results indicate that:

- (i) In microcutting at a constant strain rate, the shear band in the serrated chips can be induced by the elastic strain concentration; the shear band does not propagate from the tool tip to the free edge of the chip. Instead, the free edge creates an elastic strain concentration and the shear band can be regarded as initiating at the free edge and then propagating from the free edge towards the tool tip;
- (ii) Accumulation of elastic strain energy and the abrupt load drop caused by the formation of adiabatic shear bands can be employed to characterise micro-cutting with serrated chip formation into two distinct stages. The behaviour of the tool tip (cutting force and displacement) is cyclic, and a good correlation can be identified in both the experiments and the models;
- (iii) The proposed model of cutting force is dedicated to revealing the influence of shear bands on the amplitude and frequency of the fluctuation of cutting force, as well as chip morphology (from the serrated chips to the uniform chips).

## 8.5 Generalised Shear Angle Model

A generalised model for the prediction of the shear angle can be derived from Fig. 8.14a, which concludes all the special cases proposed by Merchant's model and its revised forms (LS and S models), as summarised in Table 3.1.

The major difference in the predicted values of the shear angle is due to the correction value ( $\Delta\phi$ ) which is measured in SEM micrographs by a method similar to that used by Merchant (1945b) (Fig. 8.14b). In both the LS and S models, the measured shear angles were affected by the friction on the tool-chip interface. Thus, in terms of cutting force ratio, the correction value is determined by the weights of the friction angle where the weight of the friction is the highest in the S model and the lowest in the M model, with the LS model in between. Such modification results in a negative value of  $\Delta\phi_S$  and in turn most possibly leads to an overcorrection by the S model. Merchant's model predicts the shear angle based on the measured data of the cutting and thrust forces, which can be regarded as an averaged shear angle in the PDZ where the assumed uniform plastic shear occurs (Fig. 8.14b). As for the serrated chips, such as observed by He et al. (2002), the generalised model is plotted in Fig. 8.14c. The nonlinear coarse shear band results from the constraint of friction force and evolves in a stepwise manner. With the evolution of the correction value ( $\Delta\phi$ ), the nonlinear coarse shear band consists of all the three models (Fig. 8.14a). This effect is pronounced when the shear deformation zone ( $l_B$ ) becomes comparable with the elastic deformation zone  $l_A$ , i.e.  $l_A/l_B \rightarrow 1$ . Actually, Merchant's model is another special case of the generalised model, where  $l_B \gg l_A$ ;

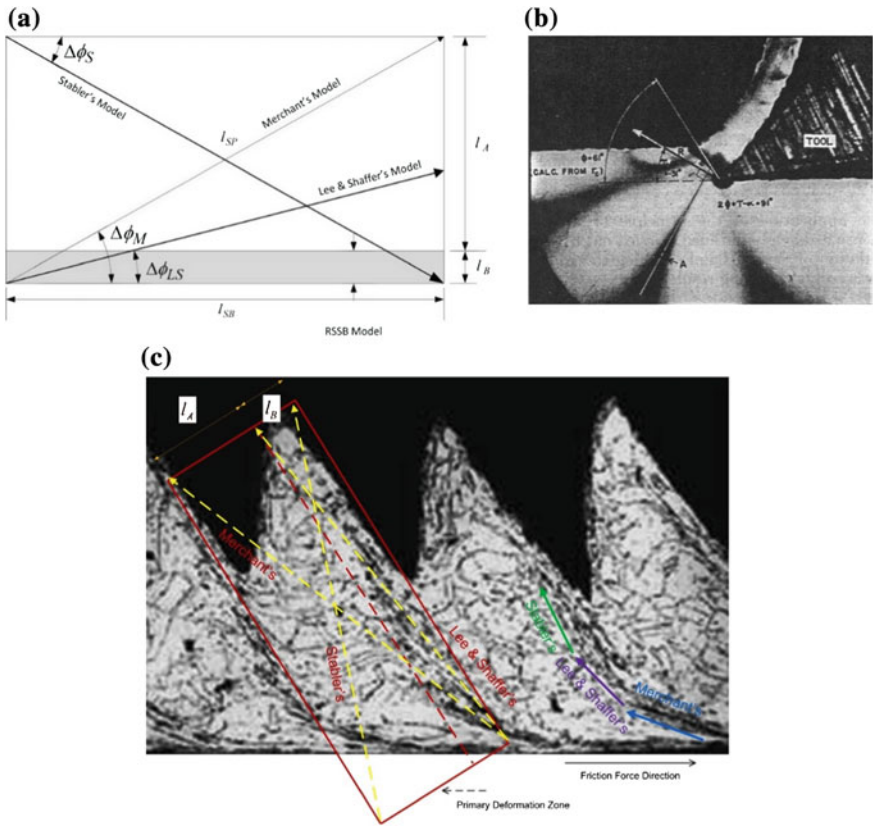


**Fig. 8.14** **a** A generalised model for shear angle prediction plotted in a block of primary deformation zone with Merchant's model, Lee and Shaffer's model, Stabler's model and the RSSB model as special cases. **b** Measurement of shear angle by Merchant (1945b). **c** Nonlinear coarse shear band and its generalised model plotted on the SEM micrograph by He et al. (2002)

thus, the PDZ undergoes a uniform plastic shear. In both cases, due to the large volume of the plastic deformation zone and the boundary condition on the tool-chip interface, the shear band and shear angle can be subjectively overrated, as shown in Fig. 8.14. In contrast, chip morphology with RSSB takes place when  $l_A \gg l_B$ ; in such cases, RSSB with a definite shear angle can be observed.

In summary, regularly spaced shear bands (RSSB) are successfully found in the orthogonal cutting of heavily cold-rolled brass. This is in accord with the findings reported on high-speed machining of HSLA steel by Duan and Wang (2005), i.e. the high yield strength materials are more likely to produce RSSB. However, the yield strength of brass is more sensitive to elevated temperatures, which leads to narrower observable shear bands than those found in HSLA steel of greater thickness. In the presence of RSSB, the extensively applied Merchant's model fails, especially for cutting tools with negative rake angle. A theoretical model is

proposed to explore the cause of the pronounced prediction error in shear angles by Merchant's model. With RSSB, a large volume of work material in the PDZ ( $l_A \cdot w$ ) endures elastic strain only, while a much smaller volume of shear zone ( $l_B \cdot w$ ) participates in the plastic deformation of the micro-cutting process. In this study, a generalised model is further proposed for the prediction of shear angle. Merchant's model, Lee and Shaffer's model, Stabler's model and the RSSB model are all special cases of the generalised model under different machining conditions.

## References

- Black, J. T. (1971). On the fundamental mechanism of large strain plastic deformation. *Journal of Engineering for Industry*, 507.
- Budak, E., & Ozlu, E. (2008). Development of a thermomechanical cutting process model for machining process simulations. *CIRP Annals-Manufacturing Technology*, 57, 97–100.
- Burns, T. J., & Davis, M. A. (2002). On repeated adiabatic shear band formation during high-speed machining. *International Journal of Plasticity*, 18, 487–506.
- Calamaz, M., Coupard, D., Nouari, M., & Girod, F. (2011). Numerical analysis of chip formation and shear localisation processes in machining the Ti–6Al–4V titanium alloy. *International Journal of Advanced Manufacturing Technology*, 52(9–12), 887–895.
- Davim, J. P., & Maranhão, C. (2009). A study of plastic strain and plastic strain rate in machining of steel AISI 1045 using FEM analysis. *Materials and Design*, 30, 160–165.
- Duan, C., & Wang, M. (2005). Some metallurgical aspects of chips formed in high speed machining of high strength low alloy steel. *Scripta Materialia*, 52, 1001–1004.
- Fang, N. (2003a). Slip-line modeling of machining with a rounded-edge tool—Part I: New model and theory. *Journal of the Mechanics and Physics of Solids*, 51, 715–742.
- Fang, N. (2003b). Slip-line modeling of machining with a rounded-edge tool—Part II: Analysis of the size effect and the shear strain-rate. *Journal of the Mechanics and Physics of Solids*, 51, 743–762.
- Guduru, P. R., Ravichandran, G., & Rosakis, A. J. (2001). Observation of transient high temperature vertical microstructures in solids during adiabatic shear banding. *Physical Review E*, 64, Paper No. 036128.
- He, N., Lee, T. C., Lau, W. S., & Chan, S. K. (2002). Assessment of deformation of a shear localized chip in high speed machining. *Journal of Materials Processing Technology*, 129, 101–104.
- Jiang, M. Q., & Dai, L. H. (2009). Formation mechanism of lamellar chips during machining of bulk metallic glass. *Acta Materialia*, 57, 2730–2738.
- Johnson, G. R., & Cook, W. H. (1983). *A constitutive model and data for metals subjected to large strains, high strain rates and high temperatures* (pp. 541–547). Hague: Seventh International Symposium on Ballistics.
- Johnson, G. R., & Cook, W. H. (1985). Fracture characteristics of three metals subject to various strains, strain rates, temperatures and pressures. *Engineering Fracture Mechanics*, 21, 31–48.
- Lee, W.B., & Duggan, B.J. (1988). Effects of grain size on rolling and annealing textures in 82–92% cold rolled  $\alpha$ -brass. *Textures and Microstructures*, 8, 155–172.
- Lee, E. H., & Shaffer, B. W. (1951). The theory of plasticity applied to a problem of machining. *Journal of Applied Mechanics*, 73, 405.
- Lee, W. B. (2005). A personal reflection of mesoplasticity and its applications. *Journal of Materials Processing Technology*, 167, 151–160.
- Lee, W. B., To, S., & Chan, C. Y. (1999). Deformation band formation in metal cutting. *Scripta Materialia*, 40, 439–443.

- Lee, W. B., To, S., Sze, Y. K., & Cheung, C. F. (2003). Effect of material anisotropy on shear angle prediction in metal cutting—A mesoplasticity approach. *International Journal of Mechanical Science*, 45, 1739–1749.
- Medyanik, S. N., Liu, W. K., & Li, S. (2007). On criteria for dynamic adiabatic shear band propagation. *Journal of the Mechanics and Physics of Solids*, 55, 1439–1461.
- Merchant, M. E. (1945a). Mechanics of the metal cutting process. I: Orthogonal cutting and A type 2 chip. *Journal of Applied Physics*, 16, 267.
- Merchant, M. E. (1945b). Mechanics of the metal cutting process. II, plasticity conditions in orthogonal cutting. *Journal of Applied Physics*, 16, 318.
- Molinari, A., & Moufki, A. (2008). The Merchant's model of orthogonal cutting revisited: A new insight into the modeling of chip formation. *International Journal of Mechanical Sciences*, 50, 124–131.
- Recht, R. F. (1985). A dynamic analysis of high speed machining. *ASME Journal of Engineering for Industry*, 107, 309–315.
- Recht, R. F. (1964). Catastrophic thermoplastic shear. *Journal of Applied Mechanics*, 31, 189–193.
- Rhim, S.-H., & Oh, S.-I. (2006). Prediction of serrated chip formation in metal cutting process with new flow stress model for AISI 1045 steel. *Journal of Materials Processing Technology*, 171, 417–422.
- Rule, W. (1997). A numerical scheme for extracting strength model coefficients from Taylor test data. *International Journal of Impact Engineering*, 19, 797–810.
- Saito, T. (1978). Machining of optics: An introduction. *Applied Optics*, 14, 1773–1776.
- Shaw, M. C. (2005). *Metal cutting principle*. New York: Oxford University Press.
- Simoneau, A., Nge, E., & Elbestawi, M. A. (2006). Chip formation during microscale cutting of a medium carbon steel. *International Journal of Machine Tools and Manufacture*, 46, 467–481.
- Stabler, G. V. (1951). The fundamental geometry of cutting tools. *Proceedings of the Institution of Mechanical Engineers*, 165, 14–21.
- Sze, Y. K. (2006). The effect of preferred orientation in the single point diamond turning of polycrystalline materials (M. Phil. Thesis). The Hong Kong Polytechnic University.
- Teng, X., Wierzbicki, T., & Couque, H. (2007). On the transition from adiabatic shear banding to fracture. *Mechanics of Materials*, 39, 107–125.
- Trent, E. M., & Wright, P. K. (2000). *Metal cutting*. Butterworth-Heinemann.
- Wang, H., To, S., Chan, C. Y., Cheung, C. F., & Lee, W. B. (2010a). A study of regularly spaced shear bands and morphology of serrated chip formation in microcutting process. *Scripta Materialia*, 63, 227–230.
- Wang, H., To, S., Chan, C. Y., Cheung, C. F., & Lee, W. B. (2010b). A theoretical and experimental investigation of the tool-tip vibration and its influence upon surface generation in single-point diamond turning. *International Journal of Machine Tools and Manufacture*, 50, 241–252.
- Wang, H., To, S., Chan, C. Y., Cheung, C. F., & Lee, W. B. (2010c). Elastic strain induced shear bands in the microcutting process. *International Journal of Machine Tools and Manufacture*, 50, 9–18.
- Zong, W. J., Li, D., Cheng, K., Sun, T., & Liang, Y. C. (2007). Finite element optimization of diamond tool geometry and cutting-process parameters based on surface residual stresses. *International Journal of Advanced Manufacturing Technology*, 32, 666–674.

# Chapter 9

## Tool-Tip Vibration at High Frequencies

**Abstract** This chapter presents a theoretical and experimental investigation of the influence of tool-tip vibration on surface generation in single-point diamond turning. Although it is well known that the relative vibration between the tool and the workpiece plays an important role in surface generation in single-point diamond turning, most of the previous work has focused on studying the relative tool-work vibration in the infeed (thrust force) direction while the significant contribution of the effect of the tool-tip vibration in the cutting force direction has been overlooked. In ultraprecision diamond turning, the characteristic twin peaks are identified and found to correspond to the tool-tip vibrations by power spectrum density analyses. The vibrations possess the features of small amplitude but high frequency. A theoretical physical model is proposed to describe and correlate the characteristic peaks in the frequency domain with the behaviour of the tool-tip vibration in the steady-state cutting process. The proposed model has the capability of capturing the dominant factors influencing the surface roughness of the machined surfaces.

### 9.1 Identification of Tool-Tip Vibration by Power Spectrum Analysis

A series of cutting experiments have been conducted on a two-axis ultraprecision lathe machine (Optoform 30 from Rank Pneumo from USA). A Kistler 9252A force transducer is mounted between the tool shank and the holder with a pre-loading force. The three-axis signals of forces are recorded during steady-state cutting with a Tektronix TDS 744A digitising oscilloscope. The equipment setup is shown in Fig. 9.1. The background information of the signal of cutting force is first collected and studied in the air-cutting experiments. The signals are recorded before and after running the spindle, under different conditions with and without coolant mist. The turning experiments are then conducted with different non-ferrous work materials, including pure copper, aluminium alloy 6061 and brass. The spindle speed is set at 5000 rpm, depth of cut at 10  $\mu\text{m}$  and feed rate at 20 mm/min. A diamond cutting tool with a nose radius of 1.49 mm is used. The sampling frequency is set at

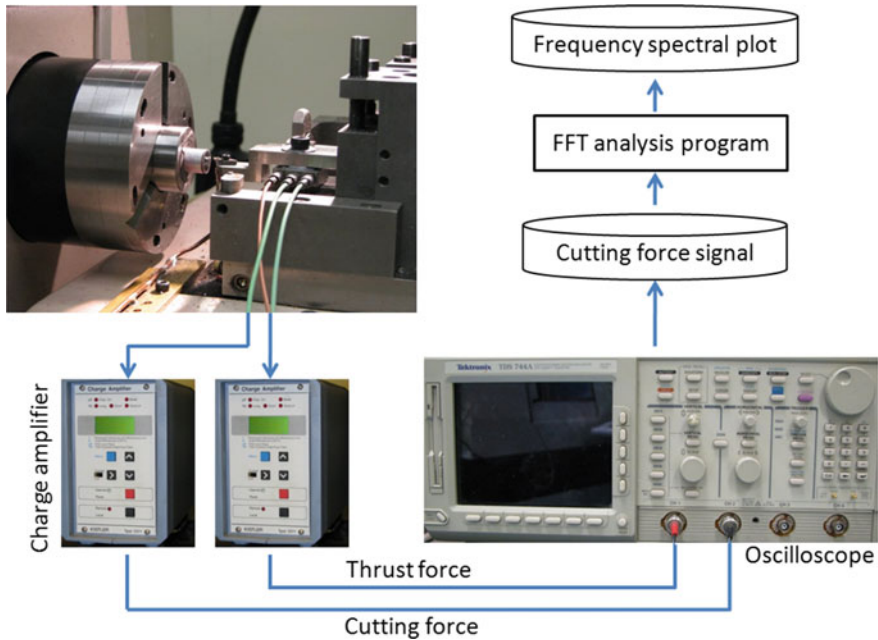


**Fig. 9.1** Equipment setup for the analysis of the signals of cutting force

50 kHz. Thus, the frequencies below 25 kHz can be accurately calculated in the power spectrum analysis with regard to the Nyquist limit. The signals obtained in the time domain are transformed to the frequency domain by Fast Fourier transform (FFT). Power spectrum density (PSD) analysis is performed based on the output of FFT transform.

For the purpose of comparison and identification of the process damping effect induced by the elastic recovery on the clearance face of cutting tool, no coolant mist or lubricant is used in the cutting tests, so that no further damping factors, such as fluid damping, are introduced into the dynamic system of the tool tip and work materials. However, the coolant mist is employed again to establish a correlation between the characteristic twin peaks of tool-tip vibration and the surface roughness in the experiments in the subsequent sections of this chapter. In a control experiment, which aims at eliminating the effect of process damping, bakelite is selected as the work material. With its brittle nature, bakelite can provide the external excitation to the tool tip without introducing new damping factors into the system.

In order to visualise the effect of tool-tip vibration on the surface finish, a micro-cutting test is conducted without overlapping of the cutting marks. Thus, a diamond-turned mark is cut with zero-feed velocity and spindle speed of 2000 rpm on a preformed aluminium alloy Al6061 workpiece. The depth of cut is set to 10  $\mu\text{m}$  in the zero-feed experiment. The surface is then examined by an optical microscope Olympus BX60.



The experimental power spectrum density plots of the cutting force signals recorded in the air-cutting tests under different conditions are shown in Fig. 9.2. It is observed that the characteristic twin peaks appear at a frequency around 13 and 14 kHz in Fig. 9.2a, c, while in Fig. 9.2b, d, the twin peaks disappear due to the absence of the excitation on the tool tip by the coolant mist. Furthermore, Fig. 9.2b, d indicate that the rotation of the spindle does not affect the twin peaks except for the introduction of some background information in the frequency domain. Figure 9.2e, f, g reveal that the characteristic twin peaks exist in the cutting of ductile non-ferrous materials due to the induced excitation of the tool tip. It is obvious that the frequencies of the twin peaks stay unchanged with different work materials, however, the relative amplitude of the twin peaks is of interest in the following sections. The right peak (around 14 kHz) is regarded as the excited natural frequency induced by the micro-cutting process, while the left peak (around 13 kHz) is generated due to the process damping effect caused by the interaction between the tool tip and the elastic recovery induced ploughing force between the diamond-turned surface and the clearance face of the cutting tool. It is interesting to note that different mechanical properties of the work materials, such as Young's modulus, yield stress, hardness and friction coefficient, lead to different extents of such process damping effects. However, due to the brittle nature of bakelite, the elastic recovery induced ploughing force is negligible, i.e. the process damping can barely be observed in the bakelite micro-cutting process. This agrees with our experimental observation. The left peak of the characteristic twin peaks does not exist in Fig. 9.2h.

According to the turned surface in Fig. 9.3, the distance ( $d$ ) between two adjacent bar-shape marks can be calculated with the help of the non-contact optical profiler Wyko NT8000. The average distance is calculated to be around 73.7  $\mu\text{m}$ . Thus, the frequency of the periodic characteristic marks is estimated to be around 14.1 kHz in Eq. (9.1), which is consistent with the above-mentioned frequencies obtained from the cutting force signals. The natural frequencies of the characteristic twin peaks (the right peak) result in the appearance of the bar-shape marks on the single turning mark.

$$f_{\text{calc}} = \frac{2\pi R \times \text{spindle}/60 \text{ s}}{d} = \frac{2\pi \times 5 \text{ mm} \times 2000 \text{ rpm}/60 \text{ s}}{0.0737} \approx 14.1 \text{ kHz} \quad (9.1)$$

## 9.2 Characteristic Twin Peaks and Material Properties

Micro-cutting trials have been conducted to reveal the correlation between the characteristic twin peaks of high-frequency tool-tip vibration and material properties. Aluminium alloy Al6061 rods, pre-compressed with different height reduction ratios (0, 10%, 30%, 50% and 70%), are prepared as the workpiece in the experiments. The experiment settings are given in Table 9.1. The signals of both cutting

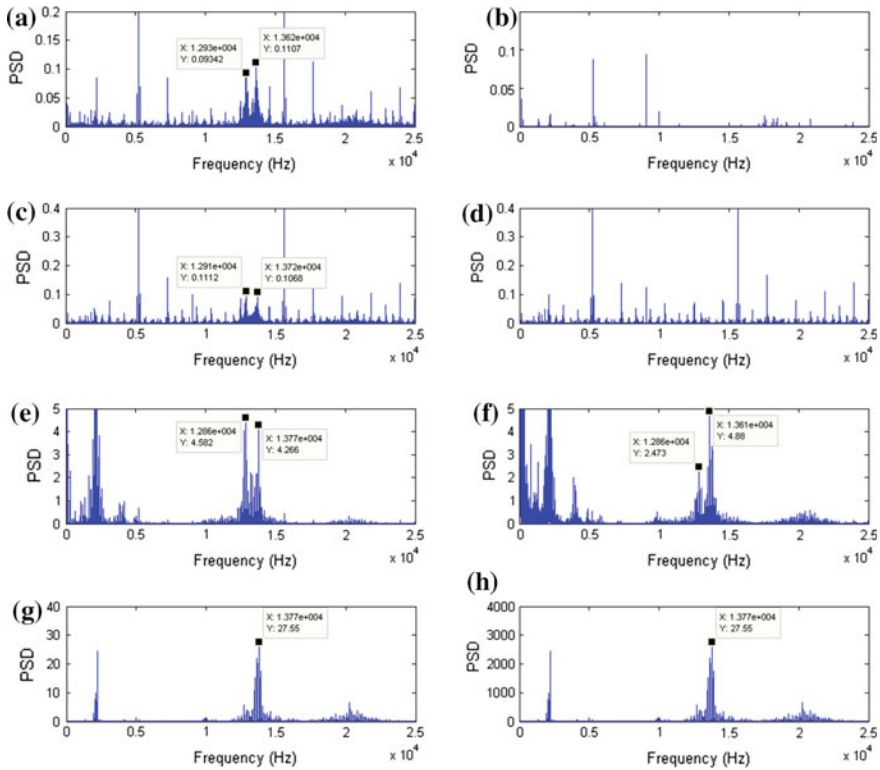


**Fig. 9.2** Characteristic twin peaks in **a** coolant excitation only; **b** spindle stops, coolant OFF; **c** air-cutting with coolant; **d** air-cutting without coolant; **e** cutting of copper; **f** cutting of Al 6061; **g** cutting of brass and **h** cutting of bakelite

force and thrust force are recorded with a sample frequency of 50 kHz. Since different height reduction ratios influence the mechanical properties of the work materials, such features can be used to identify the changes of the characteristic peaks in the frequency domain.

For the purpose of comparison, two sets of experiments are designed. In Set A, the lubricant mist is turned on, while in set B, the lubricant mist is turned off. In both sets of experiments, the background signals are first obtained during air cutting. Then the signals of cutting force are taken for the cutting of aluminium alloy Al6061 rods with different height reduction ratios, 0, 10%, 30%, 50% and 70%. The machining parameters are kept constant in all experiments. In the present study, the investigation of the characteristic peaks is focused on cutting force signals only. The corresponding measurements of arithmetic roughness ( $R_a$ ) and root-mean-square roughness ( $R_q$ ) for each set of experiments are obtained by a surface profiler, Wyko NT8000.

The power spectrum density (PSD) plots based on the cutting force signals taken in sets A and B of the experiment are tabulated in the left and right columns of

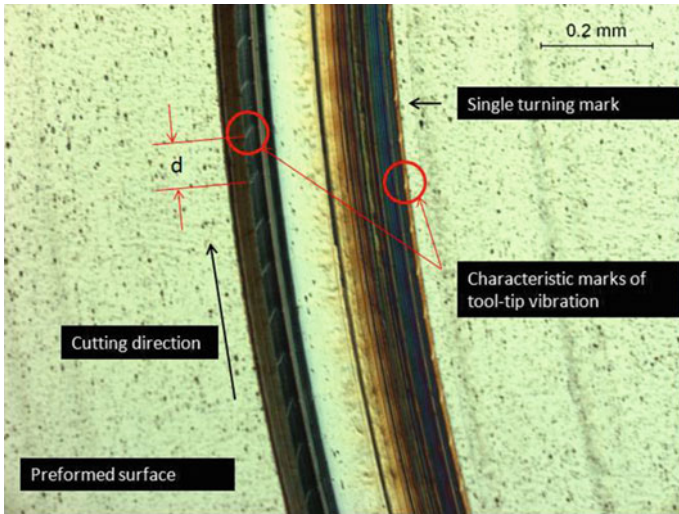


Fig. 9.3 Periodic *bar-shape* marks in the single turning mark on a preformed surface

Table 9.1 Experiment settings with different height reduction ratios (HRR) and cutting conditions

Sample no.	A	B
1	Air-cutting, lubricant ON	Air-cutting, lubricant OFF
2	0% HRR, lubricant ON	0% HRR, lubricant OFF
3	10% HRR, lubricant ON	10% HRR, lubricant OFF
4	30% HRR, lubricant ON	30% HRR, lubricant OFF
5	50% HRR, lubricant ON	50% HRR, lubricant OFF
6	70% HRR, lubricant ON	70% HRR, lubricant OFF

Fig. 9.4, respectively. The corresponding measurements of arithmetic roughness ( $R_a$ ) and root-mean-square roughness ( $R_q$ ) for each set of experiments are tabulated in Table 9.2.

As shown in Fig. 9.4a2, b2, the characteristic peaks are highlighted as P1 and P2, while such peaks are not found in other plots. In the frequency domain, P2 is located at about 14 kHz and another characteristic peak P1 is about 13 kHz lower than that of P2. Although many other peaks with smaller amplitudes are also observed in the PSD plots, they are ignored because there is no evidence that these peaks spring from the relative movement between tool tip and work material. As the peaks P1 and P2 are generated by the relative movement between cutting tool and work material, they are regarded as the dominant factors affecting surface roughness.

The frequencies of the characteristic peaks P1 and P2 for differently treated work materials are found to be not very sensitive to the cutting conditions, as shown in

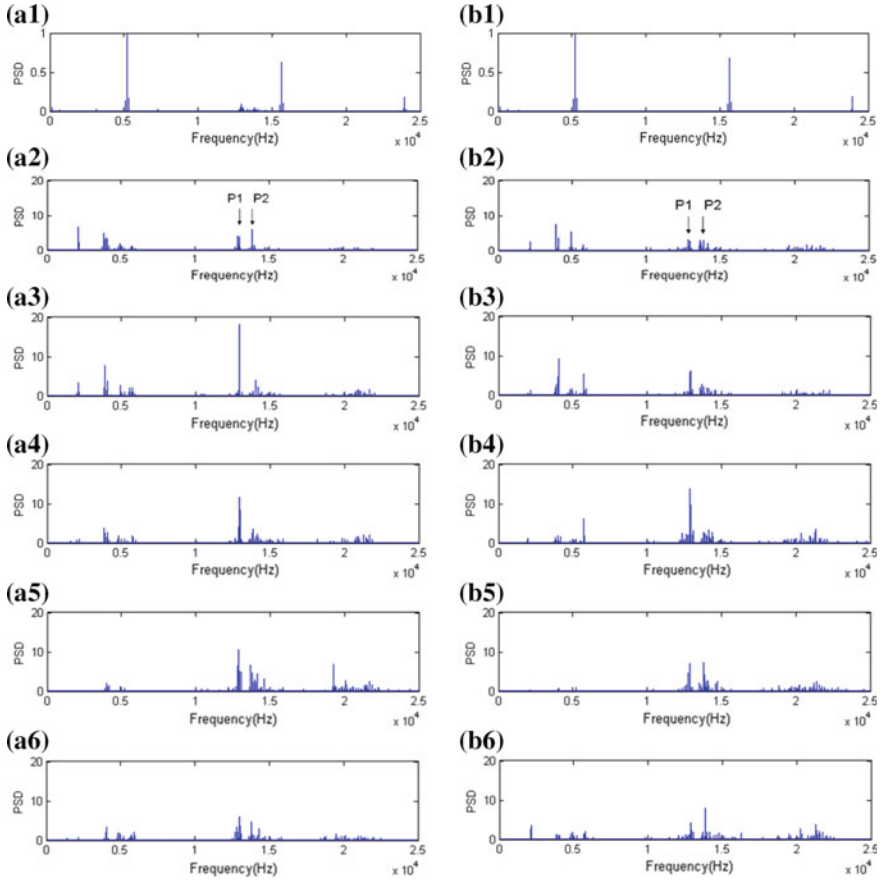


**Fig. 9.4** Power spectrum density analyses of cutting force signals for experiment sets A (lubricant ON) and B (lubricant OFF), and (1) air cutting, (2) 0%, (3) 10%, (4) 30%, (5) 50% and (6) 70% height reduction ratio, respectively

Fig. 9.4. However, the amplitude of the peaks varies significantly. In order to describe the relative amplitude of the two peaks, an index named characteristic peak ratio (CPR) is defined in Eq. (9.2) below

$$CPR = \frac{A_{P2}}{A_{P1}} \tag{9.2}$$

where  $A_{P1}$  and  $A_{P2}$  are the amplitudes of the two characteristic peaks P1 and P2. Based on the data in Fig. 9.4, the CPRs for both sets of experiments are drawn in Fig. 9.5. Therefore, the trend of the value of CPR with regard to the height reduction ratio can be identified. Furthermore, a correlation between the CPR index and surface roughness can be identified by comparing Figs. 9.5 and 9.6. For

**Table 9.2** Surface roughness data (Wyko NT8000)

Reduction ratio (%)	Lubricant mist ON (Set A)		Lubricant mist OFF (Set B)	
	$R_a$ (nm)	$R_q$ (nm)	$R_a$ (nm)	$R_q$ (nm)
0	20.90	27.11	17.45	22.50
	20.74	26.14	21.00	27.02
	19.25	24.47	17.23	21.69
	30.24	37.65	18.97	21.28
	20.71	26.02	18.86	23.72
10	20.12	25.58	20.84	25.82
	18.46	23.28	21.86	27.39
	17.62	22.43	19.08	23.88
	19.49	24.30	19.58	25.29
	19.16	24.29	20.68	26.25
30	20.34	26.33	20.40	25.36
	20.04	25.63	17.92	22.47
	18.69	24.21	17.75	26.11
	19.75	25.08	17.21	21.72
	20.55	30.32	17.53	22.28
50	19.91	26.05	23.22	29.48
	19.02	24.26	19.82	25.43
	20.47	29.97	17.65	22.19
	22.45	29.91	23.39	29.38
	19.47	26.54	17.43	22.05
70	18.89	23.93	25.23	32.55
	19.45	24.32	20.51	25.67
	20.23	20.65	22.38	27.67
	19.48	24.34	25.92	32.98
	20.07	25.01	20.48	26.23

simplicity of analysis, only the arithmetic surface roughness ( $R_a$ ) data are plotted in Fig. 9.6, since the values of root-mean-square roughness ( $R_q$ ) show a similar trend to  $R_a$ . The minimum points of both the CPR index and  $R_a$  are found at 10 and 30% height reduction ratio in the experiment sets A and B, respectively. The trends described by the CPR index are in line with the surface roughness. Thus, the CPR index can be regarded as a reflection and predictor of surface roughness. Since the CPR index is directly derived from the signals of the cutting force in the micro-cutting process and surface roughness is the output of the surface measurement, the CPR index functions as a link between machining and measurement. On the other hand, the CPR index can be used to predict the quality of surface finish and to monitor the machining process, which also takes into account the mechanical properties of the work materials and machining conditions.

**Fig. 9.5** CPR index in experiment Set A (with lubricant) and B (without lubricant)

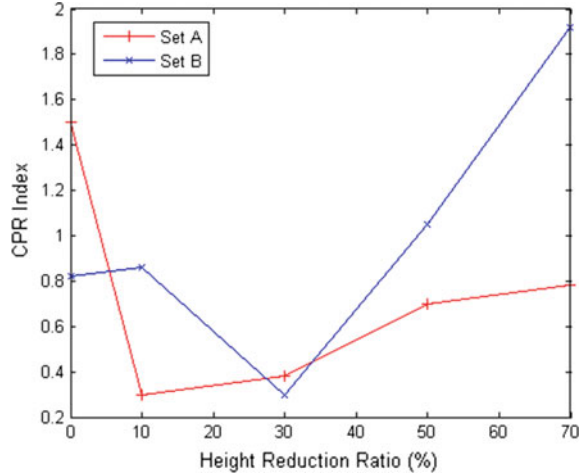
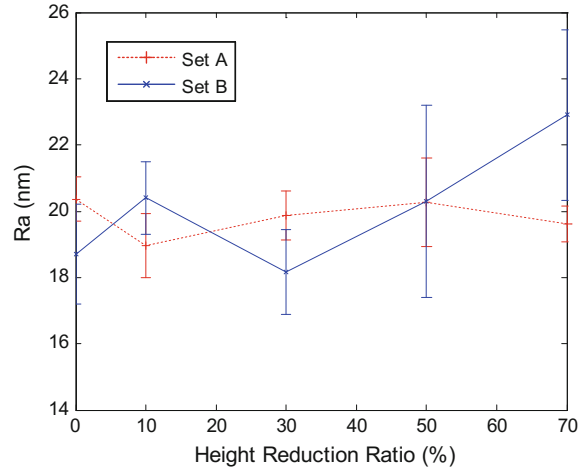


**Fig. 9.6** Surface roughness ( $R_a$ ) measured in experiment Set A (with lubricant) and B (without lubricant)



### 9.3 Modelling of Tool-Tip Vibration

#### 9.3.1 An Impact Model Without Damping

A modified pendulum impact model is proposed to describe the tool-tip vibration during the cutting process. As shown in Fig. 9.7, the small amplitude assumption is adopted following Cheung and Lee (2000b), Takasu et al. (1985) and Bispink and Weck (1992), which implies that the angle  $\theta$  is small enough to guarantee that the bob (or mass) of the pendulum impacts with the object wall A (with finite mass relative to the bob) deliberately placed perpendicularly (Fig. 9.7b). Thus, if the bob and the wall are regarded as two colliding particles, the direct impact between them

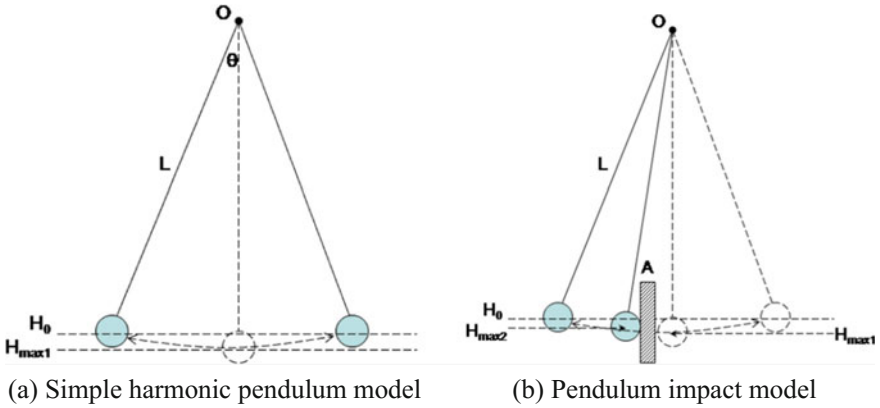


Fig. 9.7 Simple physical model for tool-tip vibration

is collinear. By assuming that the momentum of the system is conserved during impact and that the impact is completely elastic, i.e. the coefficient of restitution equals 1. (although in Fig. 9.7 the bob and the wall are not represented by “points” geometrically, they are still regarded as particles rather than bodies in term of the physics), the trajectory of the bob can be described by the position function  $h(t)$  of time  $t$ , as shown in Fig. 9.7, where  $H_0$  is the initial position and  $H_{max}$  is the maximum distance from  $H_0$  of the bob. It is assumed that the length of the pendulum measured from the pivot point to the bob’s centre of gravity and the mass of the bob are constant.

Based on the assumption of small amplitude and no damping vibration, the model shown in Fig. 9.7a is a simple harmonic oscillator. The differential equation governing such motion is

$$\frac{d^2\theta}{dt^2} + \frac{g}{L}\theta = 0 \tag{9.3}$$

The solution to Eq. (9.3) can be expressed by a cosine function as

$$\theta(t) = \theta_0 \cos\left(\sqrt{\frac{g}{L}}t\right) \quad |\theta_0| \ll 1^\circ \tag{9.4}$$

where  $g$  is the local gravitational acceleration,  $L$  is the length of the pendulum measured from the pivot point to the bob’s centre of gravity and  $t$  denotes the time. In such cases, the position function  $h(t)$  of the bob can be expressed by a sinusoidal function in the form of Eq. (9.5):

$$h_1(t) = H_{\max 1} \sin(\omega_1 t + \phi_1) \quad (9.5)$$

$$\omega_1 = \frac{2}{T_0} = \frac{1}{\pi} \sqrt{\frac{g}{L}} \quad (9.6)$$

where  $\omega_1$  and  $\phi_1$  denote the frequency and phase of simple harmonic pendulum respectively;  $T_0$  is the period of the pendulum. The trajectory of the bob can be expressed by the curve  $h_1(t)$ .

If an obstacle “wall”  $A$  is set to impact with the bob, and it is assumed that the mass of the wall is far larger than that of the bob, due to the momentum conservation in such system, the magnitude of the bob’s velocity remains unchanged, but the direction is changed to the opposite when the impact happens. The pendulum impact model is shown in Fig. 9.7b. Based on the assumption of small amplitude, the trajectory of the bob can also be approximately expressed by a sinusoidal function as

$$h_2(t) = H_{\max 2} \sin(\omega_2 t + \phi_2) \quad (9.7)$$

where  $\omega_2$  and  $\phi_2$  denote the frequency and phase of the impact vibration model. According to the position of the wall  $A$  (Fig. 9.7b), the amplitude of the impact model is smaller than that of the free vibration model ( $H_{\max 2} < H_{\max 1}$ ). The frequency of the impact model is higher ( $\omega_2 > \omega_1$ ).

Therefore, due to excitation, the tool-tip vibration based on the proposed pendulum impact model can be formulated as the summation of Eq. (9.8) of the two vibrations expressed by Eqs. (9.5) and (9.7).

$$h(t) = h_1(t) + h_2(t) = H_{\max 1} \sin(\omega_1 t + \phi_1) + H_{\max 2} \sin(\omega_2 t + \phi_2) \quad (9.8)$$

According to the mathematics of fast Fourier Transform (FFT) and power spectrum density (PSD) analysis, the amplitude and phase of vibrations cannot be considered after the transformations. To investigate how FFT deals with the proposed impact model, a simplified form of Eq. (9.8) is expressed in Eq. (9.9) and the curves of function and the PSD plot of Eq. (9.9) are shown in Fig. 9.8 (for instance,  $\omega_1 = 8.2$  and  $\omega_2 = 8.6$ ,  $t = 0-10^4$ ).

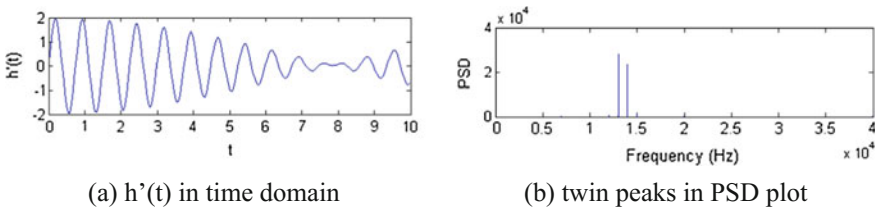


**Fig. 9.8** Twin peaks in PSD plot of the proposed impact model



$$h'(t) = \sin(\omega_1 t) + \sin(\omega_2 t) \quad (9.9)$$

Since the twin peaks identified in Figs. 9.8b and 9.4a2 are matched, the proposed model can be used to explain the emergence of the twin peaks. The impact model in Fig. 9.7b can be directly applied in the micro-cutting process, if the wall A in Fig. 9.7b is regarded as the tool-chip interface, the length of pendulum string as the tool shank length and the bob as the tool tip.

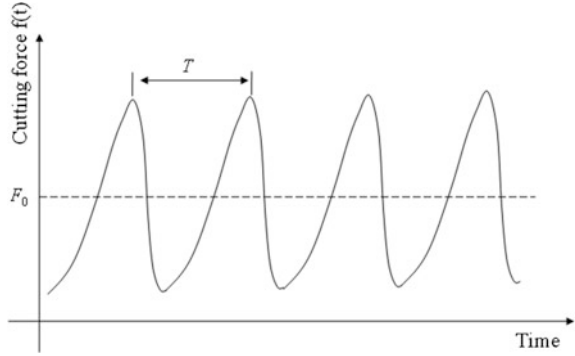
The proposed impact model of tool-tip vibration does not intend to account for all the possible factors leading to the formation of characteristic twin peaks in the PSD plots of Fig. 9.4. The proposed model is established based on the physical phenomenon (impact) in the micro-cutting process of SPDT, which is regarded as a dominant factor rather than an exclusive factor inducing the twin peaks. To substantiate the experimental results, the impact phenomenon is found to be present in all the non-ferrous materials tested in the present study. The tool tip is thus believed to vibrate in the course of machining along the cutting direction with twin frequencies. The high-frequency tool-tip vibrations are induced by the excitation of the applied forces (lubricant mist and impact with the work materials) while the characteristic twin peaks refer to the resonance frequency and the impact-induced frequency respectively.

### 9.3.2 *Non-harmonic Periodic Excitation with Process Damping Effect*

To further develop the model proposed in the preceding section, the conditions of excitation and the damping effect on the tool tip are investigated in this section. In a more realistic sense, the wall A in Fig. 9.7b is no longer assumed to be perfectly elastic to the bob of the pendulum in the emergence of impact. According to the idealised card model by Piispanen (1948) and the experimental observation and proposed model with load drop on the cutting force by Recht (1964), the cutting force can be neither constant nor regarded as a harmonic excitation to the tool tip in a dynamic system. Instead, from a macro-scale point of view on the elastoplastic behaviour of work materials, the cutting force can be qualitatively described as shown in Fig. 9.9. Though a constant cutting speed is employed in the cutting tests, the induced effective strain and strain rate on the material are never homogeneous, based on the elastoplastic behaviour of work materials, which in turn results in the non-harmonic periodic excitation to the tool tip.

According to the Fourier series of an arbitrary periodic function, the excitation force  $f(t)$  can be expressed by the superposition of the harmonic equations as expressed in Eq. (9.10), where  $T$  is the period of cutting force and the calculations of corresponding coefficients are given in Eq. (9.11).

**Fig. 9.9** Cutting force with a non-harmonic periodic nature as excitation to the tool tip



$$f(t) = \frac{a_0}{2} + \sum_{p=1}^{\infty} (a_p \cos p\omega_T t + b_p \sin p\omega_T t), \quad \omega_T = \frac{2\pi}{T} \quad (9.10)$$

$$a_p = \frac{2}{T} \int_{-T/2}^{T/2} f(t) \cos p\omega_T t dt, \quad b_p = \frac{2}{T} \int_{-T/2}^{T/2} f(t) \sin p\omega_T t dt \quad (9.11)$$

The damping factor in the tool-work or tool-chip dynamic system is a complex result of the damping factors within the work materials and the internal damping of the cutting tools. Moreover, the process damping is regarded as another damping factor, which is induced by the elastic recovery of the work materials to the clearance face of the cutting tool. The elastic recovery results in the “ploughing” or “rubbing” force which is also recognised in the literature. However, no previous work has pointed out the relationship between such process damping factor and tool-tip vibration, as well as surface roughness. In order to reveal the stress status in the micro-cutting process, a two-dimensional finite element (FE) model is proposed, following the methodologies described in the previous work by Wang et al. (2008) and utilising the commercial FE package MSC.Marc.

In the FE model, a simulation of orthogonal cutting is performed based on the assumption of plane strain. The diamond cutting tool is assumed to be rigid with a constant cutting speed and depth of cut. As in the actual cutting experiments, a small edge radius is employed in the geometric model. In order to focus on the elastic behaviour of the work material, and for simplicity, an isotropic constitutive model is adopted based on data on the mechanical properties of aluminium alloy Al6061. The displacement boundary conditions are utilised to restrict the plane movement of the nodes on the bottom of the work piece. Moreover, the advanced global remeshing option in MSC.Marc is activated to cope with the large distortion of the meshes in the geometric model. With this option, no predefined chip-work separation criteria are needed. The simulation result with chip generation is shown in Fig. 8.10. The diamond cutting tool is represented by a 2D curve, and the cutting

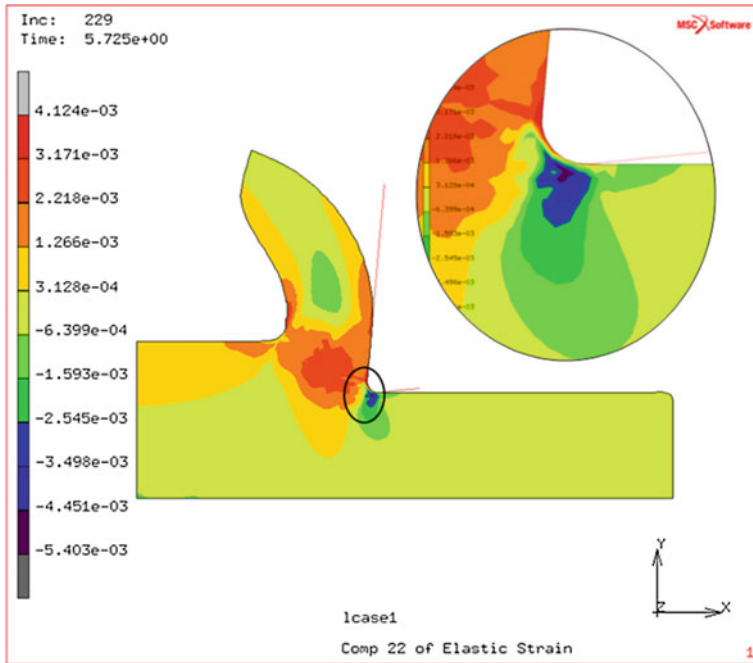


**Fig. 9.10** Elastic strain in the thrust direction (Component 22, i.e. along the Y-axis in the model)

direction is along the negative X-axis. Component 22 of elastic strain (along the Y direction, i.e. the thrust force direction) is visualised and magnified in the inset. The dark blue region under the tool nose indicates that the elastic strain is imposed by the tool nose towards the negative Y-axis, which in turn exerts a reaction force to the tool nose, i.e. the thrust force. It is interesting to note that when the tool tip advances, i.e. on the removal of the imposed downward stress, the elastic stress stored in this area causes the material to spring back to accommodate the imposed elastic strain by the tool nose (Fig. 9.10).

The mechanism of process damping factor is shown in the schematic diagram in Fig. 9.11. Compared with the ideal case of the turned surface, the elastic recovery can be identified on the actual surface in the thrust direction with the tool advancing in the cutting direction. This effect of material recovery has also been reported by Kong et al. (2006). The circled area of chip root and the tool tip is magnified in the inset. The tool-tip moves between positions 1 and 2 due to vibration. When the tool moves from position 1 to position 2, the tool tip contacts the elastically recovered surface, which in turn yields the process damping factor. The process factor  $C_{proc}$  is added with the internal damping factor  $C_t$  as the total damping factor ( $C_{tt}$ ) of the tool tip, as shown in Eq. (9.15). The dynamic system is modelled in Fig. 9.12, where  $M$ ,  $K$  and  $C$  denote the mass, stiffness and damping, and the subscripts ct and tt denote the chip root and the tool tip, respectively. The term chip root is adopted to denote the contact area between the chip (work material) and the tool tip, which is

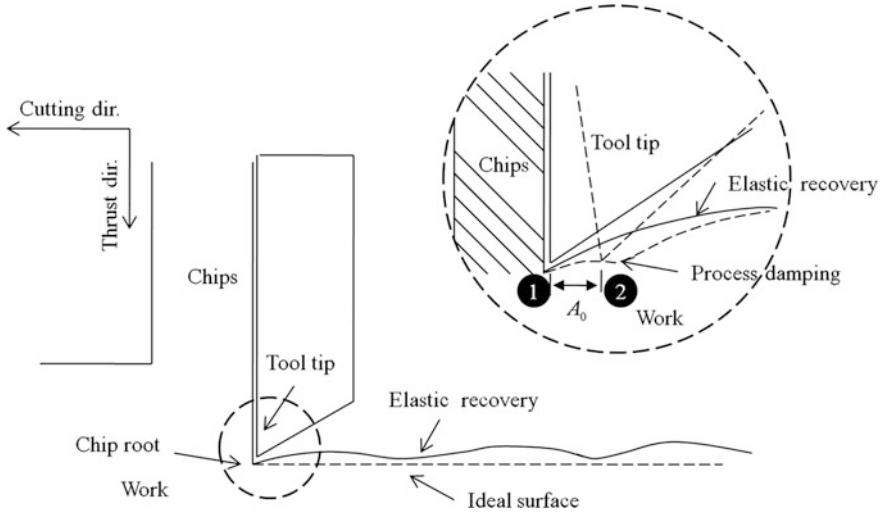


**Fig. 9.11** Schematic diagram of elastic recovery and the generation of process damping factor on the clearance face of the diamond cutting tool

an effective area in the modelling of tool-tip vibration. Due to the nature of high frequency and small amplitude of the tool-tip vibration and the dynamic properties of ductile work materials, the effective area can be confined in a relatively small region, instead of the entire chip thickness, in the calculation. The dynamic system is expressed by Eq. (9.12), where  $\zeta_{tt}$  and  $\zeta_{cr}$  denote the damping ratio of the tool tip and chip root, as obtained in Eq. (9.14). The natural frequencies of the tool tip and the chip-root volume are denoted by  $\omega_{tt}$  and  $\omega_{cr}$ , respectively. The external excitation  $f(t)$  can be expressed by Eq. (9.10).

$$\begin{bmatrix} \ddot{x}_{tt}(t) \\ \ddot{x}_{cr}(t) \end{bmatrix} + \begin{bmatrix} 2\zeta_{tt}\omega_{ntt} & 0 \\ 0 & 2\zeta_{cr}\omega_{ncr} \end{bmatrix} \begin{bmatrix} \dot{x}_{tt}(t) \\ \dot{x}_{cr}(t) \end{bmatrix} + \begin{bmatrix} \omega_{ntt}^2 & 0 \\ 0 & \omega_{ncr}^2 \end{bmatrix} \begin{bmatrix} x_{tt}(t) \\ x_{cr}(t) \end{bmatrix} = \begin{bmatrix} f(t)/M_{tt} \\ f(t)/M_{cr} \end{bmatrix} \quad (9.12)$$

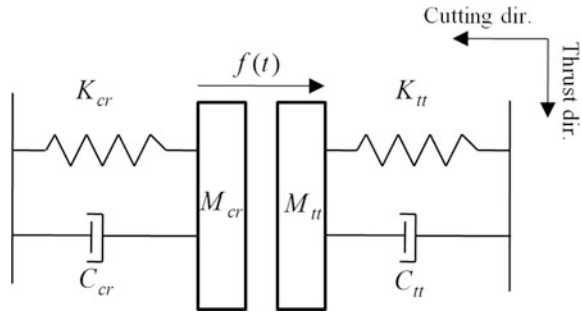
$$\omega_{ntt} = \sqrt{K_{tt}/M_{tt}}, \quad \omega_{ncr} = \sqrt{K_{cr}/M_{cr}} \quad (9.13)$$

$$\zeta_{tt} = \frac{C_{tt}}{2\sqrt{K_{tt}M_{tt}}}, \quad \zeta_{cr} = \frac{C_{cr}}{2\sqrt{K_{cr}M_{cr}}} \quad (9.14)$$

$$C_{tt} = C_t + C_{proc} \quad (9.15)$$

The natural frequency of the tool tip  $\omega_{tt}$  represents the frequency of the right peak of the characteristic twin peaks. Due to the process damping factor  $C_{proc}$ , the resultant frequency will shift to the left, such that the left peak of the characteristic twin peaks is presented. The process damping also reduces the amplitude of the tool-tip vibration, due to its nature in energy dissipation. Therefore, the proposed

**Fig. 9.12** A dynamic model of the system of tool tip and the effective volume of work material

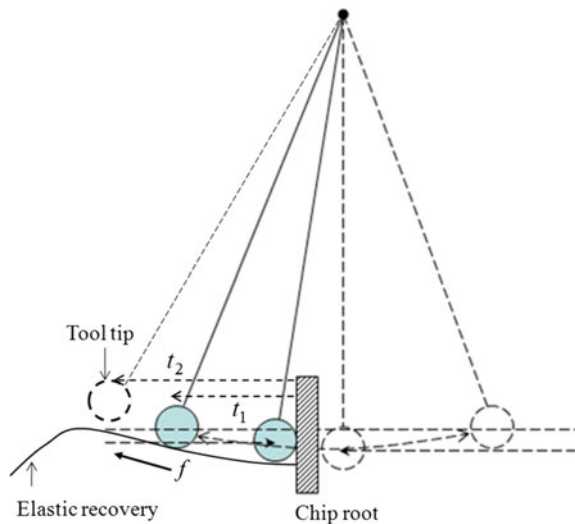


CPR index in Eq. (9.2) is also an index of the process damping factor. In the following sections, it can be seen that the process damping factor is a key factor affecting the surface roughness.

Differing from the previous dynamic models of cutting systems in the literature, the presented model studies the tool tip and the small volume of chip-root material at the microscopic scale. This model does not intend to add more factors or to study the dynamic behaviour of the cutter and the whole workpiece. Instead, the proposed model extracts the chief characteristics of interest from the complex system, and is utilised to explain and correlate with the experimental results. Furthermore, the proposed model with the process damping factor can also be utilised to establish a relationship between the tool-tip vibration and surface roughness.

The process damping factor can also be added into the previously proposed impact model of the pendulum system (Fig. 9.13). Due to the elastic recovery of the turned surface beneath the clearance face of the cutting tool, a friction force ( $f$ ) is generated by the relative displacement of the tool tip and the recovered surface.

**Fig. 9.13** Revised pendulum impact model with the effect of process damping



Such friction force can reduce the kinetic energy of the bob of the pendulum, i.e. the tool tip in vibration. Therefore, the period half time increases from  $t_1$  to  $t_2$ , and the frequency decreases to form the left peak of the characteristic twin peaks. In this theoretical model, the chip root is actually an excitation to the tool tip that forms the right peak. In such manner, the characteristic twin peaks are generated.

## 9.4 Representative Measurement Method

### 9.4.1 *Influence of Tool-Tip Vibration on the Machined Surface*

In the literature, the low-frequency process vibration has been extensively studied with its effect on surface roughness. However, high-frequency tool-tip vibration in the cutting force direction, is an intrinsic feature of ultraprecision single-point diamond turning (SPDT). The effect of the high-frequency vibration on surface generation was also supported by Hocheng and Hsieh (2004). Research work covers several key aspects of the problem, including (1) the modelling method for dynamic machining system and chatter mechanisms, (2) the relationship between vibration and surface roughness, (3) vibration direction and frequency range, (4) the effect of material swelling and recovery on tool vibration and process damping, (5) surface characterisation methods, (6) process vibration and material factors, etc.

This section is dedicated to studying of the influence of tool-tip vibration on surface roughness. The resulting periodic fluctuation of the surface profile is identified in a particular spatial frequency range by a tangential measurement method. The ISO standard provides merely a minimal, not an optimal requirement for surface measurement. To this end, a representative measurement method is proposed to better characterise the machined surface in SPDT. The conventional radial and aerial surface measurements yield a relatively biased result on surface roughness which cannot adequately reflect the detrimental effect of tool-tip vibration. Representative measurement takes account of the sample area ratios and is able to be used to objectively study the discrepancies in surface measurement. The proposed model for surface generation and representative measurement are applicable to problems in the surface generation in ultraprecision SPDT, such as the spiral turning marks and spatial errors in radial profile measurement.

This section tackles the problem of representative measurement of nano-surfaces machined in single-point diamond turning. With stylus-type measurement equipment, such as a Form Talysurf system, 2D profile measurement was conducted (Cheung and Lee 2001; Abouelatta and Mádl 2001). A special kind of measurement is radial measurement (To et al. 2001; Hocheng and Heieh 2004; Cheung and Lee 2000a), in which the data of the measured profile can be readily transformed into the spatial frequency domain with FFT. With the interferometer surface profiler, the aerial data or 3D measurement of surface roughness can be recorded (Li et al. 2010;

Lee and Cheung 2001; Hocheng and Heieh 2004). As an advantage, the aerial data contain the surface information for both cutting direction and radial direction, with which the effect of tool-tip vibration along the cutting force direction can be studied. In this chapter, a special data processing method is employed to extract the profile data along turning marks, in which the resultant profile of relative tool-work vibration can be clearly observed. Furthermore, a representative measurement method is proposed to characterise the surface roughness, based on the introduced sample area ratios ( $\eta$ ). A  $\eta$ -sensitive surface roughness ( $\tilde{R}$ ) is introduced to investigate the effect of sample area ratios and tool-tip vibration. The representative measurement is thereby conducted in the low- $\eta$ , high- $\eta$  and oversampling regions. The proposed representative measurement complies with, but is not restricted to, the international standard (ISO 4288:1996).

### 9.4.1.1 Cutting Experiments

Two face turning experiments were conducted to examine the influence of tool-tip vibration on surface roughness (Table 9.3). In Experiment 1, a polycrystalline OFHC copper specimen was machined with a depth of cut of 10  $\mu\text{m}$  and a feed rate of 20  $\text{mm min}^{-1}$  with a spindle speed of 2000 rpm. The average grain size of the OFHC copper specimen was 75  $\mu\text{m}$ . The specimen was in the shape of a cylinder with a diameter of 12.7 mm. The tool nose radius was 2.503 mm. A coolant mist was used and sprayed towards the tool-chip interface through a nozzle. The copper specimens were flattened first with the same machining parameters to remove the possible tilt angle of the sample surface incurred in the mounting procedure. Then the material was removed to a depth of 50  $\mu\text{m}$  by face turning with five passes to ensure the constant onward depth of cut of 10  $\mu\text{m}$  in the experiments.

In Experiment 2, a cylindrical specimen of copper single crystal was prepared with a diameter of 12.8 mm. The initial crystallographic orientation of the normal of machining surface was determined by an X-ray diffractometer. In this chapter, the (111) surface was selected to be machined on a two-axis single-point diamond turning machine (Optoform 30, Taylor Hobson Co.). The face turning was performed at a depth of cut of 10  $\mu\text{m}$ , and a feed rate of 20  $\text{mm min}^{-1}$  with a spindle speed of 8000 rpm. The tool nose radius was 0.5329 mm. A Kistler 9252A force transducer was mounted with a pre-loading force between the tool shank and the tool post. A 14-bit multifunction Data Acquisition (DAQ) card (PCI-6132, National Instrument) was installed on a PC workstation to convert the analogue signals of the

**Table 9.3** Machining parameters for the face turning experiments

Exp. no.	Depth of cut ( $\mu\text{m}$ )	Feed rate ( $\text{mm min}^{-1}$ )	Spindle speed (rpm)	Specimen
1	10	20	2000	Polycrystalline copper
2	10	20	8000	Cu (111)

cutting forces. Using the Kistler 5011B charge amplifier, the converted signals were recorded at the sampling rate of 1 MHz using the LABVIEW software package. The signals of the cutting force were further processed using fast Fourier transform (FFT) and studied in the frequency domain.

The geometric features of the machined surface were further characterised by an interferometric surface profiler Wyko NT8000 and an optical microscope Olympus BX60. To examine surface roughness, five sample areas were selected along the radial direction on the machine surface and were numbered from 1 (close to the centre of the machined surface) to 5 (away from the centre of the machined surface), at distances of 0.7, 0.9, 1.4, 1.7 and 2 mm from the centre, respectively. In accordance with (ISO 4288:1996), in each sample area, the surface profile data were taken five times, with sampling lengths not shorter than 0.08 mm.  $R$ -parameters were employed to characterise surface roughness, including arithmetic average roughness ( $R_a$ ), root-mean-squared roughness ( $R_q$ ), maximum height of the profile ( $R_z$ ) and the average distance between the highest peak and lowest valley ( $R_t$ ), as shown in Eq. (6.1), where  $y_i$  are the profile data,  $R_{v(p)} = \min(\max)y_i$ ,  $s$  is the number of sampling and  $R_{i}$  is the  $R_t$  for the  $i$ th sampling length (ASME 1996).

$$R_a = \frac{1}{n} \sum_{i=1}^n |y_i|, \quad (9.16a)$$

$$R_q = \sqrt{\frac{1}{n} \sum_{i=1}^n y_i^2}, \quad (9.16b)$$

$$R_z = \frac{1}{s} \sum_{i=1}^s R_{ti}, \quad (9.16c)$$

$$R_t = R_p - R_v. \quad (9.16d)$$

In the measurement of surface roughness, considering the influences of tool-tip vibration on surface generation, different sampling lengths resulted in different  $R$  values. Besides the suggested sampling lengths by the ISO standard, sampling lengths of 0.04 and 0.12 mm were also adopted to calculate the  $R$  values. Furthermore, different sample area ratios (the sample area over the machined area) also led to discrepancies in the calculated  $R$  values. This phenomenon was studied with the sample area ratio increasing from 10 to 200%, i.e. “oversampling” on the machined surface.

In each sample area, the aerial data of the surface profile were recorded by an interferometer, Wyko NT8000. Taking into consideration the process of surface generation and the critical factor of tool-tip vibration, the aerial data were decomposed into two linear compositions, along the radial and along the tangential directions of a selected turning mark, respectively. Such decomposition of aerial



data can also be regarded as the measurement of the surface profile in a stylus mode, along a predefined sampling path. The importance of such decomposition and the effect of tool-tip vibration along the tangential direction are described in the following sections. The relationship between tool-tip vibration and surface generation can only be identified from the tangential data. On the other hand, the radial data possess a random nature and a diminished value due to the overlap of scallops resulting from adjacent turning marks. Compared with the tangential data, the radial data are not as significant in relation to explaining the generation of surface roughness, thus, they are excluded from the investigation in this chapter.

#### 9.4.1.2 Identification of Tool-Tip Vibration on the Machined Surface Profile

The digitised signals of cutting force and thrust force are converted and studied in the frequency domain using fast Fourier transform. The power spectrum density (PSD) is further employed to characterise the signals. According to previous study of the characteristic twin peaks found in the PSD plots (Wang et al. 2010), similar twin peaks are also identified in Experiments 1 and 2. In this chapter, for both single crystal Cu(111) specimen (Fig. 9.14b) and polycrystalline copper specimen (Fig. 9.14c) with different spindle speeds, the twin peaks can always be observed in the high-frequency interval of cutting forces, ranging from 12 to 14 kHz. On the other hand, no peaks with significant power spectrum density can be located in such a high-frequency range for thrust forces. On the contrary, the thrust force signals are intrinsically located in the frequency range lower than 100 Hz, as studied by Lee and Cheung (2001). However, this low-frequency thrust force does not directly contribute to the relative tool-work displacement; thus, only the cutting force should

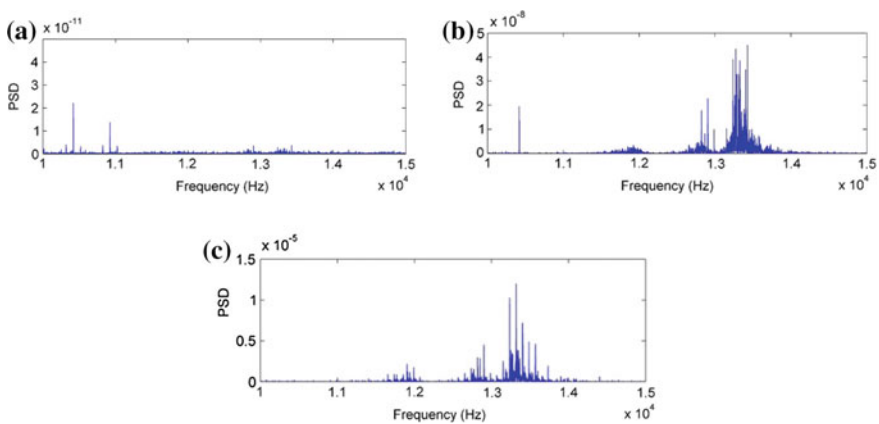


**Fig. 9.14** Power spectrum density plot of measured force signals: **a** thrust force in Experiment 2; **b** cutting force in Experiment 2 and **c** cutting force in Experiment 1

be included in the study of the mechanism of surface generation, and the modelling of the micro-cutting process.

An intrinsic property of the tool-tip vibration at 14 kHz, is utilised to reveal its influence on the profile of machined surface. In Experiment 2, the tangential data of the surface profile in a single turning mark are measured at a distance of 1.25 mm from the centre of the workpiece. The peak-to-peak distance ( $d_{pp}$ ) due to tool-tip vibration can be expressed as Eq. (9.17), where  $D$  is the distance from the turning mark to the centre of the workpiece,  $S$  is the spindle speed and  $f_{tiv}$  is the frequency of the tool-tip vibration, which is approximately assigned 14 kHz in the calculation.

$$d_{pp} = \frac{2\pi \cdot SD}{60f_{tiv}} \tag{9.17}$$

In Fig. 9.15, the measured distance is about 75  $\mu\text{m}$  on average. On the other hand, the calculation can be conducted at  $D = 1.25 \text{ mm}$  and  $S = 8000 \text{ rpm}$ , which results in a peak-to-peak distance of 0.0748 mm and a spatial frequency of  $13.33 \text{ mm}^{-1}$ . This result indicates that the influence of tool-tip vibration is significant on surface generation. The tool-tip vibration in the direction of the cutting force also induces the relative tool-work displacement in the direction of thrust force, and in turn, results in the periodic fluctuation of the surface profile during the micro-cutting process.

Since tool-tip vibration takes place at a fixed frequency during the turning of the entire surface of the specimen at a constant spindle speed, the linear velocity, or surface speed, is proportional to the distance from the location of the cutting tool to the centre of the workpiece.

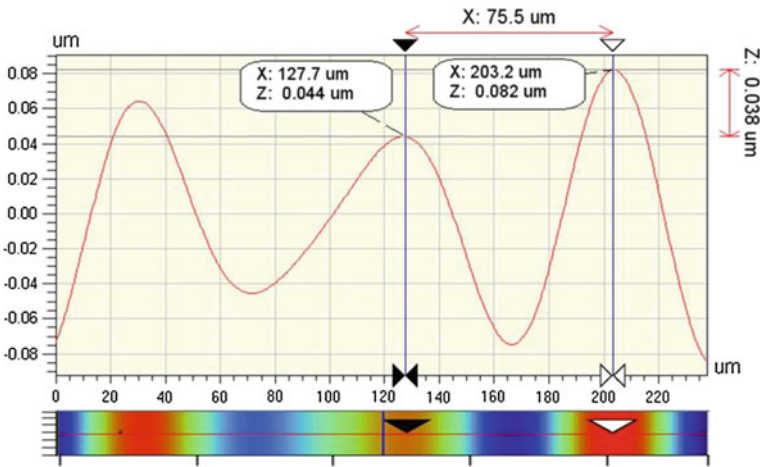


**Fig. 9.15** The surface profile in a single turning mark at a distance of 1.25 mm from the centre of the workpiece

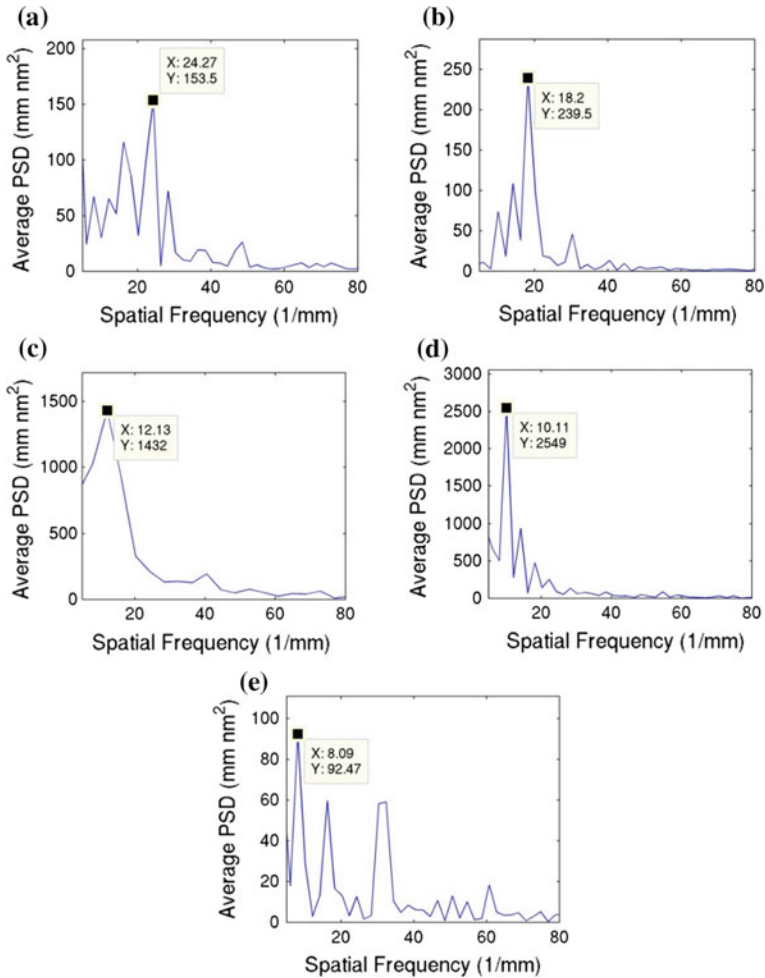


**Fig. 9.16** Left shift of identified peak at sample location 1–5 (a–e) in Experiment 1, X spatial frequency, Y average PSD

As designed in the experiments, the surface power spectrum density plots are calculated at the five sample areas along the radial direction, from 1 (close to centre of the workpiece) to 5 (away from centre of the workpiece). In each sample area, the spatial frequency is calculated along the tangential data of the surface profile, which contains the characteristics of tool-tip vibration, as proven above. In Fig. 9.16a–e, the peaks corresponding to the frequency of tool-tip vibration are indexed. A left shift to low spatial frequency can be observed, which results from an increase in surface speed.

This new method of measurement and calculation builds up a link between the temporal and the spatial frequencies in the micro-cutting process. The relationship

**Table 9.4** Spatial frequency and converted temporal frequency

Sample location	1	2	3	4	5
Spatial freq. (1/mm)	24.27	18.2	12.13	10.11	8.09
Converted temporal freq. (Hz)	14,225	13,715	14,219	14,391	13,548

between spatial frequency and temporal frequency can be expressed as  $f_{\text{spatial}} = (60 / 2\pi SD)f_{\text{temporal}}$ . The radial distance of the five sample areas are 0.7, 0.9, 1.4, 1.7 and 2 mm from the centre, respectively. Based on the measured spatial frequency, the converted temporal frequency is shown in Table 9.4 as below. A good estimation of the frequency of HFTTV can be found around 14 kHz.

In Experiment 2, further observation of the machined surface reveals the “spiral” shaped marks intersecting with the turning marks, as shown in the micrograph of Fig. 9.17a. The square area defined by broken yellow lines is magnified in Fig. 9.17b. The tangential profile of a length of 0.1 mm is selected along a single turning mark in the cutting direction. The spatial frequency is about  $90 \text{ mm}^{-1}$  calculated in Fig. 9.17b, which is about 0.2 mm from the centre of the workpiece. Substituting all the parameters into Eq. (9.17),  $d_{\text{pp}} = 2\pi \times 0.2 \times 8000 / (60 \times 14,000) = 0.012 \text{ mm}$ . Thus, the calculated spatial frequency is  $1/0.012 = 83.33 \text{ mm}^{-1}$ , which is of the same order as the measured spatial frequency.

Tool-tip vibration directly leads to relative tool-work displacement in surface generation. The relative distance between the tool-tip and the machining surface determines the process of material removal and other machining-related factors, such as cutting force, depth of cut and material removal rate, etc. The high-frequency tool-tip vibration in the direction of the cutting force is of paramount importance in understanding the micro-cutting process and surface generation. However, direct evidence is still missing to verify the relationship between low-frequency vibration in the direction of the thrust force and surface generation.

### 9.4.2 Effect of Sample Locations on Surface Roughness

As mentioned above, the tool-tip vibration factor is taken into consideration throughout the analysis. On the machined surface, the surface roughness values at the sample locations 1–5 are calculated using the aerial profile data, and are plotted in Fig. 9.18. With the same sampling length of 0.08 mm and sampling area of 0.08 mm by 0.08 mm at all the sample locations, the  $R$  values for peak-to-valley differences,  $R_t$  and  $R_z$ , increase significantly with increasing distance from the sample location to the centre of the workpiece. However, the arithmetic average  $R$  value ( $R_a$ ) does not follow the same trend. Due to the existence of tool-tip vibration, the inner sample locations contain as many more complete cycles of fluctuations than do the outer sample locations for the fixed sample area, due to the dependency on the radial distance ( $D$ ) as expressed by Eq. (9.17). On the other

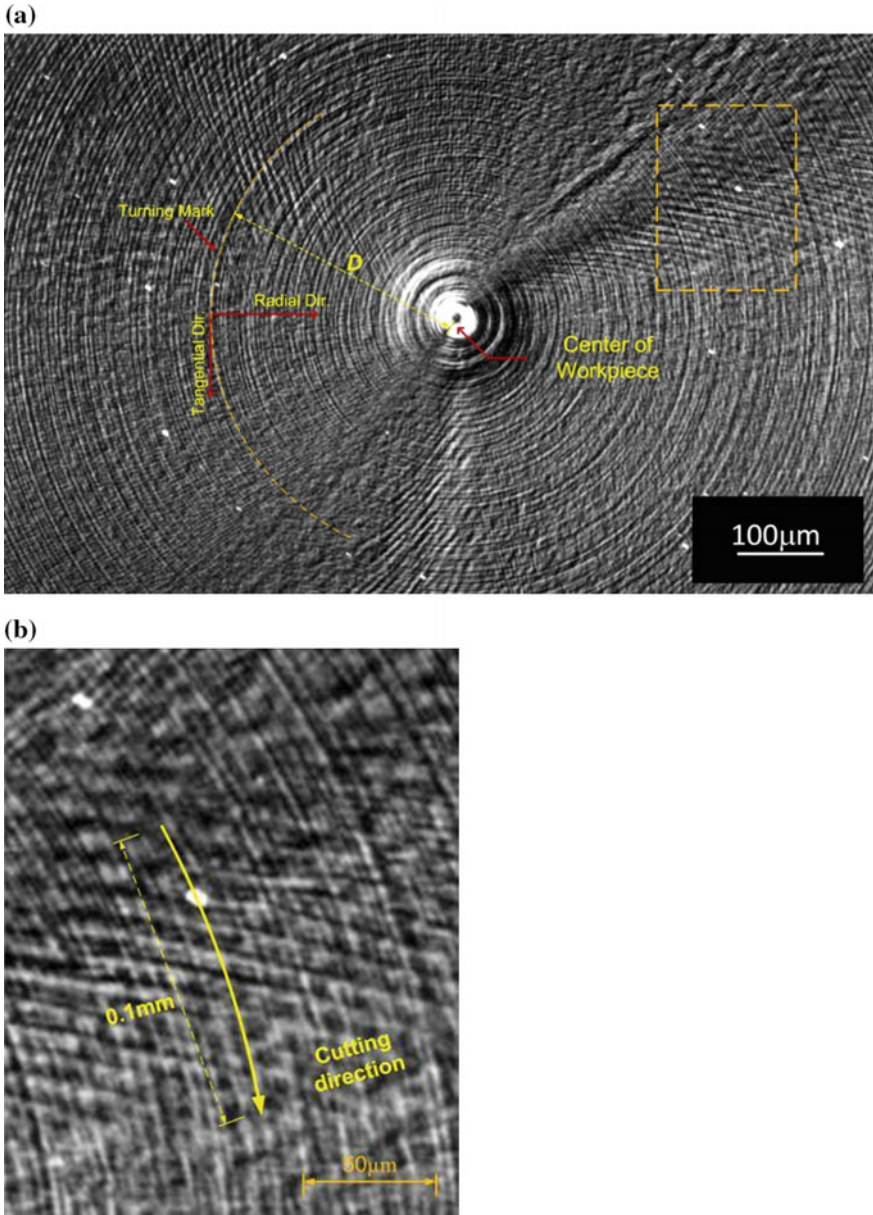


**Fig. 9.17** Micrograph of **a** the machined surface in Experiment 2 and **b** the magnified part of spiral marks at  $D = 0.2\text{--}0.3$  mm

hand, any machined surface must have a certain degree of surface waviness due to the precision of the machine tool, and single-point diamond turning possesses high form accuracy in the sub-micrometre range. Thus, from a statistical point of view,

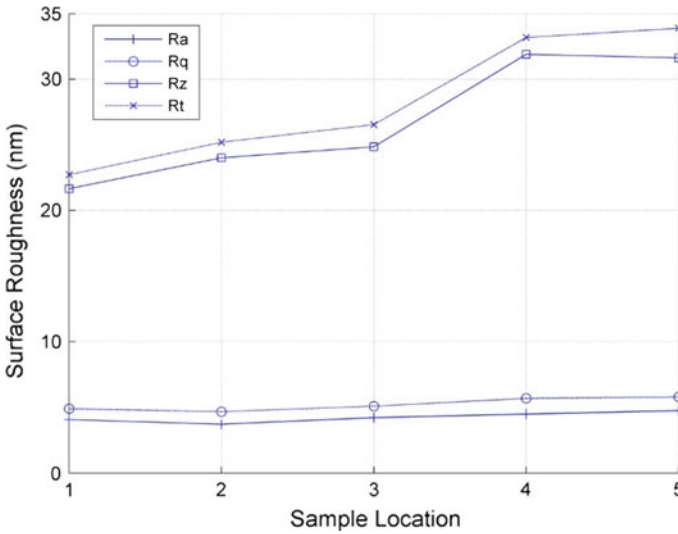


**Fig. 9.18** Measured  $R$  values of machined surface at sample locations 1–5 of Experiment 1

the inner sample location, which contains more cycles of surface fluctuation, is less sensitive to the effect of surface waviness, and in turn, a smaller peak-to-valley  $R$  value is ensured. On the other hand, a much larger value is likely to occur in the outer sample locations. However, the effect of surface waviness is never uniform, due to the nonlinear nature of the waviness itself at different sample locations. Therefore, the increase of the peak-to-valley  $R$  values is not linear either. In this regard, the experimental observation is compatible with our proposed model. Furthermore, it is well recognised that higher cutting (surface) speed is prone to generate a surface with greater surface roughness, as can be seen from the simulated and measured surface roughness in the work by Jang et al. (1996), and the cutting trials on single-point diamond turning in the work of Li et al. (2010). This is also in line with the measured surface roughness in this chapter, where both the surface speed and surface roughness increase, as the sample location becomes farther away from the centre of the workpiece.

### 9.4.3 *Effect of Sample Area Ratios and Representative Measurement*

Besides the sample locations, the effect of sample area ratios on surface roughness is studied in this section. The concept of a sample area ratio ( $\eta$ ) is first specially introduced to characterise the sampling effects on surface roughness in ultraprecision machining, with respect to the physical phenomenon of tool-tip vibration. The

sample area ratio is defined as the tool sample area over the total area of the machined surface, where oversampling is allowed on the machined surface. With the sample area ratio, the corresponding  $R$  values are redefined as  $\eta$ -sensitive  $R$  values  $\tilde{R}_{(x)}$ . In such manner, the calculation of  $\tilde{R}_{(x)}$  follows the rule given in Eq. (9.18a), where the  $R$  values obtained at  $j$ th sample location are denoted by  $R_{(x)}^j$ ,  $A^j$  is the corresponding sample area,  $A_{\text{total}}$  is the total area of the machined surface and the Einstein summation applies. An example of the derivation of  $\tilde{R}_z$  is given in Eq. (9.18b), where  $s$  is the sampling number.

$$\eta = \frac{\sum A^j}{A_{\text{total}}} \times 100\%, \quad \tilde{R}_{(x)} = \frac{A^j R_{(x)}^j}{A_{\text{total}}} \quad (9.18a)$$

$$\tilde{R}_z = \frac{A^j R_z^j}{A_{\text{total}}} = \frac{A^j \left( \frac{1}{s} \sum_{i=1}^s R_{ti}^j \right)}{A_{\text{total}}} \quad (9.18b)$$

Differing from the traditional definition of  $R$  value, whose raw data originated from a single area or a small number of sample areas, i.e. with a low  $\eta$  value, the  $\eta$ -sensitive  $\tilde{R}$  values characterise the entire machined surface in an unbiased manner. The two variables  $A$  and  $j$  in the definition of  $\tilde{R}$  (Eq. 9.18a) can be adjusted to comprehensively study surface roughness with respect to different sample areas and different numbers of samples, i.e. the  $\eta$  value. Using the concept of sample area ratio, the study of surface roughness can be divided into three regions: the low- $\eta$ , high- $\eta$  and oversampling regions.

Due to the effect of tool-tip vibration, the machined surface can be categorised as “periodic” because it has a particular surface texture or pattern. A periodic surface like that in Fig. 9.17a, is representative of the characteristics of the machined surface, if all the sample areas are selected along the radial direction with an increasing distance from the centre of the workpiece. In the machined surface of Experiment 2, a series of sample areas of 40  $\mu\text{m}$  by 40  $\mu\text{m}$ , 80  $\mu\text{m}$  by 80  $\mu\text{m}$  and 120  $\mu\text{m}$  by 120  $\mu\text{m}$  are employed to plot the  $\eta$ -sensitive  $\tilde{R}$  values, with different numbers of sample areas. The normalised  $\eta$ -sensitive surface roughness values are plotted against sample area ratios in Fig. 9.19. Based on Fig. 8.18,  $R_a$  and  $R_q$ ,  $R_z$  and  $R_t$  follow the same trend respectively; thus, for the sake of simplicity only  $\tilde{R}_a$  and  $\tilde{R}_t$  are selected to appear in Fig. 9.19 where  $\tilde{R}'_{(x)}$ ,  $\tilde{R}_{(x)}$  and  $\tilde{R}''_{(x)}$  stand for the measured roughness with the sample areas of 40  $\mu\text{m}$  by 40  $\mu\text{m}$ , 80  $\mu\text{m}$  by 80  $\mu\text{m}$  and 120  $\mu\text{m}$  by 120  $\mu\text{m}$ , respectively. Normalised values are utilised to ensure that all the curves can be presented to the same scale.

The low- $\eta$  region is defined below as having a sample area ratio less than 50%, in which region all the  $\eta$ -sensitive  $\tilde{R}$  values change dramatically, with a large standard deviation. The high- $\eta$  region is located between 50 and 100%, in which region the variation of the  $\tilde{R}$  values tends to be smooth. Over 100% of the sample

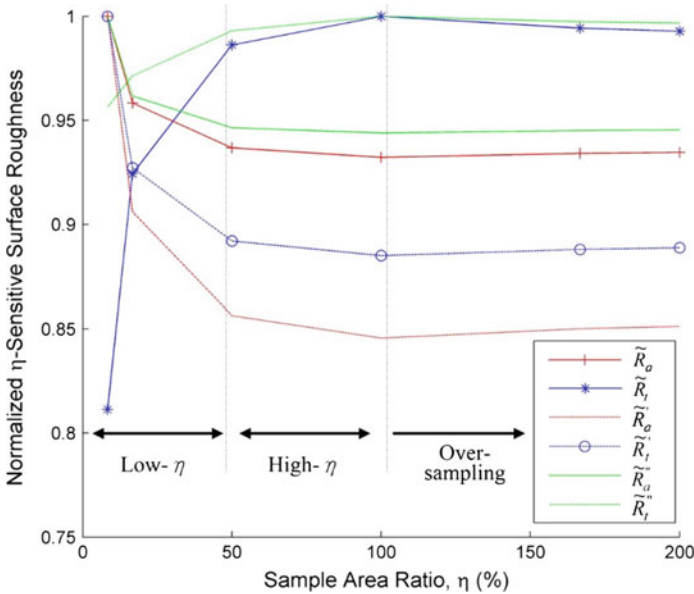


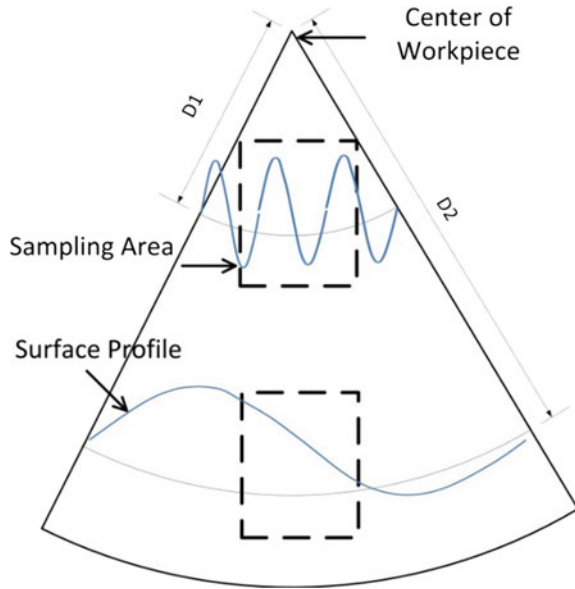
Fig. 9.19 Normalised  $\eta$ -sensitive  $R$  values in Experiment 1

area ratio is the oversampling region, in which more sampling does not yield a significant modification of the  $\tilde{R}$  values. In the low- $\eta$  region and for the sample area of  $80\ \mu\text{m}$  by  $80\ \mu\text{m}$ , if the effect of surface waviness is neglected, small surface coverage leads to lower peak-to-valley values ( $\tilde{R}_t$ ) far from the centre of the workpiece but shows a higher arithmetic average roughness ( $\tilde{R}_a$ ) at the same time. Such biased sampling results are improved in the high- $\eta$  region, where all the  $\eta$ -sensitive  $\tilde{R}$  values become stable with smaller standard deviations. As for the oversampling region, no further improvement can be found, since the machined surface is fully characterised in the high- $\eta$  region.

If an ideal case is assumed without the uncertainty induced by surface waviness, a schematic diagram of the sampling area and the  $\eta$ -sensitive  $\tilde{R}$  values would appear as shown in Fig. 9.20. At different distances from the centre of the workpieces D1 and D2, the same sampling area yields different results for a sampled profile. When  $D1 \ll D2$ , the sampled profile contains at least several complete cycles of fluctuation at D1, while only a part of a cycle is windowed at D2. In Fig. 9.20, the  $\eta$ -sensitive  $\tilde{R}$  values are calculated in the low- $\eta$  region, which in turn results in a small peak-to-valley  $R$  value. If the sample area ratio is increased, no matter if it is by increasing (1) the unit sample area or (2) the number of sample areas, more complete cycles of surface profile fluctuation can be included in the calculation; therefore, a large peak-to-valley  $R$  value can be obtained.



**Fig. 9.20** A schematic of the sampling area and the effect on the calculation of the  $\eta$ -sensitive values



A suggested sampling length of 80  $\mu\text{m}$  is given in the ISO standard (ISO 4288:1996) for roughness in the range smaller than 20 nm; however, this value does not take into consideration the important factor of tool-tip vibration in surface generation of single point diamond turning. Based on our theory, a sampling length of 80  $\mu\text{m}$  is applicable with the maximum distance from the centre of the workpiece  $D_{\text{max}}$  given by Eq. (9.19), which is derived from Eq. (9.17) for the case when a single sample area is employed.

$$D_{\text{max}} \leq \frac{0.08 \times 60 f_{\text{ttv}}}{2\pi \cdot S} \tag{9.19}$$

In the low- $\eta$  region of Fig. 9.19, with the smallest sample area, both  $\tilde{R}'_a$  and  $\tilde{R}'_t$  decrease when the sample area ratio increases. When larger sample areas are employed, the trend of  $\tilde{R}_a$  and  $\tilde{R}''_a$  remains the same as  $\tilde{R}'_a$ , but the trend of  $\tilde{R}_t$  and  $\tilde{R}''_t$  becomes the opposite of  $\tilde{R}'_t$ . This observation indicates that a sampling length far shorter than  $2\pi \cdot SD/60f_{\text{ttv}}$  is prone to yield a biased characterisation of the surface. According to Eq. (9.19), a larger sample area is required when the sample location is farther from the centre of the workpiece. However, when the sample area is larger than adequate, as with the 120  $\mu\text{m}$  by 120  $\mu\text{m}$  in Fig. 9.19, no further improvement in surface roughness can be identified. From the aspect of the sample area ratio, this sample area also results in an oversampling region.

According to the above analysis, it can be concluded that better sampling can be achieved by a larger unit sample area or an increased number of sample areas. With the introduction of the concept of  $\eta$ -sensitive  $\tilde{R}$ , a generic guideline for sampling is

to avoid the low- $\eta$  region when measuring surface roughness within sample areas. In other words, a representative measurement should be made in the high- $\eta$  region, from which the result obtained can be used to characterise the surface finish.

## 9.5 Modelling and Characterisation of Surface Roughness Generation

### 9.5.1 Surface Generation Model with Tool-Tip Vibration

High-frequency tool-tip vibration in the cutting force direction is simplified and modelled by a sinusoidal wave during the face turning process. In an ideal case where the extreme precision of the machine tool leads to negligible surface waviness, the turning process can be regarded as a surface roughening process with the cutting tool moving along the sinusoidal wave at a constant spindle speed. According to the experimental observations and previous analysis, the vibration takes place in the full frequency spectrum of the dynamic system, including low- and high-frequency vibration. However, only the effect of high-frequency tool-tip vibration is significant enough to induce relative tool-work displacement, which in turn roughens the surface. Therefore, a typical sinusoidal wave is employed in the modelling, as expressed by Eq. (9.20).

$$z = z_0(t) + z_{\text{ttv}}(t) = z_0(t) + A_{\text{ttv}} \sin(2\pi\omega t + \varphi_0) \quad (9.20)$$

The general model is defined by Eq. (9.20), where the location of the cutting tool is the function of cutting time  $t$ , and the profile of the machined surface consists of two components: the waviness  $z_0(t)$  and roughness induced by the tool-tip vibration  $z_{\text{ttv}}(t)$ . In reality, all kinds of factors, including the precision of the machine tool, dynamic performance and material-related factors, determine that the two components are time-dependent variables. If both components are studied from the aspect of periodic functions, the frequency of  $z_0(t)$  is lower than that of  $z_{\text{ttv}}(t)$  by several orders of magnitude. In this section, the first component is assumed to be time-independent, i.e. the waviness is small enough to be ignored. Since the aim of the proposed model is to explain the effect of tool-tip vibration on surface generation instead of obtaining the exact values, the amplitude of tool-tip vibration  $A_{\text{ttv}}$  and the frequency  $\omega$  are assumed to be constant. This also agrees with the experimental results (Wang et al. 2010) in that no obvious shift in the frequency of the characteristic twin peaks was observed.

Based on the model proposed in Eq. (9.20), the 3D surface is plotted (with  $\omega = 14$  kHz and  $A_{\text{ttv}} = 150$  nm) in Fig. 9.21a, with its contour plot, by projection of the profile data on the sample area. In Fig. 9.21a, the peaks and valleys are coloured orange and blue, respectively. The small black dots denote the extreme values on the surface profile. The pattern of the simulated surface profile is further verified by the experimental result shown in Fig. 9.21b.

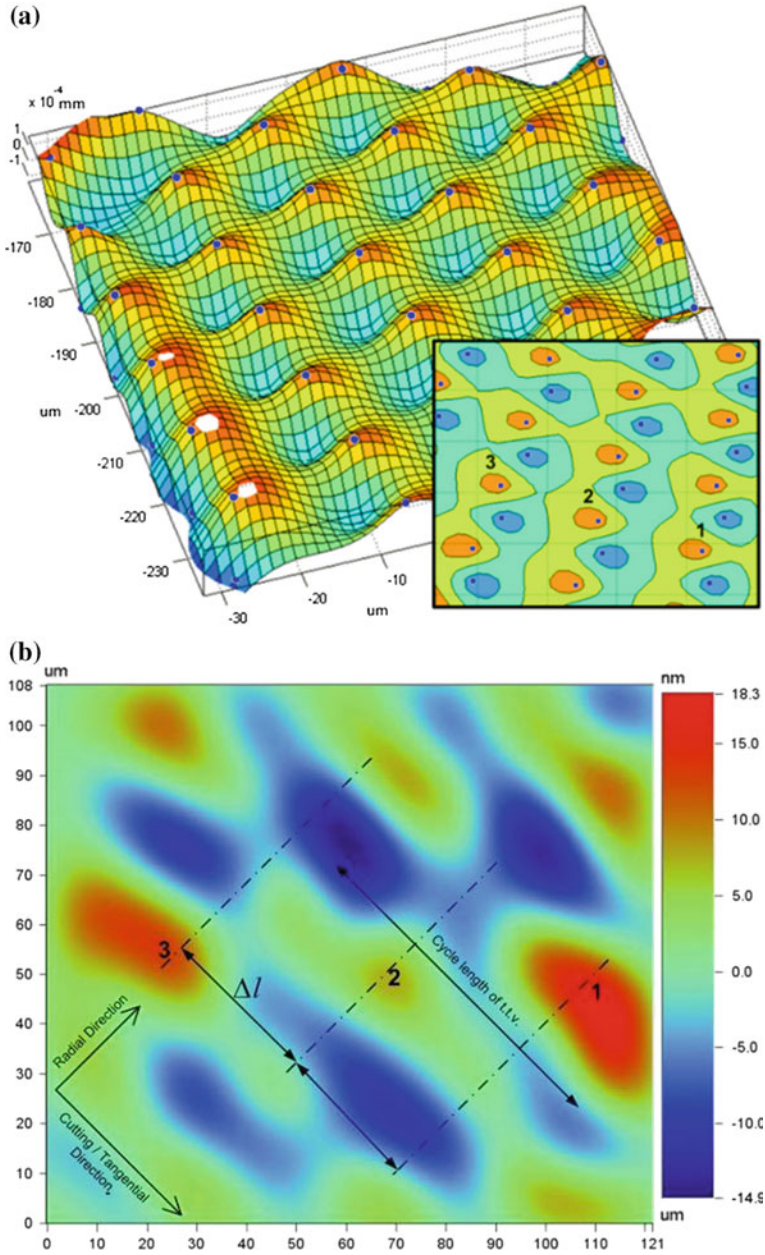


Fig. 9.21 a Simulated surface profile with tool-tip vibration and its contour plot; b corresponding measured surface profile and identified periodic fluctuations

The 3D data of the surface profile in Experiment 2 are recorded, and the noise information of the high spatial frequency and the frequency corresponding to  $z_0(t)$  are eliminated by a band-pass filter to retain the key features of the machined surface. The peaks and valleys induced by tool-tip vibration are observed along the cutting direction. As indicated, the measured cycle length also agrees with Eq. (9.17). Three consecutive peak locations are labelled with numbers (1, 2 and 3) and three corresponding valleys are identified in the bottom right region. The simulated pattern (also labelled with 1, 2 and 3 in Fig. 9.21a) perfectly matches with that appearing on the measured pattern. This result further verifies both the theory and modelling of surface generation and the importance of tool-tip vibration. Therefore, the modelling of surface roughness should consider both the kinematic surface roughness and the surface roughness induced by tool-tip vibration.

### 9.5.2 Formation of Spiral Marks on the Machined Surface

An instant application of the proposed model of surface generation can be found to explain the formation of the spiral marks observed in the experiments, as shown in Fig. 9.17. In general, the formation of spiral marks is due to the existence of incomplete tool-tip vibration cycles in adjacent turning marks. The generic temporal relationship is expressed by Eq. (9.21), where  $S$  is the spindle speed (rpm),  $T_{\text{spd}}$  is the cycle time per revolution (s),  $T_{\text{ttv}}$  is the cycle time of tool-tip vibration,  $n$  is an integral number of complete cycles and  $\Delta t$  is the total remainder time besides  $n$  complete cycles in a single cycle  $T_{\text{spd}}$ . The superscripts  $(-)$  and  $(+)$  are employed to indicate that the source of the remainder time is from the previous revolution of the spindle cycle and the remainder time accumulates and is used for the next revolution of the spindle. The condition of Eq. (9.22) holds when the feed rate is low and a very small discrepancy exists for adjacent turning marks. Although unachievable in reality, the equality holds only when the surface (linear) speed is constant for adjacent turning marks. The remainder time  $\Delta t$  directly results in a position shift of peak (and valley) locations, as shown by the numbered peaks in Fig. 9.21b. The shift length  $\Delta l$  is a variable of distance to the centre  $D$  and  $\Delta t$ , and is obtained by Eq. (9.23). The consecutive shift of peaks forms the “spiral arms” observed in the overall situation.

$$T_{\text{spd}} = \frac{60}{S} = n \cdot T_{\text{ttv}} + \Delta t = \Delta t^{(-)} + n \cdot \frac{1}{f_{\text{ttv}}} + \Delta t^{(+)} \quad (9.21)$$

$$\Delta t^{(-)} + \Delta t^{(+)} \leq \frac{1}{f_{\text{ttv}}} \quad (9.22)$$

$$\Delta l = \frac{2\pi S}{60} \cdot D \cdot \Delta t \quad (9.23)$$

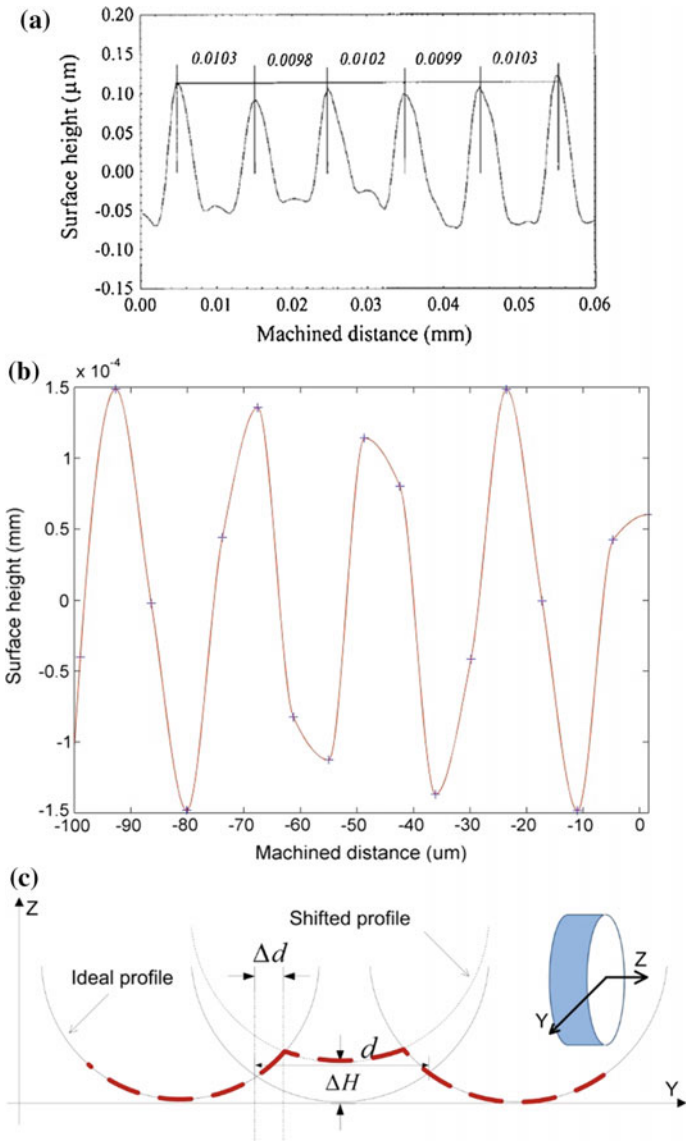


**Fig. 9.22** a Successive turning marks on the measured radial profile by To et al. (2001); b simulated profile with the model of tool-tip vibration; c Schematic of shifted profile on the adjacent turning marks

### 9.5.3 Spatial Error on the Profile in the Feed Direction

To study the influence of material swelling on surface roughness, To et al. (2001) designed a series of face turning experiments on single crystal copper and aluminium workpieces and the machined surface was measured along the radial (feed) direction. At a constant spindle speed and feed rate, the peak-to-peak intervals measured on the surface profile along the feed direction should be equally spaced in an ideal case. However, in the experiments conducted by To et al. (2001), a spatial error was identified on the continuous three intervals on the radial measurement with a particular ratio, as in the normalised form in Eq. (9.24a), where  $d_i^{(a)}$  denotes the distance of the  $i$ th ( $i = 1, 2$  and  $3$ ) intervals in the subfigure (a). A radial profile extracted from the simulated data of the surface profile is shown in Fig. 9.22(b). The distance ratio of the predicted profile is expressed by Eq. (9.24b). A good correlation is found between the simulated and the measured data. A further explanation for the spatial error can be deduced from the schematic diagram in Fig. 9.22c. The successive three turning marks along the feed direction are plotted. Since the effect of tool-tip vibration on the machine surface is approximated by a sinusoidal wave, the ideal profile and shifted profile are indicated by arrows. Following the notation of Eq. (9.22), the shifted height on the surface profile ( $\Delta H$ ) can be expressed by Eq. (9.25), in which the time shift for the current turning mark ( $\Delta t^{(-)}$ ) is equal to the remainder time ( $\Delta t^{(+)}$ ) of the last turning mark at the same radial location.

$$d_1^{(a)}:d_2^{(a)}:d_3^{(a)} = 1:0.9515:0.9903 \quad (9.24a)$$

$$d_1^{(b)}:d_2^{(b)}:d_3^{(b)} = 1:0.7566:0.9996 \quad (9.24b)$$

$$\Delta H = A_{\text{ttv}} \left[ 1 - \sin \left( 2\pi\omega\Delta t^{(-)} + \phi_0 \right) \right] \quad (9.25)$$

## References

- Abouelatta, O. B., & Mádl, J. (2001). Surface roughness prediction based on cutting parameters and tool vibrations in turning operations. *Journal of Materials Processing Technology*, 118, 269–277.
- Bispink, T., & Weck, M. (1992). Performance analysis of feed-drive systems in diamond turning by machining specified test samples. *CIRP Annals - Manufacturing Technology* 41(1), 601–604.
- Cheung, C. F., & Lee, W. B. (2000a). A multi-spectrum analysis of surface roughness formation in ultra-precision machining. *Precision Engineering*, 24, 77–87.
- Cheung, C. F. & Lee, W. B. (2000b). A theoretical and experimental investigation of surface roughness formation in ultra-precision diamond turning, *International Journal of Machine Tools & Manufacture*, 40, 979–1002.

- Cheung, C. F., & Lee, W. B. (2001). Characterisation of nanosurface generation in single-point diamond turning. *International Journal of Machine Tools and Manufacture*, 41, 851–875.
- Hocheng, H., & Heih, M. L. (2004). Signal analysis of surface roughness in diamond turning of lens molds. *International Journal of Machine Tools and Manufacture*, 44, 1607–1618.
- Jang, D. Y., Choi, Y.-G., Kim, H.-G., & Hsiao, A. (1996). Study of the correlation between surface roughness and cutting vibrations to develop an on-line roughness measuring technique in hard turning. *International Journal of Machine Tools and Manufacture*, 36, 453–464.
- Kong, M. C., Lee, W. B., Cheung, C. F., & To, S. (2006). A study of materials swelling and recovery in single-point diamond turning of ductile materials. *Journal of Materials Processing Technology*, 180(1–3), 210–215.
- Lee, W. B., & Cheung, C. F. (2001). A dynamic surface topography model for the prediction of nano-surface generation in ultra-precision machining. *International Journal of Mechanical Sciences*, 43, 961–991.
- Li, L., Collins, S. A., Jr., & Yi, A. Y. (2010). Optical effects of surface finish by ultraprecision single point diamond machining. *Transactions of ASME, Journal of Manufacturing Science and Engineering*, 132, 021002-1–021002-9.
- Piispänen, V. (1948). Theory of formation of metal chips. *Journal of Applied Physics*, 19, 876–881.
- Recht, R.F. (1964). Catastrophic thermoplastic shear. *Journal of Applied Mechanics*, pp. 189–193.
- Takasu, S., Masuda, M. & Nishiguchi, T. (1985). Influence of steady vibration with small amplitude upon surface roughness in diamond machining, *Annals of the CIRP*, 34(1), 463.
- To, S., Cheung, C. F., & Lee, W. B. (2001). Influence of material swelling on surface roughness in diamond turning of single crystals. *Materials Science and Technology*, 17, 102–108.
- Wang, H., To, S., Cheung, C. F. & Lee, W. B. (2008). Finite element simulation of the cutting process in SPDT, *Proceedings of the International Conference of the EUSPEN*, 2, 86–89.
- Wang, H., To, S., Chan, C. Y., Cheung, C. F., & Lee, W. B. (2010). A theoretical and experimental investigation of the tool-tip vibration and its influence upon surface generation in single-point diamond turning. *International Journal of Machine Tools and Manufacture*, 50, 241–252.

# Chapter 10

## Dynamic Modelling of Shear Band Formation and Tool-Tip Vibration in Ultra-Precision Diamond Turning

**Abstract** Elastic strain induced shear bands and high-frequency tool-tip vibration are two important physical phenomena associated with the chip morphology and machining dynamics of the micro-cutting process. These phenomena and related topics have been studied separately and so far, there has been no model developed that can successfully link together these phenomena in different research areas of ultra-precision machining. This chapter is based on the system approach which includes the components of the machine tool and cutting process. The embedded system time manifests its function in the cyclic behaviour of the formation of serrated chips with elastic strain-induced shear bands, the dynamic response of high-frequency tool-tip vibration, and the previously proposed characterisation method of the machined surface.

As discussed in the preceding chapters, elastic strain-induced shear band and high-frequency tool-tip vibration are two of the important physical phenomena in the micro-cutting process, in terms of chip morphology and machining dynamics. These phenomena and related topics have been studied separately and so far there has been no model developed that can successfully link these phenomena together in different research areas of ultra-precision machining.

Adiabatic shear bands (ASBs) result from the competition between thermal softening due to the plastic heating effect and strain hardening in deformed materials. In machining, the thickness and spacing of adiabatic shear bands were usually analysed in terms of the cutting velocity or cutting speed (Wright and Ockendon 1996; Molinari 1997; Molinari et al. 2002). Common assumptions were made in relation to a constant cutting speed (Molinari et al. 2002) under quasi-static conditions (Dinzart and Molinari 1998) and/or with a perfectly plastic material (Wright and Ockendon 1992). In the diversity of the previously proposed models, the thickness and spacing of the shear bands were considered approximately inversely proportional to the imposed strain rate or cutting speed. Molinari et al. (2002) conducted a series of cutting experiments to identify the relationship between the occurrence of adiabatic shear bands and cutting speed in orthogonal cutting of Ti-6Al-4V. In the speed range from 0.01 to 73 m/s, the fully formed adiabatic shear



bands were observed only at velocities of 12–36 m/s. However, in our previous study (Wang et al. 2010a, b), high-frequency tool-tip vibration (HFTTV) was identified as an intrinsic property of the dynamic process which is independent of the cutting speed in face turning where the cutting speed is proportional to the radial distance from the centre of the workpiece at a constant spindle speed. Since HFTTV is directly related to the load drop induced by the formation of adiabatic shear band, a definite correlation between the cutting speed and adiabatic shear bands does not exist in terms of a dynamic system for the micro-cutting process. Therefore, as found by many researchers, the dominant factor of cutting speed was introduced to provide an explanation for the formation of adiabatic shear bands, since quasi-static models were employed in their study. However, the quasi-static assumption oversimplified the problem, which is actually not realistic.

The effect of strain rate in the micro-cutting process is one of the critical issues that is yet fully understood. Different models have been proposed to calculate the mean or average shear strain rate in the primary deformation zone (Drucker 1949; Chao and Bisacre 1951; Kececioglu 1958; Oxley 1963). Astakhov (1998) reviewed the prior research on strain rate and concluded that the average shear strain rate in the shear zone lies in the range of  $10^3$ – $10^5$   $s^{-1}$  or even higher. According to the regimes of mechanical loading response shown in Fig. 10.1 (Wasley 1973), a dynamic model should be established instead of a quasi-static one, where the elastic and plastic stress wave need to be considered. In a recent study, the effect of strain rate in metal cutting has been examined by FEM analysis (Davim and Maranhão 2009), where the variation of strain rate was implemented by changing the cutting speed of the rigid body movement of the cutting tool. The strain-rate effect has also received attention in the development of constitutive models for work materials, such as the Johnson–Cook model and the models proposed by Dudzinski and Molinari (1997) and Shirakashi et al. (1983). With such constitutive models, the strain-rate effect was able to be studied even with a static model, such as in Budak and Ozlu (2008)

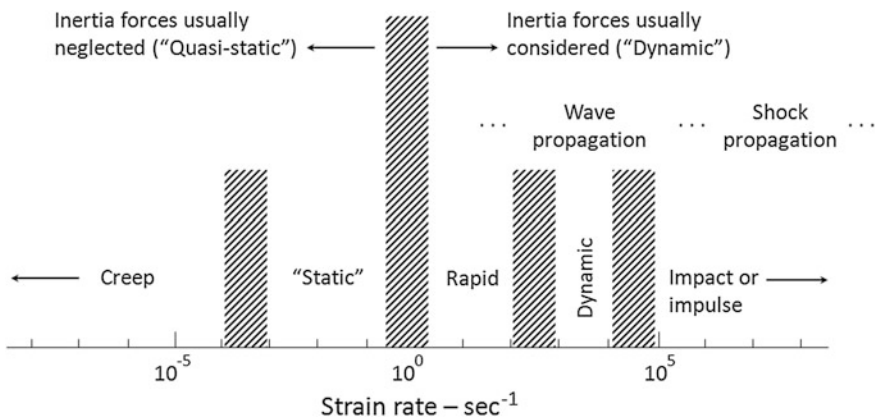


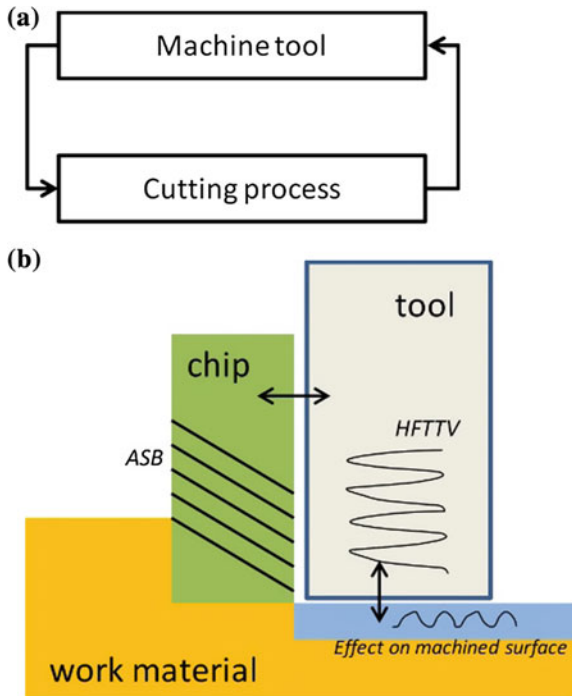
**Fig. 10.1** Regimes of mechanical loading response (Wasley 1973)

and Dirikolu et al. (2001). However, a static model overlooks the physical phenomenon of the micro-cutting process in ultra-precision diamond turning.

Based on our prior research findings, high-frequency tool-tip vibration is a dominant factor in the formation of shear bands and contributes to the fluctuation of the cutting force, heat generation and other related problems. In recent research, the tool-tip vibration in this high-frequency range was successfully applied by mode control techniques to improve surface roughness (Ostasevicius et al. 2010) in their experiments; however, the mechanism has not been fully studied. In this chapter, the relationship between HFTTV and elastic strain induced shear bands is first established. Without the popular assumptions on quasi-static process and perfectly plastic deformation, a dynamic model is proposed to further the understanding in different aspects.

The study in this chapter is on the basis of a system approach, which includes the components of the machine tool and cutting process, as shown in Fig. 10.2a. Differing from an assemblage as simple as a set of elements, the most important property of a system is the system time, i.e. the system’s component must be time dependent to achieve dynamic interaction among system components and for system control (Astakhov 1998). In this study, the system time is embedded and manifests its function in the cyclic behaviour of the formation of serrated chips with elastic strain induced shear bands, in the dynamic response of high-frequency tool-tip vibration and in the previously proposed characterisation method of machined surface by the dynamic system shown in Fig. 10.2b.

**Fig. 10.2** a The dynamic system of machining process and b a schematic plot of the components in the micro-cutting process and their connections



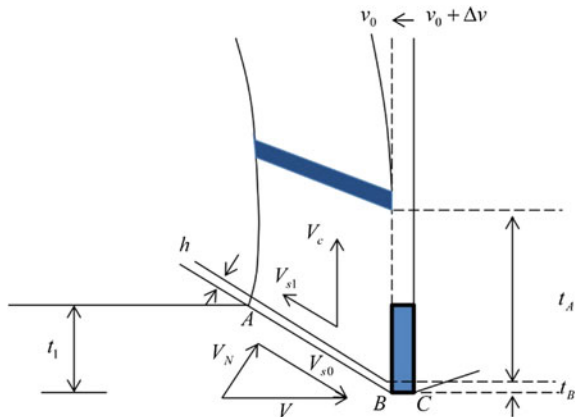
### 10.1 A Transient Analysis for Shear Band Formation

Following the assumptions adopted by Dinzart and Molinari (1998), a quasi-static model during the final stage is employed to study the relationship between cutting velocity, thickness and spacing of the shear bands first. Differing from Molinari et al. (2002), the effect of HFTTV and elastic strain is further studied based on transient analysis, using the steady-state model shown in Fig. 10.3.

First, the thickness of shear band ( $d$ ) is determined by Eq. (10.1) with applied velocity ( $V^*$ ) as defined by Dinzart and Molinari (1998), where  $m$  is the strain-rate sensitivity factor,  $k_0$  is the heat conductivity,  $a$  is the thermal softening parameter,  $\tau_0$  is the shear flow resistance and  $\theta_0$  denotes the initial temperature. The relationship between the velocity parameters is expressed by Eq. (10.2), as derived by Molinari et al. (2002). Therefore, combining Eqs. (10.1) and (10.2), the time for the formation of shear band ( $t_B$ ) can be obtained by Eq. (10.3). On the other hand, the time for the elastic deformation to achieve a large volume of deformation is determined by Eq. (10.4), which is directly derived from the equation for the shear band spacing (Wright and Ockendon 1996; Molinari 1997). Based on Eqs. (10.3) and (10.4), the parameter  $\eta_t$  employed in our previous work (Wang et al. 2010a) can be further calculated from Eq. (10.5), which links the time ratio with the cutting speed following a proportional relationship. Thus, at higher cutting speed, the thickness of the shear bands decrease and the spacing between the shear bands increases relatively. Moreover, the relationship between the frequencies of HFTTV ( $f_{itv}$ ) and the formation of ASBs ( $f_{ASB}$ ) can found in Eq. (10.6) with an integral scaling factor ( $k$ ).

$$d = 6\sqrt{2m} \frac{k_0\theta_0}{V^*a\tau_0} \tag{10.1}$$

**Fig. 10.3** A schematic of the transient model for orthogonal cutting



$$V_c = V \sin \phi, \quad V^* = \frac{V_{s0} - V_{s1}}{2} = \frac{V}{2} \cdot \frac{\cos \alpha}{\cos(\phi - \alpha)} \quad (10.2)$$

$$t_B = t_2 - t_1 = d \sin \phi / V_c = 6\sqrt{2m} \frac{k_0 \theta_0 \sin \phi}{V^* V_c a \tau_0} = \frac{12\sqrt{2mk_0 \theta_0} \cos(\phi - \alpha)}{a \tau_0 \cos \alpha \cdot V^2} \quad (10.3)$$

$$t_A = \frac{2\pi}{V \sin \phi} \left( \frac{m^2 k c (1-a)^2 \theta_0^2}{\left(1 + \frac{1}{m}\right) \beta^2 (\ddot{\gamma})^3 \hat{\tau}_0 a^2} \right)^{1/4} \quad (10.4)$$

$$\eta_t = \frac{t_A}{t_B} \approx \frac{l_A}{l_B} \propto V \quad (10.5)$$

$$f_{ASB} = \frac{1}{t_A + t_B} = k \cdot f_{iv} (k \geq 1) \quad (10.6)$$

## 10.2 Dynamic Model for Shear Band Formation

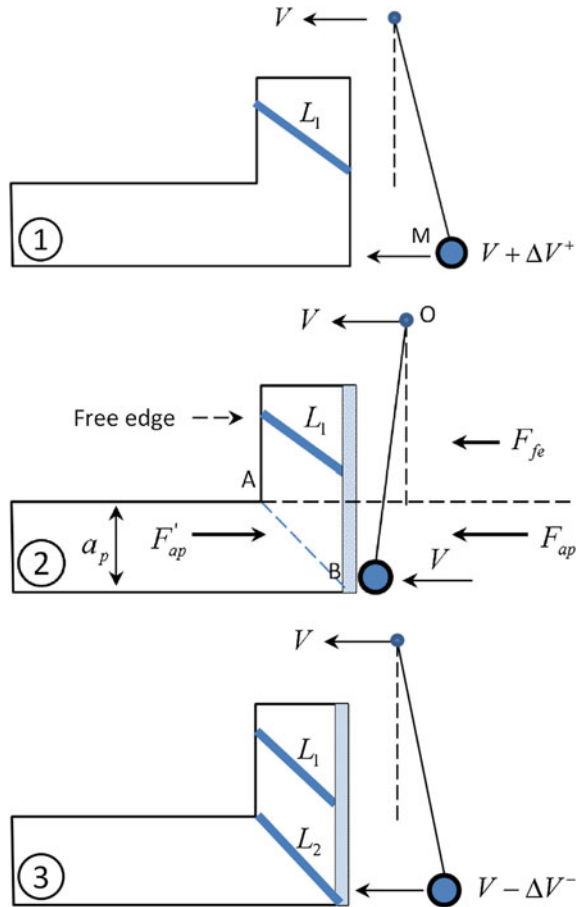
### 10.2.1 Dynamic Model

In this section a dynamic model is developed based on the previously proposed pendulum model (Wang et al. 2010b), so as to reveal the intrinsic connection between the theory and model of HFTTV and ASBs. The input of the proposed dynamic model is the introduction of HFTTV into the micro-cutting system. With the outputs of shear bands formation as well as the related parameters, such as equivalent cutting velocity and dynamic responses, the dynamic model considers chip formation, tool dynamics and surface generation as a system. Several assumptions are made in this approach.

The dynamic model is applied after full formation of the first ASB (L1, in Fig. 10.41). The frequency of ASBs is assumed to be the same as that of HFTTV, i.e.  $k = 1$  in Eq. (10.6). Solely, the situation that HFTTV is in phase with the cyclic formation of ASBs is illustrated here. The effect of phase shift is further explained in the following section.

As shown in Fig. 10.4, the tool tip of the diamond cutter is shown as a pendulum with a constant cutting speed ( $V$ ). The tool tip is modelled by a rigid bob with a mass ( $M$ ). The extra velocity ( $\Delta V^\pm$ ) due to HFTTV is superposed on the cutting speed ( $V$ ), and the sign ( $\pm$ ) of the superposed velocity is determined by its phase. In stage 1 of Fig. 10.4, the rigid bob accelerates in the same direction as the cutting speed. As a result, the actual strain rate imposed on the work material exceeds that provided solely by the cutting speed. In stage 2, a thin layer of work material directly in contact with the rake face of the tool tip experiences the process of pre-compression. In this stage, the elastic energy on the tool tip is transferred to the

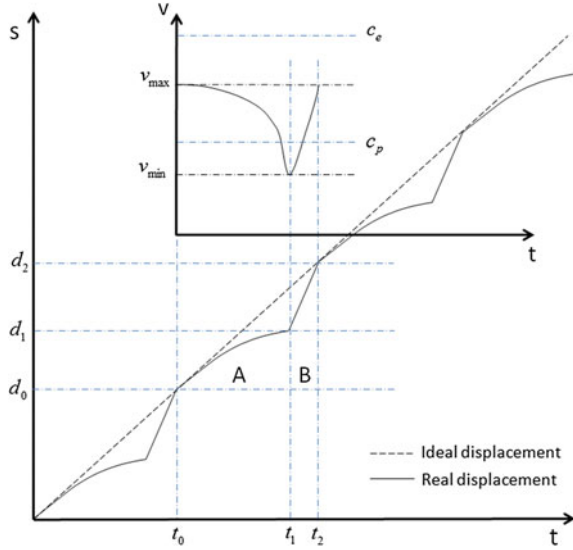
**Fig. 10.4** Dynamic model of HFTTV and ASBs



chip root by the pre-compressed layer as shown in the shaded rectangular area. The effects of pre-compression are (i) the displacement and bending moment of the chip above the depth of cut ( $a_p$ ), due to the effect of the free edge; and (ii) the elastic strain concentration at both the free edge (point A) and chip root (point B), which further lead to the initiation and propagation of ASBs, as explained in our previous work (Wang et al. 2010a). At this moment, right before the initiation of ASBs, the maximum cutting force on the tool tip is achieved and the superposed velocity vanishes. In stage 3, the formation of ASB abruptly reduces the stress capacity of the elastically strained material due to the effect of work softening, which results in a load drop on the cutting force. In this stage, an opposite speed is superposed in the negative direction to the cutting speed.

On the other hand, the three stages of a complete cycle of HFTTV with regard to the formation of ASBs lead to cyclic behaviour in the tool-tip displacement as well as the cutting speed, as shown in Fig. 10.5. The broken line illustrates the ideal

**Fig. 10.5** The cyclic displacement of tool tip and the transient cutting speed



tool-tip displacement and the solid line shows the actual displacement. Regions A and B correspond to the time notations  $t_A$  and  $t_B$  in Fig. 10.3. Considering the cutting speed and the imposed velocity by HFTTV, the equivalent cutting velocity is qualitatively plotted in the sub-coordinate system in Fig. 10.5. In region A, the cyclic fluctuation on the equivalent cutting velocity experiences stages 1 and 2, as plotted in Fig. 10.4. The velocity in region B corresponds to stage 3 in Fig. 10.4, provided that the vibrations of HFTT and the formation of ASBs are in phase.

### 10.2.2 The Effect of Equivalent Cutting Velocity

The significance of HFTTV for the equivalent cutting velocity is that it can induce a sharp increase in the cutting velocity within an extremely short interval of time. It does not affect a large volume of work material, but does effectively modify the stress distribution in the primary deformation zone, in favour of the formation of ASBs and a reduced cutting force. An explanation for this is based on the subsequent analysis of stress wave propagation in this section.

The equivalent cutting velocity is confined within its maximum ( $v_{max}$ ) and minimum ( $v_{min}$ ), as denoted in Fig. 10.5. In the dynamic region (Fig. 10.1), the wave propagation should be considered. The speeds of elastic wave ( $c_e$ ) and plastic wave ( $c_p$ ) propagation can be calculated as in Eq. (10.7), where  $\rho$  is the density of work material,  $E$  is Young's modulus and  $E'$  is defined for the plastic region. Since  $E' \ll E$ ,  $c_p \ll c_e$ .

$$c_e = \sqrt{E/\rho}, \quad c_p = \sqrt{\frac{1}{\rho} \cdot \frac{\partial \sigma^P}{\partial \epsilon^P}} \equiv \sqrt{E^P/\rho} \quad (10.7)$$

The relationship between the equivalent cutting velocity and wave propagation speed is shown in Fig. 10.5. The HFTTV induced increase in cutting speed makes the equivalent cutting velocity exceed the speed of plastic wave propagation ( $c_e$ ) in stage 1 of Fig. 10.4, i.e.  $v_{\max} > c_p$ , which reduces the plastic strain to a much smaller volume in the primary deformation zone. This is also evidenced in the review of the principle of high-speed machining in the work of Zhou et al. (2003). On the other hand, the elastic wave propagates at a much faster rate, i.e.  $c_e \gg v_{\max} > c_p$ , so the elastic strain concentration at points A and B in Fig. 10.4 can be accomplished at an infinite rate as assumed. During the pre-compression period (stage 2 in Fig. 10.4), the equivalent cutting velocity decreases to its minimum ( $v_{\min}$ ) which is possibly lower than  $c_p$ . However, the ASB occurs at this moment and the load drop takes place in the cutting force in stage 3. The fast equivalent cutting velocity or higher strain rate ensures a thinner pre-compression layer, i.e. the bulk material experiences elastic deformation only, which in turn reduces the energy loss on the pendulum bob or the tool tip in reality.

### 10.2.3 Validation and Application

As one of the most important commercial magnesium alloys, Mg–9Al–1Zn alloy (AZ91) in the shape of a rectangular plate is employed as the workpiece material in this verification experiment (Fig. 10.6). As experimental verification of the proposed model, it is of paramount importance to keep all the experiments at the same machining conditions, i.e. tool wear should be avoided. Common engineering materials for machining include steel, aluminium alloys, copper alloys and magnesium alloys, etc. In order to avoid excessive tool wear, steel is ruled out because the widely held view is that as ordinary carbon has a strong affinity for iron forming iron carbide ( $\text{Fe}_3\text{C}$ ) this should also be the case with diamond (cubic carbon) when machining steel. For non-ferrous materials, since the verification experiment possesses an impact nature, materials with high yield stress are also avoided, such as brass and aluminium bronze. Due to high wear rate on diamond tools, the experiments conducted on these materials cannot yield consistent or stable results. On the other hand, as one of the most important commercial magnesium alloys, Mg–9Al–1Zn alloy (AZ91) has a much lower hardness and is appropriate for the verification experiments. The AZ91 plate sample is concentrically mounted on a cylinder base which is fixed on the spindle of an ultra-precision diamond turning machine (Optoform 30 from Rank Pneumo, USA). The face turning is performed at a depth of cut ( $a_p$ ) of 20  $\mu\text{m}$ , and a feed rate of 20  $\text{mm min}^{-1}$  with a spindle speed of 8000 rpm. The tool nose radius is 2.503 mm and the rake angle is 15°. A force transducer Kistler 9252A is mounted with a pre-loading force under the tool shank.

A 14-bit multifunction Data Acquisition (DAQ) card (PCI-6132, National Instrument) is installed on a PC workstation to convert the analogue signals of the cutting forces. With the Kistler 5011B charge amplifier, the converted signals are recorded at a sampling rate of 1 MHz. The signals of the cutting force are further processed using fast Fourier transform (FFT) and studied with power spectrum density (PSD) analysis.

Based on the geometry of the workpiece surface, continuous face turning can only be achieved approximately at a radius of half the width of the workpiece surface from its centre. The intermittent cutting is performed at a distance from the centre larger than this radius, shown as  $z_{out}$  in Fig. 10.6. In the experiment, three sample locations,  $s_1$ ,  $s_{2a}$  and  $s_{2b}$  are selected in the inner zone ( $z_{in}$ ), and the outer zone, close to and far from the transition zone ( $z_{trans}$ ), respectively. At each sample location, the signals of cutting force are acquired and the profiles of the machined surface are examined. Surface roughness is evaluated by a non-contact 3D optical measuring system Alicona IFM G4.

The images of the machined surface are taken by an optical microscope Olympus BX60, as shown in Fig. 10.7a, b. The surface roughness in sample locations  $s_1$  and  $s_2$  are measured by Alicona IFM G4 with a profile length of 140  $\mu\text{m}$ , in accordance with ISO4288:1996. The average roughness ( $R_a$ ) is 12 nm in  $s_1$ , where the turning marks can be observed clearly, and 6.7 nm in  $s_2$ .

The force signals in the cutting direction in the three sample locations  $s_1$ ,  $s_{2a}$  and  $s_{2b}$  are trimmed and plotted sequentially in Fig. 10.8. In the sample location  $s_1$ , continuous cutting is performed. High excitation induced vibration is observed in the force signal at location  $s_{2b}$ . The transition zone is found close to the boundary between  $s_1$  and  $s_{2a}$ , where the periodic excitation from the impact between the tool tip and the edge of the plate workpiece starts to take effect. In Fig. 10.9, the normalised mean values of the measured force at different sample locations are shown with their standard deviation. Due to the effect of excitation, the standard deviation is highest at  $s_{2b}$ , which also leads to an increase in the mean force. The total force or the nominal cutting force directly acquired by the force sensor is actually the vibrational force, a major portion does not relate to the material removal process, i.e. irrelevant to the relative displacement in the tool-chip interface.

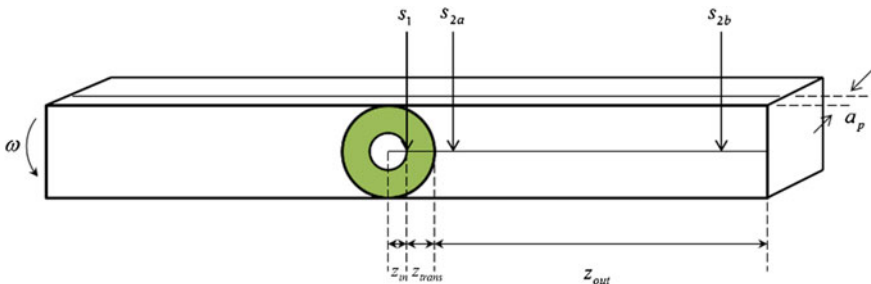
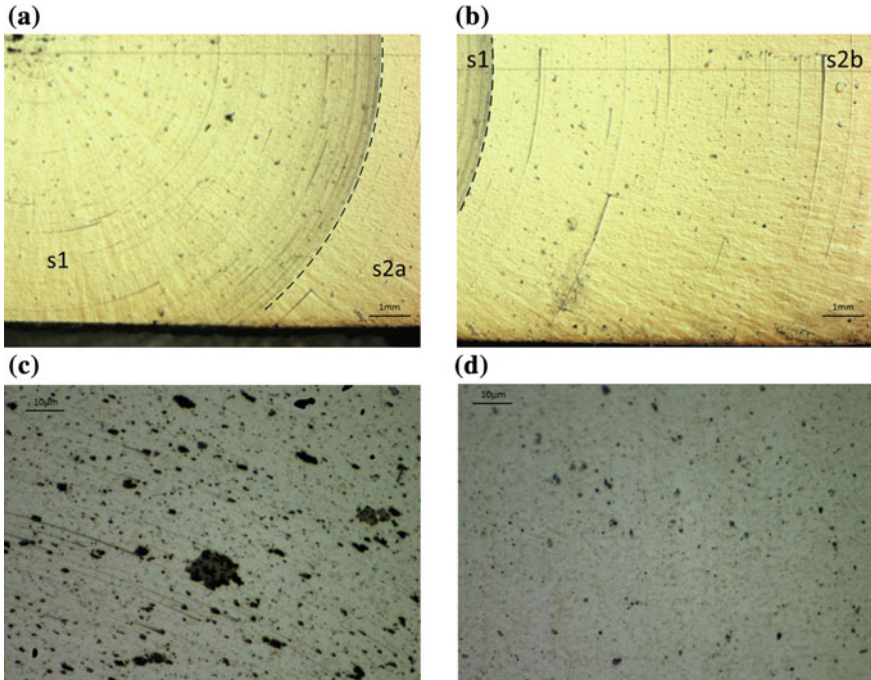


Fig. 10.6 Plate workpiece of Mg alloy AZ91





**Fig. 10.7** Optical images of the machined surface at different sample locations by Olympus BX60 (a) and (b), and Alicona IFM G4 (c) in  $s_1$  and (d) in  $s_2$

Therefore, the true cutting force is calculated based on the force resulting from the cyclic interaction between the work material and the cutting tool. As shown in Fig. 10.9, the trend of the true cutting force is significantly different from that of the nominal cutting force in that (i) the standard deviation remains at the same level in different sample locations and (ii) the effect of strain rate on the reduction of cutting force is revealed. Thus, it is of paramount importance, in the study of force signals, to clarify the concepts of vibrational force and cutting force. With the data of the true cutting force, the effect of HFTTV on the reduction of the mean cutting force is clearly observed in Fig. 10.9.

Power spectrum density (PSD) analysis is performed on the cutting force signals. The data are shown in the overlaid curves (Fig. 10.10) to reveal the frequency shift in the range of 12–14 kHz. Due to the high excitation and the lesser effect of process damping under much higher strain rates (the curve of  $s_{2b}$ ), the four primary peaks can be regarded as natural frequencies of the tool tip, which also sets up a datum line for further study. Corresponding to the identified characteristic twin peaks in the previous work (Wang et al. 2010b), the peaks  $P_2^{s_{2b}}$  and  $P_3^{s_{2b}}$  are traced for analysis in this chapter. In the case of mid-excitation, a reduction in cutting speed results in a lower strain rate and a more significant effect for process damping takes place, which leads to a left shift of the peaks  $P_2^{s_{2b}}$  and  $P_3^{s_{2b}}$  to the lower

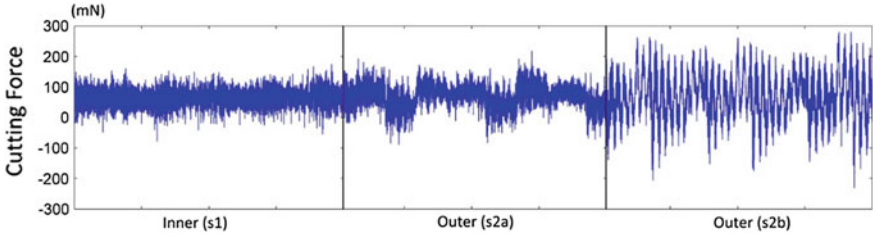
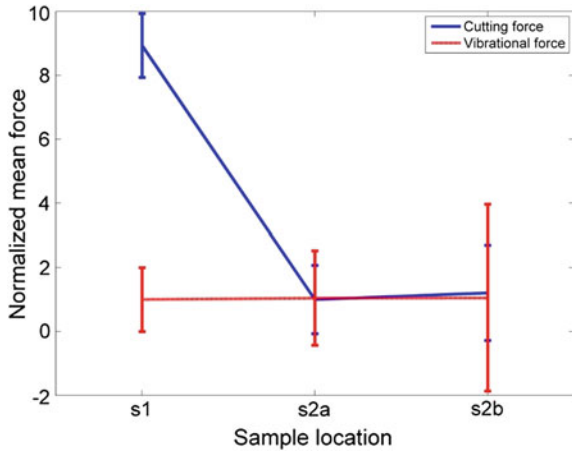


**Fig. 10.8** Measured cutting forces in sample locations of  $s_1$ ,  $s_{2a}$  and  $s_{2b}$

**Fig. 10.9** The normalised mean vibrational force and cutting force at different sample locations



frequencies, shown as the peaks  $P_2^{s_{2b}}$  and  $P_3^{s_{2b}}$ , in the curve  $s_{2a}$  of Fig. 10.5. In the continuous cutting (curve  $s_1$ ), no excitation is present since there is no impact between the tool tip and the edge of the rectangular plate workpiece in each rotational cycle. Thus, the observable peaks are the damped ones that are directly related to the material removal process, i.e. the characteristic twin peaks (CTPs).

Based on the spindle speed and the distance from the workpiece centre to the sample locations in our turning experiment, the maximum cutting speed is calculated as 0.67 m/s at the sample location  $s_{2b}$ , which is far slower than the velocity range 12–36 m/s employed in the cutting trials by Molinari et al. (2002) and other researchers. Therefore, the cutting speed cannot fully explain the formation of ASBs and the strain-rate boost induced by HFTTV can be regarded as one of the main reasons.

In conclusion, high-frequency tool-tip vibration (HFTTV) and the formation of adiabatic shear bands (ASBs) are intrinsically related physical phenomena which can be regarded as a system (ASB–HFTTV) in the micro-cutting process of ultra-precision diamond turning. The study of their relationship proposes new

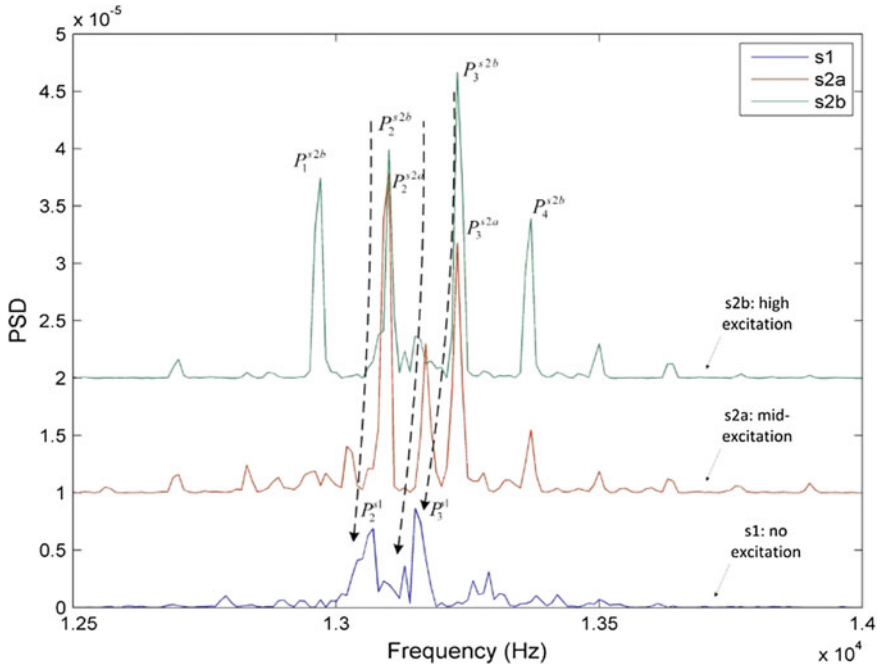


**Fig. 10.10** Power spectrum density (PSD) analysis of cutting force signals in the three sample locations s1, s2a and s2b

requirements on modelling and experimental methods. In this chapter, a dynamic model is established and a new experimental technique is proposed to verify the theoretical model and analysis. The major findings are summarised as below:

- (i) The cutting speed is not the real reason for the formation of ASBs in serrated chips. HFTTV is identified in the experiments to trigger the initiation of ASBs in terms of the boost in the strain rate in the cyclic relative tool-chip displacement during the micro-cutting process. A dynamic model is proposed to study the cyclic variation of the cutting speed and strain rate.
- (ii) A novel experimental method is proposed to examine different levels of applied excitation on a single workpiece in ultra-precision diamond turning. Based on the analysis of the natural frequencies of the structure of the cutting tool, the damped frequencies and the characteristic twin peaks (CTPs), the evolution of the frequencies reveals both the structural properties of the cutting tool and the factors of the material removal process.
- (iii) The method for the unbiased evaluation of cutting force is studied, in which the true cutting force is extracted from the vibrational force signal to exclude the effect of the excessive applied excitations. The experimental results prove that HFTTV reduces the cutting force.

- (iv) In the micro-cutting process, physical phenomena such as the ASB–HFTTV system can only be studied with a dynamic model. The elasticity factor is indispensable and plays as important a role as the plasticity factor in the material removal process. On the other hand, the static models oversimplify the analysis.

## References

- Astakhov, V. P. (1998). *Metal cutting mechanics* (pp. 95–123). CRC Press LLC.
- Budak, E., & Ozlu, E. (2008). Development of a thermomechanical cutting process model for machining process simulations. In *CIRP annals—manufacturing technology* (Vol. 57, pp. 97–100).
- Chao, B. T., & Bisacre, G. H. (1951). The effect of speed and feed on the mechanics of metal cutting. *Proceedings of the Institution of Mechanical Engineers*, 165, 1.
- Davim, J. P., & Maranhão, C. (2009). A study of plastic strain and plastic strain rate in machining of steel AISI 1045 using FEM analysis. *Materials and Design*, 30, 160–165.
- Dinzart, F., & Molinari, A. (1998). Structure of adiabatic shear bands in thermo-viscoplastic materials. *European Journal of Mechanics—A/Solids*, 17, 923–938.
- Dirikolu, M. H., Childs, T. H. C., & Maekawa, K. (2001). Finite element simulation of chip flow in metal machining. *International Journal of Mechanical Sciences*, 43, 2699–2713.
- Drucker, D. (1949). An analysis of the mechanics of metal cutting. *Journal of Applied Physics*, 20, 1013.
- Dudzinski, D., & Molinari, A. (1997). A modeling of cutting for viscoplastic materials. *International Journal of Mechanical Science*, 39(4), 369–389.
- Kececioglu, D. (1958). Shear strain rate in metal cutting and its effect on shear flow stress. *ASME Journal of Engineering for Industry*, 80, 158.
- Molinari, A. (1997). Collective behavior and spacing of adiabatic shear bands. *Journal of the Mechanics and Physics of Solids*, 45, 1551–1575.
- Molinari, A., Musquar, C., & Sutter, G. (2002). Adiabatic shear banding in high speed machining of Ti–6Al–4V: experiments and modeling. *International Journal of Plasticity*, 18, 443–459.
- Distasevicius, V., Gaidys, R., Rimkeviciene, J., & Dauksevičius, R. (2010). An approach based on tool mode control for surface roughness reduction in high-frequency vibration cutting. *Journal of Sound and Vibration*, 329, 4866–4879.
- Oxley, P. L. B. (1963). Rate of strain effect in metal cutting. *ASME Journal of Engineering for Industry*, 84, 335.
- Shirakashi, T., Maekawa, K., & Usui, E. (1983). Flow stress of low carbon steel at high temperature and strain rate (Parts I–II). *Bulletin of the Japan Society of Precision Engineering*, 17, 161–172.
- Wang, H., To, S., Chan, C. Y., Cheung, C. F., & Lee, W. B. (2010a). A study of regularly spaced shear bands and morphology of serrated chip formation in microcutting process. *Scripta Materialia*, 63, 227–230.
- Wang, H., To, S., Chan, C. Y., Cheung, C. F., & Lee, W. B. (2010b). A theoretical and experimental investigation of the tool-tip vibration and its influence upon surface generation in single-point diamond turning. *International Journal of Machine Tools and Manufacture*, 50, 241–252.
- Wasley, R. J. (1973). *Stress wave propagation in solids: an introduction* (pp. 19–24). New York: Marcel Dekker Inc.

- Wright, T. W., & Ockendon, H. (1992). A model for fully formed shear bands. *Journal of the Mechanics and Physics of Solids*, 40(6), 1217–1226.
- Wright, T. W., & Ockendon, H. (1996). A scaling law for the effect of inertia on the formation of adiabatic shear bands. *International Journal of Plasticity*, 12, 927–934.
- Zhou, L., Shimizu, J., Muroya, A., & Eda, H. (2003). Material removal mechanism beyond plastic wave propagation rate. *Precision Engineering*, 27, 109–116.